Measuring Laminar Burning Velocities using Constant Volume Combustion Vessel Techniques

Nathan I. D. Hinton

Balliol College

A thesis submitted in partial fulfilment of the requirements

for the degree of Doctor of Philosophy

Department of Engineering Science

University of Oxford

Michaelmas 2014

Measuring Laminar Burning Velocities using Constant Volume Combustion Vessel Techniques

Nathan Hinton DPhil

Balliol College, University of Oxford Department of Engineering Science

A thesis submitted in partial fulfilment of the requirements for the degree of Doctor of Philosophy, Michaelmas term 2014

Abstract

The laminar burning velocity is an important fundamental property of a fuel-air mixture at given conditions of temperature and pressure. Knowledge of burning velocities is required as an input for combustion models, including engine simulations, and the validation of chemical kinetic mechanisms. It is also important to understand the effect of stretch upon laminar flames, to correct for stretch and determine true (unstretched) laminar burning velocities, but also for modelling combustion where stretch rates are high, such as turbulent combustion models.

A constant volume combustion vessel has been used in this work to determine burning velocities using two methods: a) flame speed measurements during the constant pressure period, and b) analysis of the pressure rise data. Consistency between these two techniques has been demonstrated for the first time. Flame front imaging and linear extrapolation of flame speed has been used to determine unstretched flame speeds at constant pressure and burned gas Markstein lengths. Measurement of the pressure rise during constant volume combustion has been used along with a numerical multi-zone combustion model to determine burning velocities for elevated temperatures and pressures as the unburned gas ahead of the spherically expanding flame front is compressed isentropically. This burning velocity data is correlated using a 14 term correlation to account for the effects of equivalence ratio, temperature, pressure and fraction of diluents. This correlation has been modified from an existing 12 term correlation to more accurately represent the dependence of burning velocity upon temperature and pressure.

A number of fuels have been tested in the combustion vessel. Biogas (mixtures of CH_4 and CO_2) has been tested for a range of equivalence ratios (0.7–1.4), with initial temperatures of 298, 380 and 450 K, initial pressures of 1, 2 and 4 bar and CO_2 fractions of up to 40% by mole. Hydrous ethanol has been tested at the same conditions (apart from 298 K due to the need to vaporise the ethanol), and for fractions of water up to 40% by volume. Binary, ternary and quaternary blends of toluene, n-heptane, ethanol and iso-octane (THEO) have been tested for stoichiometric mixtures only, at 380 and 450 K, and 1, 2 and 4 bar, to represent surrogate gasoline blended with ethanol.

For all fuels, correlation coefficients have been obtained to represent the burning velocities over wide ranging conditions. Common trends are seen, such as the reduction in burning velocity with pressure and increase with temperature. In the case of biogas, increasing CO_2 results in a decrease in burning velocity, a shift in peak burning velocity towards stoichiometric, a decrease in burned gas Markstein length and a delayed onset of cellularity. For hydrous ethanol the reduction in burning velocity as H_2O content is increased is more noticeably non-linear, and whilst the onset of cellularity is delayed, the effect on Markstein length is minor.

Chemical kinetic simulations are performed to replicate the conditions for biogas mixtures using the GRI 3.0 mechanism and the FlameMaster package. For hydrous ethanol, simulations were performed by Carsten Olm at Eötvös Loránd University, using the OpenSMOKE 1D premixed flame solver. In both cases, good agreement with experimental results is seen. Tests have also been performed using a single cylinder optical engine to compare the results of the hydrous ethanol tests with early burn combustion, and a good comparison is seen.

Results from tests on THEO fuels are compared with mixing rules developed in the literature to enable burning velocities of blends to be determined from knowledge of that of the pure components alone. A variety of rules are compared, and it is found that in most cases, the best approximation is found by using the rule in which the burning velocity of the blend is represented by weighting by the energy fraction of the individual components.

Acknowledgments

In the writing of this thesis, I owe many thanks to a vast number of people who have contributed in a multitude of ways. None of this work would have been possible without such tremendous support.

My first thanks go to my supervisor, Professor Richard Stone for the huge amount of time and effort he has put into assisting my work. His guidance and direction have been invaluable, as have his vast knowledge and continual advice, as well as countless hours of practical assistance. I could not have asked for a more attentive or dedicated supervisor.

Financial support from EPSRC and Shell Global Solutions has also been vital for the running of the project, and is gratefully acknowledged. My thanks to Roger Cracknell from Shell Global Solutions for his support, both financially and in terms of technical direction. Thanks also to Trevor Davies for his input in the initial stages of the project.

I am also grateful for the insight and advice offered by other members of the combustion research community, too numerous to list in full here. Particular thanks to Dr. Martin Davy for timely suggestions (as well as the odd chat about motor racing and football), Paul Ewart and also to Kendal Bushe of the University of British Columbia for guidance on getting started with the FlameMaster package. A special mention is also due to Steve Marshall, for his assistance at the start of my project, and for setting a great foundation on which to base my research. Within the Department of Engineering Science, thank you to all of the staff who have been willing to lend a hand when needed, in particular Derek Pobgee, John Brumfitt and Maurice Keeble-Smith.

My colleagues and friends in the Combustion and Cryogenics group have been a tremendous source of support, amusement and distraction, not just on Friday afternoons. Thank you to Huayong Zhao, Fan Xu, Mengchen Hu, Kun Liang, Felix Leach, Joe Camm, Ian Berryman, Neil Scott, Farrukh Siddiqui, Johannes Mutzke, Safwan Bin Mohd Murad, Nick Papaioannou and Riyaz Ismail. Slightly further afield, thanks to Mike Dadd, Paul Bailey and Ben Williams. I also owe much to my friends both in Oxford and beyond; I am privileged to have met some wonderful people in my time at here, who have contributed to making it such an enjoyable place to live and work.

Finally, I would like to express my sincerest gratitude to all of my family for their unwavering support, and for believing in me at every stage of my studies; in particular my Mother and Father, for their ability to grant me perspective and self-belief; my Sister and Brother-in-law, for their patience in putting up with me here in Oxford; and to my dear late Grandmothers – I am so sorry that you couldn't see the end of this with me, but your encouragement has been, and will continue to be, a real inspiration. Thank you.

Contents

1 Introduction

Whilst the future of automotive transport is expected to consist of a mix of energy sources, with increased electrification of vehicle fleets and continued research into fuel cell technologies, the internal combustion engine will undoubtedly continue to remain one of the most common propulsion systems for the next 50 years, due largely to the far superior energy density offered by liquid fuels, and the cost effectiveness of the fuel distribution network. Furthermore, many sections of the transport network appear unsuitable for complete electrification. Beyond the transport sector, combustion will remain important in power generation and research of all aspects of combustion remains significant.

Recent developments in engine technology have seen vast improvements in both compression ignition and spark ignition engines with regards to performance and emissions, and a number of emerging technologies are receiving attention. Alongside this, pressure to reduce dependence upon fossil fuels primarily as a result of concerns regarding the impact of CO_2 emissions on global warming, decreasing air quality and long term availability and security of supply has demanded research into alternative fuels.

Further improvements in engine technology are dependent upon detailed simulations of the combustion process, which requires knowledge of the fundamental combustion properties of the fuel. One such property is the laminar burning velocity, which describes the propagation speed of a premixed flame relative to the fresh gas mixture. Whilst most practical uses of premixed combustion seldom feature laminar flames, the laminar burning velocity, as a fundamental parameter of a fuel-air mixture at given conditions, is an important input parameter for turbulent combustion models, as well as engine simulations, e.g. Lindström *et al.* (2005). Therefore, knowledge of the laminar burning velocity for fuels of interest is required for accurate simulations of new technologies.

Laminar burning velocities can be determined from chemical kinetic mechanisms, although the accuracy of the result will be dependent upon the accuracy of the mechanism itself. Unfortunately, chemical kinetic mechanisms are immensely complex for all but the simplest of fuels, making accurate modelling difficult and simulations computationally complex. Mechanisms can be improved by tuning the specific reactions within the mechanism using sensitivity analysis, as well as comparing values of fundamental properties from the simulations to values obtained experimentally. One such fundamental property frequently used is the laminar burning velocity. Therefore, in addition to providing direct values of burning velocity for use in simulations, experimental results are also needed to assist with the refinement of increasingly complex mechanisms of fuels of interest.

Numerous techniques have been used to determine laminar burning velocities over the years, although large discrepancies in the results can be seen. Figure 1.1 shows the maximum burning velocity of methane-air flames from a range of studies over the past century, demonstrating a wide range of values. Convergence of results is apparent only recently. This is largely attributable to the effects of stretch upon measurements, and so a greater understanding of these (and other) effects is required in order to produce more accurate and reliable data. Understanding of the effects of stretch is important not only for the accurate determination of burning velocities, but also because of the direct importance of stretch in flamelet modelling

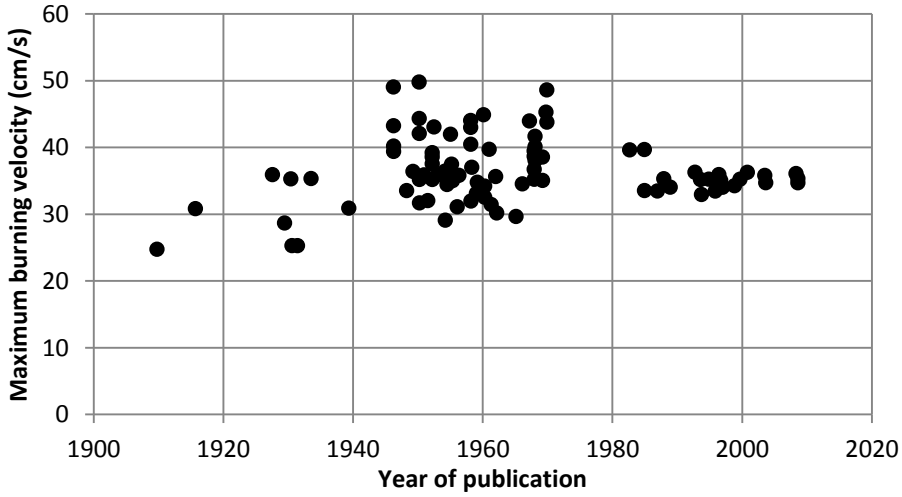

Figure 1.1 – Measured maximum burning velocity of methane-air mixtures at atmospheric conditions plotted against year of study. Reproduced using data from Egolfopoulos *et al.* (2014).

and turbulent combustion, Bradley *et al.* (1996). Furthermore, much of the data available corresponds to the burning velocity at ambient conditions, and so greater understanding of the effects of temperature and pressure is required in order to obtain values for engine relevant conditions.

Alongside development of combustion systems, and driven by a need to de-carbonise fuels, new alternative fuels are required. This then demands the determination of burning velocities for a range of temperatures and pressures for these fuels, both to understand the fundamental combustion behaviour but also to allow the performance of these fuels to be assessed in engine simulations. Biogas offers potential for reducing dependence upon fossil fuels, and in the case of liquid fuels, ethanol has received much attention as a readily available gasoline displacement, either as a pure fuel, or blended with gasoline.

Premixed combustion in a constant volume spherical vessel allows high pressure and temperature burning velocity data to be obtained in addition to allowing the effects of stretch to be examined through the use of flame front imaging. This technique also allows the development of a burning velocity correlation, facilitating easier use in combustion models, Vancoillie *et al.* (2012). This study uses a constant volume vessel to determine laminar burning velocities over a range of temperatures and pressures for a number of conventional and alternative fuels, and compares the results from both imaging and pressure measurement techniques.

2 Literature Review

2.1 Laminar premixed flames

2.1.1 Types of flames

Flames can be described firstly in terms of how the fuel and oxidizer are mixed and subsequently in terms of the fluid flow conditions. Regarding mixing of fuel and oxidiser, flames can be broadly divided into two classes: premixed and non-premixed (diffusion) flames. In a premixed flame, the fuel and oxidant are mixed on a molecular level prior to any combustion. In a diffusion flame, the fuel and oxidant are initially separated, and the flame front propagates as the reactants mix, with the reaction taking place at the interface. Depending on flow conditions, flames can be laminar or turbulent. The conditions of premixing and fluid flow will depend upon the combustion system considered. Table 2.1 gives some examples of combustion systems and the flame types involved.

Table 2.1 – Example combustion systems in terms of flame type (developed from Warnatz *et al.* (2006)).

Fuel/Oxidizer mixing	Fluid motion	Examples
Premixed	Turbulent	Spark-ignited gasoline engine Low NO_x stationary gas turbine
	Laminar	Stationary flame burners Constant volume combustion vessels Early flame growth in SI engines
Non-premixed	Turbulent	Pulverized coal combustion Aircraft turbine Diesel engine H_2/O_2 rocket motor
	Laminar	Wood fire Radiant burners for heating Candles

For the determination of laminar burning velocity, flames considered will be limited to laminar premixed flames.

2.1.2 Flame structure

A basic overview of structure of a laminar premixed flame front is useful to be able to form a definition of laminar burning velocity. Turns (1996) defines a flame as "a self-sustaining propagation of a localized combustion zone at subsonic velocities". A premixed flame is considered as a propagating combustion wave through a nominally homogeneous mixture, Strahle (1993). The standard description of flame structure found in the literature such as the overview by Rallis and Garforth (1980), divides the flame front into two regions: the preheat and reaction zones. The preheat zone is where the mixture receives its temperature rise primarily via thermal conduction and a small amount of convection from the reaction zone (radiative heat transfer is negligible). The reaction zone is where the actual combustion reactions take place; upon reaching the ignition temperature T_i, each element of gas begins undergoing chemical reaction, producing more heat, until an equilibrium temperature T_f (or often T_b, where the subscript b refers to 'burned' gas) is reached. The chemistry in the reaction zone can be described by chemical kinetic models (introduced in section 3.2) and will often also contain a luminous zone. Figure 2.1 shows a typical temperature profile of a flame front, over the entire flame thickness (which is more commonly denoted by δ). Since the temperature profile reaches T_u and T_b asymptotically, the boundaries of the flame front are commonly defined by 99% of the difference from the ignition temperature T_i.

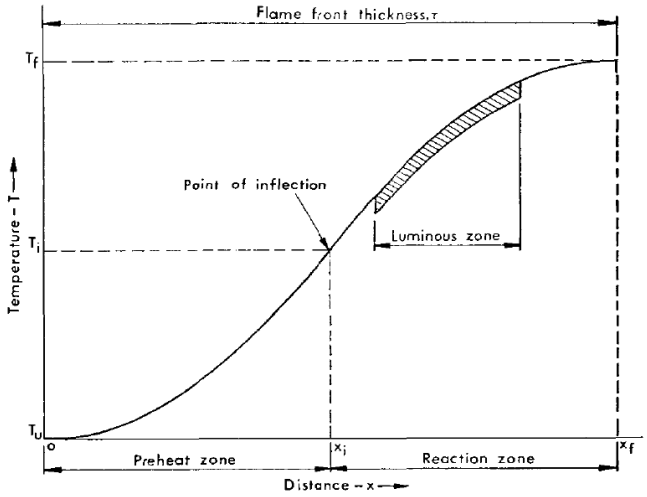

Figure 2.1 – Typical temperature profile of a flame front, Rallis and Garforth (1980).

2.1.3 Definition of laminar burning velocity

Widely acknowledged as a fundamental property of a given fuel/oxidant mixture at specified conditions, the laminar burning velocity is defined as the velocity at which an unstretched 1D flame front moves, relative to the velocity of the gas into which it is propagating (see Figure 2.1). In other words, it is the propagation speed of the flame in a stationary gas:

$$S_u = S_s - S_g \quad \textbf{(2.1)}$$

where: S_u is the unstretched laminar burning velocity

S_s is the unstretched laminar flame speed

S_g is the unburned gas velocity immediately ahead of the flame front.

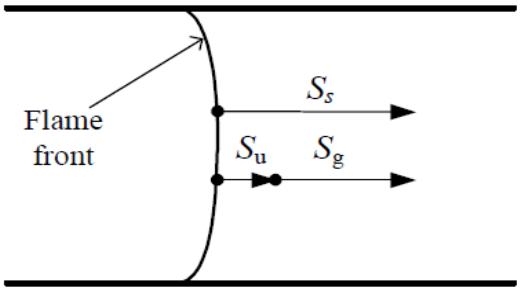

Figure 2.2 – Premixed flame in a tube, from Marshall (2010).

This implies that the laminar burning velocity is then derived only from the chemical reactions and transport phenomena at the conditions of interest; at a given temperature, pressure and mixture composition a single value of burning velocity is obtained, that is independent of the flow conditions. If we fix the frame of reference so that the flame is stationary, and apply continuity, we can relate the velocities v of the unburned and burned gases via their densities:

$$S_u \rho_u A_f = v_u \rho_u A_f = v_b \rho_b A_f \quad \textbf{(2.2)}$$

The product density is much lower than that of the reactants as a result of being heated by the flame; for a typical hydrocarbon-air flame at atmospheric pressure the density ratio is approximately seven, Turns (1996), which will require that the burned gas velocity is higher than the unburned gas velocity, meaning that there is significant acceleration of gases across the flame.

Since burning velocity as defined in Figure 2.2 is the speed at which the flame front is propagating into the unburned gas, the second term in Equation (2.2) can be considered the rate at which unburned gas is being consumed:

$$S_{\mathrm{u}} A_{\mathrm{f}} \rho_{\mathrm{u}} = -\frac{\mathrm{d}m_{\mathrm{u}}}{\mathrm{d}t} \qquad \textbf{(2.3)}$$

where A_{f} is the area of the flame front, ρ is density, m is the mass and the subscript u refers to the unburned gas. In terms of the rate of production of burned gas:

$$S_{\mathrm{u}} = \frac{1}{A_{\mathrm{f}} \rho_{\mathrm{u}}} \frac{\mathrm{d}m_{\mathrm{b}}}{\mathrm{d}t} \qquad \textbf{(2.4)}$$

These definitions of burning velocity allow us to investigate existing methods of making measurements. Laminar burning velocities for typical fuels are of the order of 10s of cm s^{-1}, Strahle (1993). As a fundamental parameter, burning velocity should be independent of the techniques used in its determination (section 2.2). However, it is clear that this is not the case, and so the impacts of experimental techniques need to be addressed (sections 2.5, 2.6 and 2.7).

2.1.4 Simplified analysis of laminar premixed flames

Many theories of laminar flames have been developed over the years with an intention of reaching analytical solutions providing expressions for properties such as the laminar burning velocity. Kuo (1986) cites many published theories and these have focused on either heat or mass diffusion effects, or combined both into more detailed theories. These will not be detailed here, as their intricacies fall beyond the scope of this report, but some results are given as they provide some insight into the factors that affect the burning velocity, as detailed in section 2.3.

Turns (1996) presents a simplified analysis of a laminar premixed flame which combines the principles of heat transfer, mass transfer, global chemical kinetics and thermodynamics, relying on the 1D conservation equations for mass, species and energy, and simplifying assumptions for thermodynamic and transport properties. The assumptions stated are not assessed for their validity for the flames of interest; however the analysis still provides insight

into general dependencies of burning velocity reflected in experimental studies. The following expression for burning velocity is obtained:

$$S_{\mathrm{u}} \propto \bar{T}^{0.875} \cdot T_{\mathrm{u}}^{0.5} \cdot T_{\mathrm{b}}^{-n/2} \cdot \exp\left(\frac{-E_{\mathrm{a}}}{2R_{\mathrm{u}}T_{\mathrm{b}}}\right) \cdot P^{(n-2)/2} \qquad \textbf{(2.5)}$$

where T_{u}, T_{b} and $\bar{T}$ are the unburned gas, burned gas and mean flame temperatures respectively, which in the simplified analysis is $\bar{T} = 0.5(T_{\mathrm{u}} + T_{\mathrm{b}})$ assuming a linear temperature profile in the flame front itself, n is the overall reaction order (more detail given in section 3.2.2) and E_{a} is the activation energy. The analysis also results in the relationship between burning velocity and flame thickness:

$$\delta = \frac{\alpha}{S_{\mathrm{u}}} \qquad \textbf{(2.6)}$$

where $\alpha = k/\rho_{\mathrm{u}}c_{\mathrm{p}}$ is the thermal diffusivity in terms of thermal conductivity k, unburned gas density ρ_{u} and specific heat capacity of the mixture c_{p}, resulting in

$$\delta \propto \bar{T}^{0.875} \cdot T_{\mathrm{u}}^{-0.5} \cdot T_{\mathrm{b}}^{n/2} \cdot \exp\left(\frac{E_{\mathrm{a}}}{2R_{\mathrm{u}}T_{\mathrm{b}}}\right) \cdot P^{-n/2} \qquad \textbf{(2.7)}$$

Figure 2.3, adapted from Andrews and Bradley (1972) shows how the flame thickness varies with equivalence ratio for methane-air flames at atmospheric temperature and pressure. Flame thickness has important implications on turbulent burning, as thinner flames are wrinkled more easily by smaller turbulence length scales.

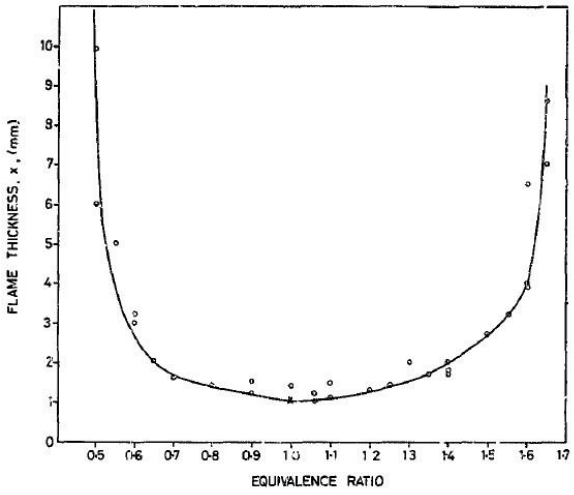

Figure 2.3 – Flame thickness of atmospheric methane-air flames. Adapted from Andrews and Bradley (1972).

2.2 Techniques for measuring laminar burning velocities

Methods of measuring laminar burning velocities fall into two main groups: stationary flame and non-stationary flame methods. Commonly used techniques are reviewed here, since existing burning velocity data has been obtained via a wide variety of these methods and so an awareness of the methods used is necessary.

2.2.1 Stationary flame methods

Stationary flames can be used to measure burning velocities by establishing a flame at the mouth of a burner, into which a continuous mixture of fuel and oxidant is fed at a constant velocity. Various types of burner have been used with different approaches to determining the burning velocity, with differing degrees of accuracy. These are summarised below.

2.2.1.1 Bunsen burner

This is one of the most common methods used for early burning velocity measurements, largely because of the simplicity of the equipment involved. Burning velocity can be established from Bunsen type burners from a variety of methods described here. Burners can be either cylindrical or slot burners; cylindrical burners produce a cone-shaped flame, whereas slot burners produce a more prismatic flame. Singer (1953) provides an early comparison of cylindrical and slot burners and found that the slot burners reduced curvature of the flame front and were more suited to measurements using the flame area measurement method.

Flame area measurement – The simplest and earliest method of making burning velocity measurements from a cylindrical burner was by dividing the volume flow rate of premixed fuel and oxidant mixture by the estimated surface area of the flame, using the principle given by Equation (2.3). Although simple, there are some significant problems with the method, as described by Rallis and Garforth (1980). Perhaps the most significant issue here is that in using the area of the flame front, the burning velocity obtained will necessarily be an average burning velocity over the entire flame surface. It is found that the burning velocity will vary spatially,

due both to curvature resulting in stretching of the flame front (see section 2.5.2), and temperature variations; heat transfer to the burner rim will reduce the flame temperature from the adiabatic flame temperature causing a lowering of burning velocity whereas at the tip the temperature may be increased as the result of being heated from all sides of the cone. This heating or cooling of different regions of the cone will also cause additional curvature of the flame front. By considering a frustum of the cone as described by Harris *et al.* (1949), the most significant areas of error (the flame tip and base of the flame at the burner mouth) can be removed although there will then be uncertainty of the mass flow rate associated with the frustum. Also significant is the difficulty in establishing the position of the flame front from which to measure the flame front area. Various methods are available; natural light photography, shadowgraphs and schlieren photography, and each method produces a different flame front position. As described by Andrews and Bradley (1972), the area required to accurately determine the burning velocity is the locus of points where the gas temperature rises just above the initial temperature, since in Equation (2.3) burning velocity was derived by considering flow rate of unburned gas into the flame front which corresponds to the left hand side of the profile shown in Figure 2.1. However, this cone will always be within those that can be visualised by the above methods. In a review of burner techniques, Linnet (1953) concludes that using the cone produced by Schlieren images provides the most accurate representation of the flame edge, but clearly this is an issue that introduces uncertainty in subsequently calculated burning velocities. Discussion of the schlieren flame front position is given in section 2.2.3.

Cone angle measurement – from the angle of the flame cone, and the speed of the incoming premixed fuel and oxidant mixture, it is possible to make an estimation of burning velocity, since the burning velocity can be considered the vector normal to the surface of the flame front once the flame has been stabilised:

$$S_{\mathrm{u}} = U \sin\alpha \qquad \textbf{(2.8)}$$

where U is the unburned gas velocity and α is the cone angle.

However, this method retains the problem of identifying the exact location of the flame front, which will introduce errors into measurements, since α will need to be the angle of the cone produced by the cold flame front. It is also another source of error that the angle of the flame will vary along the flame front as a result of varying burning velocity again due to curvature and variations in temperature, so the burning velocity measured will depend on the region of the flame chosen.

Flame thrust method – By measuring the pressure difference across the flame front and applying the 1D momentum equation, the burning velocity can be established, Lewis and von Elbe (1961). The pressure difference can be measured using a Pitot tube, such as in the work by Edmondson and Heap (1969). The difficulty here is that the pressure difference is very small, and so measurements are prone to significant error.

Particle Image Velocimetry (PIV) – In this technique, the fuel/oxidant mixture is seeded with inert particles, which can be tracked through a succession of photographs to establish the flow field. Since the technique measures the speed of the particle, the particle must be chosen to ensure that the gas velocity and particle velocity are able to be considered equal, by having a suitably large drag/inertia ratio. From this the burning velocity can be established.

Laser-Doppler Velocimetry (LDV) - Alternative seeding technique, whereby the seeded particles scatter light leading to a Doppler effect, i.e. a shifting of the frequency of the scattered light, as described by Warnatz *et al.* (2006). When the scattered light is mixed with laser light the difference in frequency can be detected and is proportional to the speed of the particle. This method is used successfully by Cohé *et al.* (2009) in their study of lean premixed CO_2 diluted methane flames.

In summary, whilst Bunsen burner methods have been extensively used in the past due to their relative simplicity, the inherent disadvantages mean they are considered amongst the least reliable methods and their use in early burning velocity measurements is a factor in the large

disparity seen in these early methods (see Figure 1.1). However, developments in nozzle design and PIV and LDV techniques mean that this method has improved and is still in use.

2.2.1.2 Flat flame burner

The formal definition of laminar burning velocity presented in Section 2.1.3 requires that the flame is flat and 1D. Clearly none of the above burner methods produce such a flame, but flat flame burners can be designed to provide a relatively close approximation, with negligible stretch rates. The Powling (1949) burner developed an approach whereby a flat flame could be stabilised above the burner by ensuring "a) that the reacting gases should be made to issue from a burner port with perfectly uniform velocity distribution, that is, free from the effect of friction at the tube walls, and b) that this flow should remain undisturbed by the behaviour of the hot products", when the burning velocity is equal to that of the unburned mixture from the burner. The temperature of the incoming gases is controlled by a cooling jacket, before passing through a diffuser to ensure laminar flow. The issue of flow retardation due to friction is addressed by providing a flow of inert gas around the edge of the burner, which was shown to have negligible mixing with the reacting flow. The burning velocity is then calculated in a similar way to the flame area method used for cylindrical burners:

$$S_{\mathrm{u}} = \frac{\dot{V}}{\pi r^2} \qquad \textbf{(2.9)}$$

Whilst this technique allowed a closer approximation to a flat flame, it still suffered with problems of heat loss to the burner rim, which meant that the calculated burning velocity is not the adiabatic burning velocity. To counter this, more advanced designs have been developed and have gained increased popularity in recent years. The most prominent is the "Heat flux burner" discussed in section 2.2.1.3.

2.2.1.3 Heat flux burner

The heat flux burner as described by Bosschaart and de Goey (2003) addresses the problem of heat transfer to the burner, to enable a more accurate determination of the adiabatic burning

velocity, without requiring extrapolations to correct for either heat loss or stretch effects. A thin brass burner plate with a hexagonal perforation pattern is used to stabilize a flat flame and is fitted with thermocouples to determine the radial temperature profile which corresponds to the heat loss from the flame to the burner. The outer edge of the plate is held at typically 60 K above the unburned gas temperature so that it is capable of transferring heat to the incoming unburned gas. The burner plate will be gaining heat by conduction from the flame front, but for the case of the adiabatic flame, the heat gained by the plate will be matched by the heat lost to the incoming unburned gas. In this case, the radial temperature profile across the plate will be flat. The velocity of the incoming unburned gas is varied, and the adiabatic burning velocity is found from interpolation between temperature profiles. Very good accuracy is claimed using this method, as good as ±0.5 cm/s for stoichiometric methane/air flames at atmospheric conditions. As a result, this method is becoming widely used by many groups investigating laminar burning velocities. The method is also being extended to pressures up to 5 atm, as seen in the work of Goswami *et al.* (2013).

2.2.1.4 Counter-flow burner

This method works on the principle of providing a stagnation surface ahead of the flame, which can be a plate, a counter-flow of inert gas, or a second flame, such as in the method used by Egolfopoulos *et al.* (1989). The use of a second flame is intended to prevent heat loss to the surrounding gases. PIV or LDV can be used to find a minimum velocity, which corresponds to a stretched burning velocity. The stretch rate can also be calculated, allowing extrapolation back to the unstretched burning velocity. Pressures above 6-7 atm are not possible, apparently due to instabilities resulting from the effects of increased flow Reynolds number at increased pressures, Tse *et al.* (2000)

A significant limitation of all the burner methods is that it is difficult to control the pressure and temperature. In many applications, such as an internal combustion engines, combustion takes place at an elevated temperature and pressure, so burning velocity data for

these conditions is needed. Whilst there are recent improvements to enable certain burner methods, such as the heat flux method, to produce higher pressure and temperature results, data for the more extreme conditions cannot yet be obtained in this way.

2.2.2 Non-stationary flame methods

A variety of methods are available to measure burning velocities from propagating flames. The earliest and most straightforward involve measuring a flame propagating down a length of tube, but have many associated problems with heat transfer to the walls of the tube, and led Rallis and Garforth (1980) to consider such methods as being "inherently unsatisfactory". These methods do not appear to be commonly used in current measurements of burning velocity and so will not be considered further. More successful and versatile methods involve spherically expanding flames within a combustion vessel and can generally be divided into constant pressure and constant volume methods.

2.2.2.1 Constant Pressure Methods

Constant pressure combustion can be achieved by a variety of methods. An early method of measuring burning velocity from constant pressure flame propagation is the so-called 'soap bubble method', in which the combustible mixture is contained within a soap bubble at a determined pressure and ignited. As the combustion process takes place, the bubble (and hence volume filled by the gases) expands allowing the pressure to remain constant. Flame speeds are determined by measuring the flame radius, and have been found to be essentially constant under this condition of constant pressure. Linnet (1953) reviews this method, stating the advantages of simple spherical geometry and constant temperature of the burned gas, leading to more straightforward modelling of the flame propagation. Disadvantages include sensitivity to radius measurements introducing a source of error, as well as problems with contamination of the mixture from the soap bubble itself and diffusion through the film. There are also limitations on the range of burning velocities that can be considered by this method.

In a constant volume chamber, the initial stages of combustion occur without any overall rise in pressure, so measurements made during these initial stages (usually by schlieren photography) can be considered as constant pressure results.

Some more complex constant pressure combustion chambers have been used, such as that reported by Tse *et al.* (2004), where the main combustion chamber sits within a larger outer chamber which become linked to allow the expanding gases to flow into the outer chamber in order to obtain constant pressure during combustion, the aim being to enable higher initial pressures to be used (initial pressure in constant volume vessels is limited by the need to keep the final pressure within safe working limits).

2.2.2.2 Constant Volume Methods

Constant volume combustion vessels are used for producing spherically propagating flames. Hence constant volume combustion chambers are often spherical (or near spherical), although some reported in the literature are cylindrical or even cuboidal, e.g. Liao *et al.* (2004). Central ignition, usually spark ignition via a pair of electrodes but sometimes laser ignition such as described by Bradley *et al.* (2004) results in a spherical flame propagating outwards through the unburned mixture. Two distinct methods are available: flame speed measurements during the initial pre-pressure combustion phase, and analysis of the pressure-time history during combustion. There are a number of advantages of using such apparatus, perhaps the most important being that combustion at elevated temperatures and pressures is possible, since these vessels are typically able to withstand high absolute pressures. This overcomes a large problem with many of the burner methods discussed previously. When an appropriate method of analysing flame front images is used, the effect of stretch on the burning velocity can be accurately determined since the conditions of flame stretch are inherently well defined for the case of an outwardly propagating spherical flame. Analysis of the pressure-time history allows burning velocities to be deduced for a large range of temperatures and pressures from a single

experiment, which led Rallis and Garforth (1980) to describe the constant volume technique as "the most versatile and accurate" of the propagating flame methods.

As described in section 2.2.2.1, the initial stages of flame propagation take place at conditions of constant pressure and in many cases where constant volume vessels are used, analysis is limited only to the initial pre-pressure rise period. This technique has been commonly used in recent studies such as Bradley *et al.* (2009). In this case, it is necessary to image the flame front, typically using schlieren photography, to make an estimate of unstretched flame speed (S_s as shown in Figure 2.2) . This unstretched flame speed must first be determined by extrapolating for conditions of flame stretch, a process which is discussed further in section 2.5.6. Unstretched burning velocity (our defined laminar burning velocity) can be deduced from unstretched flame speed by the relation

$$S_u = S_s \frac{\rho_b}{\rho_u} \qquad \textbf{(2.10)}$$

However, the use of this method is limited to unstretched burning velocities, and so cannot be used directly to determine the effects of stretch on burning velocities, only upon flame speed. Therefore, to determine burning velocity by this method an extrapolation of flame speed to conditions of zero stretch is first required. The phenomenon of flame stretch, the effect upon both flame speed and burning velocity, and methods of extrapolation are more fully explained in section 2.5.

Recently a novel method has been proposed by Varea *et al.* (2012), which is designed to extract laminar burning velocity data from outwardly expanding spherical flames at constant pressure, based upon flame speed and fresh gas velocity. It is argued that this technique is advantageous in determining burning velocity and the effect of stretch, as it more closely represents the true definition of burning velocity, without needing to use physicochemical properties. In the more traditional method described by Equation (2.10), the flame speed must first be extrapolated to zero stretch, before the density ratio at chemical equilibrium for adiabatic combustion is applied. Firstly, as previously mentioned this prevents the

determination of the effect of stretch on burning velocity, characterised by the Markstein length, L (sometimes referred to as the unburned gas Markstein length, L_u). Secondly, the burned gas temperature is calculated for adiabatic conditions, which may be inaccurate for some mixtures, particularly those where the CO_2 or H_2O content is high and effects of radiation are potentially greater. This could therefore lead to an erroneous measurement of unstretched laminar burning velocity. Returning to the definition given in Equation (2.1), burning velocity can be calculated if both the flame speed and unburned gas velocity are both known, which is what this method aims to find. Hence the dependence upon calculation of the density ratio is avoided, and since this method is based upon the disappearance of cold unburned gas, it allows determination of the unburned gas Markstein length. The authors claim that this is the first time that direct measurements of unburned Markstein length have been made.

Measurement of the unburned gas velocity at the entrance of the preheat zone of the flame front is the main difficulty with this method, since the accurate measurement has to be made within a zone of approximately 1 mm. The method requires the fresh gas mixture to be seeded with silicone oil particles, which evaporate at the entrance of the flame front. This enables the flame front to be visualized (and hence flame speed deduced), but also allows PIV along with an adaptive window algorithm to determine the speed of the unburned gas.

Beyond the initial pre-pressure period, burning velocity can be deduced from the measured pressure-time history measured within the vessel. As the flame continues to propagate, the expansion of the burned gases behind the flame front causes an increase in pressure as well as an increase in the burned and unburned gas temperature. By using an appropriate combustion model, it is possible to determine burning velocity from the pressure history inside the bomb, which can be determined using a pressure transducer mounted inside the vessel. Various models have been developed over the years, and are described separately in section 3.1.4 for clarity. The result is that the values of burning velocity obtained are for conditions of temperature and

pressure following an isentrope from the original conditions. As is seen in section 2.3, both temperature and pressure affect the burning velocity, hence it is necessary to perform tests at differing initial conditions of temperature and pressure in order to decouple the effects. This will lead to many computed values of burning velocity, particularly if tests are performed at a range of equivalence ratios or diluent fractions and so this can typically lead to large data sets. To make sense of this data, it is typically fitted to a correlation designed to represent the effects of the influencing variables. Correlation forms used within the literature are presented in section 2.4.

2.2.3 Schlieren photography

Schlieren photography works on the principle of refraction of light due to density gradients in the medium through which it is propagating, typically due to gradients in pressure and temperature. In a schlieren image, the refraction of light passing through such density gradients will result in areas of relative light and dark. In the case of a flame front, where large temperature gradients exist, schlieren photography is particularly effective at producing an image of the flame front. The refractive index is given by

$$n = 1 + k\rho \tag{2.11}$$

where k is known as the Gladstone-Dale coefficient. For an ideal gas this becomes:

$$n = 1 + \frac{kp}{RT} \tag{2.12}$$

To exploit this phenomenon, a system of mirrors or lenses is required. In the simplest case of a 2D system with a point light source, as depicted in Figure 2.4, the light is initially collimated (so that the light rays run parallel to the optical axis) into which the density disturbance i.e. the flame front in introduced. The image is generated using a knife-edge placed to partially block the beam. As the diagram shows, a ray deflected upwards will brighten a point on the detector, whereas a downward deflected ray will be blocked by the knife edge, meaning that the corresponding point on the detector will appear darker.

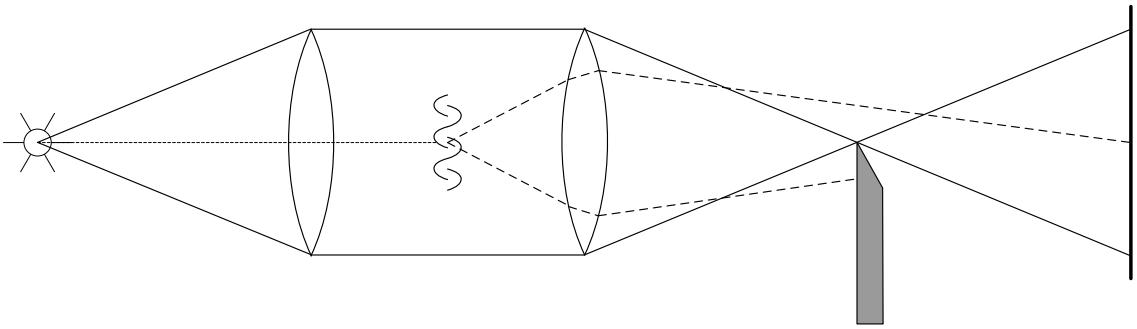

Figure 2.4 – Schematic of a simple schlieren system with a point light source.

In a computational study of spherically expanding flames, Bradley *et al.* (1996) define the flame radius as the cold front radius r_u where the isotherm is 5 K above the ambient temperature of the unburned gas, and subsequently use this value for calculation of burning velocity and stretch rates. This is trivial in a computational study, but perhaps less so in experimental procedures, where the schlieren front is more likely to represent an isotherm of about 450 K. The differences between these isotherms are found to be less than 0.25 mm for stoichiometric methane flames but decreases with flame thickness. This difference could introduce an error into values of burning velocity and stretch rate. The empirical relationship

$$r_u = r_{sch} + 1.95\delta_l \left(\frac{\rho_u}{\rho_b}\right)^{0.5} \quad \textbf{(2.13)}$$

was derived to calculate the cold front radius from the schlieren radius, where δ_l is a characteristic hydrodynamic length given by

$$\delta_l = \frac{v}{S_u} \quad \textbf{(2.14)}$$

where v is the kinematic viscosity.

2.3 Factors affecting burning velocity

Since this investigation includes burning velocity results for a variety of fuels at different conditions, some background on the factors affecting burning velocity is provided. This is also of importance when considering the form of burning velocity correlations in section 2.4.

2.3.1 Fuel/air mixture composition

The burning velocity will be very dependent upon the composition of the mixture under investigation, both in terms of the type of fuel, and the ratio of fuel and air. In the field of laminar burning velocities, it is most common to refer to the equivalence ratio φ of the mixture, defined as the ratio of the fuel/air ratio (FAR) to the stoichiometric fuel/air ratio (FAR_{st}). Therefore, a fuel rich mixture will have an equivalence ratio greater than 1, and a fuel lean mixture less than 1.

2.3.1.1 Fuel type

Burning velocities are strongly affected by the adiabatic flame temperature, and so the enthalpy of combustion of a fuel will have a big impact upon the burning velocity. This effect is studied in the work of Bradley *et al.* (1991), and a clear trend is seen between the burning velocity and enthalpy of combustion within families of fuels. However, fuel structure is also significant, since it has an impact upon the reaction kinetics, and this is shown in Figure 2.5, where particularly for aromatics, the correlation between burning velocity and adiabatic flame temperature is poor, suggesting that kinetic effects are playing a significant role.

Comparative studies of groups of fuels, for example that of Davis and Law (1998) where the C1 to C8 hydrocarbon fuels were tested using a counter-flow burner technique, have sought

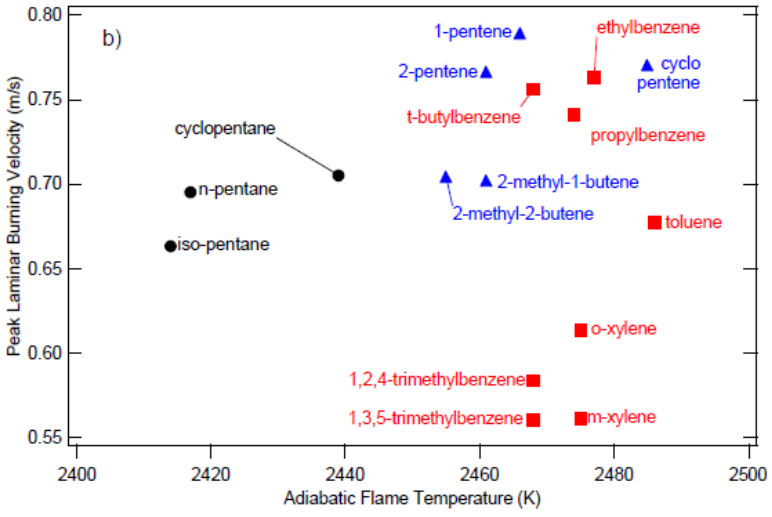

Figure 2.5 – Peak laminar burning velocity against adiabatic flame temperature, Farrell *et al.* (2004). Black circles: alkanes, blue triangles: dienes, red squares: aromatics. Reproduced with permission from SAE international.

to establish the effect of fuel structure on burning velocity. They found that for a given number of carbon atoms, the lesser the degree of saturation, the faster the burning velocity (i.e. alkynes have higher burning velocities than alkenes which in turn are faster than alkanes). Structural branching was also shown to reduce burning velocity. A more recent study by Farrell *et al.* (2004) used spherically expanding flames to obtain both pressure and optically derived burning velocity measurements at a single condition of temperature and pressure, and extended the investigation to include some oxygenated and aromatic fuels, finding that the oxygenated fuels have a higher burning velocity than their corresponding alkanes, and aromatics have a wide spread of burning velocities (as again illustrated in Figure 2.5)

2.3.1.2 Equivalence Ratio

The effect of equivalence ratio is primarily tied to the effect it has on the adiabatic flame temperature, since the effects of kinetics will be less dependent upon equivalence ratio, although this is not always the case for rich mixtures. Marshall (2010) demonstrated this link with adiabatic flame temperature by comparing experimental results for burning velocity of mixtures with varying equivalence ratio with the theoretical adiabatic flame temperature for the mixtures as calculated by an equilibrium solver. Peak adiabatic flame temperature, and hence peak burning velocity is usually found to occur slightly rich of stoichiometric, as a result of dissociation. Figure 2.6 shows the findings of Farrell *et al.* (2004), demonstrating typical trends for burning velocity with equivalence ratio.

Various expressions have been used by different workers to express the dependence upon equivalence ratio. Metghalchi and Keck (1982) used an expression based on the equivalence ratio for maximum burning velocity:

$$S_u = B_m + B_2(\varphi - \varphi_m)^2 \qquad \textbf{(2.15)}$$

where B_m and B_2 are constants for a given fuel, and φ_m is the equivalence ratio according to maximum burning velocity for that fuel. Many expressions found in the literature use a form of

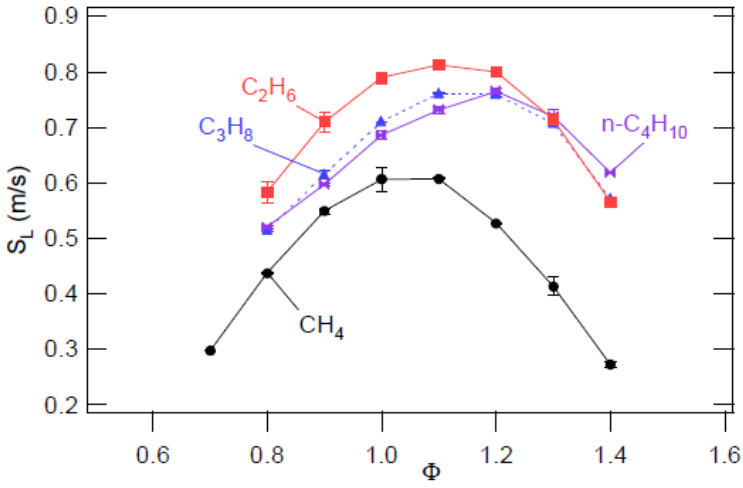

Figure 2.6 – Laminar burning velocity of C1 – C4 alkanes against equivalence ratio, Farrell *et al.* (2004). Reproduced with permission from SAE International.

polynomial expression. For example, Sharma *et al.* (1981) proposed a relation of the form

$$S_u = A + \frac{B}{\varphi} + \frac{C}{\varphi^2} + \frac{D}{\varphi^3} \qquad \textbf{(2.16)}$$

Elia *et al.* (2001) present a quadratic dependence upon equivalence ratio, and Clarke (1994) used a quartic expression:

$$S_u = S_{u,0} + S_{u,1}(\varphi - 1) + S_{u,2}(\varphi - 1)^2 + S_{u,3}(\varphi - 1)^3 + S_{u,4}(\varphi - 1)^4 \qquad \textbf{(2.17)}$$

where it can be seen that $S_{u,0}$ is the stoichiometric burning velocity at reference conditions.

Subsequently, Marshall *et al.* (2010) used some modelling data of methane flames to assess the quality of fit whilst changing the order of the polynomial. Whilst the number of modelling points used was relatively small, their findings suggest that the quartic gives the best fit to the trend, and so continued to use this form. It is also found that the temperature and pressure dependence of burning velocity is also a function of equivalence ratio.

2.3.2 Temperature

Temperature has been found to be one of the biggest factors affecting flame speed. This can be seen from analytical solutions, such as in Equation (2.5). This relationship implies a strong dependence upon temperature, although this will be dependent upon the fuel being considered; for most hydrocarbons the global reaction orders are around 2, Turns (1996).

Many previous experimental studies of burning velocity have investigated temperature dependence. For example Andrews and Bradley (1972) performed such an investigation on stoichiometric methane-air mixtures and found:

$$S_{\mathrm{u}} = 10 + 0.000371 T_{\mathrm{u}}^2 \tag{2.18}$$

where S_{u} is in cm s^{-1} and T_{u} is in K, demonstrating that an increasing temperature results in an increasing burning velocity according to a power law. In studies of the effect of temperature where equivalence ratio has also been varied, the power exponent has been found to be dependent upon equivalence ratio. Sharma *et al.* (1981) performed a study of non-stoichiometric methane mixtures and derived:

$$S_{\mathrm{u}} = C \left(\frac{T_{\mathrm{u}}}{300}\right)^n \tag{2.19}$$

where C is the burning velocity of the mixture at 300 K (itself a function of equivalence ratio and temperature) and power exponent n is dependent upon the equivalence ratio:

$$\begin{aligned} n &= 1.68\, \varphi^{-0.5} \quad (\varphi < 1.0) \\ n &= 1.68\, \varphi^{0.5} \quad (\varphi > 1.0) \end{aligned} \tag{2.20}$$

Subsequent investigations suggested alternative forms of power exponent to represent the temperature dependence in terms of equivalence ratio. Metghalchi and Keck (1982) fitted the following temperature exponent with a linear dependence on equivalence ratio to a collection of results for methanol, propane and isooctane (claiming that the temperature dependence was independent of fuel for their results):

$$S_{\mathrm{u}} = S_{\mathrm{uo}} \left(\frac{T_{\mathrm{u}}}{T_0}\right)^{\alpha} \left(\frac{p}{p_0}\right)^{\beta} \tag{2.21}$$

$$\alpha = 2.18 - 0.8(\varphi - 1) \tag{2.22}$$

Such an exponent with linear dependence upon equivalence ratio has been used relatively extensively to represent experimental results, and in the formation of burning velocity correlations (section 2.4).

More recently, a study of temperature dependence of burning velocity of ethanol-air flames by Konnov *et al.* (2011) presented results from a heat flux burner which suggested that a minimum in the value of the power exponent existed with respect to equivalence ratio, and as such a linear relation may not be the most accurate description of the experimental behaviour. These conclusions were backed up by results from kinetic modelling. Figure 2.7, taken from Konnov *et al.* (2011) shows these findings, and compares them with the simulations and experimental results where a constant or linear fit has been used.

An earlier study of temperature dependence by Liao *et al.* (2004) for natural gas flames used a non-linear power exponent of

$$n = 5.75\varphi^2 - 12.15\varphi + 7.98 \qquad \textbf{(2.23)}$$

although as Figure 2.7 shows, for their later study with ethanol, a linear function of equivalence ratio was used. Another temperature exponent was trialled by Marshall *et al.* (2010), where the temperature exponent was itself a function of temperature as well as equivalence ratio:

$$\alpha = \alpha_0 + \alpha_1 T + (\varphi - 1)\alpha_2 \qquad \textbf{(2.24)}$$

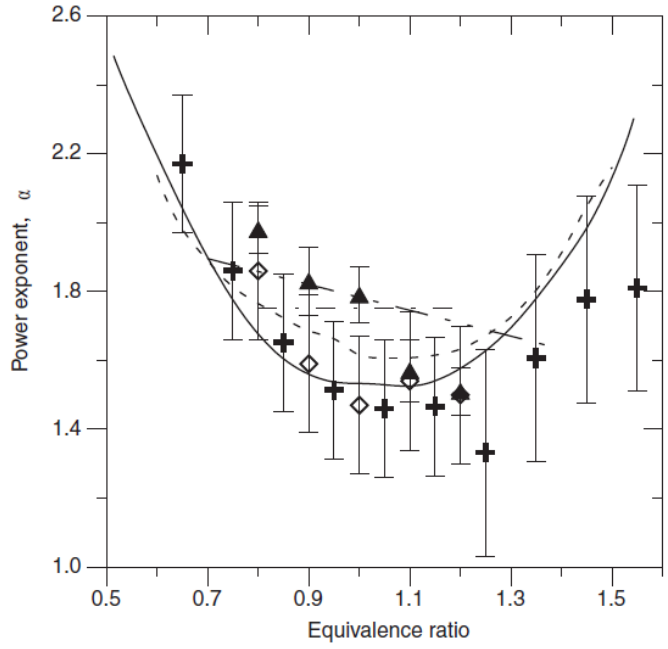

Figure 2.7 – Power exponent coefficient α, for ethanol-air flames. Diamonds and crosses: Konnov *et al.* (2011); solid triangles: Bradley *et al.* (2009); dash-dot line: Gülder (1982); dash-double dot line: Liao *et al.* (2007). Solid and dashed line: modelling using Konnov (2009) and Saxena and Williams (2007) respectively.

where all α terms are constants. However, this found to produce little difference when used to fit to experimental data compared to the form used by Metghalchi and Keck (1982).

It is worth noting as an aside, that the temperature exponent for Equation (2.21) is the same as that in the expression for flame thickness, which after taking into account the variation of dynamic viscosity μ with temperature is obtained by Kalghatgi (2014) as:

$$\delta = (\mu_0/\rho_0 S_{L0})(P/P_0)^{(-\beta-1)}(T/T_0)^{(1.5-\alpha)} \quad \textbf{(2.25)}$$

This fact becomes important in considerations of pre-ignition with combustion in engines, discussed briefly further in section 2.9. This illustrates further the importance of having accurate values for the temperature dependence in particular.

2.3.3 Pressure

As with the effect of temperature, some information about the effect of pressure on burning velocity can be obtained from Equation (2.5) derived from the simplified flame analysis:

$$S_u \propto P^{(n-2)/2} \quad \textbf{(2.26)}$$

However, if an overall reaction order of 2 were used, the implied result would be that burning velocity is independent of pressure. In fact, pressure is seen to have a weak inverse effect on the burning velocity. Rozenchan *et al.* (2002) calculate reaction order from the measured burning velocity with pressure, finding that reaction order varies non-monotonically with pressure, suggesting changes in relative significance of various reaction pathways. As with temperature, Andrews and Bradley (1972) investigated pressure dependence for stoichiometric methane-air mixtures, correlating results from different workers using different measurement methods, presenting the relationship:

$$S_u = 43P^{-0.5} \quad \textbf{(2.27)}$$

where S_u is in cm s^{-1} and P is in atmospheres for pressures of more than 5 atm. Sharma *et al.* (1981) reported a pressure dependence of the form

$$S_u = C_1 + C_2 \log_{10} P \quad \textbf{(2.28)}$$

where C_1 and C_2 are both functions of equivalence ratio. The fitting of a logarithmic function of pressure was consistent with that of Agnew and Graiff (1961). Other investigations examined the effects of equivalence ratio on pressure dependence. Metghalchi and Keck (1982) used a pressure exponent dependent upon equivalence ratio similar to that used for temperature:

$$\beta = -0.16 + 0.22(\varphi - 1) \quad \textbf{(2.29)}$$

As with temperature, Liao *et al.* (2004) used an exponent which was second order with respect to equivalence ratio, and Marshall *et al.* (2010) examined the possibility of the pressure exponent being a function of pressure also, although this was again not pursued.

2.3.4 Diluents

A diluent is a component added to the unburned mixture which does not take part in the reaction process. Addition of a diluent does not change the stoichiometry of the mixture but will have an effect on the thermodynamic properties of the mixture such as the specific heat capacity c_p and thermal diffusivity α. This will change the adiabatic flame temperature, so diluents can have a large effect on the burning velocity. The effect of heat capacity is significant and is well demonstrated in the study of Rahim *et al.* (2002), where the nitrogen in air (which typically is 79% by volume) is replaced by argon. The argon has a much lower specific heat capacity compared with nitrogen, which results in much higher flame temperatures and faster measured values of burning velocity. On this basis, if the base oxidiser is standard air containing around 79% nitrogen, further addition of diluents will be expected to lower the burning velocity.

Numerous studies have investigated the impact of a range of diluents upon burning velocities of various fuel/air mixtures. For example, Stone *et al.* (1998) conducted tests using a constant volume spherical vessel and present results for the effect of nitrogen, carbon dioxide and a mixture of both upon methane-air flames, using the factor

$$gX^{(h+(\varphi-1)i)} \quad \textbf{(2.30)}$$

upon the undiluted burning velocity, where g, h and i are all constants and X is the diluent fraction. Halter *et al.* (2009) performed similar investigations, but also conducted simulations with a 'false CO_2' to determine the effect on burning velocity of dissociation of the CO_2 and concluded that the effect of dissociation is not insignificant, yet its importance decreases as the dilution percentage is increased.

In many cases, the diluent studied is a mixture of CO_2 and N_2, chosen to simulate combustion products. This is relevant to the case of exhaust gas recirculation (EGR) in internal combustion engines, where a small amount of combustion products are returned to the cylinders to dilute the mixture and reduce combustion temperatures and subsequently NO_x emissions. Metghalchi and Keck (1982) is one such example of diluting with simulated combustion residuals, where the effect of dilution on stoichiometric iso-octane/air mixtures at ambient initial conditions is found to be a factor multiplied by the undiluted burning velocity:

$$1 - 2.1f \tag{2.31}$$

where f is the diluent mass fraction. Other studies on different fuels such as hydrogen, Verhelst *et al.* (2005) have used a similar relation. Liao *et al.* (2005) present a factor which has a second order dependence upon dilution fraction, and Elia *et al.* (2001) use a third order dependence.

Marshall *et al.* (2011) extended the idea of combustion residuals by pioneering the use of actual combustion residuals as the diluent within a constant volume vessel. It was considered that the effect of real residuals could be different to that of the simulated residuals used by other workers because of the existence of water vapour and the possibility of containing additional non-inert components such as hydrogen.

2.3.5 Mixing rules for fuel blends

Recent studies have begun to introduce mixing rules to describe the burning velocity of blends. The simplest rules are those which base the predicted behaviour upon the composition of the blend (typically in terms of volume fraction). However, such rules will not take into account changes in flame temperature with composition which will in turn result in changes to the

chemical kinetics, causing the relationship to be non-linear with respect to composition. Since reaction mechanisms for blends are unavailable and would be computationally intensive, mixing rules that attempt to take into account kinetic, thermal and transport effects are of interest, and some are reviewed by Sileghem *et al.* (2012). A mixing rule based upon energy fraction is proposed by van Lipzig (2010), in addition to the simple mole or mass fraction:

$$S_{\mathrm{u,blend}} = \sum_{i=1}^{n} \alpha_{\mathrm{i}} S_{\mathrm{u},i} \qquad \textbf{(2.32)}$$

where α is either the mass fraction, mole fraction, or energy fraction as given below:

$$\alpha_{\mathrm{i}} = \frac{\Delta H_i^0 x_i}{\sum_{i=1}^{n} \Delta H_i^0 x_i} \qquad \textbf{(2.33)}$$

where ΔH_{i}^0 is the heat of combustion of the component. Disarli and Benedetto (2007) suggested a correlation based upon Le Chatelier's rule, which states that a change to a system at equilibrium is met by a shift in equilibrium to counteract the imposed change. Their rule is summarised by:

$$S_{\mathrm{u,blend}} = \frac{1}{\sum_{i=1}^{n} \frac{x_i}{S_{\mathrm{u},i}}} \qquad \textbf{(2.34)}$$

Hirasawa *et al.* (2002) developed an empirical mixing rule for mixtures where flame temperature is the dominant factor over the effects of kinetic coupling, which is dependent upon a mole fraction weighted average of burning velocities and flame temperatures:

$$S_{\mathrm{u,blend}} = \prod_{i=1}^{n} S_{\mathrm{u},i}^{\frac{x_i n_i T_{\mathrm{f},i}}{n_{\mathrm{blend}} T_{\mathrm{f,blend}}}} \qquad \textbf{(2.35)}$$

where n_{i} is the number of moles of products (including diluents) per mole of fuel, and $T_{\mathrm{f,i}}$ is the adiabatic flame temperature of the pure component *i*. This rule was found to accurately represent burning velocities of a number of hydrocarbon blends.

Sileghem *et al.* (2012) compare the above rules for binary blends of ethanol and n-heptane and ternary blends of ethanol, n-heptane and iso-octane and find that the energy fraction mixing rule and that of Hirasawa *et al.* (2002) give the best fit to experimental data. There is also a further development of the Le Chatelier's principle in terms of energy fraction, replacing the

mole fraction in Equation (2.34) with the energy fraction in Equation (2.33), which appeared to give an improvement in prediction when compared with results from a chemical kinetic mechanism for the simulation of gasoline surrogate mixtures.

2.4 Burning velocity correlations

In section 2.3 the effect of different parameters upon burning velocity was discussed, and some expressions to represent these trends were presented. Whilst it is informative to present values of burning velocity at a range specific conditions to enable validation of results from chemical kinetic models, engine models such as that described by Lindström *et al.* (2005) can require values of burning velocity for any number of possible combinations of conditions of temperature, pressure, equivalence ratio and residuals level. Obtaining data for the fuel of interest at every combination of such conditions is clearly impossible, and hence it is desirable to be able to produce a burning velocity correlation to combine the effects of temperature, pressure, equivalence ratio and levels of diluents into one expression, with the correlation coefficients being determined experimentally for a given fuel by fitting to the results of a number of experiments that cover the range of conditions of interest. Given a set of correlation coefficients for the fuel of interest, the burning velocity at any combination of parameters required by an engine model can be easily obtained. More detail on the use of burning velocity correlations in engine models is given in section 2.9.

Producing a correlation is also a particularly useful way of combining results from a range of experiments where burning velocities can be derived for multiple conditions of temperature and pressure from a single experiment, such as a constant volume combustion bomb with analysis of the pressure rise. In such an experiment, the pressure and temperature of the unburned gas will rise together during combustion, so experiments at a range of initial temperatures and pressures would have to be performed to allow decoupling of linked parameters.

One of the earlier full correlations to take combine all the variables was that of Metghalchi and Keck (1982). Their findings for each individual parameter are given in section 2.3, and these effects can be combined to give the overall correlation

$$S_{\mathrm{u}} = S_{\mathrm{u,o}} \left(\frac{T_{\mathrm{u}}}{T_0}\right)^{\alpha} \left(\frac{p}{p_0}\right)^{\beta} (1 - 2.1f) \tag{2.36}$$

where T_0 and p_0 are the reference temperature of 298 K and pressure of 1 atm and:

$$S_{\mathrm{u,0}} = B_{\mathrm{m}} + B_2(\varphi - \varphi_{\mathrm{m}})^2 \tag{2.37}$$

$$\alpha = 2.18 - 0.8(\varphi - 1) \tag{2.38}$$

$$\beta = -0.16 + 0.22(\varphi - 1) \tag{2.39}$$

and only B_{m}, B_2 and φ_{m} are dependent upon fuel type. However, with the trend towards obtaining high accuracy values of burning velocity, assumptions of temperature and pressure dependency being independent of fuel are no longer acceptable. In the same study, a second relation was used to correlate the data, based upon the Arrhenius form based upon thermal theory similar to that described in section 2.1.4:

$$S_{\mathrm{u}} = U \left(\frac{T_{\mathrm{u}}}{T_0}\right) \left(\frac{p}{p_0}\right)^{b} \exp\left(\frac{-E_{\mathrm{a}}}{2R_{\mathrm{f}}T_{\mathrm{f}}}\right) \tag{2.40}$$

where U, E_{a} and b are fitted parameters and R_{f} is the specific gas constant. Whilst this was found to correlate the data as well as Equation (2.36), the fitted parameters are found to vary erratically with equivalence ratio, making smooth interpolation and extrapolation difficult. In addition, this form was found to be very dependent upon the adiabatic flame temperature T_{f} which is very sensitive to the thermodynamic model used to obtain its value, and so the former expression was considered a better correlation. Many other correlations have been used based upon a similar format such as Stone *et al.* (1998) and Elia *et al.* (2001), and recently, developed to include the effects of combustion residuals, that of Marshall (2010):

$$\begin{aligned} S_{\mathrm{u}} = {} & \left[S_{\mathrm{u,0}} + S_{\mathrm{u,1}}(\phi - 1) + S_{\mathrm{u,2}}(\phi - 1)^2 + S_{\mathrm{u,3}}(\phi - 1)^3 + S_{\mathrm{u,4}}(\phi - 1)^4\right] \\ & \times T^{\alpha} \times P^{\beta} \times \left(1 - \mu_1 x_{\mathrm{r}}^{(\mu_2 + (\phi - 1)\mu_3)}\right) \end{aligned} \tag{2.41}$$

where

$$\alpha = \alpha_0 + (\varphi - 1)\alpha_1 \quad \textbf{(2.42)}$$

$$\beta = \beta_0 + (\varphi - 1)\beta \quad \textbf{(2.43)}$$

$$T = \frac{T_\mathrm{u}}{298} \; ; \; P = \frac{P_\mathrm{u}}{1.0} \quad \textbf{(2.44)}$$

The data obtained from propagating flames in a constant volume vessel is subjected to a finite (if small) value of stretch by the time pressure rise occurs (described further in section 2.5). Unlike constant pressure, extrapolation to zero stretch (described in section 2.5.6) is not possible, since the combustion is not taking place at constant pressure and temperature. Marshall investigated the possibility of accounting for this by adding a term for stretch rate into the correlation. This was done by adding a term based upon a linear Markstein length, extending the correlation form in Equation (2.41) to:

$$\begin{aligned} S_\mathrm{u} = \left[S_{\mathrm{u},0} + S_{\mathrm{u},1}(\phi - 1) + S_{\mathrm{u},2}(\phi - 1)^2 + S_{\mathrm{u},3}(\phi - 1)^3 + S_{\mathrm{u},4}(\phi - 1)^4\right] \\ \times T^{\alpha} \times P^{\beta} \times \left(1 - \mu_1 x_\mathrm{r}^{(\mu_2 + (\phi - 1)\mu_3)}\right) \times (1 - L\alpha) \end{aligned} \quad \textbf{(2.45)}$$

where α is the stretch rate as defined by Equation (2.51). A couple of problems were identified with this approach. Firstly, the addition of the stretch term introduces another free variable, complicating an already large correlation. Secondly, whilst tests performed on an iso-octane data set showed an improvement in correlation fitting at stoichiometric conditions, little improvement was seen overall. This was attributed to the dependence of Markstein length upon equivalence ratio, as seen in section 2.5.7, which undermines the use of a linear stretch term, which requires a constant Markstein length. Subsequently, the value of Markstein length deduced in the fitting algorithm will not be accurately representative of the true behaviour, and so the addition of a stretch term was not pursued further.

Recently, a new form of correlation was developed for hydrogen-air mixtures by Verhelst *et al.* (2011), and has subsequently been used by Vancoillie *et al.* (2012) for ethanol-air mixtures including combustion residuals. This correlation form differs from those shown previously in that it has been developed from numerical results from the chemical kinetic mechanism of Li *et al.* (2007). This mechanism was chosen following comparison with other

kinetic mechanisms, experimental data and existing correlations. The correlation form takes into account the noted interaction between pressure and equivalence ratio:

$$S_{\mathrm{u}}(\varphi, p, T_{\mathrm{u}}, f) = S_{\mathrm{u},0}(\varphi, p)\left(\frac{T_{\mathrm{u}}}{T_0}\right)^{\alpha(\varphi,p)} F(\varphi, p, T_{\mathrm{u}}, f) \tag{2.46}$$

where both $S_{\mathrm{u},0}(\varphi, p)$, $\alpha(\varphi, p)$and $F(\varphi, p, T_{\mathrm{u}}, f)$ are polynomial functions including cross terms due to the interaction of these variables:

$$\begin{aligned}\alpha(\varphi, p) = a_1 + a_2\varphi + a_3\frac{p}{p_0} + a_4\varphi\frac{p}{p_0} + a_5\varphi^2 + a_6\left(\frac{p}{p_0}\right)^2 + a_7\varphi^3 + a_8\left(\frac{p}{p_0}\right)^3 \\ + a_9\varphi^2\frac{p}{p_0} + a_{10}\varphi^2\left(\frac{p}{p_0}\right)^2 + \frac{a_{11}}{\varphi} + \frac{a_{12}}{\varphi}\frac{p}{p_0}\end{aligned} \tag{2.47}$$

$$\begin{aligned}\ln\left[S_{\mathrm{u},0}\right](\varphi, p) = b_1 + b_2\varphi + b_3\frac{p}{p_0} + b_4\varphi\frac{p}{p_0} + b_5\varphi^2 + b_6\left(\frac{p}{p_0}\right)^2 + b_7\varphi^3 \\ + b_8\left(\frac{p}{p_0}\right)^3 + b_9\varphi^2\frac{p}{p_0} + b_{10}\varphi^2\left(\frac{p}{p_0}\right)^2 + \frac{b_{11}}{\varphi}\end{aligned} \tag{2.48}$$

$$F(\varphi, p, T_{\mathrm{u}}, f) = \min[1, F_1(\varphi, p, T_{\mathrm{u}}, f)] \tag{2.49}$$

$$\begin{aligned}F_1(\varphi, p, T_{\mathrm{u}}, f) = c_1 + c_2\varphi + c_3\frac{T_{\mathrm{u}}}{T_0} + c_4\frac{p}{p_0} + c_5 f + c_6\varphi^2 + c_7\left(\frac{T_{\mathrm{u}}}{p_0}\right)^2 + c_8 f^2 \\ + c_9\varphi\left(\frac{T_{\mathrm{u}}}{T_0}\right) + c_{10}\varphi\frac{p}{p_0} + c_{11}\varphi f + c_{12}\left(\frac{T_{\mathrm{u}}}{T_0}\right) f + c_{13}\varphi^3 + c_{14} f^3 \\ + c_{15}\left(\frac{T_{\mathrm{u}}}{T_0}\right)\varphi^2 + c_{16}\left(\frac{p}{p_0}\right)\varphi^2 + c_{17}\varphi\left(\frac{T_{\mathrm{u}}}{T_0}\right)^2 + c_{18} f\left(\frac{T_{\mathrm{u}}}{T_0}\right)^2 \\ + c_{19}\varphi f^2 + c_{20}\left(\frac{T_{\mathrm{u}}}{T_0}\right) f^2\end{aligned} \tag{2.50}$$

The added complexity of this form of correlation will make it much harder to fit experimental data, and it would not be expected to achieve the same level of accuracy unless the experimental data covers as broad a range of conditions as can be obtained from numerical modelling. In the work of Vancoillie *et al.* (2012), the mechanism of Li *et al.* (2007) was used to provide data for temperatures 400-1000 K, pressures 5-105 bar, equivalence ratios 0.5-2.0 and diluent ratios 0-50% vol., which is larger than can be obtained experimentally.

2.5 Flame stretch

The definition of laminar burning velocity in section 2.1.3 requires that the components of velocity of the flame (and unburned gas) remain straight and parallel. This will correspond to

the unstretched burning velocity. Where this is not the case, the flame is considered to be stretched. Flame stretch is shown to have an effect upon the measured burning velocity, and as seen in section 2.2, most methods of measuring burning velocity do not produce an unstretched flame. Therefore, this effect needs to be given due consideration if true values of unstretched burning velocity are to be reported and the effects of stretch are to be characterised. In early measurements of burning velocity, the effect of stretch was poorly understood and usually unaccounted for. Studies such as that of Wu and Law (1984) begin to demonstrate the effect of flame stretch on experimentally determined values, and Bradley *et al.* (1996) conclude that stretch is the "neglected key variable" that causes discrepancies between burning velocities obtained by different workers, and as such results should be presented with an associated stretch rate.

2.5.1 Definitions

The concept of flame stretch was first introduced by Karlovitz *et al.* (1953) in a study of flame propagation across velocity gradients with respect to turbulent flames. In turbulent flames, the effect of flame stretch is critical, and so characterisation of the effects of stretch is vital if laminar burning values are to be of use. The effect of flame stretch is equally applicable to the case of a moving flame or a flame with curvature, which would represent a non-uniform flow field with respect to the flame front. Karlovitz *et al.* (1953) defined stretch rate α as the rate of change of area A of an infinitesimal element $\mathrm{d}A$ of the flame surface:

$$\alpha = \frac{1}{A}\frac{\mathrm{d}A}{\mathrm{d}t} \qquad \textbf{(2.51)}$$

Candel and Poinsot (1990) describe the contributions to stretch rate arising from both curvature and strain, which both occur when a flame propagates.

2.5.2 Curvature

Curvature is able to contribute to flame stretch even in a stationary flame, demonstrating that it is distinct from the effects of flame movement and hence straining. For example, for a

stationary conical flame stabilized on a burner, at the curved tip where the curvature is greatest and concave to the oncoming unburned mixture, heat will be focused ahead of the flame. However, velocity components through a curved flame front will necessarily be divergent (since they are normal to the flame front) and so considering a streamtube passing through a segment of the flame front, whilst it is diffusively heated by a larger segment of the reaction sheet (tending to increase the flame temperature above the adiabatic flame temperature T_{ad}), the concentration of the deficient reactant approaching the flame will decrease (decreasing the flame temperature). Therefore, the effects of curvature will be determined by the ratio of thermal and mass diffusion, characterized by their respective diffusivities α and D, which is described by the Lewis number:

$$\mathrm{Le} = \frac{\alpha}{D} \tag{2.52}$$

Law (2006) describes the effect thus: "the downstream burning flux remains the same as that of the one-dimensional planar flame, while the upstream burning flux is increased by an amount that is dependent on the curvature".

2.5.3 Strain

Strain is best thought of by considering the effect of flame expansion upon an element of the flame surface; such an element will increase in size as the flame propagates. As a control volume in the flame front increases in volume, thermal energy in that control volume will decrease due to greater heat transfer away from the region. However, the volume increase means more reactant can be supplied to the region. Therefore the effects of strain are also dependent upon the Lewis number of the mixture. For an equidiffusive flame, where $\mathrm{Le} = 1$, the loss in thermal energy is balanced by the gain in chemical energy. For $\mathrm{Le} > 1$, the net decrease in energy decreases the flame temperature, and for $\mathrm{Le} < 1$, there is an increase in flame temperature. Hence the burning velocity is affected by the strain rate.

2.5.4 Stretch in spherically expanding flames

The case of the spherically expanding flame is of significant interest in this work, since it is produced by the constant volume method with central ignition. Taking Equation (2.51) and applying to the case of a sphere, where

$$A = 4\pi r_f^2 \tag{2.53}$$

then the overall stretch rate is given by:

$$\alpha = \frac{2}{r_f}\frac{dr_f}{dt} \tag{2.54}$$

$$= \frac{2}{r_f} S_f \tag{2.55}$$

where r_f is the radius of the flame and S_f is the stretched flame speed (i.e. rate of change of flame radius with respect to time). The effect of measurement of flame radius upon determined stretch rate is discussed in section 6.2.1.3.

The effects of curvature and stretch as described by Candel and Poinsot (1990) can be similarly quantified. Bradley *et al.* (1996) perform the vector analysis and obtain the following expressions:

$$\alpha = \alpha_c + \alpha_s \tag{2.56}$$

$$\alpha_c = 2\frac{S_n}{r_u} \tag{2.57}$$

$$\alpha_s = 2\frac{S_g}{r_u} \tag{2.58}$$

where S_n is the stretched burning velocity with respect to the unburned gas and S_g is the gas velocity ahead of the flame front, as given in Figure 2.2.

2.5.5 Markstein Lengths

The effect of stretch upon flame speed and burning velocity is characterised through Markstein lengths. Considering first the flame speed, the unstretched flame speed S_s is related to the measured stretched flame speed S_f by the burned gas Markstein length L_b:

$$S_f = -L_b\alpha + S_s \tag{2.59}$$

Hence, a positive value of Markstein length will reduce the speed of a positively stretched flame relative to the unstretched flame speed, whereas a negative value will increase the flame speed. This burned gas Markstein length is so called since the flame speed in absolute terms is characterised by the appearance of burned gas behind the flame front as it propagates. Conversely, the burning velocity is defined by the consumption of unburned gas by the flame front as described by Figure 1.2, and so the relationship between unstretched burning velocity S_u and stretched burning velocity S_n is characterised by the unburned gas Markstein length, L_u (commonly referred to as just the Markstein length, L):

$$S_n = -L_u \alpha + S_u \tag{2.60}$$

If the stretch rate were to be divided into contributions from curvature and strain as in Equation (2.56), then it would also be possible to define Markstein lengths associated with each of these contributions:

$$S_u - S_n = L_c \alpha_c + L_s \alpha_s \tag{2.61}$$

In their computational study, Bradley *et al.* (1996) explain how the above expression is accurate to the first order although the finite flame thickness gives different possible definitions of Markstein length. If we consider a propagating spherical flame with radius r_u, and apply conservation of mass then the expression

$$\frac{\mathrm{d}m_u}{\mathrm{d}t} = -\frac{\mathrm{d}}{\mathrm{d}t}\left(\int_0^{r_u} 4\pi r^2 \rho \, \mathrm{d}r\right) \tag{2.62}$$

is obtained. Equation (2.3) showed that burning velocity is related to the rate of change of mass of unburned gas. If A_f in Equation (2.3) is replaced with the surface area of a sphere from Equation (2.53), then by equating for rate of change of mass of unburned gas:

$$S_n = \frac{1}{r_u^2 \rho_u} \frac{\mathrm{d}}{\mathrm{d}t}\left(\int_0^{r_u} r^2 \rho \, \mathrm{d}r\right) \tag{2.63}$$

Now if the finite thickness of the flame front is considered, then the mean gas density within the sphere can be regarded as a mixture of burned gas at its adiabatic temperature with a density of ρ_b, and unburned gas with a density ρ_u:

$$S_{\mathrm{n}} = \frac{1}{r_{\mathrm{u}}^2 \rho_{\mathrm{u}}} \frac{\mathrm{d}}{\mathrm{d}t} \left[\int_0^{r_{\mathrm{u}}} r^2 \rho_{\mathrm{u}} \left(\frac{\rho_{\mathrm{b}} - \rho}{\rho_{\mathrm{b}} - \rho_{\mathrm{u}}} \right) \mathrm{d}r + \int_0^{r_{\mathrm{u}}} r^2 \rho_{\mathrm{b}} \left(\frac{\rho - \rho_{\mathrm{u}}}{\rho_{\mathrm{b}} - \rho_{\mathrm{u}}} \right) \mathrm{d}r \right] \quad \textbf{(2.64)}$$

Therefore the first term on the right represents the rate of entrainment of unburned gas by the flame front that remains unburned and the second term represents the rate of formation of burned gas. The stretched burning velocity S_{n} here represents by definition the rate of entrainment of the unburned gas. A burning velocity S_{nr} may be associated with the second term, representing the formation of burned gas:

$$S_{\mathrm{nr}} = \frac{1}{r_{\mathrm{u}}^2 \rho_{\mathrm{u}}} \frac{\mathrm{d}}{\mathrm{d}t} \left[\int_0^{r_{\mathrm{u}}} r^2 \rho_{\mathrm{b}} \left(\frac{\rho - \rho_{\mathrm{u}}}{\rho_{\mathrm{b}} - \rho_{\mathrm{u}}} \right) \mathrm{d}r \right] \quad \textbf{(2.65)}$$

Therefore, the difference between these two burning velocities will represent the accumulation of mass within the flame front, which for an unstretched planar flame will be zero. The burning velocity S_{nr} will be the value determined by measurements of pressure rises such as Metghalchi and Keck (1982). Further algebraic manipulation yields

$$S_{\mathrm{nr}} = \frac{\rho_{\mathrm{b}}}{\rho_{\mathrm{b}} - \rho_{\mathrm{u}}} (S_{\mathrm{n}} - S_{\mathrm{f}}) \quad \textbf{(2.66)}$$

Bradley *et al.* (1996) also assigned Markstein lengths for the deficit between unstretched burning velocity S_{u} and the stretched burning velocity based on formation of burned gas S_{nr}, which can also be split according to contributions from curvature and strain:

$$S_{\mathrm{u}} - S_{\mathrm{nr}} = L_{\mathrm{cr}} \alpha_{\mathrm{c}} + L_{\mathrm{sr}} \alpha_{\mathrm{s}} \quad \textbf{(2.67)}$$

where L_{cr} and L_{sr} are shown to be dependent upon L_{b}, L_{c}, and L_{s}:

$$L_{\mathrm{cr}} = \frac{1}{\rho_{\mathrm{u}}/\rho_{\mathrm{b}} - 1} (L_{\mathrm{b}} - L_{\mathrm{s}}) \quad \textbf{(2.68)}$$

$$L_{\mathrm{sr}} = \frac{1}{\rho_{\mathrm{u}}/\rho_{\mathrm{b}} - 1} (L_{\mathrm{b}} - L_{\mathrm{c}}) \quad \textbf{(2.69)}$$

Therefore, determination of such Markstein lengths will depend on the accuracy of those upon which it is based.

Also commonly used in the literature are Markstein numbers, which are defined as the ratio of the burned gas Markstein length and the unstretched laminar flame thickness of an adiabatic planar flame:

$$\mathrm{Ma} = \frac{L_\mathrm{b}}{\delta_\mathrm{L}^0} \tag{2.70}$$

Using our definition of flame thickness as given in Equation (2.6) we see that the determination of the Markstein number will be dependent upon the unstretched laminar burning velocity also, which necessitates an iterative process.

2.5.6 Extrapolation to zero stretch

Since many methods of burning velocity measurement produce flames with varying degrees of stretch, then typically an extrapolation to zero stretch is performed. From the definition of flame stretch in Equation (2.51), the stretch rate at any point is known, and so the burning velocity measured at that point can be associated with the current stretch rate. As shown by Equation (2.55), in the case of a spherical flame the stretch rate is well defined, and is a function of flame speed and flame radius. In an outwardly propagating flame, this will generally decrease as the flame propagates and the radius of curvature increases.

In experiments where the flame front propagation is tracked, the flame speed and stretch rate at each time step are recorded, and can be plotted against each other. On a plot of S_f against α obtained from an experimental run (since α is a function of time), unstretched flame speed S_s is found by extrapolating back to the case of zero stretch (α =0). Given the basis of the definition of Markstein lengths such as described by Equation (2.59), this extrapolation is commonly a linear relationship, where the gradient of the extrapolated line gives the burned gas Markstein length. Figure 2.8 shows the extrapolation of flame speed to conditions of zero stretch using a linear fit for methane-air mixtures at a temperature of 300 K and a pressure of 1 bar in a 380 mm diameter vessel with optical access of diameter 150 mm.

The plotted values of stretched laminar flame speed against stretch rate show scatter of a periodic nature. This is seen in many similar experiments such as those by Bradley *et al.* (1998), who attributed the effect to acoustic disturbances. However, the use of a linear extrapolation tends to avoid problems associated with this scatter.

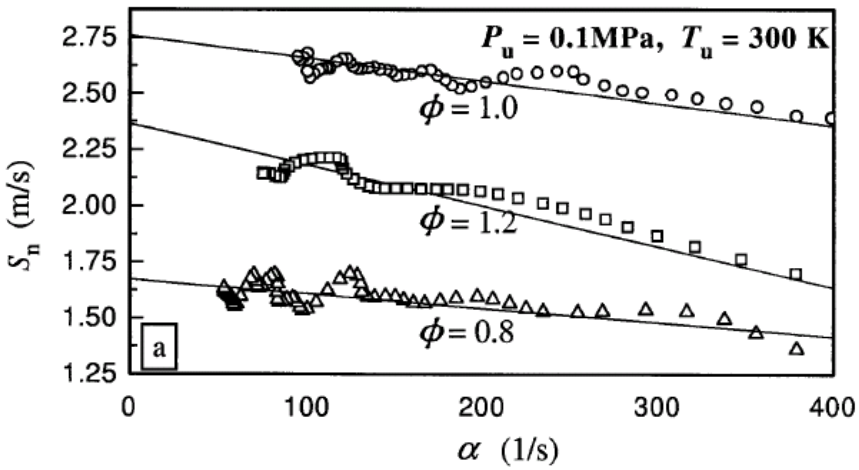

Figure 2.8 - Linear extrapolation of flame speed against stretch rate, from Gu *et al.* (2000).

Extrapolation can be problematic since there is a shortage of data at low stretch rates, limited by the size of the vessel and optical access, and the exact gradient of the extrapolated line is strongly dependent upon the range of data points selected – this will strongly influence the extrapolated value for unstretched flame speed. In particular, measurements made in the early stages of flame propagation may be influenced by ignition effects, and measurements made later during combustion could be affected by cellularity or other flame front instabilities (see section 2.6.4). Even with carefully selected ranges of data to which the fit is made, it can be found that a linear fit does not always represent the stretch behaviour well. Some studies have been carried out to test non-linear extrapolations in an attempt to obtain a better fit. Kelley and Law (2007) propose the relation:

$$\left(\frac{S_f}{S_s}\right)^2 \ln\left(\frac{S_f}{S_s}\right)^2 = -2\left(\frac{L_b \alpha}{S_s}\right) \qquad \textbf{(2.71)}$$

Their results suggested that the use of a linear extrapolation will tend to over-predict the unstretched flame speed, with a greater effect for richer mixtures (for results of n-butane-air experiments at atmospheric pressure).

Chen (2011) compared the linear relation, the non-linear relation in Equation (2.71) and an additional non-linear relation given by:

$$S_f = S_s - 2\left(\frac{S_s L_b}{r_f}\right) \qquad \textbf{(2.72)}$$

which is superficially similar to the linear extrapolation but is not linearly dependent upon the stretch rate due to the inclusion of the unstretched flame speed in the term multiplied by the Markstein length. The study aimed to determine the accuracy of each of the models for the study of spherical flames and the extraction of burning velocity and Markstein length. A completely theoretical simulation was set up using the three models (one linear, two non-linear) which showed that the relative accuracy of each of the models was dependent upon the Lewis number of the mixture being represented. For mixtures of unity Lewis number, all of the models were shown to represent spherical flame behaviour well, whereas for Le < 1 the non-linear model represented by Equation (2.71) gave the best fit and for Le > 1 that represented by Equation (2.72) was most accurate. This result was validated with detailed numerical simulation results for methane using the GRI 3.0 mechanism at different equivalence ratios, and finally by using actual experimental data from Taylor (1991). Figure 2.9 shows the sensitivity of the determined burned gas Markstein length to the extrapolation technique, and the effect that has on the subsequently deduced flame speed.

Tahtouh *et al.* (2009) compared a number of methods of performing the linear fit to experimental data obtained from shadowgraph images. The first method used is the fitting of a third order polynomial to the flame radius data, which is then differentiated to find the flame front velocity. Since the temporal flame radius evolution is not described exactly by a polynomial function, it is found that the fit deviates at either end of the data range. This requires that the data to which the linear extrapolation is applied is limited to avoid these regions. The second method uses a direct analytical approach, which is based upon a least squares minimisation of a function derived by direct substitution of the stretch rate term of Equation (2.54) into the linear relation of Equation (2.59), based on the approach of Burluka *et al.* (2007). The third method uses a novel approach whereby the exact solution to the equation obtained by combining Equations (2.54) and (2.59) is used to fit the experimental data. The expression for radius as a function of time that is found to be the exact solution includes a

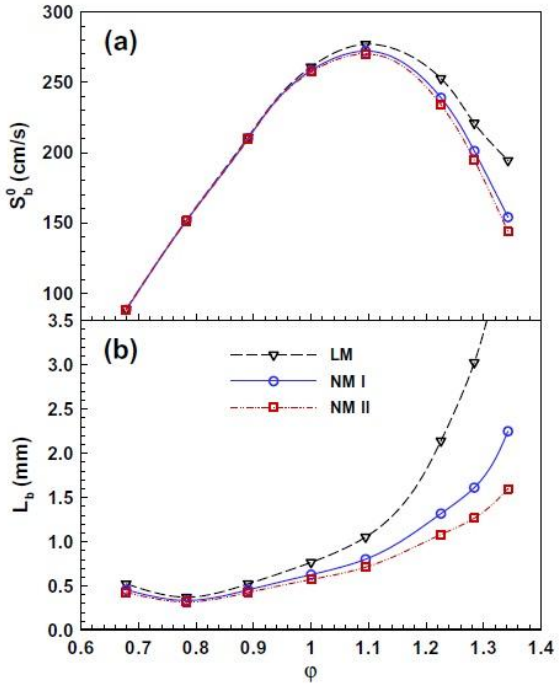

Figure 2.9 – Effect of extrapolation techniques on (a) unstretched burning velocity and (b) burned gas Markstein length, for atmospheric methane-air mixtures, Chen (2011). LM is the linear model represented by Equation (2.59); NM I and NM II are the non-linear models of Equations (2.72) and (2.71) respectively.

Lambert function which remains a positive real number for cases where L_b is positive. The value of L_b and unstretched flame speed are then obtained by performing a least squares minimisation of the difference between the data and the corresponding values from the fit. Each of the methods are subjected to different systematic and random errors. Random error is introduced in the detection of flame radius from the images. This is most pronounced in the analytical method since no fitting is used, although the effect can be reduced prior to differentiation by filtering the data. Random error is also introduced by applying a fit to the data with the polynomial being most affected since the relation is not completely described by such a function. A systematic error is introduced due to the initial assumption of a linear relation, which is not necessarily accurate for all mixtures. The three methods were tested for methane-air mixtures at atmospheric conditions, and the results for laminar burning velocity and burned gas Markstein length are shown in Figure 2.10. This shows that there is generally little difference between the three methodologies. For rich mixtures, the difference is larger, which is largely due to the assumption of linear behaviour. The authors claim that their new method is the most accurate and cite the fact that all Markstein lengths remain positive when using this

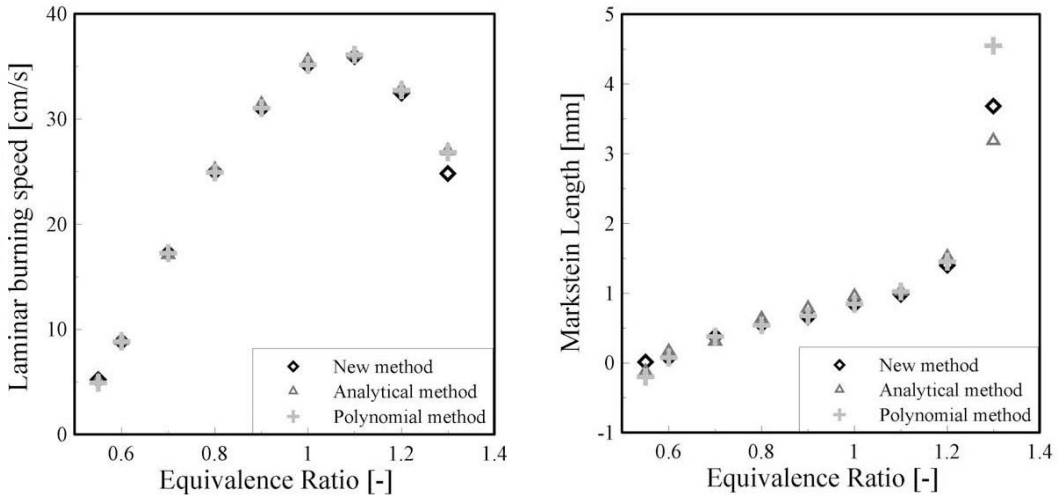

Figure 2.10 – Comparison of linear extrapolation techniques for methane-air flames at atmospheric conditions. Taken from Tahtouh *et al.* (2009).

approach, which is consistent with the observation that no instabilities occurred for lean mixtures; negative Markstein lengths would be expected to result in the development of flame front instabilities. However, given the large scatter in experimentally determined Markstein lengths (for example in Figure 2.14), these differences remain comparatively small.

Halter *et al.* (2010) also compared the discrepancies between linear and non-linear methodologies when applied to their own experimental data for methane and iso-octane. These fuels were chosen since they present opposite trends in Markstein length when the equivalence ratio is increased. They also found that the discrepancy between the linear and non-linear methodologies increased as the value of Markstein length increased, concluding that the linear method becomes invalid for these cases. However, they also showed that the initial flame radius used in the extrapolation of flame speed has an impact on the magnitude of this discrepancy. Initially, an initial flame radius of 8 mm was used, since a preliminary investigation showed that the critical radius beyond which the spherical flames are no longer affected by ignition was 6.5 mm. This result is corroborated by the findings of Bradley *et al.* (1996). By increasing the initial radius of flame used in the extrapolation, the relative difference between the linear and non-linear methodologies is reduced. This is shown in Figure 2.11, for methane-air mixtures at ambient temperature and pressure. When the initial radius of 20 mm is used, the relative difference for an equivalence ratio of 1.3 is reduced to just 0.6%. Clearly, by increasing the

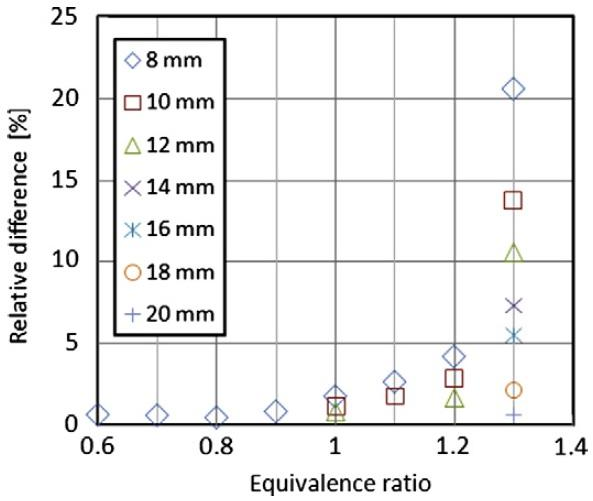

Figure 2.11 – Relative difference between burning velocities of atmospheric methane-air mixtures derived from linear and non-linear methods with varying initial flame radius. Taken from Halter *et al.* (2010).

initial radius from which the extrapolation is performed the number of points used for extrapolation is reduced. This is discussed by the authors and identified as a potential source of discrepancy, although in their own study this meant 44 points for 20 mm compared to 137 for 8 mm, which was deemed acceptable. A parameter Δ was defined as the ratio of burned gas Markstein length to the initial radius considered in the extrapolation, as a measure of the validity of the linear relation:

$$\Delta = \left| \frac{L_\mathrm{b}}{R_\mathrm{f,initial}} \right| \qquad \textbf{(2.73)}$$

This implies that as the burned gas Markstein length is increased, the initial flame radius should be increased also.

Further investigations on the range of data that can be used for extrapolations has been carried out by Chen *et al.* (2009), with particular emphasis upon determination of burning velocity from smaller combustion vessels and/or with higher initial pressures. The use of smaller vessels is advocated by the authors for a number of reasons, including the ability to use higher initial pressures without compromising on safety, ease of ensuring homogeneous mixtures in the vessel, and reducing the effects of radiation and hydrodynamic instabilities, which become more significant at larger flame radii. The radius of vessel considered in their study is 6 cm. However, the use of smaller vessels reduces the range of data for which an extrapolation (linear or otherwise) of flame speed data with respect to stretch can be performed,

since pressure rise will occur at smaller radii, and data can only be taken at conditions of constant pressure. Even before there is sufficient pressure rise to violate the assumptions of constant pressure, compression effects can result in a flow velocity in the burned gas behind the flame front which can affect the stretched flame speed. This is represented by the second term in the following equation:

$$S_{\mathrm{u}} = \frac{\rho_{\mathrm{b}}}{\rho_{\mathrm{u}}}\frac{\mathrm{d}r_{\mathrm{f}}}{\mathrm{d}t} + \frac{\rho_{\mathrm{b}}}{\rho_{\mathrm{u}}}\frac{r_{\mathrm{f}}}{3\gamma_{\mathrm{u}}P}\frac{\mathrm{d}P}{\mathrm{d}t} \qquad \textbf{(2.74)}$$

Additionally, the temperature effect on the density ratio can be considered, although this was shown to be very small. The unstretched burning velocity obtained by linear extrapolation of Equation (2.74) is referred to by the authors as the compression corrected flame speed (CCFS). The relative error compared to the laminar burning velocity obtained from numerical simulations for stoichiometric methane, for the case where the correction has been used is compared to the uncorrected case for a number of flame radius ranges used for extrapolation is presented in Figure 2.12.

So far only extrapolation of flame speed back to zero stretch has been discussed. As described by Equation (2.10), the unstretched burning velocity can be determined from the density ratio and the unstretched flame speed, but the stretched burning velocity cannot. The physical reason for this is based in the fact that there will be accumulation of mass within the flame front for a stretched flame, meaning that the multiplication of flame speed by density as in Equation (2.10) will only give the true burning velocity if the accumulation is zero, which will only occur when the stretch rate is zero. Therefore, it is not possible to plot stretched burning velocity against stretch rate to determine unburned gas Markstein length from Equation (2.60) using the same technique as for unstretched flame speed. Rozenchan *et al.* (2002) use the following relation to calculate L_{u} from L_{b}:

$$L_{\mathrm{u}} = \frac{\rho_{\mathrm{b}}}{\rho_{\mathrm{u}}}L_{\mathrm{b}} - (\beta\int_0^1 \frac{\rho}{\rho_{\mathrm{u}}}\mathrm{d}\left(\frac{x}{\delta}\right) - \frac{\rho_{\mathrm{b}}}{\rho_{\mathrm{u}}})\delta \qquad \textbf{(2.75)}$$

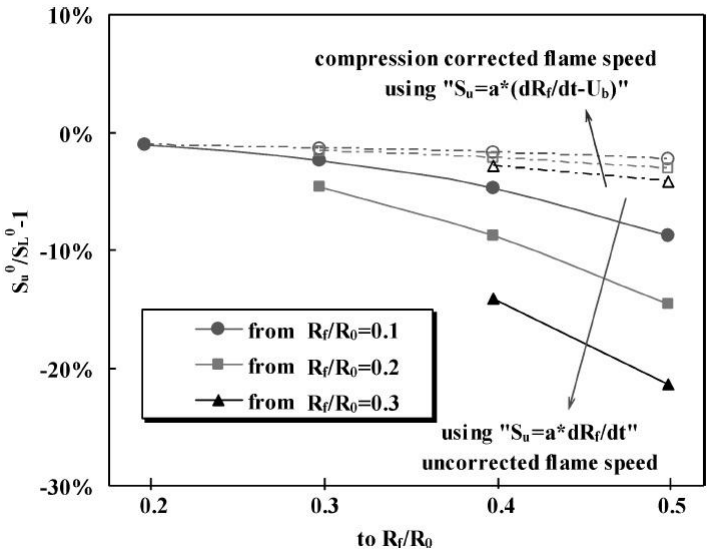

Figure 2.12 – Accuracy if unstretched flame speed with and without compression correction over different extrapolated flame ranges for stoichiometric methane-air flames. Taken from Chen *et al.* (2009).

where the second term accounts for the mass accumulation in the flame front, demonstrating that stretched burning velocity and stretched flame speed (and hence L_u and L_b) cannot be simply related by density ratio. However, this does suggest we should see similar trends in behaviour of the burned and unburned gas Markstein lengths, as is indeed shown in the analysis of Rozenchan *et al.* (2002).

In section 2.2.2.2, the technique of Varea *et al.* (2012) was introduced, whereby the burning velocity at non zero stretch rates can be obtained from Equation (2.76) using a novel post-processing procedure to measure both stretched flame speed S_f and fresh gas velocity u_g.

$$S_n = S_f - u_g \qquad \textbf{(2.76)}$$

This then allows Equation (2.60) to be used to obtain the unstretched burning velocity without use of the fuel properties (density ratio), and also the direct measurement of the unburned gas Markstein length L_u. The authors claim that this is the first technique that allows a direct measurement of L_u. In their study, the new method and the more traditional method using density ratio were compared. With the new method, there remains the option of a linear or non-linear extrapolation, again with a discrepancy based upon the Lewis number of the mixture as seen in the case of the traditional method. The difference between the two methods is shown to depend upon the fuel being considered. For example, when nonlinear extrapolations were used

the results for methane-air flames from the two methods were largely similar. However, when the two methods were applied to iso-octane-air mixtures at 1 bar and 373 K, the results from the direct measurement of unstretched burning velocity were found to be 5-10% higher than those derived from unstreched flame speed and density ratio, though the trends with equivalence ratio are consistent as shown in Figure 2.13. A similar result is found in the tests with ethanol. The authors explain that this discrepancy is due to the burned gas density estimation, which is calculated based upon adiabatic combustion, and so differences are likely to mean that the experimental flame is subjected to radiative effects (emission and absorption) or that the burned gases have not reached chemical equilibrium.

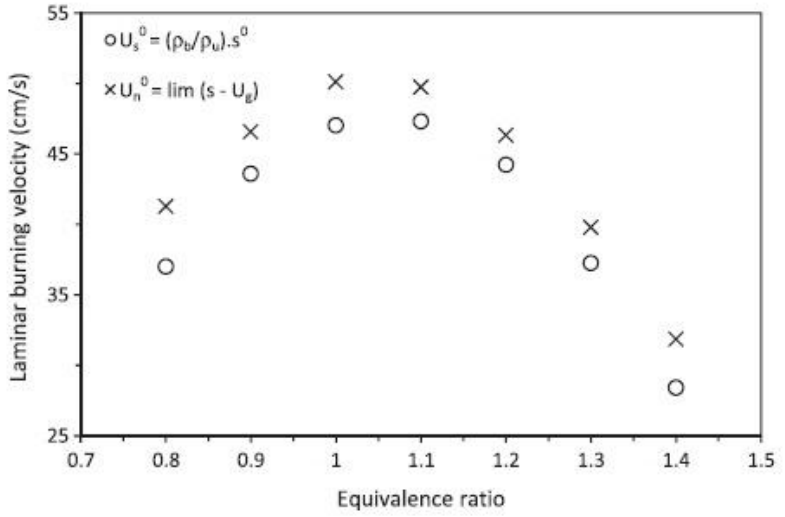

Figure 2.13 – Unstretched laminar burning velocity for iso-octane-air mixtures at $p_u = 1$ bar and $T_u = 373$ K, obtained by the traditional (circles) and new (crosses) methods. Taken from Varea *et al.* (2012).

2.5.7 Factors affecting Markstein lengths

Markstein lengths have been obtained in the literature for a small number of fuels using a spherically expanding flame method. However, discrepancies in the values obtained are significant, and are typically much larger than discrepancies in measured burning velocities. Figure 2.14 is taken from Chen (2011), and shows some of the scatter involved in these measurements, with relative differences being larger than 300% in some cases. It should be noted that all workers have used a linear extrapolation to determine their values. Nevertheless, it is possible to see the effects on burned gas Markstein lengths of the same parameters as had

an effect on burning velocity, as described in section 2.3. Understanding how Markstein lengths are affected by such parameters is crucial for flamelet modelling and modelling of turbulent combustion where high stretch rates are observed.

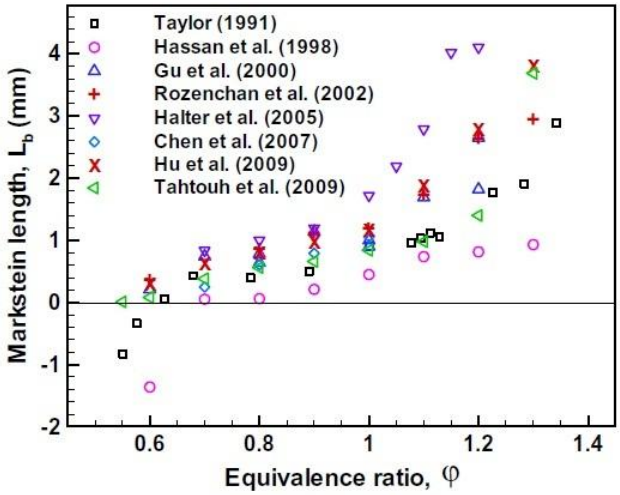

Figure 2.14 – Burned gas Markstein lengths for methane-air mixtures at atmospheric temperature and pressure from a variety of workers. Taken from Chen (2011).

2.5.7.1 Mixture composition

The values of burned gas Markstein length determined at a given set of conditions will unsurprisingly be different for different fuels since the effect of stretch is strongly related to the Lewis number of the mixture. Therefore the dependence of Markstein length upon factors such as equivalence ratio will vary between fuels. For example, the Markstein length for methane-air mixtures is seen to increase with increasing equivalence ratio (Figure 2.14), whereas for iso-octane, the trend is opposite as found by Bradley *et al.* (1998) for example.

Additives will also change the measured Markstein lengths. Hu *et al.* (2009) investigated the effect of hydrogen addition to methane-air mixtures and found that the Markstein lengths decreased with increased hydrogen fraction. Similarly, the addition of an inert diluent could be expected to change the Markstein lengths, again through the effect that this will have on the Lewis number of the mixture. Verhelst *et al.* (2005) investigated hydrogen-air mixtures, and found that as the concentration of a diluent consisting of water and nitrogen (to represent combustion residuals) was increased, the effect of increasing equivalence ratio lessened.

2.5.7.2 Temperature

Whilst temperature is one of the biggest factors affecting burning velocity, it appears that for Markstein lengths the effect of changing temperature is relatively small. Bradley *et al.* (1998) investigated iso-octane mixtures and determined that whether or not increasing temperature had a positive or negative effect on the value of the Markstein length appeared to be dependent upon the pressure also. Figure 2.15 shows the small effect of temperature on stoichiometric iso-octane-air mixtures. Note also the relatively large discrepancies between experiments performed at the same temperatures, demonstrating the difficulty in obtaining consistent values. Also note that for pressures greater than 5 bar, the range of data from which to perform the extrapolation will have been limited by cellularity (see section 2.6.4).

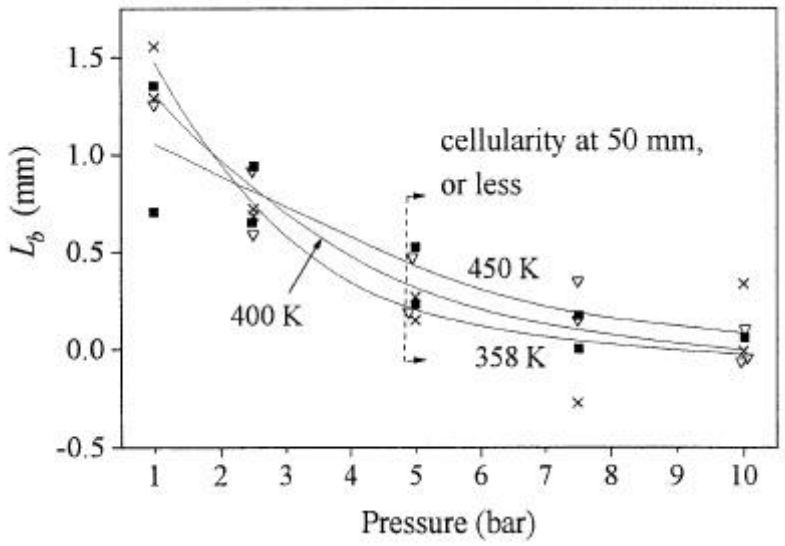

Figure 2.15 – Dependence of Markstein length of stoichiometric iso-octane-air mixtures on pressure and temperature. Symbols represent experimental values, lines show best fit. Taken from Bradley *et al.* (1998).

2.5.7.3 Pressure

With reference to Figure 2.15, it can be seen that the effect of increasing pressure is to reduce the Markstein length at all temperatures. Gu *et al.* (2000) report a similar trend for methane-air mixtures, with the burned gas Markstein length becoming negative as the pressure increased from 1 bar to 5 bar, and relatively little change as the pressure was further increased to 10 bar. Rozenchan *et al.* (2002) present similar results obtained with the dual chamber constant pressure vessel which show good agreement with Gu *et al.* (2000).

2.5.8 Stretch in flames with large radii

Considering the expression for stretch rate given in Equation (2.55), it can be expected that as the flame radius tends towards infinity, the stretch rate will asymptotically approach zero. This can be of use when determining burning velocities for flames using the pressure rise method as detailed in section 2.2.2.2, since this method does not allow the extrapolation of flame speed to determine Markstein length; conditions of temperature and pressure are changing during the experiment, and so the extrapolated value would not be attributable to a single condition of temperature and pressure. This appears to be the approach used in the work of Jerzembeck *et al.* (2008).

Work by Andrews and Bradley (1972) claims that for flame radii greater than 50 mm, the effects of stretch on burning velocity can be considered negligible. However, further investigation is needed as quantifying the effects of stretch on burning velocity measurements is increasingly important and for cases where the Lewis number greatly deviates from unity, stretch effects may be important. Chen and Ju (2007) investigate the effects of stretch in constant volume vessels and present a stretch corrected flame speed (SCFS), in effect analogous to their compression corrected flame speed (CCFS) used for constant pressure combustion. Using a linear relationship between stretch rate and burning velocity (via the unburned gas Markstein length), and that to zeroth order $S_u \sim S_n$, substitution of an analytical expression for flame radius derived from pressure, Equation (3.19), into the definition of stretch in a spherical expanding flame, Equation (2.54), yields an expression allowing the error introduced by neglecting stretch to be evaluated, which is shown to be proportional to the Markstein length and inversely proportional to the vessel radius. Figure 2.16 shows an example representing a mixture with a large unburned Markstein length (corresponding to a Lewis number of 2.0), and a small vessel radius, making this a somewhat extreme case. When the pressure increase is below 20%, the stretch effect on flame speed is greater than 10%, leading the authors to make a correction using values of unburned Markstein length obtained from either the constant pressure

method or counterflow experiments. Corrected values agree well with simulations performed using the PREMIX flame code and the GRI 3.0 mechanism. This effect is investigated for the current experimental setup in section 6.2.2.8.

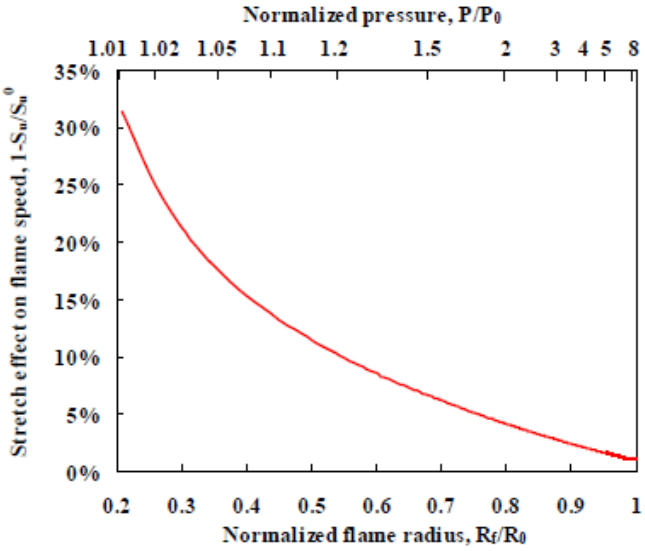

Figure 2.16 – Error introduced by ignoring stretch effect, for a run with $P_e/P_0 = 8.27$, $\gamma_u = 1.37$, $L_u = 0.25$ mm, $R_0 = 6$ cm. From Chen and Ju (2007).

2.6 Cellularity

Cellularity describes the phenomenon whereby a flame front develops an instability causing deviation from a smooth flame front to one which has an uneven or 'cellular' structure. This kind of flame front instability can occur in both stationary and non-stationary flames. In stationary flames stabilised on conical burners, this is in the form of ridges on the surface of the cone, resulting in a polyhedral shape; in flat flame burners, the instability is seen as a series of cells on the surface. In the case of a spherically propagating flame, the flame will change from a smooth spherical flame front, to one where the surface is cellular. These represent regions of intensified or weakened burning, caused by local inhomogeneity in the mixture composition within the flame front, meaning that the burning rate is no longer uniform over the flame front resulting in the uneven surface. According to Law (2006), "there are three modes of intrinsic cellular instability, namely diffusional-thermal instability, hydrodynamic instability and buoyancy driven instability".

2.6.1 Diffusional-thermal instability

This instability occurs in inhomogeneous fuel air mixtures and is caused by differences in the thermal diffusivity and mass diffusivity of the mixture. In the flame front, the increase in temperature resulting from combustion will cause a decrease in the concentration of fuel and air. This results in the diffusion of both species towards the area of lower concentration. This will cause a change in the local equivalence ratio since the fuel and air will diffuse at different rates. For a mixture, the Lewis number can be defined as the ratio of the thermal diffusivity of the mixture and the mass diffusivity of the deficient reactant:

$$\mathrm{Le} = \frac{\alpha_{\mathrm{mixture}}}{D_{\mathrm{deficient}}} \tag{2.77}$$

For a wavelike deformation of the flame, at the crest of the wave there will be diverging conductive heat flux away from the flame front into the cold reactants and a converging diffusive flux of the deficient reactant into the surface, as shown in Figure 2.17. For the case where the Lewis number is greater than unity, there will be a decrease in enthalpy by the flame and subsequently the local burning velocity decreases, Bradley and Harper (1994). The opposite is true at the trough of the wave, where the enthalpy increases and so the burning velocity subsequently increases. This tends to decrease the amplitude of the perturbation, hence causing the flame to be considered stable. By the same reasoning, the opposite is true for a Lewis number less than unity, where the effect is to increase the amplitude of the perturbation, which leads to an unstable mode of propagation, in the form of a cellular flame. Law (2006) explains that the cell size is expected to be of the order of the flame thickness. Since Lewis number is often a function of equivalence ratio, it would be expected that the susceptibility of the mixture to this kind of instability will vary with equivalence ratio.

In addition, the fact that wrinkling introduces localised curvature to the flame front means that strain will also have an effect. For the case of an equidiffusive mixture, the effect of a disturbance in the flame front is that in the convex segments (peaks) the flame speed is reduced and in the concave segments flame speed is increased. This has a stabilising effect on the flame,

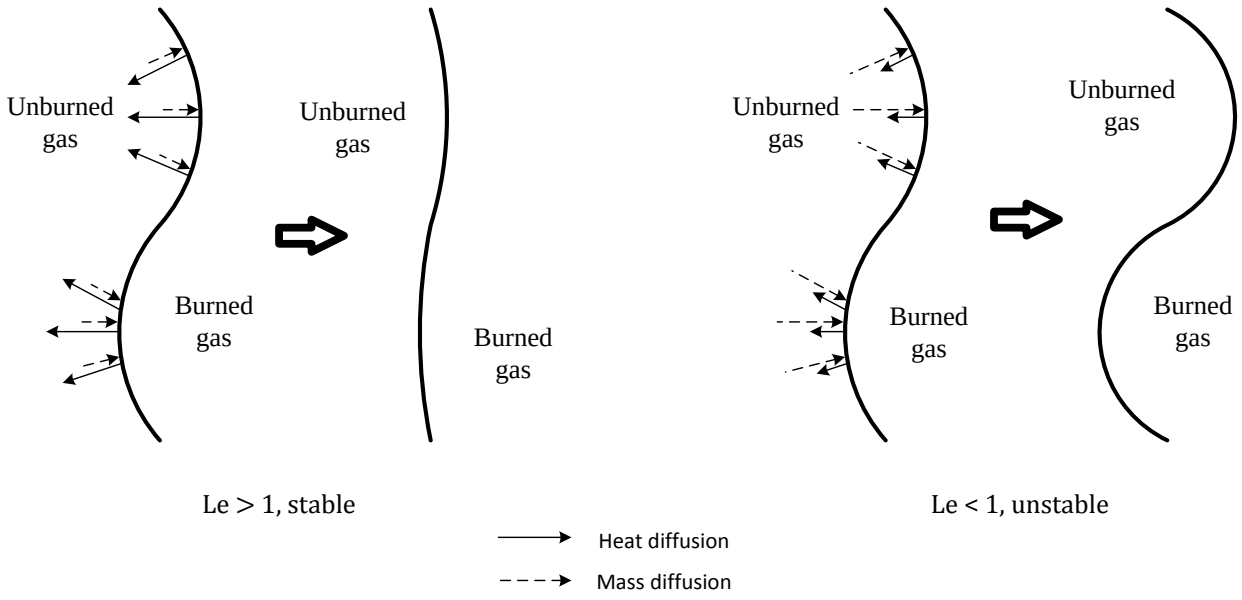

Figure 2.17 – Effect of flame front perturbation for varying Lewis number, developed from Law (2006).

so that in actual fact the stability boundary is shifted to slightly lower values of Lewis number. The larger the Markstein number, the more the flame will tend to be stabilised. The combination of nonequidiffusive and pure curvature instabilities is what is referred to as diffusional-thermal instability.

2.6.2 Hydrodynamic instability

A second cause of instability in the flame front is the hydrodynamic instability, also known as the Darrieus-Landau instability, which can result in flames becoming unstable even for mixtures where the Lewis number is greater than unity. This is caused by the fact that there is a density change across the flame front. If the flame is assumed to be infinitely thin, separating the upstream region of constant density ρ_u and the downstream region of constant density ρ_b, then a perturbation in the flame front will cause the instability to form.

Consider the flame to be propagating relative to the unburned gas with the laminar burning velocity. Whilst the velocity components tangential to the flame front must remain constant, the normal component of velocity to the flame front will be higher on the downstream side than the upstream side because of the density gradient. This means that the streamlines approaching a convex section of the flame front will diverge, as shown in Figure 2.18. For a laminar flow far

from the disturbance, we will expect the area of a streamtube to be constant. So, for the convex section, the diverging of the streamlines implies a widening of the streamtube and hence the reduction in flow speed. For the flame speed to remain constant, as defined by the downstream flow speed, this segment of the flame must advance further into the unburned gas. By a similar reasoning, the concave section will recede further into the burned gas region.

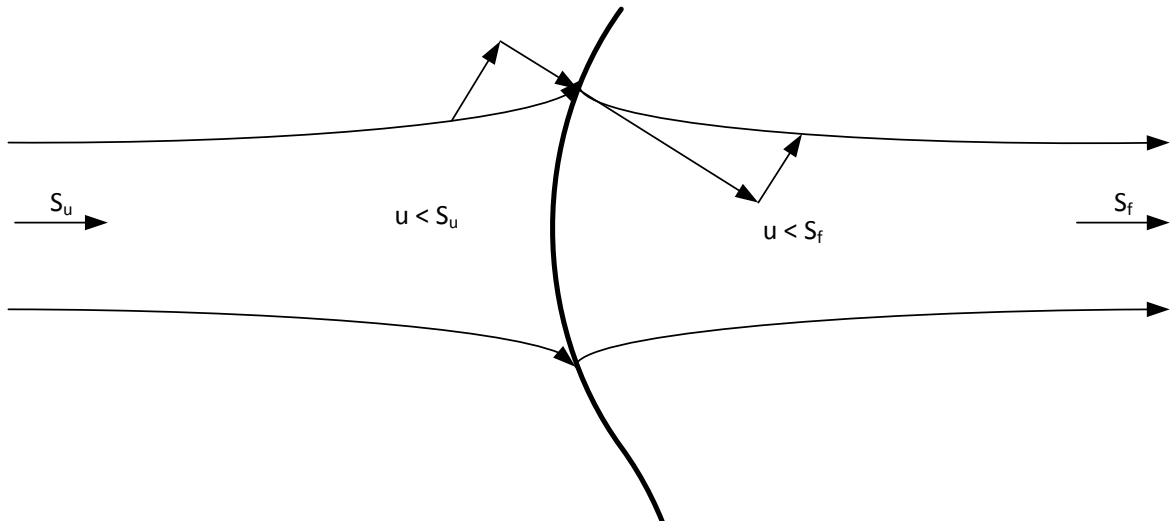

Figure 2.18 – Schematic showing the basis of hydrodynamic instability, based on Law (2006).

This is clearly an unstable mode of flame propagation, for all mixtures since it is independent of the mixture properties. The greater the density difference, the stronger the instability. Equally, due to the absence of length scales in the derivation, the flame will be unstable for all wavelengths of perturbation. However, this analysis is based upon the assumption of an infinitely thin flame, whereas in reality the finite flame thickness will enable the flame stabilisation effect of curvature discussed for the thermo-diffusive instability in section 2.6.1 to occur.

2.6.3 Initiation of instabilities

The implication of the stabilising effect of curvature mentioned in section 2.6.1 is that at high stretch rates the amplitude of any disturbances in the flame front will be reduced and any thermo-diffusive instability will be overcome, Bradley and Harper (1994). It is seen that after a given duration of flame propagation the instability will develop. In the case of spherically

expanding flames, the instability is typically initiated by disturbances caused by the electrodes, which lead to cracks on the surface of the flame front. These perturbations are then either stabilised or destabilised by the above mechanisms; Bradley and Harper (1994) explain how crack propagation occurs when the Peclet number, Equation (2.78), reaches a critical value. This effect is clearly seen in the results of Gu *et al.* (2000), which also show a correlation between critical Peclet number and Markstein number.

$$\mathrm{Pe} = \frac{r}{\delta} \tag{2.78}$$

In a study of high pressure methane-air flames using a constant volume spherical vessel, Rozenchan *et al.* (2002) delay the onset of cellularity by replacing the inert component in the air with helium; the higher diffusivity increases both the flame thickness and Lewis number of the mixture, supressing the diffusional-thermal instability.

2.6.4 Effect of cellularity on burning velocity measurements

The onset of cellularity in the case of a spherically expanding flame prevents further measurement of burning velocity, meaning that accurate detection is essential to prevent misreporting of values. The reason for this is that when the cellular structure forms, the area of the flame is increased, which leads to faster burning velocity even if the local flame speed at the surface is not affected by stretch, Law (2006). The models for constant pressure and constant volume propagation assume a smooth spherical surface, and so the value calculated based upon these models will be erroneous. It is not possible to determine the true area of the flame in its cellular state. In addition, the local stretch rate of the flame will be altered by the wrinkling of the flame, leading to a change in the burning velocity. This means that once cellularity has occurred, no further measurements of burning velocity can be made.

2.7 Further experimental effects on burning velocity measurements

In addition to stretch and cellularity, a number of other factors will have an impact upon the measured burning velocity, including buoyancy and ignition energy.

2.7.1 Buoyancy

For flames with low burning velocities, especially very lean mixtures or those with high levels of diluents, effects of gravity on the flame propagation become significant. Due to the difference in temperature between the burnt and unburnt gases, and corresponding lower density of the burnt gas, a buoyancy force causes the burnt gas to rise. For the case of the spherically propagating flame, this motion causes the flame kernel to rise, resulting in the flame reaching the top of the vessel first with accompanying significant heat transfer to the walls of the vessel before combustion is complete. This heat transfer reduces the pressure in the vessel, and as the flame kernel continues to rise, a point of inflexion will be seen in the pressure-time history. This reduces the period for which calculations of burning velocity can be made. The upwards motion of the flame kernel also has the effect of distorting the flame kernel shape from an ideal sphere centred on the spark gap, due to the greater velocity of the flame at the top of the kernel relative to the bottom. This complicates calculation of burning velocities since the analysis is based upon the assumption of a spherical flame, and also results in non-radial movement of the unburned gas from the top of the vessel being displaced downwards, further violating our assumptions regarding unburned gas movement ahead of the flame front.

Clarke (1994) conducted more extensive research into buoyancy effects, and compared burning velocities derived from experiments on slow burning mixtures in a constant volume bomb in both normal and zero-gravity conditions. Zero-gravity conditions were simulated by using a drop rig, which eliminates the effect of buoyancy. Andrews and Bradley (1973) derived an expression for the speed of the flame kernel upwards due to buoyancy, S_c:

$$S_c = \left(\frac{\rho_u}{\rho_b} - 1\right)\frac{gt}{4} \qquad \textbf{(2.79)}$$

Therefore, creating zero- or micro-gravity environments will eliminate the upwards movement of the flame kernel. Figure 2.19 shows the results from two experiments performed by Clarke (1994) on lean (equivalence ratio of 0.602) methane-air mixtures at an initial pressure of 1 bar and initial temperature of 298 K. Initially, the burning velocity for normal gravity is slightly

faster than for zero-gravity, due to the distortion of the flame resulting in a larger surface area than assumed in the analysis. However, it can be seen that the point of inflection in the pressure trace occurs much earlier in the normal gravity case as the effect of heat transfer becomes significant, causing the calculated burning velocity to fall off. This clearly limits the range of pressure for which data can be obtained. Also, the peak pressure obtained during combustion is significantly lower for the normal gravity case. Note that the burning velocities in these experiments are extremely low, so these will be flames for which the effects of buoyancy are particularly severe. Ronney and Wachman (1985) also investigated the effect of gravity on spherical flames propagating in a closed vessel using a similar method of creating near zero-gravity conditions, and found that for burning velocities of >15cm s^{-1}, there was no difference between flames propagating in normal and zero-gravity conditions.

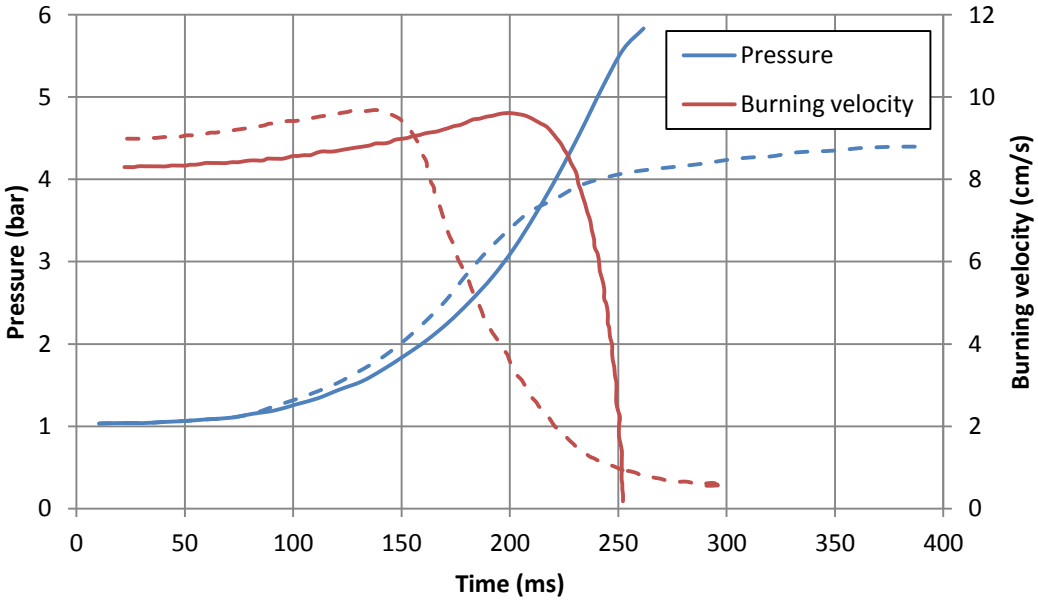

Figure 2.19 – Comparison of pressure-time and burning velocity-time results for experiments of lean methane-air mixtures at 1 bar initial pressure and 298 K initial temperature in zero gravity (solid lines) and normal gravity (dashed lines). Reproduced using data from Clarke (1994).

2.7.2 Ignition energy

In the case of spherical expanding flames, combustion is initiated with either a spark or laser pulse. This will constitute an addition of energy, which can influence the measured burning velocity. For spark ignition, Bradley *et al.* (1996) found that for spark energies slightly above the minimum spark energy, measured flame speeds reach a stable value by a radius of 6 mm.

Bradley *et al.* (1998) showed that overdriving the flame was possible using very high ignition energies via laser ignition, but this should not present a problem in the present work. Chen *et al.* (2009) performed numerical simulations and found that the effect of ignition energy also depended strongly upon the Karlovitz number of the mixture.

Marshall (2010) used a variable dwell time (section 4.1.8) to control the coil energy in the current experimental setup. For the range of available coil energies, no overdriving of the spark was evident, and the effect of varying ignition energy was minimal.

2.8 Fuels

In this section, the fuels investigated will be presented, including motivations for study and an overview of existing data available in the literature. Both gaseous and liquid fuels have been tested.

2.8.1 Biogas

Biogas is a non-fossil gas produced from waste products by anaerobic digestion, and consists of CH_4 (typically 50-80%) and CO_2 (15-45%), with smaller concentrations of other gases, including trace levels of hydrogen sulfide (of order 1000-5000 ppm). The feedstock can be farm waste, energy crops, sewage and waste food, and the resulting biogas is used almost interchangeably with natural gas. Wide availability of biogas sources makes it attractive as a renewable option, and the use of waste materials that would otherwise decompose and produce greenhouse gases is particularly beneficial. According to a report compiled by Plombin (2003), the CO_2 liberated by the combustion of the biogas has no net impact on the greenhouse effect, since it originates from organic matter, as opposed to the 'gas freeing' resulting from the combustion of natural gas produced from fossil deposits. Biogas is used in spark ignited gas engines and dual fuel engines (often as part of a CHP system), burners, gas turbines and fuel cells. Gaseous fuels are generally considered good for internal combustion engines due to their ability to form combustible mixtures with air, and their ability to operate engines with high

compression ratios and lean mixtures which gives good thermal efficiency and low emissions e.g. Swami Nathan *et al.* (2010).

In the case of biogas, the CO_2 is a diluent; it reduces the laminar burning velocity, the flame stability and the flammability range, all of which can have adverse effects on combustion system performance. Biogas is often 'upgraded' by extracting the non-combustible gases (primarily the CO_2) such that the CH_4 concentration is at least 96%, before it is used as a vehicle fuel, with very similar properties to natural gas. Whilst most biogas is 'upgraded' before being used as a vehicle fuel, there are certain applications where it may be advantageous to use the biogas without first extracting the CO_2. Biogas can be used in SI engines directly; Huang and Crookes (1998) performed an assessment of biogas as a fuel in an SI engine, concluding that the main positive impacts of the CO_2 were reduced NO_x emissions and the possibility of a higher compression ratio. High concentrations of CO_2 have been shown to be feasible; Porpatham *et al.* (2008) performed tests on biogas in a spark ignition engine whilst Bedoya *et al.* (2009) demonstrated use of biogas with up to 40% CO_2 in a dual fuel engine. Disadvantages exist, due to the drastically reduced energy density of the fuel, a reduction in output and thermal efficiency, and an increase in HC emissions. However, Crookes (2006) states that "the ability to accept the fuel without excessive treatment to remove non-fuel components would enable production costs to be pegged in developing nations". A study by Swami Nathan *et al.* (2010) suggests that biogas can also be used effectively in Homogeneous Charge Compression Ignition (HCCI) engines without the need to remove CO_2. Cohé *et al.* (2009) also explain how the presence of increased levels of CO_2 is beneficial for NO_x emissions and lean burn combustion in stationary gas turbines. The inclusion of CO_2 in gas turbine fuel can also improve the performance efficiency of subsequent carbon capture and sequestration technologies.

Given the potential for using biogas as a vehicle fuel, research into its combustion performance (of which laminar burning velocity is a fundamental parameter) is of value. When used in gas turbines, spark ignited gas engines and dual fuel engines, laminar burning velocity

data for high temperatures and pressures is needed. In particular, the effect of CO_2 content needs investigation. Within the literature, methane is one of the most widely studied fuels since it has one of the simplest chemical kinetic mechanisms and so provides the easiest comparison between experimental data and results from numerical simulations. Most of the data in the literature covers ambient conditions of temperature and pressure, although burning velocity correlations have also been obtained allowing values to be quoted for higher conditions. Previous studies of burning velocity of simulated biogas mixtures (CH_4/CO_2) have been performed, most notably as detailed in Clarke (1994) and later in Stone *et al.* (1998), using results from the same experimental apparatus but with the addition of a drop-rig to remove the effects of buoyancy. The effect of CO_2 addition has been investigated using a slot burner by Cohé *et al.* (2009), whilst Halter *et al.* (2009) and Galmiche *et al.* (2011) used imaging of spherically expanding flames to extract burning velocities.

2.8.2 Hydrous Ethanol

With increasing oil prices and environmental concern regarding the emissions of CO_2 from the transport sector, liquid biofuels are seen as a way of reducing reliance on fossil fuels whilst maintaining the high energy density provided by liquid fuels. For example, Directive 2009/28/EC of the European Parliament and of the Council of 23 April 2009 (2009) requires a "mandatory 10 % minimum target to be achieved by all Member States for the share of biofuels in transport petrol and diesel consumption by 2020". Despite acknowledged issues regarding production and the effect of associated indirect land use change, ethanol has received much attention as a potential biofuel, and is already in use globally, either as a neat fuel (E100), or blended with a base gasoline (e.g E85). In some countries, such as Brazil, flex fuel engines, designed to run on any blend of gasoline and ethanol are widespread.

Ethanol has been used extensively in automotive fuels primarily as a fuel extender and anti-knock agent in ethanol gasoline blends, with numerous advantages including higher octane number (allowing higher compression ratios), reductions in unburned hydrocarbons (HC), CO

and NO_x emissions, as well as easing overall air pollution and demand on petroleum fuels, e.g. Al-Baghdadi (2008). Pure ethanol fuel (E100) has also been studied e.g. Brewster (2007), demonstrating higher output and brake efficiency, as well as lower CO_2 emissions.

To minimise the impacts of ethanol production, processing routes should be examined to determine where savings in terms of energy production can be made. Some of the biggest savings are achieved by reducing the energy required for removal of water from the produced ethanol. Fermentation will typically produce an ethanol concentration of around 12% by volume, meaning that to produce neat ethanol, extensive distillation is required. The left hand plot in Figure 2.20 shows the distillation energy requirement as a fraction of the Lower Heating Value (LHV) of ethanol. This plot also shows the fact that an azeotrope is formed at 96.5% ethanol by volume (95.6% ethanol by mass), beyond which higher concentrations of ethanol cannot be achieved by distillation. Further increases in concentration can only be achieved by expensive and energy intensive dehydration procedures. The right hand chart in Figure 2.20 shows the overall energy output of ethanol and its co-products for a specific case of ethanol production from corn feedstock. The energy required at each stage of production is represented by the various sectors. This shows that 14% of the energy is required for dehydration beyond the azeotrope, and 23% required for distillation. Considering this and the very non-linear energy usage during distillation, utilising hydrous ethanol potentially offers significant energy

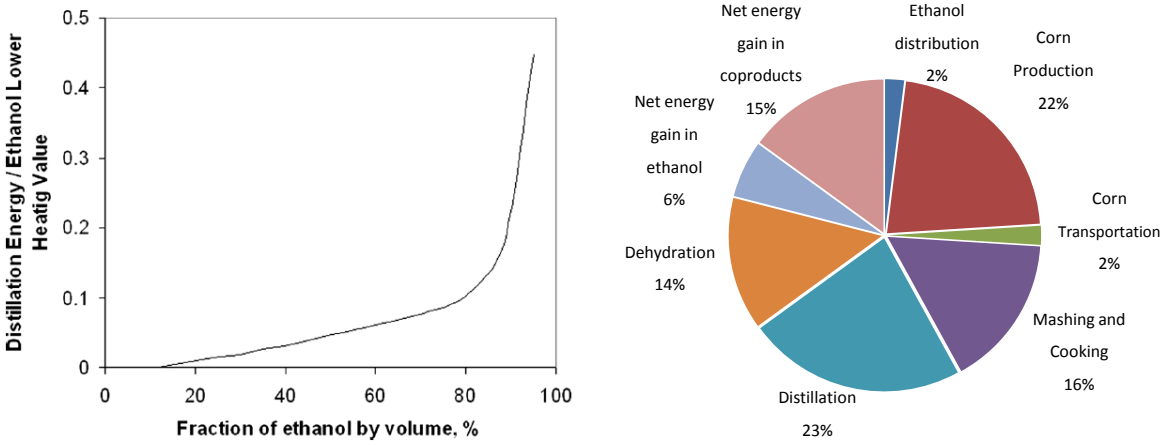

Figure 2.20 – energy required for ethanol distillation as a fraction of the LHV of ethanol, left, and the net energy balance for ethanol production, right, with the full circle representing the energy output of ethanol and co-products. Adapted from Martinez-Frias et al. (2007).

savings in the ethanol production life cycle. A study by Brewster *et al.* (2007) investigated the effect of water content on the performance of a direct injection multi-cylinder turbocharged engine developed to run on E100, and found that increasing water content resulted in reduced output and efficiency, but the technology carries merit. In addition, the increased water content results in lower combustion temperatures and hence lower NO_x, as well as supressing knock and pre-ignition, presenting opportunity to extend the engine operating regime. Wyman and Hinman (1990) report less volatile organic compounds (VOCs) and less smog producing compounds. Costa and Sodré (2010) compared the performance of a 1.0 litre flex-fuel engine when operated on a gasoline-anhydrous ethanol blend (22% by volume) and a hydrous ethanol fuel (6.8% water by mass), to provide a comparison with a typical ethanol blend. This study showed that it is possible to achieve comparable power output, although advanced ignition timing is required to enable this. A further application for hydrous ethanol is in Homogeneous Charge Compression Ignition (HCCI) engines. Whilst fuel with high concentrations of water can be problematic in SI or diesel engines, HCCI is better suited to hydrous ethanol, provided the fuel can be fully vaporised before entering the combustion chamber. Mack *et al.* (2009) successfully ran a HCCI engine on hydrous ethanol mixtures with up to 60% water. Hydrous ethanol also provides opportunities for steam reforming. Shimada and Ishikawa (2013) tested such a system, and reported thermal efficiencies of 1.18 times that of a conventional spark ignition engine.

Whilst hydrous ethanol clearly presents opportunities for improved energy efficiency, blending with gasoline can be problematic due to the immiscibility of water and gasoline, which can lead to phase separation within the fuel blend. Figure 2.21 shows the phase separation curves of blends of ethanol, water and gasoline at -2°C and -25°C, as given by Johansen and Schramm (2009). This shows that the phase separation boundary is temperature dependent. It would also be expected to vary with exact composition of the gasoline. The overlaid points demonstrate the phase separation as water content is increased. The point on the

right hand axis represents a blend of E85 made using anhydrous ethanol. The red line indicates the addition of water in the blend. The phase separation boundary is seen to occur with the addition of 18% water by volume in the ethanol component (15% of the overall blend). A more extreme example (50% water in ethanol by volume), is included which will give a clear phase separation as shown. The relative fractions of the two phases are calculated by minimisation of the Gibbs free energy. This analysis therefore shows that it is possible to use anhydrous ethanol with relatively modest water content as a blending component with gasoline.

Filho (2008) investigated the possibility of using hydrous ethanol with a maximum water content of 4.9% by volume as part of a blend containing 22% hydrous ethanol, and concluded that the blend is feasible whilst avoiding phase separation. Melo *et al.* (2012) also tested blends of E25 as a base fuel, blended with increasing fractions of hydrous ethanol containing 4.3% water by volume, showing that blending with hydrous ethanol can provide attractive options in terms of energy efficiency.

Therefore it is appropriate to conduct fundamental studies upon hydrous ethanol fuels to assist with development of the technology. Some burning velocity data does exist in the literature, such as that of Zhang *et al.* (2011), who present results for mixtures of 75% hydrous

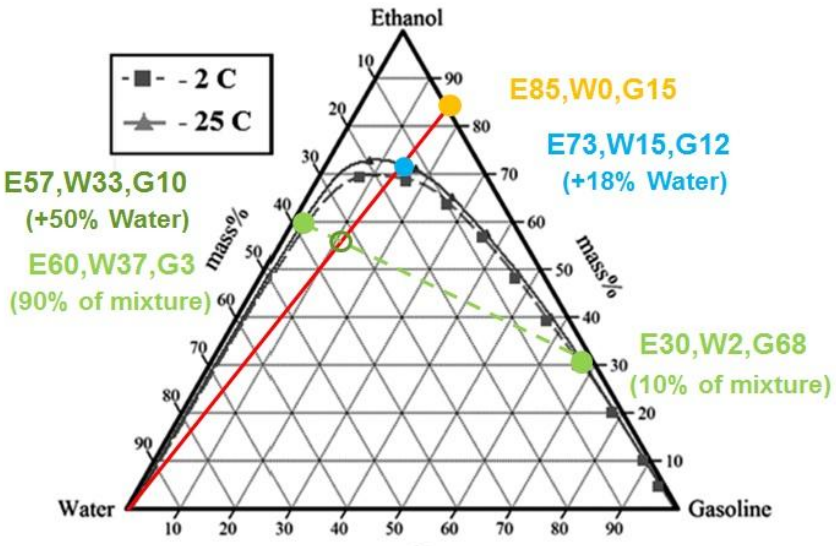

Figure 2.21 - Phase separation curves of ethanol/gasoline/water at -2°C and -25°C, adapted from Johansen and Schramm (2009).

ethanol (25% water by volume) mixed with varying levels of hydrogen to represent reformer gas. However, the range of water fractions and conditions for which data is available is very limited, so more data on the effect of water addition to ethanol-air mixtures is of interest.

2.8.3 THEO fuels

The term THEO fuels used here references blends of toluene, n-heptane, ethanol and iso-octane in any combination. These mixtures are of interest since they can be used to represent surrogate gasoline-ethanol blends. Primary reference fuels (PRFs) are binary blends of iso-octane (RON = 100) and n-heptane (RON = 0), used to simply represent a gasoline with a desired octane rating. Ternary blends of isooctane, n-heptane and toluene are referred to as toluene reference fuels (TRFs) and are used as surrogate fuels to more accurately model the performance of fuels with differing RON and MON, which is increasingly necessary for the development of future engine technologies since real gasoline exhibits fuel sensitivity, e.g. Morgan *et al.* (2010). Such reference fuels provide a way of determining gasoline behaviour and allow chemical kinetic modelling; it is not currently possible to model complex chemistry of gasoline since it is made up of hundreds of different species.

A study by Morgan *et al.* (2010) experimentally determined the RON and MON of TRFs to produce a simple response surface model for the octane number and sensitivity of any TRF. Their results showed non-linear mixing behaviour with regards to RON and sensitivity, suggesting influence of low temperature chemistry, and importance of the Negative Temperature Coefficient (NTC) region in ignition delay curves. Following this result, it was decided to perform experiments on blends of these components to determine burning velocities of such blends. It was hoped that this would highlight any unexpected behaviour when blending the pure components, and that mixing rules to describe burning velocities of blends could be evaluated. Including ethanol to produce quaternary blends of iso-octane, n-heptane, toluene and ethanol then allows a surrogate of gasoline with ethanol to be produced.

Some published work has been performed recently looking at the behaviour of pure components, such as that of Sileghem *et al.* (2013) which presents data for TRF components using the heat flux method at atmospheric pressure and two initial temperatures (298 K and 358 K) and Kumar and Sung (2010) who use the twin flame counterflow technique and PIV to produce data at 400 K and 470 K. Sileghem *et al.* (2014) includes ethanol and methanol, and makes comparisons with mixing rules as described in section 2.3.5 to predict burning velocities of blends of pure components. Whilst some data is available, it remains desirable to obtain further data on a wider range of blends to investigate the non-linear behaviour seen with the modelling of RON and sensitivity.

2.9 Influence of burning velocity in engines and engine modelling

The laminar burning velocity has a significant impact upon the performance of a particular fuel in the context of internal combustion engines. As summarised by Stone (2012), "the combustion in a homogeneous charge spark ignition engine is commonly divided into three parts:

a) An initial laminar burn, before the flame kernel is large enough to be influenced by turbulence; this can be considered as corresponding to the first few per cent mass fraction burned.
b) Turbulent burning, with a comparatively wide flame front, and pockets of unburned mixture entrained behind the flame front.
c) A final burn period ('termination period' or 'burn up'), in which the mixture within the thermal boundary layer is burned at a slow rate, because of a reduced fluid motion and a lower temperature."

This description implies that as a result of the initial burn being under laminar conditions, the flame propagation speed will be strongly related to the laminar burning velocity, albeit under highly stretched conditions as in the case of combustion in a spherical vessel.

Additionally, it would not be expected that the initial burning velocity will be exactly the determined burning velocity at the same conditions, as spark initiation would be expected to also have an effect, as suggested by Kalghatgi (1985). However, there will clearly be a strong link between initial burning velocity and laminar burning velocity.

Using burn durations for a given mass fraction burned (mfb) is a common way of summarising the burn rate such as described by Stone (2012). The 0-10 % mass fraction burn duration is considered to completely encompass the laminar burn phase at the start of combustion and the transition to fully developed turbulent combustion. Using a shorter mass fraction burned interval of just a few percent would isolate the initial laminar burn phase more precisely, although the error introduced by using such small values of mass fraction burned would negate such an advantage. The 10-80 % mass fraction burn duration describes the fully turbulent combustion period.

Whilst the initial laminar burn period accounts for a relatively small proportion of the overall combustion process, it can be shown that the speed of the initial combustion has an impact upon the remainder of the turbulent combustion. This can be seen in Figure 2.22, which shows the relationship between the 0-10% mass fraction burn duration and the 10-80% mass fraction duration for the case of a stoichiometric W0 mixture tested in a single cylinder optical engine as described in section 4.2. The points represent a number of individual cycles from a single test condition, showing a degree of cycle-by-cycle variation. Despite this, it is clear that there is a trend between a slow initial burn and a subsequently slower burn during the fully turbulent stage of combustion. This illustrates the importance of the early laminar burn phase on the overall combustion performance.

Furthermore, the speed of turbulent combustion is itself dependent upon the laminar burning velocity of the mixture. Turbulent combustion models are necessary for modelling of engine combustion performance, and early models such as that of Tabaczynski *et al.* (1980) for the rate at which mass is entrained into the flame front clearly show the dependence upon

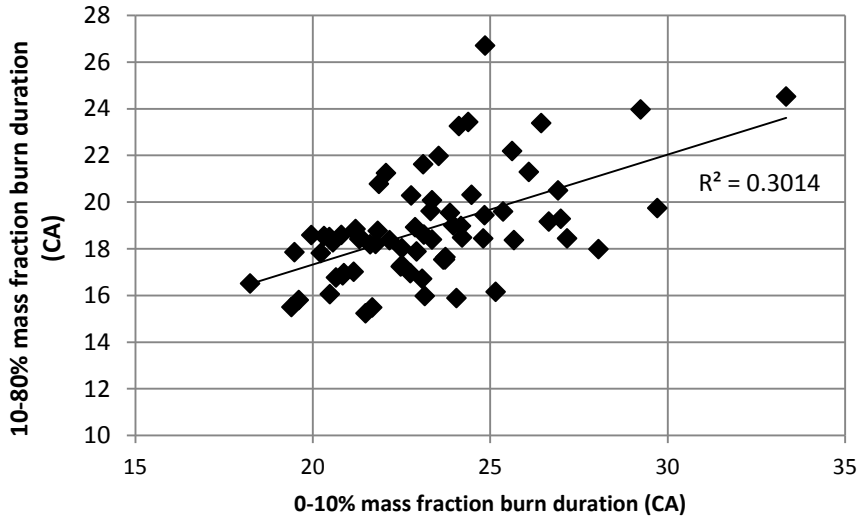

Figure 2.22 – 10-80% against 0-10% mass fraction burn duration for a stoichiometric W0 mixture at MBT and conditions specified in section 7.3.6.

laminar burning velocity:

$$\frac{\mathrm{d}m_\mathrm{e}}{\mathrm{d}t} = \rho_\mathrm{u} A_\mathrm{e} (U' + S_\mathrm{L}) \qquad \textbf{(2.80)}$$

where m_e is the rate of mass entrainment into the flame front, A_e is the flame front area, U' is the turbulence intensity and S_L is the local laminar burning velocity. Various other phenomenological approaches to turbulent flames are covered in the literature, e.g. Kuo (1986), and will not be detailed here, but all result in turbulent flame speeds scaled relative to the laminar burning velocity, clearly indicating the importance in turbulent combustion.

Since engine simulation is becoming increasingly important as a tool for reducing the cost and time required for engine development, engine models are developing in their complexity, and although many phenomena require three dimensional CFD modelling, simplified one-dimensional simulation is still used. As mentioned in section 2.4, 1D models require burning velocity data, and can also involve the use of burning velocity correlations to simplify the process. Engine models commonly make use of the Wiebe function, and various correlations of the Wiebe function parameters to engine operating conditions have been trialled. The model of Lindström *et al.* (2005) uses "correlations of laminar burning velocity as a function of pressure, temperature, air-fuel ratio and residual gas content to predict the relative change in the Wiebe parameters total burn duration and combustion mode". By investigating the independent effects

of equivalence ratio, temperature, pressure and residuals fraction on the total burn duration, it was seen that total burn duration could be described as proportional to the inverse of laminar burning velocity, which itself is a function of these parameters. The resulting model will end up with the form:

$$\Delta\theta = \Delta\theta_0 g(S_\mathrm{L}) g(\mathrm{spark}) g(\mathrm{speed}) \qquad \textbf{(2.81)}$$

where the functions described by g are functions for the relative influence of different operating parameters. It is claimed that the use of such correlations will "increase the generality of the combustion model and reduce the need to calibrate the model for dependencies already captured in the laminar burning velocity correlations". Figure 2.23 shows a result presented by Lindström *et al.* (2005) for the total burn duration predicted by their model including the burning velocity correlation given in Heywood (1988) which appears to be of the form developed by Metghalchi and Keck (1982), but uses the coefficients developed for an indolene-air-diluent mixture by Rhodes and Keck (1985). The results of the model are compared to measurements made for the same conditions, and the result shows that inclusion of the burning velocity correlation results in a fairly good agreement with the measured values. The optimised values are obtained by altering the temperature and temperature exponents α and β, demonstrating the importance of having accurate values of these exponents.

It can also be shown that burning velocity is a factor in pre-ignition, with an increase in burning velocity suggesting a higher tendency for pre-ignition according to results plotted by Kalghatgi (2014). However, this tendency can be countered practically by effects such as evaporative cooling. In addition, as mentioned in section 2.3.2 the value of temperature exponent is influential in the flame thickness and in the case where the temperature exponent is greater than 1.5 the flame thickness will increase with decreasing temperature which will make pre-ignition less likely. For fuels such as ethanol the tendency of high values of burning velocity leading to pre-ignition can be mitigated by this effect. This therefore again highlights

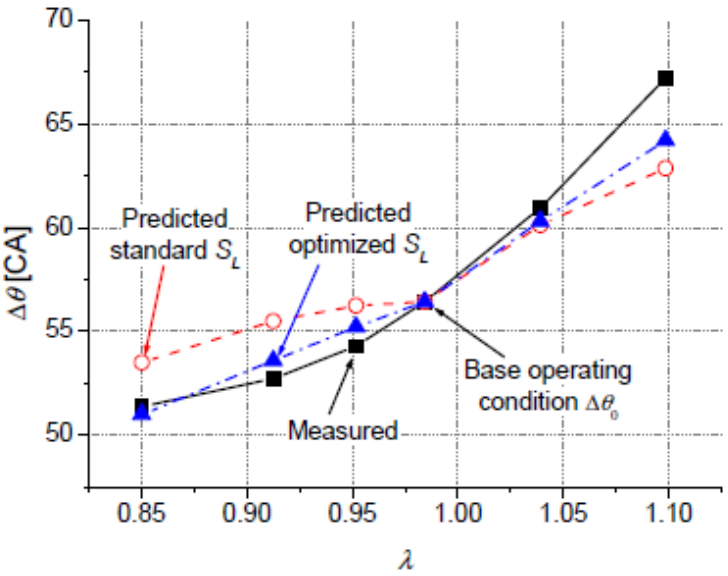

Figure 2.23 – Measured and predicted burn duration as a function of λ. The value of S_L used is that at the conditions at the spark crank angle, using the burning velocity correlation in Heywood (1988), and with optimised pressure and temperature exponents. From Lindström *et al.* (2005). Reproduced with permission from SAE International.

the importance of not only accurate burning velocity measurements for modelling purposes, but also of accurate understanding of the effects of temperature and pressure in the context of other phenomena such as pre-ignition. It should be noted that whilst a factor, temperature dependence of laminar burning velocity is only one part of a complex set of factors leading to pre-ignition.

2.10 Concluding remarks

This literature review has introduced the background to the laminar burning velocity, and highlighted the importance of obtaining accurate measurements and representation of trends, in terms of application in internal combustion engines, but also as a tool for validating increasingly complex chemical kinetic models. Along with the background and motivation for study of the chosen fuels of interest, there is a strong basis for the investigation that follows. The various factors that have an effect on the value of burning velocity of a given fuel have been outlined, namely equivalence ratio, temperature, pressure and residuals/diluents, informing the essential parameters to be investigated and reported. The 'state of the art' in terms of techniques for measurement of burning velocity has been reviewed, with particular focus upon dealing with the effects of stretch and cellularity, to ensure that the subsequent experiments will provide sufficiently accurate data.

3 Modelling

In this chapter, the various models used throughout this project are described. A number of models have been used in the past to determine burning velocity from both constant volume and constant pressure combustion in constant volume vessels, and have been included here for completeness in section 3.1.

For validation and comparison, some numerical simulation results are obtained. For this, some chemical kinetic modelling software is used. Since the focus of this project is upon experimental measurement and not development of reaction mechanisms, only a brief description will be given, in section 3.2.

3.1 Combustion modelling

Accurate combustion models are required to determine burning velocity from experimental measurements. Constant volume modelling allows laminar burning velocity measurements to be made using the record of measurement of pressure rise in the bomb during combustion. To be able to apply these models, some assumptions first need to be made and validated.

3.1.1 Constant volume vessel assumptions

Assumptions made in modelling constant volume combustion are well documented in the literature. The work on modelling constant volume combustion by Luijten and De Goey (2007) lists the following 10 assumptions:

1. The unburned mixture is initially at rest. This is important if effects of flow on measured flame speed are not modelled. To justify this assumption, it is necessary to ensure suitable settling time after filling the vessel. This is checked in section 6.1.4.2. Additionally, if the combustion vessel is heated, then it is necessary to ensure a uniform temperature to prevent convection driven bulk flow. Alternatively the assumption would need to be made that the flow is sufficiently slow compared to that due to combustion.

2. Pressure and temperature of the gas are initially uniform.
3. Pressure remains uniform during combustion. This is a justifiable assumption when considering that the flame speeds will be significantly less than the speed of sound.
4. Total mass and volume of gas in the vessel is conserved. This is a totally justifiable assumption since the bomb is sealed during combustion meaning that no gas can leave during combustion.
5. Central ignition with negligible heat input. The position of the electrode spark gap can be set so that the ignition is central to exploit the symmetry of the propagating flame. Effect of ignition energy is discussed in section 2.7.2.
6. The process is adiabatic. This will mean no external heat loss, since there is no heat input into the system. This also implies that there is no radiative transfer to or from the flame front, or burned and unburned gases.
7. The effect of buoyancy is negligible. Buoyancy will tend to distort the flame and cause non-symmetrical flame propagation. Since the model assumes spherical propagation, distortion from buoyancy will cause erroneous measurements. Some slow burning mixtures may have flames which are affected by buoyancy. Effect of buoyancy is discussed in section 2.7, and elimination of buoyancy affected results in section 6.2.2.3.
8. The flame front is spherical. Modelling in both constant pressure and constant volume combustion assumes a spherical flame in the determination of flame speed and stretch rate. This assumption is violated by buoyancy (see above) or by the onset of cellularity.
9. The flame front is thin. In constant volume combustion, a thin flame front is assumed to separate the regions of burned and unburned gas. In multi-zone combustion models, the thin flame front will pass through each of the pre-determined zones in turn. In reality, the flame front has an appreciable thickness, which will contain mass neither assumed to be in the burned or unburned region. This can be a source of error when the flame is small. In the case of constant pressure analysis, the thickness of the flame front leads to differing

definitions of Markstein length, as described in section 2.5.5. The effect of flame thickness on constant pressure measurements is discussed in section 6.2.2.3.

10. Effects of flame stretch are negligible for large flame radii. This assumption is made for constant volume combustion only, and has been explained in section 2.5.8. Further analysis is provided in section 6.2.2.8.
11. The unburned gas is compressed isentropically. This assumption is required to determine the temperature of the unburned gas as the pressure increases.

Garforth and Rallis (1978) additionally present the following assumptions:

1. The temperature immediately behind the flame front corresponds to the theoretical equilibrium adiabatic value. However, the authors accept that this is a potential source of error. In multi-zone models, the temperature of the unburned gas is modelled more accurately.
2. Chemical equilibrium is achieved immediately behind the flame front. This is required to analyse the behaviour of the burned gases.
3. No dissociation occurs in the unburned gas zone. The authors claim this as a highly accurate assumption.

3.1.2 Flame structure and propagation

The one dimensional flame structure described by Figure 2.1 can be adapted for the constant volume vessel with a spherically expanding flame, and flame propagation is defined before burning models can be developed.

1. Central ignition initiates flame propagation.
2. The initial period of flame propagation takes place with negligible pressure rise, referred to as the pre-pressure period. In this phase of combustion, **constant pressure modelling** is required.

3. As flame propagation continues, the burned gas expands and compresses the isentropic gas ahead of the flame front. As given in section 3.1.1, the compression of the unburned gas is assumed to be isentropic, resulting in a coupled increase in pressure and temperature. Combustion then takes place at increasingly higher pressures and temperatures as the flame propagates, requiring **constant volume modelling**. Recompression of the burned gas behind the flame front also results in a temperature gradient in the burned gas, which can be taken into account if more accurate multi-zone combustion models are used as described in section 3.1.5.3.
4. As the flame approaches the wall, quenching will take place due to heat transfer to the wall, at which point the pressure in the vessel will decrease.

The overall duration of the process from ignition to quenching will depend on the flame propagation speed, but for mixtures tested here will typically be in the order of tens of ms.

3.1.3 Constant pressure combustion models

Modelling of constant pressure combustion during the pre-pressure phase is based upon measurements of the flame front propagation, and is simplified since the conditions of temperature and pressure are considered to be the same as the initial conditions. Therefore, modelling needs to determine flame speed and burning velocity solely from measurements of the flame front radius, typically using schlieren photography. The flame speed is simply defined as the rate of change of radius with respect to time, and so can be found simply from numerical differentiation of measured flame radii, allowing subsequent extrapolation back to zero stretch as described in section 2.5.6.

3.1.4 Constant volume combustion models

Various models have been used to relate burning velocity to pressure over the years, and these will be reviewed briefly. In addition to these general models, a specific combustion model

relating pressure to mass fraction burned or flame radius is needed to be able to fully determine the burning velocity.

Amongst the first combustion models presented was that proposed by Fiock *et al.* (1940), where a burning shell of thickness $S_u \mathrm{d}t$ was proposed, whose expansion results in an increase in pressure $\mathrm{d}p$ and a shifting of the unburned gas boundary by $\mathrm{d}r$. The corresponding change in volume of the unburned gas resulting from the expansion is

$$\mathrm{d}V_u = -4\pi r^2(\mathrm{d}r - S_u \mathrm{d}t) \quad \textbf{(3.1)}$$

where r is the radius of the unburned gas boundary and the volume of unburned gas V_u is:

$$V_u = \frac{4}{3}\pi(R^3 - r^3) \quad \textbf{(3.2)}$$

where R is the radius of the vessel. If isentropic compression is assumed, then the following result is achieved:

$$S_u = \frac{\mathrm{d}r}{\mathrm{d}t}\left[1 - \frac{\mathrm{d}p}{\mathrm{d}r}\frac{(R^3 - r^3)}{3p\gamma_u r^2}\right] \quad \textbf{(3.3)}$$

Lewis and von Elbe (1961) found this to be potentially inaccurate, magnifying any errors in r or p, due to the fact that the second term in the bracket will be close to unity. Additionally, the derivative of pressure can be subject to error in measurement in the initial stages of the pressure rise.

Lewis and von Elbe (1961) instead proposed their own model, where two expressions for volume of an elemental shell are equated. The shell is considered at time $t = 0$, before any combustion has taken place and at time t, when it undergoes combustion. This is illustrated in Figure 3.1. Before ignition, an elemental shell has volume given by:

$$\mathrm{d}V_s^0 = 4\pi r_i^2 \mathrm{d}r_i \quad \textbf{(3.4)}$$

When it burns at time t, the same shell is now at radius r_b due to the difference in density of the burned and unburned gas. However, due to the change in both pressure and temperature from their initial values, the volume of the shell will have become:

$$\mathrm{d}V_s = 4\pi r_i^2 \mathrm{d}r_i \left(\frac{T_u p_i}{T_i p}\right) \quad \textbf{(3.5)}$$

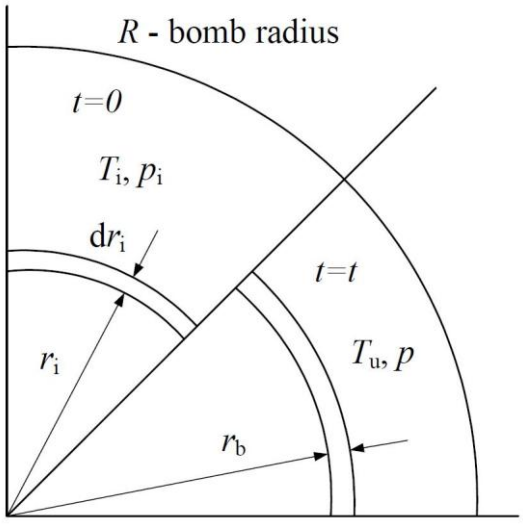

Figure 3.1 – Combustion of an elemental shell. From Marshall (2010).

The second expression for the volume of the shell is from the thickness of the shell, $S_u dt$:

$$dV_s = 4\pi r_b^2 S_u dt \tag{3.6}$$

If we again assume isentropic compression of the unburned gas then:

$$T_u = T_i \left(\frac{p}{p_i}\right)^{\frac{\gamma_u - 1}{\gamma_u}} \tag{3.7}$$

Using the above assumption and combining Equations (3.5) and (3.6), then an expression for burning velocity is derived:

$$S_u = \frac{dr_i}{dt}\left(\frac{r_i}{r_b}\right)^2 \left(\frac{p_i}{p}\right)^{\frac{1}{\gamma_u}} \tag{3.8}$$

The initial radius of the elemental shell before combustion takes place, r_i is related to the mass fraction burned, x, by:

$$r_i = \sqrt[3]{xR^3} \tag{3.9}$$

Therefore, to solve Equation (3.8) pressure, flame radius and mass fraction burned are all required. In the experiment pressure is measured. Similarly, r_b could be measured, but would require full optical access of the flame front to be able to track the flame front for the full duration. Instead, the flame radius can be deduced if the mass fraction burned (mfb) is known. This is another unknown in Equation (3.8), and so a combustion model to determine mfb is required. Mass fraction burned models are described in section 3.1.5.

Metghalchi and Keck (1982) proposed a method whereby burning velocity is determined by considering the mass burning rate:

$$S_{\mathrm{u}} = \frac{1}{\rho_{\mathrm{u}} A_{\mathrm{f}}} \frac{\mathrm{d}m_b}{\mathrm{d}t} \tag{3.10}$$

In this case, the rate of change of burned gas is related to the mass fraction burned:

$$S_{\mathrm{u}} = \frac{\rho_0 V}{\rho_{\mathrm{u}} A_{\mathrm{f}}} \frac{\mathrm{d}x}{\mathrm{d}t} \tag{3.11}$$

$$S_{\mathrm{u}} = \frac{\rho_0 R^3}{\rho_{\mathrm{u}} 3 r_{\mathrm{b}}^2} \frac{\mathrm{d}x}{\mathrm{d}p} \frac{\mathrm{d}p}{\mathrm{d}t} \tag{3.12}$$

This equation can then be solved with the use of an appropriate mass fraction burned model, as covered in section 3.1.5, and differentiation of the pressure record.

A further equation has been derived by Luijten and De Goey (2007) which is again based upon the mass burning rate as in Equation (3.10). Conservation of volume leads to

$$\frac{{r_{\mathrm{b}}}^3}{R^3} = \frac{V_{\mathrm{b}}}{V} \tag{3.13}$$

$$\frac{{r_{\mathrm{b}}}^3}{R^3} = 1 - \frac{\rho_0 m_{\mathrm{u}}}{\rho_u m_{\mathrm{t}}} \tag{3.14}$$

and application of the equation for isentropic compression

$$\frac{\rho_0}{\rho_{\mathrm{u}}} = \left(\frac{p_0}{p_{\mathrm{u}}}\right)^{\frac{1}{\gamma_{\mathrm{u}}}} \tag{3.15}$$

yields an expression for r_{b}:

$$r_{\mathrm{b}} = R\left[1 - \left(\frac{p_0}{p_{\mathrm{u}}}\right)^{\frac{1}{\gamma_{\mathrm{u}}}} (1 - x)\right]^{\frac{1}{3}} \tag{3.16}$$

Substituting this, along with the assumption of isentropic compression given in Equation (3.15) into Equation (3.12), a further expression for burning velocity can be obtained:

$$S_{\mathrm{u}} = \frac{R}{3}\left[1 - \left(\frac{p_0}{p}\right)^{\frac{1}{\gamma_{\mathrm{u}}}} (1 - x)\right]^{-\frac{2}{3}} \left(\frac{p}{p_0}\right)^{-\frac{1}{\gamma_{\mathrm{u}}}} \frac{\mathrm{d}x}{\mathrm{d}p} \frac{\mathrm{d}p}{\mathrm{d}t} \tag{3.17}$$

3.1.5 Mass fraction burned models

To determine burning velocity from any of the derived relations, it is necessary to employ a model to relate the pressure in the vessel to the mass fraction burned. From this it is also

possible to determine the radius of the flame from the pressure, and subsequently the burning velocity. These models can be analytical relations or numerical models.

3.1.5.1 Linear mass fraction burned model

A common model used in the literature is the assumption that the mass fraction burned is linearly related to the pressure rise, as described by Lewis and von Elbe (1961):

$$x = \frac{p - p_0}{p_e - p_0} \tag{3.18}$$

where p_e is the pressure at the end of combustion. The flame radius as given in Equation (3.16) can then be obtained once the mass fraction burned is known:

$$r_b = R\left[1 - \left(\frac{p_0}{p_u}\right)^{\frac{1}{\gamma_u}} \frac{p_e - p}{p_e - p_0}\right]^{\frac{1}{3}} \tag{3.19}$$

This result can then be substituted into Equation (3.8), along with the corresponding r_i found from Equation (3.9) and the measured pressure to obtain burning velocity.

Alternatively, the linear model can be applied to Equation (3.17). Equation (3.19) gives us the flame radius, and differentiating Equation (3.18) gives:

$$\frac{dx}{dp} = \frac{1}{p_e - p_0} \tag{3.20}$$

which can be substituted into Equation (3.17) along with Equation (3.19) to give:

$$S_u = \frac{R}{3(P_e - P_0)}\left(\frac{p_0}{p}\right)^{\frac{1}{\gamma_u}}\left[1 - \left(\frac{p_0}{p}\right)^{\frac{1}{\gamma_u}} \frac{p_e - p}{p_e - p_0}\right]^{-\frac{2}{3}} \frac{dp}{dt} \tag{3.21}$$

The linear model was favoured in the earlier studies due to its simplicity; however there are some significant problems with the method. The most significant of these is the need to determine the end pressure, p_e. At the end of combustion, when the flame front approaches the wall, there is significant heat transfer to the wall which will reduce the pressure in the vessel, meaning that the measured maximum pressure in the vessel cannot be used. A better estimate is achieved if a value from an equilibrium model such as STANJAN, Reynolds (1986) or Gaseq, Morley (2005) is used. Figure 3.2 shows a comparison between the measured peak pressure during combustion for methane-air mixtures at an initial pressure of 2 bar and initial

temperature of 350 K, compared with the values from chemical equilibrium solvers. This clearly shows that the measured end pressure cannot be used in the linear model, and is the main drawback to this technique. Despite this, the technique has been frequently used in the literature due to its relative simplicity, and has been shown to be surprisingly accurate, although it is shown that the pressure in the middle part of combustion is slightly underestimated relative to other models, e.g. Luijten *et al.* (2009).

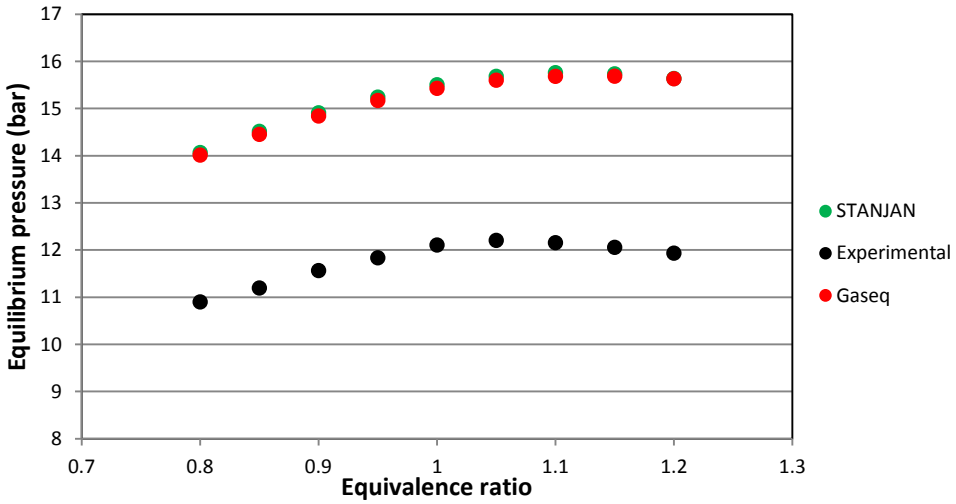

Figure 3.2 – Comparison of measured peak pressures for tests at initial pressure of 1 bar and theoretical values from chemical equilibrium solvers.

3.1.5.2 Numerical two-zone model

Rather than assume a linear relation between the fractional pressure rise and the mass fraction burned, Metghalchi and Keck (1980) devised a two-zone model, whereby the gas in the bomb is divided into burned and unburned gas regions, separated by a thin flame front. Their approach is to solve equations for conservation of mass and energy for the two zones, as given in Equations (3.22) and (3.23), and ensure agreement at the flame front.

$$v = \frac{V}{M} = x v_{\mathrm{b}}(p, \bar{T}_{\mathrm{b}}) + (1 - x) v_{\mathrm{u}}(p, S_0) \qquad \textbf{(3.22)}$$

$$e = \frac{E}{M} = x e_{\mathrm{b}}(p, \bar{T}_{\mathrm{b}}) + (1 - x) e_{\mathrm{u}}(p, S_0) \qquad \textbf{(3.23)}$$

where v and e are the specific volume and energy, $\bar{T}_{\mathrm{b}}$ is the mean burned gas temperature and S_0 is the entropy of the unburned gas.

The method assumes that the burned gas remains at equilibrium conditions and so does not take into account the recompression of the burned gas. In a second paper using this method, Metghalchi and Keck (1982), consider the effects of various possible inaccuracies, including displacement volumes resulting from wall and flame preheat zone boundary layers related to the unburned gas, and contributions from the ignition energy input, electrode boundary layer, radiation heat loss and burned gas temperature gradient related to the burned gas. Their conclusion was that all of these effects have negligible effect on the determined burning velocity, although the analysis of the temperature gradient appears to be limited to that of conduction, rather than the effects of recompression, which is taken to be a uniform isentropic compression. The effect of isentropic recompression of the burned gas using a two-zone model is seen by tracking particles in the burned and unburned gas, as seen in Figure 3.3 from Eisazadeh-Far *et al.* (2010). Note that radial position has been normalised by the chamber radius in this case. Whilst this shows that the effects of recompression are taken into account, there is no possibility of a temperature gradient being described, since the burned gas is treated as a single zone. Development of multi-zone combustion models has addressed this.

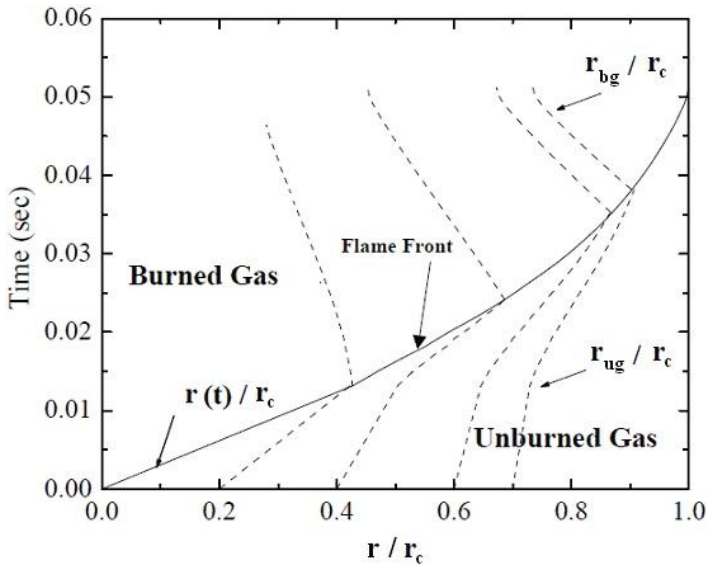

Figure 3.3 – Radial position of gas particles as they are isentropically compressed, burned and compressed further. Taken from Eisazadeh-Far *et al.* (2010).

3.1.5.3 Numerical multi-zone models

Following on from the work of Metghalchi and Keck, further numerical models were developed to solve the equations of conservation of mass and energy based on multiple zones, rather than just a burned and unburned gas zone. Elia *et al.* (2001) developed such a model, where the burned gas is divided into a number of separate zones. As with the numerical two-zone model, there is no analytical solution to the equations of conservation of mass and energy that need to be solved. These models also have the advantage that the individual zones can have different heat capacities, which is an important feature missing from the analytical models described in section 3.1.5.4.

A comprehensive numerical model was developed by Saeed and Stone (2004). Henceforth, this model is referred to as the BOMB program. The code is based upon the ISIS (Integrated Spark Ignition Simulation) program, which is an engine simulation program developed in Oxford for the prediction of NO_x production in the burned gas region, written in FORTRAN 77, Raine *et al.* (1995). The BOMB program is a reduced version of this package, where combustion is limited to a constant volume and can be run with any number of zones. The model is a ten species equilibrium model. Equations (3.21), (3.22) and (3.23) are extended to account for the multiple burned gas zones and are solved as a set of ODEs based upon the analysis of Ferguson (1985). The solution of the equilibrium equations is by the minimisation of the Gibbs free energy.

Upon setting up the simulation, the system is divided up into the desired number of zones in the form of concentric shells (which allow us to exploit the symmetric nature of the experiment and reduce the problem to a 1D propagation). These can be divided according to equal mass or equal radius. For modelling of the burning velocity, dividing the zones for equal mass is preferred, since it provides a more linear consumption of zones with respect to burn rate. These zones are further sub-divided into elemental shells. A typical number of zones in a model is 10, consisting of 20 elemental shells. At any given point in time, a zone within the

model will be either burned, unburned, or currently burning. Additionally, the model incorporates the assumptions listed in section 3.1.1.

At the start of combustion, consumption of the first shell within the first zone takes place at the conditions of initial temperature and pressure. As a result of combustion a step increase in the temperature and pressure of the shell takes place, along with an expansion of the shell, causing the movement of the boundaries of the currently burning zone and all the other zones in the outward direction. The expansion of the shell results in the compression of the remaining shells and a corresponding increase in pressure, which is assumed to be uniform before the next shell is burnt. The next shell is subsequently burnt at the new conditions of temperature and pressure. This time, the expansion of the shell takes place in both directions, moving the unburned zones ahead of the flame front outwards, but recompressing the burnt shell and subsequently increasing its temperature. Once all the shells in the first zone have been burnt in this manner, this zone will move into the burned gas region of the model, and is considered as being recompressed as a single entity rather than individual shells. The variation in mean bulk temperature due to recompression resulting from the burning of subsequent zones is modelled. This allows temperature and density gradients within the burned gas region to be represented.

The temperature gradient exists as a result of recompression, and the fact that combustion of successive zones takes place at conditions of increasing temperature and pressure. This is demonstrated in Figure 3.4, where the temperature of the first zone to be burned is around 500 K hotter than the tenth zone at the end of combustion. Burning at initial pressure followed by isentropic compression results in a higher temperature than being initially compressed to the end pressure before being burned. This is due to the fact that for the first burned gas, isentropic compression at a higher initial temperature results in a greater overall temperature increase, while combustion of the final gas at higher initial unburned temperature results in a lower overall temperature rise.

The BOMB program therefore also allows the flame front position to be tracked from knowledge of the mass fraction burned. Marshall (2010) performed a visualization of the flame front using the equal mass BOMB routine, showing the position of the flame front with mass fraction burned, as well as a visualisation of the temperature in the bomb, again showing how the central zones achieve higher pressure due to recompression. The number of zones and steps used has an impact upon the detail and hence accuracy of the solution, but it was shown by Saeed and Stone (2004) that increasing beyond 10 zones and 200 steps gives minimal improvements.

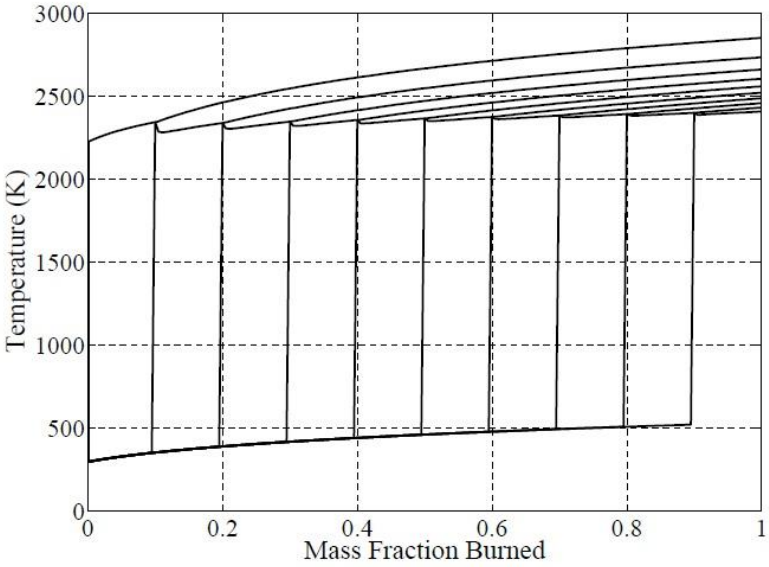

Figure 3.4 – Temperature against mass fraction burned for a 10 zone, 200 step BOMB simulation of stoichiometric methane-air with initial temperature 298 K and pressure 1 bar. From Marshall (2010).

3.1.5.4 Analytical multi-zone models

Luijten and De Goey (2007) proposed an analytical multi-zone model, noting that most multi-zone models take into account the change in specific heats and chemical equilibrium with temperature, but "inclusion of these phenomena requires numerical methods". They solve for the equations of conservation of volume and energy as given in Equations (3.22) and (3.23), using the limiting case that at the end pressure, the mass fraction burned is unity. These equations mean the analysis is a two-zone model, but they arrive at the result:

$$x = \frac{p - p_0\left[\frac{\gamma_b - 1}{\gamma_u - 1} + \frac{T_u}{T_i}\left(\frac{\gamma_u - \gamma_b}{\gamma_u - 1}\right)\right]}{p_e - p_0\left[\frac{\gamma_b - 1}{\gamma_u - 1} + \frac{T_u}{T_i}\left(\frac{\gamma_u - \gamma_b}{\gamma_u - 1}\right)\right]} \quad \textbf{(3.24)}$$

They note that this is the same as the result achieved by extending the analysis of Lewis and von Elbe (1934). Since this relation can be substituted into Equation (3.17), it is an analytical two-zone model. In a similar way to how Elia *et al.* (2001) extended the equations to a multi-zone model, the analytical model is also modified to produce an analytical multi-zone model.

Their model enables the representation of a burned gas temperature gradient, due to the presence of multiple zones. However, the validity of this method is strongly disputed by Marshall (2010), who claims that the method requires the assumption of constant specific heats with respect to temperature, which will have a small effect on the unburned mixture (which will only vary over the range of a couple of hundred kelvin), but will have more of an impact in the burned gas where the temperature gradient exists. Additionally, this model still requires a known end pressure, the estimation of which is affected by neglecting the effects of dissociation and the issue of constant specific heats.

3.1.5.5 Comparison of models

It has been shown that the use of different models will result in different values of burning velocity. For example, the comparison of the linear model and a numerical multi-zone model demonstrates that the relationship between mass fraction burned and pressure does indeed deviate from a linear relationship, with the difference greatest for the middle part of combustion. For stoichiometric methane-air mixtures, Saeed and Stone (2004) report differences of around 5%, with the difference in subsequently derived burning velocities having a similar figure. A similar validation exercise performed by Marshall (2010) for a stoichiometric iso-octane-air experiment, combined with both the linear model and BOMB program demonstrated that the agreement between the two methods is reasonably good. However, it should be noted that the end pressure required for the linear model was obtained

from the final output of the BOMB program, which would differ from a single chemical equilibrium result such as that obtained from STANJAN or Gaseq, if more than one zone is used in the multi-zone model, and so demonstrates the sensitivity of the linear method upon this choice of end pressure. However, it does provide a good validity check on the functionality of the BOMB program.

Marshall (2010) also compared the numerical multi-zone model against that of Luijten and De Goey (2007) for the stoichiometric methane case and saw a significant difference in the zone temperature results. As described in section 3.1.5.4, the biggest cause of this discrepancy is the assumption of constant specific heat, which is more significant at higher temperatures. The effect of neglecting dissociation within the burned gas, the assumption of complete combustion, and the need to deduce the end pressure all count against this model.

The model used in this investigation is the numerical multi-zone model provided by the BOMB program. This allows Equation (3.8) to be solved for burning velocity from the pressure measured experimentally. The implementation of the BOMB program and the solution of the burning velocity equation are described further in section 5.1.

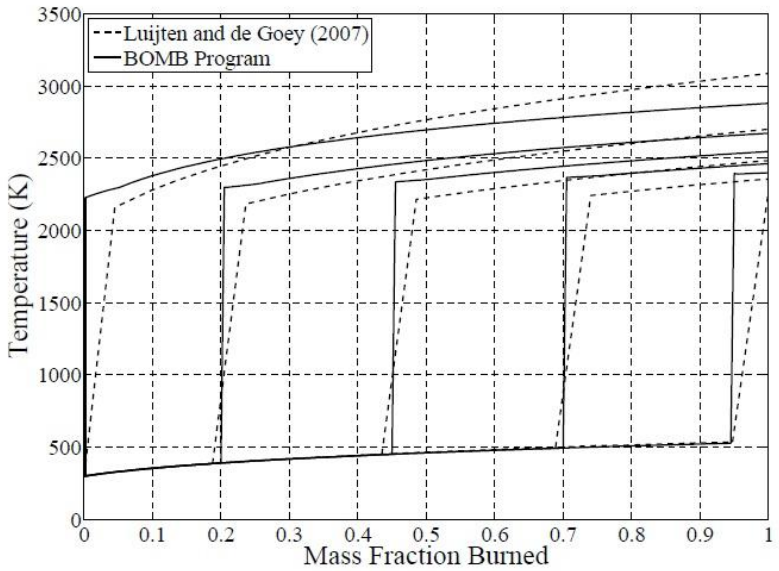

Figure 3.5 – Results from the BOMB model and that of Luijten and De Goey (2007) for the case of 20 zones. The lines correspond to the temperatures of zones 1, 5, 10, 15 and 20. From Marshall (2010).

3.2 Chemical kinetic modelling

3.2.1 Background and relevance to burning velocity measurements

One important use of laminar burning velocity data is in the validation of chemical kinetic mechanisms. These mechanisms are increasingly important in the improvement of efficiency and cost of design of combustion devices, since problems involving reactive flows in CFD modelling require accurate knowledge of the chemical reaction process. Capability to accurately predict pollutant emissions for example, requires accurate and detailed representation of the combustion chemistry and kinetic pathways within the reaction scheme, e.g. Pepiot-Desjardins and Pitsch (2008).

For short chain fuels such as methane, complete mechanisms can be used, but for larger molecules (even as small as ethanol) the mechanisms become very large. A number of ethanol kinetic mechanisms exist (highlighting the difficulty in obtaining an accurate mechanism), and one such example is the Marinov (1999) mechanism, which consists of 57 chemical species and 383 elementary reactions. As molecules increase in size, or as the number of different species in the fuel increases, so the number of reactions will increase dramatically. A detailed mechanism for n-heptane by Curran *et al.* (1998) features 556 species and 2540 reversible reactions. For larger molecules, and blends such as standard gasolines which are a mixture of hundreds of different chemical compounds involving complex highly nonlinear processes, it is increasingly necessary for simplified reduced mechanisms to be used to reduce the complexity of the mechanisms and therefore the computing power required to perform numerical simulations of combustion devices. Reduced mechanisms are obtained by systematically identifying and removing less significant reactions within the mechanism. Sensitivity analysis is performed to confirm the effect of removing each reaction from the mechanism. A reduced mechanism presented by Rohl (2009) sees the Marinov mechanism reduced down to just 38 species and 228 reactions, and a similar reduction by Liu *et al.* (2004) upon the Curran n-heptane mechanism sees the number of species reduced down to just 43 with 185 reactions retained in

their skeletal mechanism. In the case of detailed mechanisms but particularly for reduced mechanisms, it is important to validate results from simulations against experimentally determined values to ensure that the simulations are accurately representing the real world combustion behaviour. Burning velocity is one of the most widely used parameters for checking the results of chemical kinetic modelling.

3.2.2 Basic theory of chemical kinetic modelling

Since the focus of this work is experimental and not primarily concerned with the development and implementation of chemical kinetic mechanisms, full details of the mechanisms used will not be presented, and only a brief description of kinetic modelling theory will be given.

Chemical kinetic mechanisms differ from a global reaction mechanism, which will merely represent the rate of the overall one-step reaction. For a fuel (*F*) and oxidant (*Ox*) mixture reacting to form products (*Pr*) the global reaction is expressed as:

$$F + aOx \rightarrow bPr \tag{3.25}$$

with the rate of consumption of fuel described by

$$\frac{\mathrm{d}[X_\mathrm{f}]}{\mathrm{d}t} = -k_G(T)[X_F]^n[X_{Ox}]^m \tag{3.26}$$

where the values in square brackets represent the molar concentration of the species, $k_G(T)$ is the global rate coefficient (which is strongly dependent upon temperature) and the exponents *n* and *m* give the reaction order with respect to each species, with the sum of the two giving the overall order. Such a global mechanism is useful for expressing the reaction rates from the viewpoint of thermodynamics, but for detailed understanding of the reaction, chemical kinetic mechanisms are needed. These consist of a range of elementary reactions and associated reaction rates, which are used to determine the relative speed of forward and reverse elementary reactions. Many reactions are bimolecular, where two molecules react to form two different molecules, and are overall second order, as they are first order with respect to each of the reacting species.

$$A + B \rightarrow C + D \tag{3.27}$$

$$\frac{\mathrm{d}[A]}{\mathrm{d}t} = -k_{\mathrm{bimolec}}[A][B] \tag{3.28}$$

For the rate coefficient, a modified Arrhenius form is used which includes temperature dependence:

$$k = AT^{n}\exp\left(\frac{-E}{RT}\right) \tag{3.29}$$

where A is the pre-exponential (or frequency) factor, n is the pre-exponential temperature coefficient, and E is the activation energy of the reaction. These are the three empirical parameters that need to be included in the reaction mechanism. In addition, reactions can include third-body reactants which will cause the reaction to be dependent upon the effective concentration of the third body M, which is represented for specific species using third-body efficiencies which will also be included within the mechanism. Important in combustion are unimolecular reactions, involving a single species decomposing into two product species, as occurs in dissociation reactions. In this case pressure dependence is seen, since the mechanism for a unimolecular reaction will actually be a multi-step reaction involving a third body. For treatment of such pressure dependent reactions, the rate coefficient is found using the Lindemann form combined with the F-centre treatment of Troe, which allows the rate constant to be determined at a specified temperature and pressure. Details of this process are not given here; more complete explanations can be found in many textbooks, such as Turns (1996) and Warnatz *et al.* (2006).

3.2.3 Implementation using FlameMaster code

In this work, it was decided that results from numerical simulations would provide a useful comparison for the results obtained experimentally. The FlameMaster application, developed by Pitsch (1993), has been used to perform the simulations. The software is a C++ program for 0D combustion and 1D laminar flame calculations which can be run from within a UNIX-like environment. The solver requires mechanisms to be presented in a specific format, however it is

possible to convert these from the more widely used CHEMKIN format. The mechanism files, thermodynamic data and transport properties of each species are passed to the FlameMaster code, which formulates and solves conservation equations for the case of a 1D premixed unstretched flame, converging to an equilibrium solution profile. Such an output profile will show temperature, heat release rates and species concentrations across the flame front. The laminar burning velocity is also returned. The code includes an option to account for the effects of radiation. This was tested for the full range of biogas mixtures (see section 7.2.2), but the effect upon burning velocity results was negligible for this configuration.

4 Experimental apparatus and procedure

In this section, two separate experimental rigs will be described: firstly, the combustion bomb rig from which all experimental values of laminar burning velocity were obtained; secondly, the single cylinder optical access engine used to compare burn rates to measured values of the laminar burning velocity.

4.1 Combustion bomb rig

Laminar burning velocity measurements were made using a spherically expanding flame in a constant volume vessel. The advantages of this method have been explained in section 2.2. This technique enables determination of burning velocity by two methods: image analysis of the early flame front propagation at conditions of constant pressure, and analysis of the pressure rise in the vessel, combined with appropriate combustion models as described in section 3.1.4. The details of the combustion vessel, mixture preparation system, data acquisition systems and schlieren system are described below.

4.1.1 Combustion bomb

The combustion bomb is a spherical vessel with a diameter of 160 mm, constructed from two stainless steel halves, held together with 12 bolts and sealed with a Viton O-ring and is rated to a pressure of 34 bar. The vessel is situated within a temperature controlled chamber constructed from Sindanyo plates, further insulated with a layer of Melafoam, all housed within aluminium cladding as depicted in Figure 4.1. Holes in the walls of this chamber allow connections for the thermocouple and pressure transducer, HT lead, pipework, valves and window access. The temperature of the environment and bomb is controlled using a fan heater and West 5600 controller with 1˚C resolution mounted on top of the chamber. The controller acts as a thermostat, which was set separately from the main LabVIEW control system. The high overall

heat capacity of the system requires heating periods of up to several hours to reach the highest temperatures in the bomb. The maximum rated temperature is 200˚C.

The bomb is fitted with two 40 mm diameter fused silica windows to allow optical access for the schlieren photography system, sealed with O-rings. The windows can be replaced with curved blanking sections (shown on the right hand side of Figure 4.1) should optical access not be required.

A pair of electrodes is used to provide the central ignition, one earth electrode and one connected to a coil unit from a Jaguar AJ133 engine, allowing use of variable spark energy. Further details of the ignition system can be found in Marshall (2010).

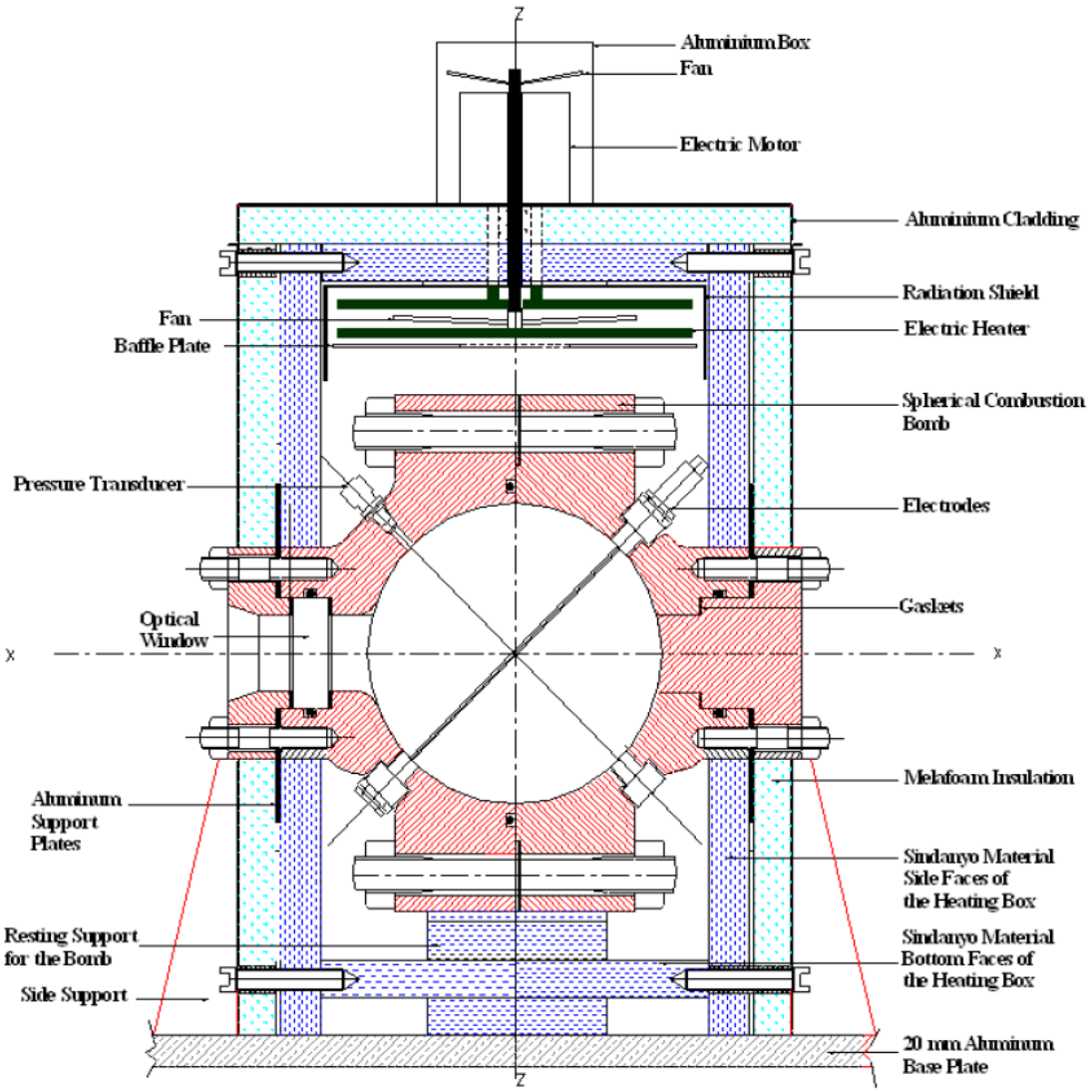

Figure 4.1 – Cross section of combustion vessel and environmental chamber. From Saeed (2002).

Ports in the wall of the vessel allow for the mounting of the pressure transducer and thermocouple, as well as pipework to allow gases into and out of the vessel. Each of these adds an extra small volume beyond that of the perfect sphere, although small in comparison to that of the windows, which were shown to have negligible effect.

The pipework within the environmental chamber is shown schematically in Figure 4.2. Since various different mixture preparation systems are used throughout the work, the integration of these systems into the pipework shown will be explained in the relevant sections. The pressure transducers used to monitor the vessel pressure during mixture preparation (section 4.1.5) are all mounted on the transducer manifold on the upstream side of the bomb.

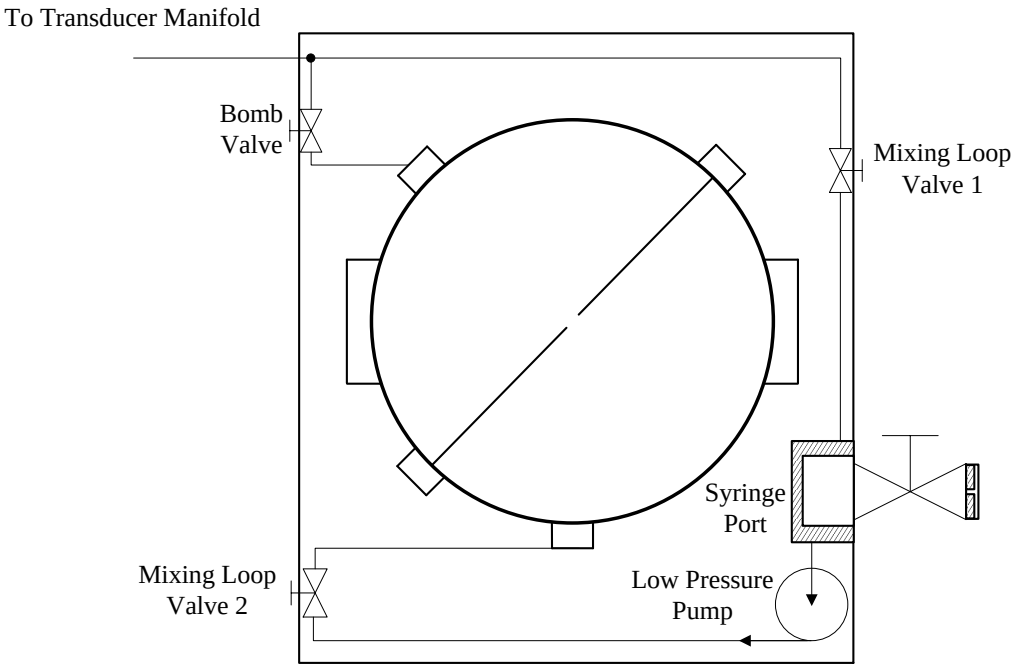

Figure 4.2 – Schematic of the original bomb pipework.

4.1.2 Data acquisition (DAQ) system

Measurements of pressure and temperature within the bomb are required for both mixture preparation and logging the pressure rise during combustion. The DAQ system that records all outputs from the system consists of a National Instruments PCI-6024E PCI DAQ card mounted within a PC, with a break-out box mounted with the other electronics to the front of the bench on which the whole rig is secured. LabVIEW software on the DAQ PC provides the main user interface. The DAQ card has sixteen 12-bit analogue input channels with a maximum sampling

rate of 200 kS s^{-1}, two analogue output channels, two input/output (I/O) channels and two counter/timer channels. The DAQ card used has a software selectable gain, meaning the input voltage range can be varied from ±10 V to ±50 mV, allowing calibration to enable full use of the number of bits available to the DAQ system. Inputs to the DAQ system are from pressure transducers and thermocouples, described in the following sections.

4.1.3 LabVIEW interface

A LabVIEW program, modified from that of Marshall (2010) is used as an interface to display the data from the DAQ system, perform calculations required during mixture preparation, and record the pressure rise during combustion.

4.1.3.1 Mixture preparation tab

During mixture preparation via the means of partial pressures as described in section 4.1.6, the partial pressures of each component have to be calculated, and added in turn. Required fuel properties are loaded into the program, and the fuel under test can be selected from a drop down menu. For the calculation, it is necessary to use an expression to represent the number of moles required, and relate this to the partial pressure required. The representative used is based upon the assumption of ideal gases (as described in section 4.1.6):

$$n = \frac{p}{T} \tag{4.1}$$

From this, given the current temperature in the bomb, as provided by a thermocouple described in section 4.1.4, the required partial pressure of each component can be calculated. This is presented to the user in real time, and guides the mixture preparation process (according to that described in section 4.1.6), showing the user how much of each component to add via virtual dials on the main panel.

The mixture preparation tab also includes a check on the vapour pressure of the fuel in real time using the correlation and data from Reid *et al.* (1987):

$$p_{\mathrm{vp}} = p_{\mathrm{c}} \times \exp\left((1-a)^{-1}(Aa + Ba^{1.5} + Ca^3 + Da^6)\right) \tag{4.2}$$

$$a = 1 - \frac{T}{T_c} \quad \textbf{(4.3)}$$

If the vapour pressure is less than the partial pressure of fuel, then a warning is displayed that there may be condensation of the fuel. For the case of hydrous ethanol, the same was done for the water in the fuel, to ensure that there were no issues with condensing water vapour. In reality, at higher temperatures, this did not prove a problem.

4.1.3.2 Combustion tab

Once the desired mixture has been produced, the user switches over to the combustion tab. This allows the selection of settings regarding the number of samples to capture, and the charge amplifier setting, as described in section 4.1.5.2. Once set, the user clicks on the 'Ready to fire' button which switches the program into high speed data acquisition mode, where it waits for a trigger input, which is provided when the ignition button is pressed. The pressure is then recorded for the preset number of samples and is saved in a file to be read by either Excel or MATLAB, before switching back to real time mode allowing evacuation of the combustion products from the bomb and preparation of the next mixture to be tested.

4.1.4 Temperature measurement

For the partial pressure method of preparation of gaseous fuel mixtures as described in section 4.1.6.1.1, temperature and pressure in the vessel during mixture preparation are required. Temperature during combustion cannot be measured accurately due to the response time of the thermocouple being too slow, as shown by Marshall (2010).

A sealed thermocouple fitting in the surface of the bomb allows for an exposed junction K-type thermocouple to be positioned so that the junction just protrudes into the sphere. A second thermocouple is used to measure the ambient room temperature, which becomes important when the density of liquid fuel needs to be calculated. A thermocouple amplifier circuit is used to amplify the output from the thermocouple (typically a few mV) to produce an output of

10 mV per °C. The accuracy of the amplifier and thermocouple are determined to be ± 1 K and ± 1.5 K respectively.

4.1.5 Pressure measurement

Pressure transducers are required for the measurement of pressure in the vessel both during preparation of the mixtures for determining the partial pressures of the added components and the final pressure during mixing, and the setting of the initial pressure prior to combustion.

4.1.5.1 Mixture preparation

For mixture preparation, three Drück PMP14000 transducers are connected to a manifold mounted outside the bomb, with the pressure ranges -1 to +1.6 barG, 0-6 barG and 0-250 mbarG. The error associated with combined non-linearity, hysteresis and repeatability is determined to be 0.15%. The first two sensors are used for filling the bomb to high pressure (either as part of the flushing process or in the later stages of mixture preparation) and evacuating to low pressures, below atmospheric pressure. The sensor with the smallest range is used during addition of gaseous components with smaller partial pressures to allow greater accuracy. Calibration of the pressure transducers is performed with reference to manometers and a dead weight tester depending upon the range being calibrated. The least significant bit in the LabVIEW program corresponds to 0.0003 bar for the 250 mbarG transducer, and 0.003 bar for the 0-6 barG transducer. Zero error is removed by calibrating against the atmospheric pressure as measured in the lab using a Fortin barometer at the start of each experimental session. The output voltage range for the transducers is 0-5 V.

4.1.5.2 Combustion

For pressure measurement during combustion, the sensor used is mounted inside the bomb itself, unlike those used for mixture preparation. The pressures and temperatures involved during combustion are significantly higher, and so the sensor is chosen to be able to withstand

these conditions. It also requires a fast response time over a wide range of pressures if the pressure rise is to be recorded accurately.

The sensor used is a Kistler 701A piezo-electric sensor in conjunction with a Kistler type 5007 charge amplifier to produce a voltage output for the DAQ system. Amplifier ranges of 1, 2 and 5 bar V^{-1} were used to ensure the full voltage input range of the DAQ card was utilised. The range could be selected on the charge amplifier for each experiment individually, since the experiments at 4 bar initial pressure will reach significantly higher pressures than those at 1 bar. Therefore, 3 separate quadratic calibration curves are produced that relate voltage to pressure, with high levels of accuracy; the calibration of the 5 bar V^{-1} curve gave an R^2 value of 0.999995, with the maximum deviation from the parabolic fit of 0.04 bar. Further details of the fitting of these calibration curves are given in Marshall (2010).

4.1.6 Mixture preparation

Methods of mixture preparation are based around the method of partial pressures. Since both gaseous and liquid fuels are tested, two different mixture preparation procedures are needed.

Prior to each experiment, it is important that the bomb is free from any products of combustion from previous experiments. A flushing procedure is used whereby the bomb is evacuated with a vacuum pump down to a pressure of around 35 mbar, before being filled with dry bottled air to 5 bar. Repeating this a further two times is shown to reduce the concentration of combustion residuals down to around 0.3 ppm.

4.1.6.1 Gaseous fuels

Mixtures using gaseous fuels were prepared using the method of partial pressures throughout. A method utilising mass flow controllers (MFCs) was also tested for pure methane mixtures as a cross validation of the techniques, and so will be described briefly also. Gaseous mixtures tested are simulated biogas mixtures, comprised of methane and carbon dioxide, and so description will be specific to such mixtures.

4.1.6.1.1 Partial pressure method

The preparation of the gaseous fuel mixtures is based upon the addition of fuel, air and diluents according to Dalton's law of partial pressure, which states that the total pressure of a mixture of gases is equal to the sum of the partial pressures exerted by each individual component:

$$p_{\mathrm{mix}} = p_{\mathrm{f}} + p_{\mathrm{dil}} + p_{\mathrm{air}} \tag{4.4}$$

and so the partial pressure of any given component, *i*, will be related to the molar fraction of that component

$$p_{\mathrm{i}} = \frac{n_{\mathrm{i}}}{n_{\mathrm{total}}} \times p_{\mathrm{total}} \tag{4.5}$$

Therefore by knowing the mole fraction of each component required in the mixture for a desired equivalence ratio and diluent fraction, the partial pressure of each component can be calculated, and added in turn to produce the overall mixture. The total number of moles in the mixture will be the sum of the individual components:

$$n_{\mathrm{mix}} = n_{\mathrm{f}} + n_{\mathrm{dil}} + n_{\mathrm{air}} \tag{4.6}$$

The assumption of ideal gases allows us to use the ideal gas law:

$$n = \frac{pV}{R_0 T} \tag{4.7}$$

which for our constant volume vessel at conditions of constant temperature, implies that the number of moles is proportional to the pressure.

Therefore, the number of moles of each component can be used to determine the partial pressure required of each component, once the mixture pressure has been decided, using the relation in Equation (4.1). Whilst addition of gases is carried out at a low flow rate for maintaining isothermal conditions, the measured temperature in the bomb during filling is used to provide a real time target partial pressure. Gaseous fuel, diluent and air are supplied from bottles to a manifold, with flow rates controlled using needle valves. The pressure of the bottled gas supply is set via the regulator at a higher pressure than the maximum pressure anticipated in the vessel during the filling procedure. Figure 4.3 shows a schematic for the case of a 3 component gaseous mixture. This links up to the combustion bomb via the pipework shown in

Figure 4.2, with the two mixing loop valves within the bomb environment remaining closed at all times.

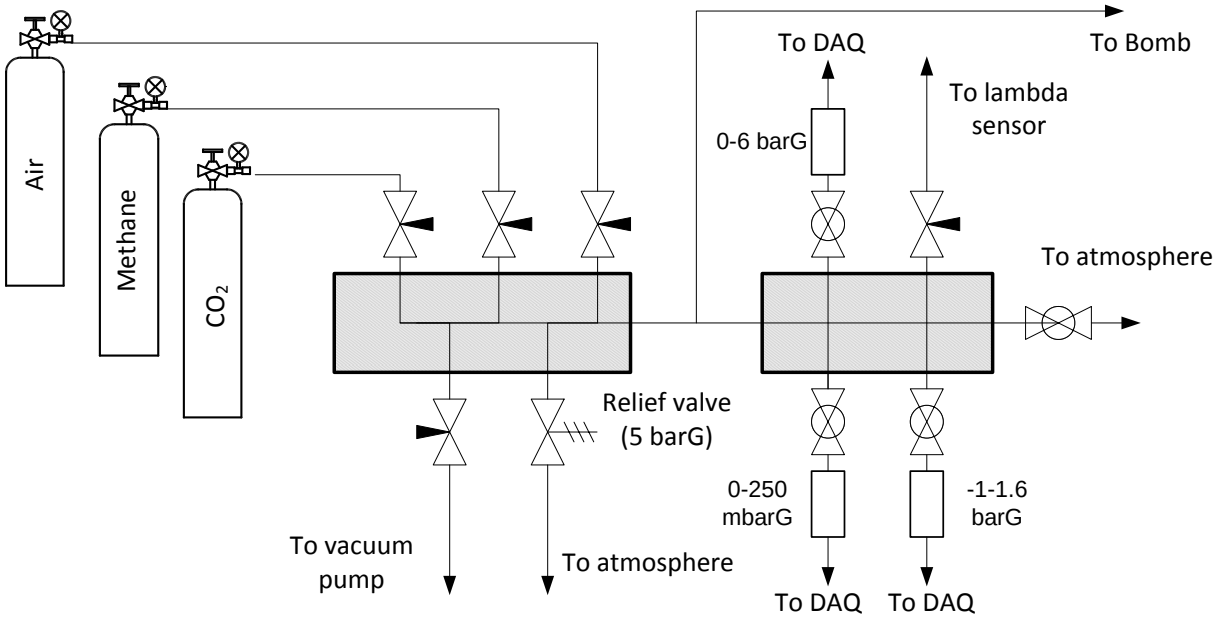

Figure 4.3 – Schematic of gaseous mixture preparation system for a three component mixture.

For the methane and carbon dioxide, the partial pressures will be small compared with that of the air. To improve accuracy of measurement when adding the gases, the mixture pressure was chosen to be higher than the chosen initial pressure for combustion, to increase the partial pressure of each component. Once a mixture was prepared to this higher pressure, mixture was removed to reduce the pressure down to the desired initial pressure. The full preparation procedure for biogas mixtures is as follows, under the guidance of the LabVIEW program introduced in section 4.1.3. The original LabVIEW system from which this was developed included the option to leave in residuals from the previous experiment, and this was left in the current program, although it was not used in the current work:

1. Flushing procedure, or just reduce pressure down to leave in the required amount of combustion residuals.
2. Addition of air to around 0.8 barA.
3. Addition of methane according to calculated partial pressure.
4. Addition of CO_2 according to calculated partial pressure.

5. Addition of air up to the final target pressure (4.2 bar).
6. 5 minutes of mixing time, to ensure a homogeneous mixture.
7. Reduction down to desired initial pressure.

At each stage of the mixture preparation, the ratio of pressure to temperature, shown to be proportional to the number of moles by Equation (4.1) is recorded.

$$n_1 = n_\mathrm{r} \tag{4.8}$$

$$n_2 = n_\mathrm{r} + n_\mathrm{air} \tag{4.9}$$

$$n_3 = n_\mathrm{r} + n_{\mathrm{air},1} + n_{\mathrm{CH_4}} \tag{4.10}$$

$$n_4 = n_\mathrm{r} + n_{\mathrm{air},1} + n_{\mathrm{CH_4}} + n_{\mathrm{CO_2}} \tag{4.11}$$

$$n_5 = n_\mathrm{mix} = n_\mathrm{r} + n_{\mathrm{air},1} + n_{\mathrm{CH_4}} + n_{\mathrm{CO_2}} + n_{\mathrm{air},2} \tag{4.12}$$

The target *n*, and hence given that the temperature is being monitored in real time, the target *p* at each stage can be calculated, based upon the target mixture pressure, initial temperature and equivalence ratio of the mixture under preparation. The target for each stage is updated based upon the actual *n* calculated from the previous stage where possible.

The number of moles of each component is determined from the stoichiometry of the global reaction. Considering a hydrocarbon burned at a stoichiometric AFR, the global reaction will be:

$$\mathrm{C}_x\mathrm{H}_y + \left(x + \frac{y}{4}\right)\left(\mathrm{O}_2 + \frac{79}{21}\mathrm{N}_2\right) \rightarrow x\mathrm{CO}_2 + \frac{y}{2}\mathrm{H}_2\mathrm{O} + \left(x + \frac{y}{4}\right)\frac{79}{21}\mathrm{N}_2 \tag{4.13}$$

For the case of biogas, the composition is defined in terms of molar fraction of methane in the biogas. For example, a biogas consisting of 80% CH_4 and 20% CO_2 by mole is represented as $X = 0.8$, allowing the overall stoichiometric reaction to be defined as:

$$[X\mathrm{CH}_4 + (1 - X)\mathrm{CO}_2] + 2X\left(\mathrm{O}_2 + \frac{79}{21}\mathrm{N}_2\right) \rightarrow \mathrm{CO}_2 + 2X\mathrm{H}_2\mathrm{O} + 2X\frac{79}{21}\mathrm{N}_2 \tag{4.14}$$

For non-stoichiometric mixtures, the expression is modified most simply by dividing the number of moles of air by the equivalence ratio. From the global reaction, it is possible to determine the required mole fractions of each component. Our definition of X is as follows:

$$X = \frac{n_{\mathrm{CH_4}}}{n_{\mathrm{CH_4}} + n_{\mathrm{CO_2}}} \tag{4.15}$$

Rearranging this allows the number of moles of CO_2 to be found:

$$n_{CO_2} = n_{CH_4} \frac{(1-X)}{X} \tag{4.16}$$

To find the number of moles of CH_4, we start by considering the overall pressure of the mixture in terms of the partial pressures of the individual components, as given in Equation (4.4), and combining with Equation (4.5), gives:

$$p_{CH_4} = \frac{n_{CH_4}}{n_{air}} (p_{mix} - p_{CH_4} - p_{CO_2}) \tag{4.17}$$

$$p_{CH_4} \left(1 + \frac{n_{CH_4}}{n_{air}}\right) = \frac{n_{CH_4}}{n_{air}} (p_{mix} - p_{CO_2}) \tag{4.18}$$

$$p_{CH_4} = \frac{n_{CH_4}}{n_{air} + n_{CH_4}} (p_{mix} - p_{CO_2}) \tag{4.19}$$

Considering this in terms of one mole of biogas, then this becomes:

$$p_{CH_4} = \frac{X}{2X\frac{100}{21\emptyset} + X} (p_{mix} - p_{CO_2}) \tag{4.20}$$

Because of our assumption of ideal gases in Equation (4.7), we can exploit the proportionality between pressure and number of moles to obtain:

$$n_{CH_4} = \frac{n_{mix} - n_{CO_2}}{1 + \frac{100}{21\emptyset}(x + \frac{y}{4})} \tag{4.21}$$

Combining with Equation (4.16) we arrive at:

$$n_{CH_4} = \frac{n_{mix}}{\left[1 + \frac{100}{21\emptyset}(x + \frac{y}{4}) + \frac{(1-X)}{X}\right]} \tag{4.22}$$

Note that these will be the target partial pressures, based upon the target p_{mix} and initial temperature T_0. Hence temperature does not feature in the above equations. However, during mixture preparation, real time values of n will be calculated according to Equation (4.1) and so will be a function of temperature. Once mixture preparation is complete, then the actual equivalence ratio and CO_2 fraction X, as determined from the measured values during the preparation is calculated. Provided that the gases were added at low flow rates, it was seen that these values closely matched the targets.

4.1.6.1.2 Mass flow controller (MFC) method

A second method of mixture preparation was developed in conjunction with Hu (2013) in which two mass flow controllers (MFCs) are used to add fuel and air simultaneously, at relative mass flow rates determined to provide the desired equivalence ratio. With reference to the schematic in Figure 4.3, the MFCs are placed between the gas cylinders and the gas intake manifold, with the needle valves shown completely open so that the flow rate is controlled entirely by the MFCs.

This aimed to provide validation of the equivalence ratio of prepared mixtures in light of disagreement with measurements taken with a lambda sensor (details given in section 6.1.3). The second method also has the advantage of reducing the mixture preparation time compared with the partial pressure method, since the different stages of gas addition are avoided, faster flow rates can be used, and due to the fact that the gases mix upstream of the combustion bomb, the allocated mixing time can be avoided. However, the technique was only used for methane-air mixtures, due to the complication of adding a third mass flow controller, and the difficulty in calibrating accurately for a smaller mass flow rate (since less CO_2 is needed than CH_4).

The mass flow controllers used are thermal-type mass flow controllers which measure the flow rate of the gas directly using two resistance thermometers externally wound around a tube through which gases are passing. These measure the temperature difference caused by the flow of gas, converting the change in resistances into a 0-5 V DC voltage via a Wheatstone bridge. This voltage is compared with an external demand voltage, and allows feedback control of the main solenoid controlled valve.

This requires the MFC to be calibrated for the specific gas of interest, since the temperature difference (and hence output voltage) for a given mass flow rate will depend upon the specific heat capacity of the gas. For methane-air mixtures, a UFC-1200A MFC was used for the methane, and an MKS MFC for the air, since they were the most appropriate for the required flow rates and heat capacities. Calibrations were performed using a positive

displacement wet gas flow meter. A linear relationship between mass flow rate and output voltage was found for the air calibration, but for methane the calibration was less linear. Hence the demand voltage for the methane MFC was fixed at 1.76 V in a region where small deviations allowed a linear relation to be fitted, and the demand for the air MFC is varied correspondingly to achieve the desired equivalence ratio:

$$\dot{m}_{\mathrm{CH_4}}(\mathrm{g/min}) = 0.0961 V_{\mathrm{CH_4}} - 0.0282 \quad \textbf{(4.23)}$$

$$\dot{m}_{\mathrm{air}}(\mathrm{g/min}) = 0.9372 V_{\mathrm{air}} - 0.0848 \quad \textbf{(4.24)}$$

For more details on MFC operation and calibration, see Hu (2013).

4.1.6.2 Liquid fuels

In the case of liquid fuels, the method of partial pressures is not as straightforward as for gaseous fuels, since the evaporation of the liquid fuel is required before addition, either by use of a preheated chamber and a heated line, such as in the approach used by Farrell *et al.* (2004) or by injecting increments of fuel directly into the vessel, checking the pressure rise once it has evaporated, and repeating until the desired partial pressure has been reached. In the work of Marshall (2010), neither method was chosen due to the need for significant extra equipment and the time consuming nature of the procedure respectively. Instead, the volume of fuel required to produce the required partial pressure of fuel p_f is calculated and added directly to the bomb. The same approach is adopted here, albeit with a slightly different procedure regarding delivery of fuel.

Assuming again the case of complete combustion, this time including the possibility of oxygenated fuel the global reaction is:

$$\mathrm{C}_x\mathrm{H}_y\mathrm{O}_z + \frac{1}{\varphi}\left(x + \frac{y}{4} - \frac{z}{2}\right)\left(\mathrm{O}_2 + \frac{79}{21}\mathrm{N}_2\right) \rightarrow x\mathrm{CO}_2 + \frac{y}{2}\mathrm{H}_2\mathrm{O} + \frac{1}{\varphi}\left(x + \frac{y}{4} - \frac{z}{2}\right)\frac{79}{21}\mathrm{N}_2 \quad \textbf{(4.25)}$$

As before, we can obtain expressions for the relative amounts of fuel and air for such a reaction. For a mole of fuel:

$$n_{\mathrm{air}} = \frac{100}{21\varphi}\left(x + \frac{y}{4} - \frac{z}{2}\right) \quad \textbf{(4.26)}$$

which if we consider the case without residuals once again gives

$$n_{\mathrm{f}} = \frac{n_{\mathrm{mix}}}{1 + \frac{100}{21\varphi}\left(x + \frac{y}{4} - \frac{z}{2}\right)} \tag{4.27}$$

Treating the mixture as an ideal gas, and using the initial temperature T_0, then the amount of mixture can be expressed as

$$n_{\mathrm{mix}} = \frac{p_{\mathrm{mix}} V_{\mathrm{bomb}}}{R_0 T_0} \tag{4.28}$$

$$n_{\mathrm{f}} = \frac{p_{\mathrm{mix}} V_{\mathrm{bomb}}}{R_0 T_0 \left(1 + \frac{100}{21\varphi}\left(x + \frac{y}{4} - \frac{z}{2}\right)\right)} \tag{4.29}$$

From this, we are then able to calculate the volume of fuel to be added to the mixture:

$$V_{\mathrm{f}} = \frac{m_{\mathrm{f}}}{\rho_{\mathrm{f}}} \tag{4.30}$$

where

$$m_{\mathrm{f}} = n_{\mathrm{f}} M_{\mathrm{f}} \tag{4.31}$$

and so

$$V_{\mathrm{f}} = \frac{M_{\mathrm{f}} p_{\mathrm{mix}} V_{\mathrm{bomb}}}{\rho_{\mathrm{f}} R_0 T_0 \left(1 + \frac{100}{21\varphi}\left(x + \frac{y}{4} - \frac{z}{2}\right)\right)} \tag{4.32}$$

or in terms of the partial pressure of fuel which this should correspond to, from Equation (4.5) and the relation

$$n_{\mathrm{f}} = \frac{n_{\mathrm{mix}}}{\left(1 + \frac{100}{21\varphi}\left(x + \frac{y}{4} - \frac{z}{2}\right)\right)} \tag{4.33}$$

then

$$V_{\mathrm{f}} = \frac{M_{\mathrm{f}} p_{\mathrm{f}} V_{\mathrm{bomb}}}{\rho_{\mathrm{f}} R_0 T} \tag{4.34}$$

where T is the temperature in the bomb. It is therefore also necessary to obtain the density of the fuel. Daubert and Danner (1997) provide correlation coefficients for the liquid density of many types of fuels, given in kmol m^{-3}:

$$Y = \frac{A}{B^{\left(1 + \left(1 - \frac{T}{C}\right)^{D}\right)}} \tag{4.35}$$

Relating this quantity to the definition of density (in kg m^{-3}) used in Equation (4.34), the liquid density Y is

$$Y = \frac{\rho}{M} \tag{4.36}$$

meaning that the calculation performed by the LabVIEW program to inform the user of the volume of fuel to be injected, based on the density Y is

$$V_{\mathrm{f}} = \frac{n_{\mathrm{f}} V_{\mathrm{bomb}}}{Y R_0} \tag{4.37}$$

Since the liquid density is temperature dependent, the temperature in the vicinity of the syringe is measured with a second thermocouple to provide a more precise real time estimation of the density of the fuel. Marshall (2010) showed that an 8 K deviation in temperature would lead to a 1% error in calculated liquid density.

4.1.6.2.1 Fuel delivery

Fuel delivery is performed using a syringe based system, developed from that used by Marshall (2010). The syringe used is a 1000 μL Hamilton syringe, with a 150 mm Luer tapered needle. Injection is controlled by a kdScientific Model 310 Plus syringe actuator, which can be programmed to inject a desired volume of fuel and a controlled injection rate. For the 1000 μL syringe used, the resolution of volume injected is 0.1 μL.

The existing system used a separate mixing loop (as shown in Figure 4.2) into which fuel was injected, fitted with a low pressure pump to assist with mixing and creating a homogeneous mixture throughout the vessel. In terms of procedure, injection of fuel takes place at the same point in the preparation process as the gaseous fuel as described in section 4.1.6.1.1. The injection takes place using a specially designed ball valve and septum arrangement, shown in Figure 4.4, attached to the syringe port shown in Figure 4.2. The septum is a PTFE disc with a 0.83 mm diameter hole through which the needle of the syringe is inserted, forming a tight fit. For fuel delivery the needle is inserted through the septum, stopping short of the ball valve. The valve is then opened, and the needle is inserted further into the syringe port. Procedure for removing the needle is simply the opposite. Whilst the septum provides a reasonable seal, it will not be sufficient to completely prevent leakage. Therefore, fuel injection was performed at a pressure below atmospheric, so that any leakage would see small amounts of lab air leaking in

to the system, rather than fuel/air mixture leaking out. As the partial pressure of fuel was determined from the mass of fuel injected rather than the measurements of pressure before and after injection, this would not lead to any errors in calculation. To maintain the best seal possible, the septum was replaced frequently due to wear, which was especially noticeable at higher temperatures.

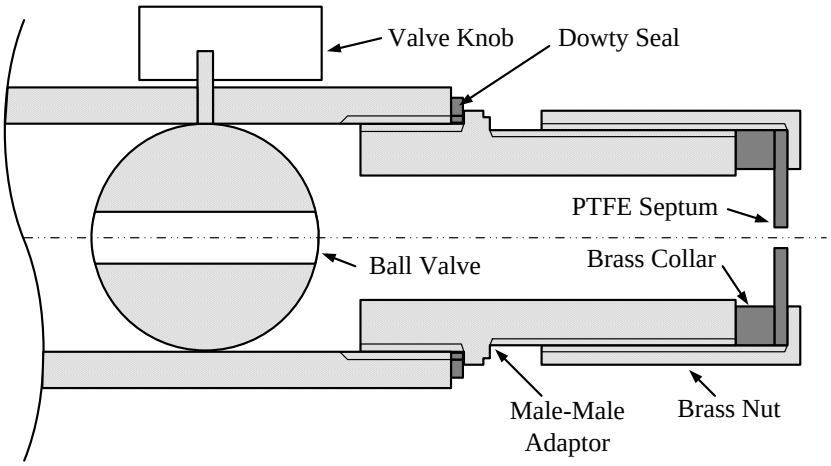

Figure 4.4 –Injection port assembly cross-section, Marshall (2010).

A disadvantage of a syringe based system compared to methods using either a fuel injector, or pre-vaporised fuel in conjunction with a heated line is that the fuel is introduced to the system in large droplets rather than a fine spray, and so it is important to ensure complete vaporisation. Whilst the existing procedure involved injecting into the syringe port at the same temperature as the bomb, the reliance upon the low pressure pump to ensure all the fuel is removed from the port raised concerns over the accuracy of the procedure following disagreement with the lambda sensor regarding the mixture equivalence ratio. Additionally, leaks associated with the low pressure pump were a concern. Particularly in anticipation of injection of hydrous ethanol (which will have a much higher enthalpy of vaporisation), a new procedure was developed to ensure complete evaporation and entrainment of all fuel into the combustion vessel.

The new liquid fuel injection system changes the location of injection to be upstream of the bomb, into the incoming air stream. The system is shown schematically in Figure 4.5.

Therefore, the mixing loop valves as depicted in Figure 4.2 remain closed during the preparation. The outlet to the lambda sensor is also relocated, from its original position on the transducer manifold to the opposite side of the bomb, with the outlet from the original syringe port as shown in Figure 4.2.

Injecting the fuel into the air stream ensures that it is entrained within the air as it evaporates and is drawn into the combustion bomb, rather than risking condensing in the mixing loop. An injection block was designed and constructed, as shown in Figure 4.6. The injection port assembly shown in Figure 4.4 is connected to the left hand end of the heating block, allowing insertion if the needle for fuel delivery. The injection block itself is constructed from aluminium, and has two holes drilled through parallel to the air flow, into which two heating elements are inserted. Conduction to the aluminium block is aided by use of heat conducting copper paste to give a good thermal contact. The heating block is insulated with sheets of 20 mm thick Melafoam, which is housed in a box folded from thin aluminium sheet. A thermocouple is placed into the aluminium block, and the block temperature controller is set to 100°C before injecting fuel. The short section of pipe from the heating block to the bomb casing is also insulated with Melafoam.

The rate of fuel injection was varied depending on the volume of fuel to be injected, so that a constant injection duration of 5 minutes was used. In conjunction with a constant flow rate of air, this ensured that injection of fuel occurred over a consistent pressure range for all experiments. The flow rate of air is controlled using a MFC, and the air is heated prior to mixing with fuel to help ensure complete vaporisation. The tip of the needle is located downstream from the T-section, which will ensure that air flow is in the direction of the bomb.

Under the new arrangement, it is not possible for the partial pressure of fuel to be measured once the fuel has been added and vaporised, since the addition of fuel and air is

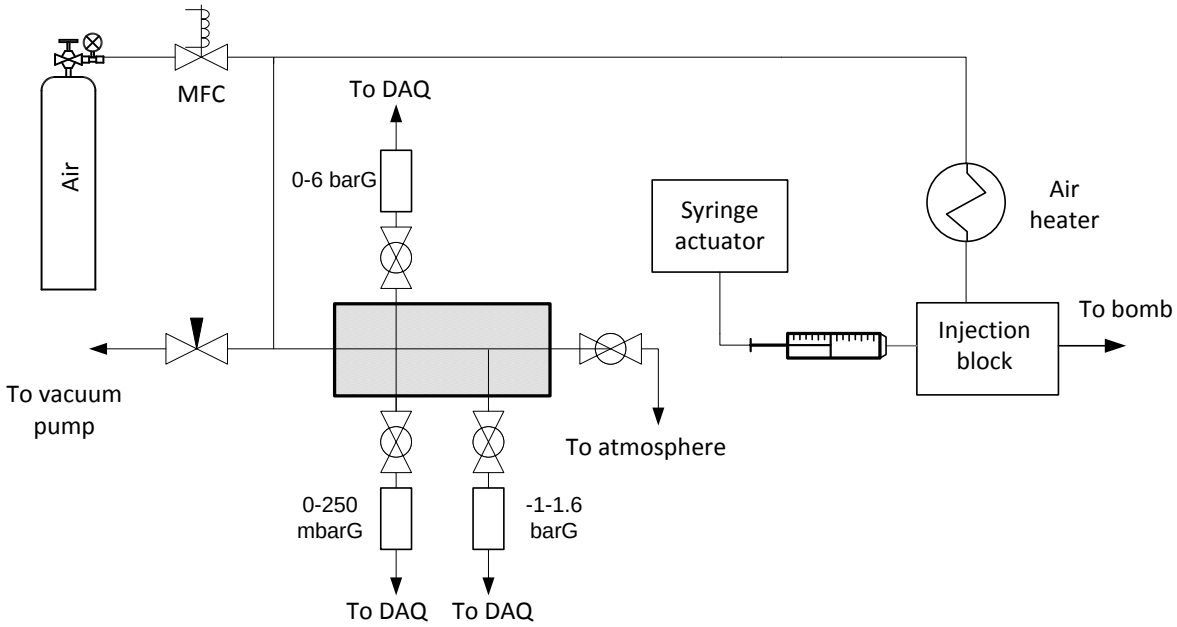

Figure 4.5 – Schematic of the liquid fuel injection system.

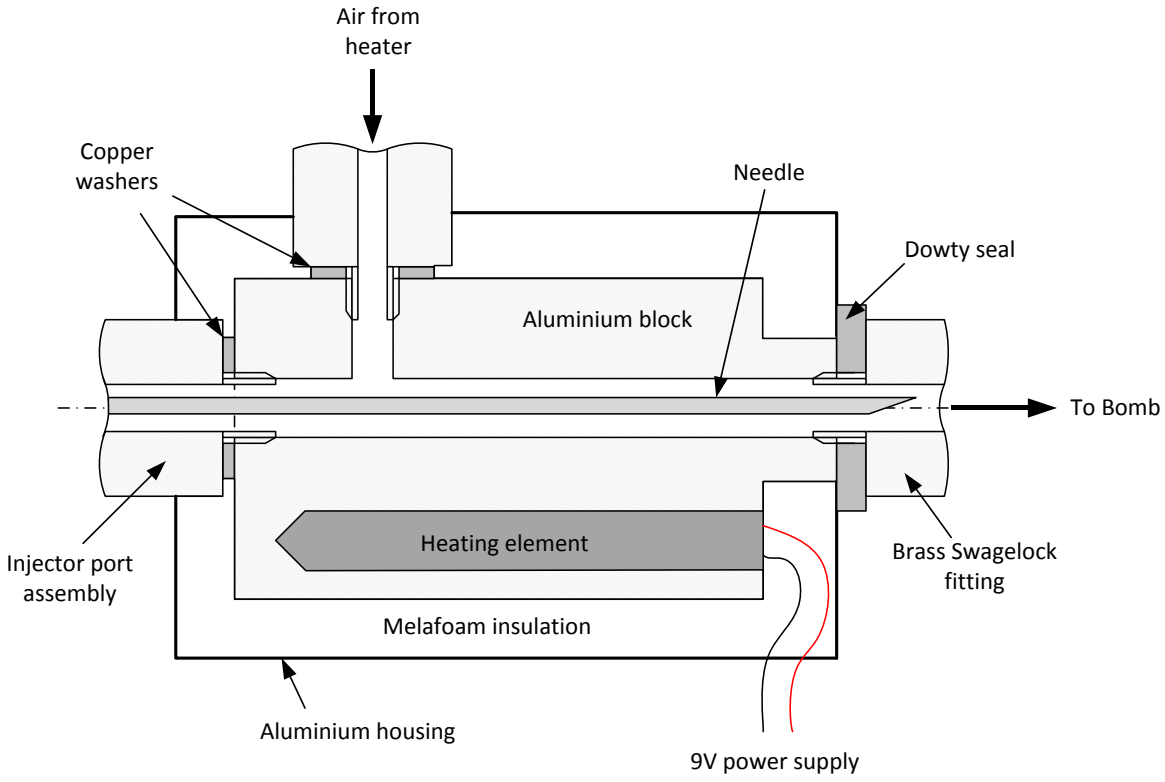

Figure 4.6 – Heating block cross-section.

simultaneous. Therefore it is necessary to determine the equivalence ratio from the mass of fuel added. The mass of fuel is calculated by recording the combined mass of the syringe and fuel before and after injection. The balance used is an Ohaus Galaxy 160 and has a resolution of 0.0001 g. Slight fluctuations in the readings appeared to be caused by air movement in the lab,

but did not typically result in uncertainties of more than 0.0005 g. In some cases, such as when hydrous ethanol is used, the volume of fuel to be injected exceeded that of the syringe. In this case, the injection was performed in two batches, with the mass of fuel injected in each batch measured separately and summed to give the total mass.

The expected partial pressure of fuel corresponding to the measured mass of injected fuel is found by rearranging Equation (4.34):

$$p_{\mathrm{f}} = \frac{m_{\mathrm{f}} R_0 T}{M_{\mathrm{f}} V_{\mathrm{bomb}}} \tag{4.38}$$

Once the final mixture pressure has been obtained, then the difference can be attributed to the partial pressure of the air, allowing the actual equivalence ratio based upon the mass of fuel injected to be calculated.

4.1.7 Fuel blends

In cases where liquid fuels are of a single component (such as neat ethanol), the volume of fuel to be injected is calculated simply using the expression in Equation (4.34). For the case where the liquid to be injected is a blend, further data and calculation are required to determine the volume to be injected.

4.1.7.1 Hydrous ethanol

Addition of water to the ethanol will result in a larger volume of the blended fuel to be injected to maintain stoichiometry. The number of moles of ethanol, n_{ethanol} can be calculated from the desired equivalence ratio and final mixture pressure as before, meaning the total amount of fuel to be injected will be

$$n_{\mathrm{f}} = \frac{n_{\mathrm{ethanol}}}{MF_{\mathrm{ethanol}}} \tag{4.39}$$

where MF_{ethanol} is the mole fraction of ethanol. Therefore it is necessary to establish the molar fractions of the blends, which have been mixed on a volumetric basis. The molar densities of ethanol and water at 25°C are given as 58.68 $\mathrm{cm^3 mol^{-1}}$ and 18.07 $\mathrm{cm^3 mol^{-1}}$ by Poling *et al.* (2001). The relationship between volume fraction and molar fraction is non-linear as shown in

Figure 4.7. This is used for all subsequent conversions, since the blends were mixed at a single temperature and so the composition is fixed regardless of further changes in temperature of the mixture.

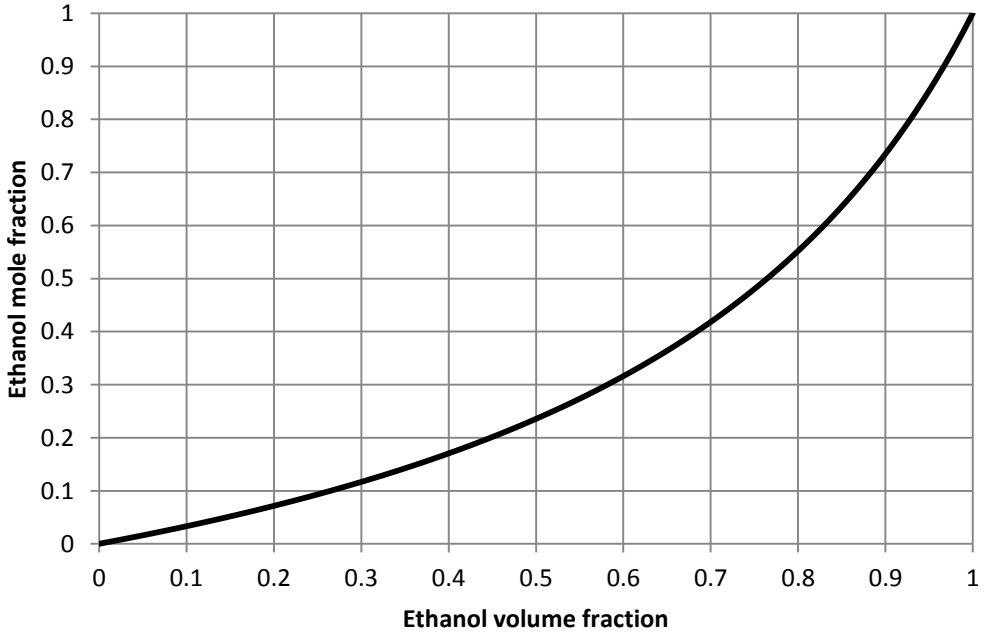

Figure 4.7 - Ethanol molar fraction for hydrous ethanol blends for varying ethanol volume fraction.

To be able to calculate the volume of a hydrous ethanol blend using Equation (4.37), then the density of the blend in kmol m^{-3} needs to be known. The International Critical Tables, West and Hull (1933), provide data for the density (in g ml^{-1}) of hydrous ethanol blends in terms of % weight at 20°C. This data is plotted in Figure 4.8, and a polynomial was fitted to allow calculation from mass fraction within the LabVIEW program. Data is also provided in terms of specific gravity (the density of the blend relative to the density of water at the same temperature) at 60°F (15.56°C), which allows the effect of temperature to be seen. Since the temperature of the lab was close to 20°C during mixture preparation, a linear interpolation to correct for temperature is acceptable. The ethanol fraction by mass for a given volume fraction of ethanol and temperature is found by considering the relative molar mass of ethanol and water. Along with the molar mass for the given blend (weighted based upon mole fraction), the density of the blend (in kg m^{-3}) as found from the fitted polynomial in Figure 4.8 is used to give the density (in kmol m^{-3}) in Equation (4.35).

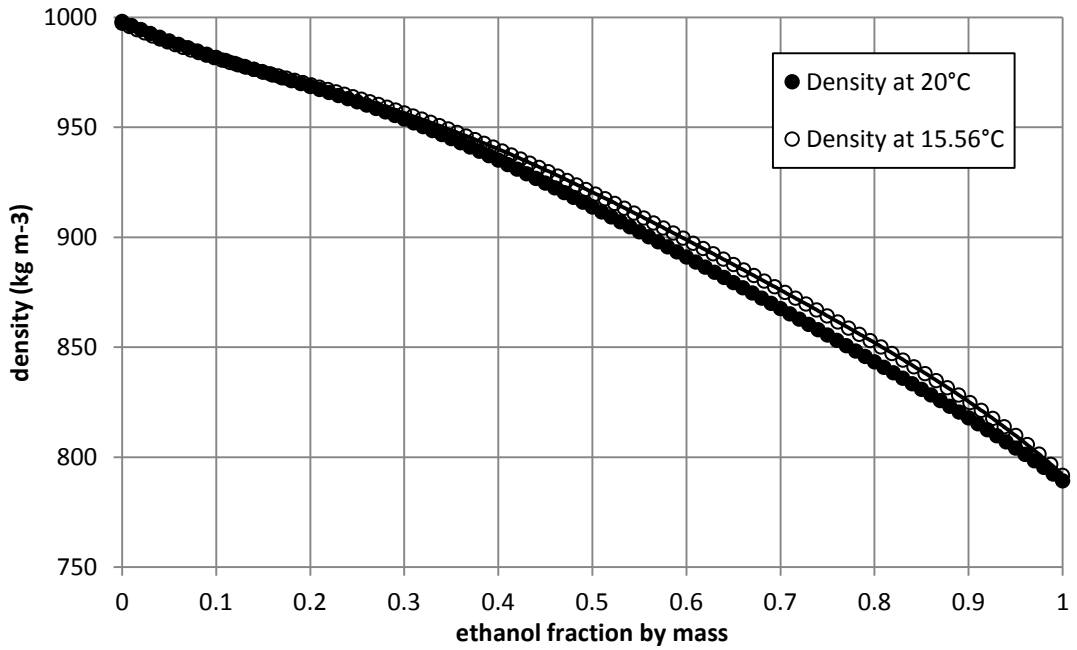

Figure 4.8 – Density of hydrous ethanol blends for ethanol fraction by mass.

4.1.7.2 THEO fuels

All blends have been mixed on an equal volume basis, meaning 50/50 vol/vol for binary mixtures for example. As with the hydrous ethanol blends, it is necessary to know the molar fractions of the individual components within the blends. It is illustrative to show the molar fractions of binary blends for varying volume fractions; considering binary blends involving iso-octane, it can be seen in Figure 4.9 that the most significant non-linear effect is with ethanol, due to ethanol being polar and having the biggest difference in molecular weight compared with iso-octane. Equally, blends of n-heptane and toluene are fairly linear, whereas blends with ethanol all exhibit a more strongly non-linear relationship between volume fraction and mole fraction.

Data for density of all blends tested is not available, and so a volume based average density approximation is used. Upon mixing of components, less volume change was seen when compared to the case of mixing ethanol and water, hence it was deemed that attempting to measure the volume change would not yield additional accuracy in estimating the blend density compared with the assumption of a volume based average.

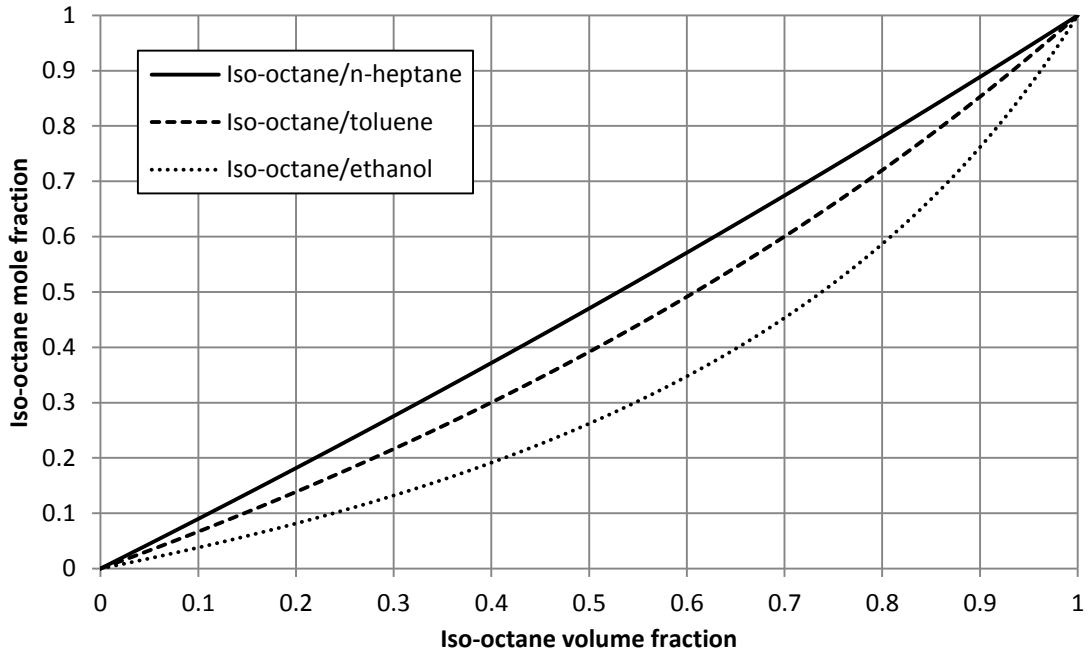

Figure 4.9 – Iso-octane mole fractions in binary blends with n-heptane, toluene and ethanol for varying iso-octane volume fractions.

This assumption can be further justified by considering a few cases where blending data is available. For example, using a linear interpolation of the experimental data of Ku and Tu (2005), a 50/50 vol/vol blend of ethanol and iso-octane at 298 K is found to have a density of 733.92 kg m^{-3}, compared with 740.5 kg m^{-3} using a volume average density. This gives an error of less than 0.9% on the density, which is an acceptable level for determining the volume of fuel to be injected. This would be expected to be the most non-ideal blend due to the alcohol presence. For mixtures of n-heptane and iso-octane, the experimental data of Aucejo *et al.* (1995) is used and for a 50/50 vol/vol blend at 298 K reports a density of 688.96 kg m^{-3} compared with 688.00 kg m^{-3} obtained using a volume average density. The error here is less than 0.2%, which is again acceptable for the estimation of fuel density. Therefore, for the all the blends (binary, ternary and quaternary), an average density on a volume basis is used throughout.

To account for temperature effect on blends, a relationship given by Davy and Kowsari (2010) representing the density change with respect to temperature for ethanol-gasoline blends as given in Equation (4.40) is used. Given that the THEO blends are representing gasoline

surrogates blended with ethanol, this appears a justifiable method of accounting for temperature.

$$\rho = \rho_{298\,\mathrm{K}} + 0.89(298 - T) \quad \textbf{(4.40)}$$

Additionally, the actual equivalence ratio is determined from the measured mass of fuel injected, so any errors in density causing significantly more or less fuel to be injected than required to achieve the desired equivalence ratio, will be picked up in the measurement of the mass of fuel injected. The molar mass of the blends is simply found by a molar basis weighting of the molecular weight of the individual components.

4.1.8 Ignition

Central ignition of the prepared air/fuel mixture is achieved with two co-linear electrodes forming a spark gap at the centre of the bomb; its position is checked using images taken with the high speed camera (section 4.1.10). The spark gap was set to approximately 1.2 mm.

The electrodes were sharpened to increase the electric field intensity in the spark gap. One electrode acts as a ground; a thin stainless steel electrode is connected to a brass section which screws into the bomb wall, which is grounded. The other was manufactured from a regular spark plug; the original electrode and most of the original thread is removed, and a steel welding rod is connected with assistance from a specially made jig. The rod is then machined to a point, and screwed into the port in the bomb. A custom made copper washer is used to provide the seal, as well as to set the distance and maintain the desired spark gap. The spark plug could be removed through a small hole in the wall of the oven with a 16 mm socket and wrench.

The spark is created using a Jaguar coil pack as would be used on one cylinder of a gasoline engine, which is triggered by a TTL pulse, the duration of which can be varied to set the charging time and hence vary the spark energy. However, the energy supplied to the coil can be calculated by modelling the coil as a resistor and inductor in series and determining the current for the relation

$$V = IR + L\frac{\mathrm{dI}}{\mathrm{dt}} \quad \textbf{(4.41)}$$

Whilst this would imply an exponential relation, the low resistance of the coil and the limiting circuitry in the coil pack causes the current to saturate. The increase in current can be considered linear up to saturation, which is found to be 11.5 A after a rise time of 4 ms. Beyond this time, no increase in spark energy would be achieved, but rather a steady magnetic field will be sustained. The energy stored in the coil is given by:

$$E = \frac{1}{2}LI^2 \quad \textbf{(4.42)}$$

The dwell time was set in the range of 0-4 ms using a 555 timer reconfigured from that originally intended for setting the injection duration of an automotive fuel injector.

Marshall (2010) estimated a coil inductance of $4.17\text{x}10^{-3}$ H, which corresponded to a maximum coil energy of 0.276 J when the maximum dwell time of 4 ms was used. Tests were also performed to measure the HT energy, by measuring the voltage and current in a special HT lead using a Pearson 411 current transducer through which the HT lead is run, and the output voltage is amplified and sent to the DAQ. Measured voltage and current are multiplied to determine the power and integrated up to the end of the discharge phase to give HT energy. For the 4 ms dwell time, the HT energy at 1 bar pressure was 68 mJ, which represents an efficiency of around 25%. Exact spark energy cannot be estimated accurately, since the efficiency of the transfer of energy to the spark is unknown.

4.1.9 Lambda sensor

To act as a check on the equivalence ratio of the fuel-air mixture burned in the bomb, exhaust gases are fed past an ECM AFRecorder lambda sensor before being extracted from the laboratory. This check is used since the value of equivalence ratio according to the partial pressures of the mixture components could be susceptible to any errors in the experimental procedure, or in the pressures as measured by any of the transducers used in the mixture preparation. For the exhaust gases to pass over the sensor, the bomb needs to be at a higher pressure than atmospheric. This means that the sensor can only be used for initial pressures

greater than 1 bar. The position of the lambda sensor varied depending on the mixture preparation; for the gaseous fuel mixtures, the outlet to the lambda sensor was via a needle valve on the transducer manifold but for the new liquid fuel delivery, the lambda sensor was attached at the original syringe port as shown on Figure 4.2. A summary of the principle of operation of the lambda sensor is given in the Appendix, section A.1.

4.1.9.1 Calibration

The sensor is calibrated in still air by setting the O_2 content to be that of the surrounding air. The concentration of oxygen in dry air is taken to be 20.95%, with the concentration dropping as the humidity is increased, in accordance with

$$\%O_2 = 20.95\% \times \frac{\left(p_\mathrm{b} - p_\mathrm{ws} \times \frac{R_\mathrm{h}}{100}\right)}{p_\mathrm{b}} \qquad \textbf{(4.43)}$$

where p_b is the barometric pressure, p_ws is the saturation pressure of water vapour and R_h is the relative humidity. Relative humidity is measured using a sling psychrometer.

The calibration was then tested against bottled air, nitrogen and two calibration gases: CalGas to test the lean mixture case (a mixture of 6.59% O_2 in N_2, expected to give $\lambda = 1.455$), and an MOT Mix to test the rich mixture case (14.02% CO_2, 3.52% CO, and 1965ppm propane, expected to give $\lambda = 0.889$). For the testing with bottled air, the O_2 content measured appeared to be a function of the speed at which the gases were fed past the sensor. A flow meter was used to monitor the flow rate when recording this variation. However, when using the calibration gases the measured values of lambda were not seen to vary by more than the least significant bit of the display, and are given in Table 4.1. The variation in measured equivalence ratio with flow rate raised concerns over the performance of the sensor in the combustion bomb application, and prompted further investigations into the performance of the lambda sensor with actual combustion products. Lambda sensor consistency is discussed further in section 6.1.3.

The results in the table suggests that the sensor may read slightly too rich for lean mixtures and slightly too lean for rich mixtures when there are high levels of hydrocarbons. However,

this is in line with previous calibrations performed on the sensor with these gases, and so the sensor was deemed to be calibrated correctly.

When using the lambda sensor for real mixtures, it is necessary to enter details of the fuel composition in the control unit, specifically the C/H ratio and O/H ratio. This is particularly important for oxygenated fuels, since the presence of fuel bound oxygen will have a significant effect on the stoichiometric air/fuel ratio, which needs to be known to determine the equivalence ratio.

Table 4.1 - Calibration of lambda sensor against two calibration gases.

Gas	Expected λ	Measured λ
CalGas	1.455	1.43 - 1.44
MOT Mix	0.888 - 0.890	0.93

4.1.10 Schlieren system

A schlieren photography system has been constructed, Marshall (2010), for the purpose of imaging the flame front to determine flame speed in the initial stages of combustion (up to the diameter of the windows, 40 mm), and also for detection of cellularity in the later stages of combustion when the pressure rise is more significant. A schlieren system was chosen as opposed to normal light photography, since it provides a more definite edge and gives a better measurement of the position of the flame front, Rallis and Garforth (1980).

The schlieren system constructed by Marshall (2010) is a folded z-type arrangement. Further details of the design and construction of the system can be found in the original work by the same author. The system uses two oppositely tilted off-axis spherical mirrors to produce the collimated beam, as depicted in Figure 4.10. This allows a more compact system than could be achieved using a linear system of lenses. Further plane folding mirrors were used to reduce the system size further to ensure it could be fully fitted on the optical bench. The optical axis is through the centre of the bomb windows, found to be 223 mm above the plane of the optical bench. The first pin-hole is used to create an effective point source, which is required for a

collimated beam. The second pin-hole is used in place of a knife edge, to provide 2D resolution whereas a single knife edge would only detect density gradients in the perpendicular direction; this is important since the physical problem of the propagating spherical flame front is axisymmetric, and so density gradients in orthogonal directions need to be depicted. The pin-hole is created using an adjustable iris. Reducing the size of the hole increases sensitivity of the schlieren system, but loses focus of the image due to diffraction. Adjustment of the iris allows the sensitivity of the system to be adjusted depending upon initial pressure, since increasing pressure results in a change in density across the flame front and the flame front thickness, both of which affect the density gradient and hence the darkness of the detected schlieren edge.

The illumination source used is a 1 W green Prolight Power Star/O LED, with an inner cone angle of 6.4° which makes it more appropriate than either a tungsten or halogen bulb, and avoids safety issues associated with lasers (which are often used for schlieren systems). The green LED was originally chosen due to concerns of light from combustion interfering, and since radiation from soot is primarily in the red region then use of a green light source and an appropriate bandpass filter would allow this light to be removed. Whilst this was found to be unnecessary, the green LED was still used.

To capture the images at a suitable frame rate for early flame propagation, high speed cameras were required. Two Photron 1024 PCI cameras were available, one colour and one monochrome. The frame rate at which the camera can record is dependent upon the resolution of the image, meaning a compromise between frame rate and resolution is required. The chosen settings were a resolution of 512 x 512 pixels allowing a frame rate of 3000 fps, which was deemed to be sufficient. The camera contains on-board buffer memory which allows more than sufficient number of frames to capture the duration of the combustion.

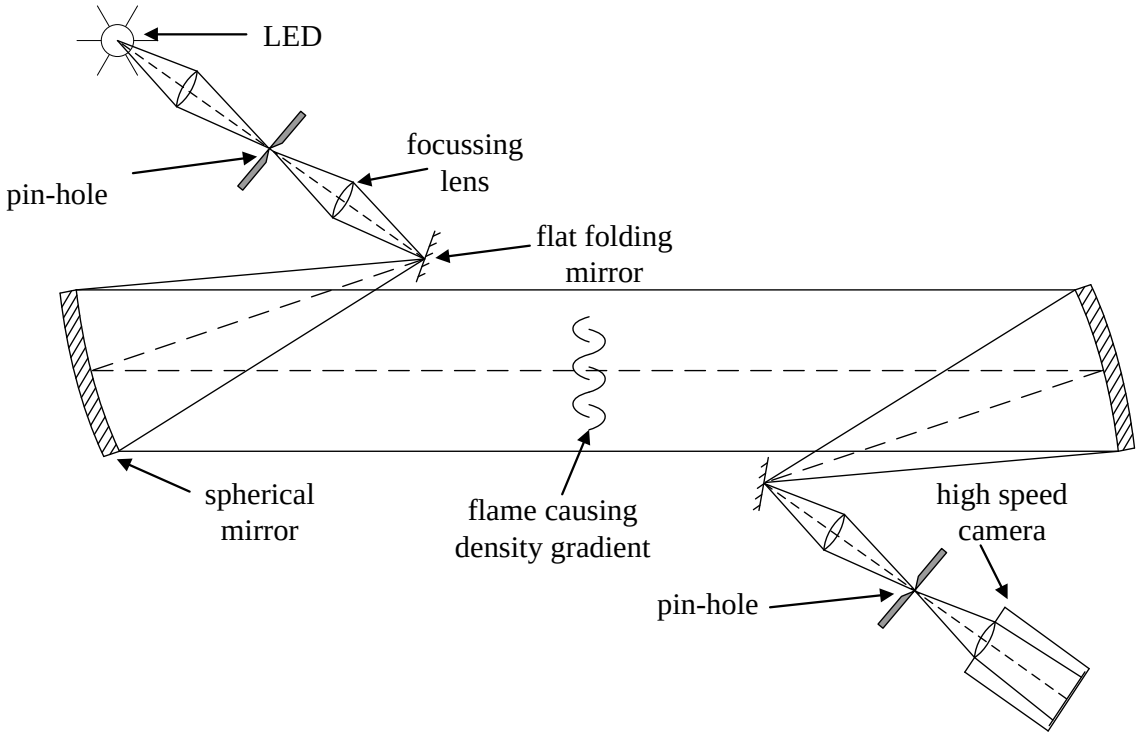

Figure 4.10 – Folded z-type schlieren system. Adapted from Marshall (2010).

The camera uses a simple trigger mode, which starts recording on a rising edge fed into the external TTL input, and records until the buffer memory has been filled. This enables the recording to be triggered to synchronise with the spark, and hence the start of combustion. The recording is saved as a sequence of TIFF images, which were numbered to allow easy processing with the *BVICS* GUI (section 5.1).

4.2 Optical engine rig

Tests were performed in a single cylinder optical engine for some hydrous ethanol blends, to compare trends in burn rates in an engine with laminar burning velocities determined from the combustion bomb. As described in section 2.9, early flame growth in SI engines is laminar, with a transition to fully turbulent combustion by 10% mfb. Therefore, the early burn is expected to be closely related to the laminar burning velocity. Since the tests run simply to provide a comparison with the burning velocity data, the details of the optical engine test rig are not provided extensively, but rather a brief overview is provided. Further details can be found in previous work from the group, such as Twiney (2010).

The single cylinder engine allows optical access, which enables imaging of both the fuel spray and combustion. Optical access to the combustion chamber is provided via two windows; the first is through a fused silica window in the piston crown, using a mirror arrangement allowing images of the fuel spray and combustion to be reflected out through the 'Bowditch' piston as shown in Figure 4.11; the second is through a fused silica window in the pent roof of the combustion chamber. This is not large enough to allow camera access, but gives access for illumination using LEDs which can be used to illuminate the fuel sprays.

The engine can operate in both Plenum Fuel Injection (PFI) and Gasoline Direct Injection (GDI) modes, up to 2000 rpm (limited by the mass of the Bowditch piston assembly). In GDI mode, the fuel is injected directly into the combustion chamber with timing controlled by the operator via a LabVIEW interface, whereas in PFI mode the fuel is injected into a plenum upstream of the intake valves. The main engine parameters are shown in Table 4.2. The combustion system consists of a centrally mounted spark plug and fuel injector, which operates at fuel pressures of up to 150 bar, and is capable of multiple injections per cycle. The six jet spray is guided such that four jets spray downwards into the combustion chamber, and two straddle the spark plug, which offers the potential for stratified operation.

Table 4.2 - Single cylinder engine parameters.

Bore (mm)	89
Stroke (mm)	90.3
Cylinder capacity (cc)	562
Compression ratio	11.1
Fuel injection pressure (bar)	150
IVO (CAD aTDC)	33.5
IVC (CAD aTDC)	241.5
EVO (CAD bTDC)	245
EVC (CAD aTDC)	5

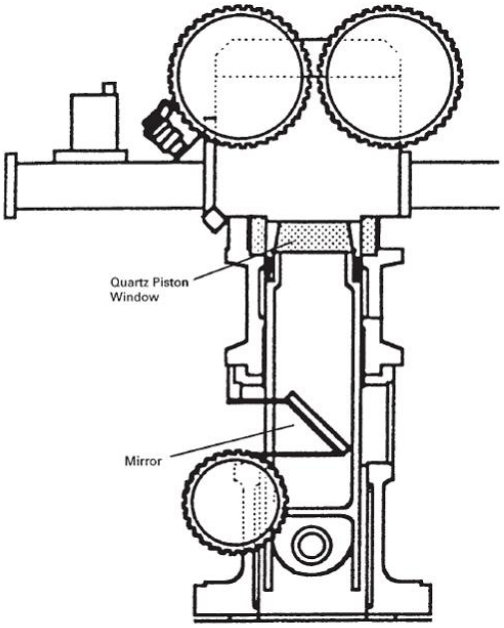

Figure 4.11 - Optical engine schematic showing the Bowditch piston with a quartz window and mirror arrangement, Stone (2012).

The engine can also be run in non-optical mode, where the window is replaced by a steel blanking section. This has the advantage of allowing the engine to be run at higher loads, since this configuration is significantly more robust than when the engine is run in optical mode. The fused silica window is prone to fracture, and so will often need to be replaced.

A LabVIEW program titled ETCS (Engine Timing and Control System) is used for selecting whether the engine is run in GDI or PFI mode, and is responsible for the control of injection and ignition timings. A second computer is used for data acquisition at both low and high speed (LDAQ and HDAQ), again using a LabVIEW interface.

5 Data Analysis

5.1 *BVICS* overview

In this section, the data analysis procedures are described and validation of the analysis is provided. The overall system architecture is developed from the *BVICS* (Burning Velocity Integrated Calculation System) reported in the previous work of Marshall (2010). This architecture contains a number of programs that are used to analyse the experimental data. The overall *BVICS* architecture, and the programs of which it consists are implemented in MATLAB, with the data and constituent programs managed via a GUI (graphical user interface), enabling straightforward processing and transfer of the data between the individual programs. All programs are run from the main GUI. The flow of data is represented schematically in Figure 5.1. Experimental sets are typically composed of a number of experiments for one specific fuel, with varying equivalence ratio, initial temperature and pressure, and diluent fraction.

For constant pressure combustion analysis, the flame front propagation is measured using the high speed camera described in section 4.1.10. This image data is processed by the *BVImage* routine detailed in section 5.1.2, to produce flame radius and stretch rate with respect to time. This data is then analysed according to models for stretch extrapolation to determine flame speeds, burning velocity, and burned gas Markstein lengths. *BVImage* is also used for detection of cellularity, which feeds back into the *Burnvel* code (section 5.1.3), to ensure that cellular flame data is not included within the burning velocity data set.

For constant volume combustion analysis, the pressure during combustion for each experiment in the experimental set is recorded by the DAQ system (section 4.1.2). Alongside this, the multi-zone model (section 3.1.5.3) is run via the BOMB program (section 5.1.1) with inputs representing the experimental conditions. The outputs from these are passed to the *Burnvel* routine, which along with the sub-routine *bvcalc*, calculates the burning velocity for the

temperatures and pressure during the experiment. This burning velocity data is concatenated with other experiments with different experimental conditions within the same set into one large data matrix. This data is then passed to the *fitcorr* routine (section 5.1.4) which performs the least squares minimisation fitting to produce the correlation coefficients. The *BVICS* architecture also contains the options for user to save the outputs and correlation coefficients, and a facility for plotting burning velocity data against various conditions, derived correlations at various conditions, and the onset of any cellularity as detected by *BVImage*. Within the GUI is a set of axes, which show the desired plots, and is also involved in the selection of the burning velocity data during the running of *Burnvel*.

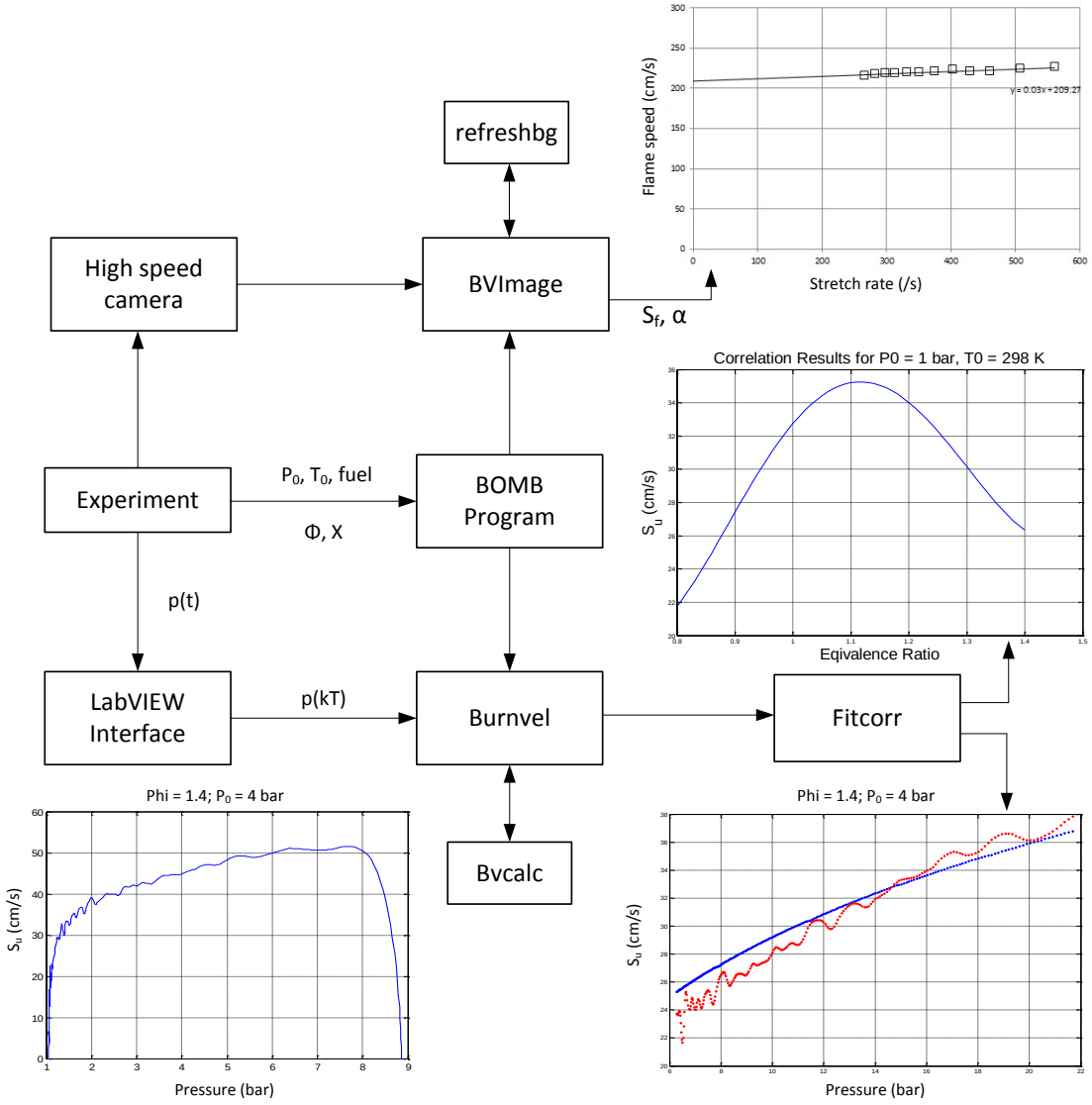

Figure 5.1 – Schematic representation of the data flow within the *BVICS* architecture.

To run a data set from the GUI, the user specifies the fuel name to enable an appropriate data file to be located, the camera frame rate and the directory in which the experimental data for that set is stored. To run, an experimental summary spreadsheet is required, which is read by the BOMB program, *Burnvel* and *BVImage*. This spreadsheet contains information about each experiment, including:

1. Experiment number.
2. Equivalence ratio.
3. Initial temperature (K).
4. Initial pressure (bar).
5. Diluent fraction.
6. A Boolean describing whether pressure data is to be used.
7. A Boolean describing whether schlieren images are to be used.
8. The diameter of the window (pixels).

5.1.1 BOMB program

The BOMB program solves the equations of conservation of energy and volume for combustion in a constant volume, and the equilibrium of 10 species (H_2O, CO_2, N_2, O_2, CO, H_2, H, O, OH and NO_x) in the burned gas for each zone of the multi-zone model (as described in section 3.1.5.3). For the given fuel, equivalence ratio, diluent fraction and initial temperature and pressure, the BOMB program calculates the pressure, unburned gas temperature, ratio of specific heats, specific volume and flame radius as a function of mass fraction burned. For each experiment, the conditions are read in from the experimental summary file.

5.1.1.1 BOMB program inputs

The BOMB program is designed to be run from an MS-DOS script, however when run from the GUI, the relevant inputs are read from the experimental summary file and the program is run via a batch file. The inputs that the program requires relate to the size of the vessel, number of

zones and steps to be used (10 zones and 200 steps were used throughout), the burn rate model used (set to be equal mass zones), initial conditions of equivalence ratio, pressure, temperature and diluent fraction, and the fuel ideal gas properties (specific heats, enthalpies, entropies and higher and lower gravimetric calorific values). In addition, many of the original inputs needed for the full ISIS simulation are required, although their values are chosen in a way as to not have an effect on the results of constant volume combustion.

A fuel data file is needed which contains the coefficients required for the equations of specific heat capacity, enthalpy and entropy, in the form used by Ferguson (1985):

$$\frac{c_{\mathrm{p}}}{R} = a_0 + b_0 T + c_0 T^2 \qquad \textbf{(5.1)}$$

$$\frac{h}{RT} = a_0 + \frac{b_0}{2} T + \frac{c_0}{3} T^2 + \frac{d_0}{T} \qquad \textbf{(5.2)}$$

$$\frac{s^0}{R} = a_0 \ln T + b_0 T + \frac{c_0}{2} T^2 + e_0 \qquad \textbf{(5.3)}$$

For many standard fuels, these coefficients are given directly in Ferguson (1985), but for others, or for blends on fuels for which data was not available, it was necessary to determine these properties from other sources. One such source is Reid *et al.* (1987), which provides coefficients for a third order polynomial expression for specific heat capacity with respect to temperature. To fit the required form, a quadratic was fitted to the third order polynomial, giving the coefficients a_0, b_0 and c_0. The reduction from a third order to second order polynomial showed negligible loss of accuracy over the temperature range considered. The remaining coefficients (d_0 and e_0) were found using the values of enthalpy of formation and absolute entropy from the thermodynamic data tables of Daubert and Danner (1997). The higher and lower gravimetric calorific values also require the enthalpy of formation of CO_2 and H_2O, which were obtained from Atkins (1994). In addition, the BOMB program required a 2nd law term, representing the difference in Gibbs energy between the products and reactants, which were also obtained from Atkins (1994) and Daubert and Danner (1997) respectively.

Where CO_2 and H_2O were used as diluents, a built in function within the BOMB program allowed this to be taken into account. For the binary, ternary and quaternary THEO blends, the values needed for the fuel data file are found from molar averages.

5.1.1.2 BOMB program outputs

The outputs are given in the form of two text files, which provide information on:

1. Progress of combustion
    a. Mass fraction burned
    b. Flame radius
    c. Pressure
    d. Burned gas composition
2. Unburned gas
    a. Temperature
    b. Specific volume
    c. Ratio of specific heats, γ_u
3. Individual zone information
    a. Temperature
    b. Radius of zone boundaries
    c. Specific volume of the burned gas

The two text files containing this information are saved in the working directory, ready to be read by the *BVImage* and *Burnvel* programs.

5.1.2 BVImage

The *BVImage* routine, used directly as described by Marshall (2010) has two purposes: flame front detection from the images obtained from schlieren photography to calculate the flame speed and stretch rate during the initial pre-pressure period of combustion, and detection of the transition from smooth to cellular flames, to ensure that cellular flame data is not incorporated

into the burning velocity data set obtained from *Burnvel*. The program allows many images to be analysed sequentially, speeding up the process significantly.

5.1.2.1 Flame speed measurement

To determine flame speed from the sequence of schlieren images of the initial flame propagation, the radius of the flame needs to be calculated. The field of view is limited to 40 mm by the diameter of the windows. Within this, the schlieren flame front appears as a dark circle which expands as the flame propagates, the thickness of which is determined by the flame front thickness, temperature difference between the burned and unburned gases and the sensitivity of the schlieren system. An image analysis algorithm is used to determine this flame radius, exploiting the approximate circularity of the flame front in the early stages of combustion. This algorithm has not been modified from the form which was developed by Marshall (2010), who investigated several methods for successful determination, and finalised by Taylor (2008), and so will only be outlined here. The processing is performed by the subroutine *refreshbg*, which is run for each experiment in turn within the set. The procedure is a thresholding method, which relies upon detecting the circle representing the flame front, and isolating it from additional objects in the image, namely the electrodes and combustion deposits that build up on the inside of the bomb windows. The procedure is as follows:

1. Median filtering
2. Background subtraction
3. Thresholding
4. Removal of small regions
5. Morphological closing operation
6. Calculation of flame area, and corresponding equivalent radius

Median filtering is performed on the images with the aim of smoothing noise without distortion, particularly of edges, which is imperative for this application. The MATLAB script *medfilt2*

was used. Background subtraction is performed to remove the objects that remain constant in each frame such as the electrodes and deposits of the windows, leaving just the flame front. A reference image (before the appearance of the flame) is used to provide the reference for the background removal. Thresholding is then performed to determine the flame front and produce a Boolean matrix, where pixels with a value greater than the threshold are given the value 1, and those below given the value 0. Regions in this binary image with an area smaller than a chosen threshold are considered to be image artefacts and not part of the flame and are subsequently removed. Morphological closing of the image utilises a dilation process followed by erosion, which fills small or thin holes and smoothes the boundary of large objects. Performing this closing also has the effect of filling in the gaps where the flame front crosses the electrodes. This results in the flame being represented by a solid filled area representing the flame front. This area will not be perfectly circular, and so the equivalent radius is found by determining the area of the closed region and assuming it to be circular:

$$r_\mathrm{b} = \sqrt{\frac{A_\mathrm{measured}}{\pi}} \tag{5.4}$$

However, the assumption of flame speed being the rate of change of radius with respect to time requires that the flame front is perfectly circular. Therefore, if the flame front is determined to be insufficiently circular, it is necessary to exclude it from the analysis. To do this, a measure of circularity is used as follows:

$$\text{circularity} = \frac{P_\mathrm{actual}}{P_\mathrm{calculated}} \tag{5.5}$$

$$P_\mathrm{calculated} = 2\pi r_\mathrm{b} \tag{5.6}$$

This measure of circularity will be unity if the detected flame is a perfect circle. If the circularity is higher than a determined threshold, then the flame radius r_b is kept in the data set; if not, the data for that image is discarded. Lack of circularity can be caused by the flame itself being insufficiently circular (common in the initial stages after ignition), or the schlieren flame front being too faint for accurate detection.

For each experiment, data is saved into an overall data matrix for every frame where the radius could be reliably detected, and fitted the criteria of circularity. This data matrix contains columns for: burning velocity, flame speed, equivalence ratio, pressure, temperature, initial pressure, initial temperature, diluent fraction, stretch rate, flame radius, time and experiment number. The initial conditions, mixture composition and experiment number read in directly from the summary spreadsheet, time is determined from frame rate and frame number. Pressure and temperature are determined by interpolating from the output of the BOMB program for the measured flame radius (although the rise in pressure and temperature is expected to be small, and indeed is assumed negligible for the sake of analysis). Flame speed is the derivative of flame radius with respect to time, calculated using a central difference method. Linear extrapolation to zero stretch is performed as described in section 2.5.6, and this process is evaluated in section 6.2.1.3.

Marshall (2010) did not successfully determine unstretched burning velocities, due to an error meaning the extrapolations did not yield sensible results. The reasons for this are twofold.

Firstly, in attempting to apply stretch extrapolation to burning velocity data, the stretch extrapolation performed required a spline fitting with cubic and quadratic relations. However, this was found to be unreliable, and dependent upon the form of the fit, and was particularly susceptible to the values of the last few data points. This was found to be due to the fact that in determining burning velocity via the relation

$$S_{\mathrm{u}} = \frac{\mathrm{d}r_{\mathrm{b}}}{\mathrm{d}t}\frac{v_{\mathrm{u}}}{v_{\mathrm{b}}} \qquad \textbf{(5.7)}$$

the specific volume of burned gas v_{b}, was determined by mass conservation calculated from the measured flame radius. Whilst in theory this should produce a correct answer, due to the fact that the measured radii are comparatively small at the stages after ignition, the calculated specific volume is subject to a large error, and is also skewed by the large initial stretch rates. Therefore, the calculated burning velocities at high stretch rates are significantly higher than they should be, leading to this problem with fitting. In the current work, this was corrected by

instead using an interpolated value of burned gas specific volume from the BOMB output files, which provided a more accurate density ratio and values of burning velocity which when plotted against stretch rate produced a linear trend allowing extrapolation.

Secondly, recalling the work of Bradley *et al.* (1996), and as recently highlighted as the basis of the new technique of Varea *et al.* (2012), applying the density ratio to obtain burning velocity is only theoretically correct at conditions of zero stretch and so using this method will not provide correct values of burning velocity or unburned gas Markstein length. In reality the results for burning velocity will be close as we would expect the results to begin to converge for the case of zero stretch, and may be less significant than errors in estimated density ratio. However, the results for unburned gas Markstein length are unlikely to be similarly reliable, and should not be used.

Identification of these errors and their causes has enabled the current study to extend the preliminary work of Marshall (2010), and allow useful flame speed and burned gas Markstein length data to be obtained from this rig for the first time. This also opened up the possibility of comparison and reconciliation of results from the constant pressure and constant volume measurement techniques, which has not been previously possible nor reliably shown elsewhere in the existing literature.

5.1.2.2 Cellularity detection

The second purpose of *BVImage* is to detect the onset of cellularity for the reasons described in section 2.6.4. At the onset of cellularity, the determined burning velocity will often see a significant increase. *BVImage* identifies the pressure at which cellularity first occurs (if at all) in each experiment, and saves the value. This is then passed to the *Burnvel* routine, allowing the user to exclude cellularity affected data when running the *Burnvel* routine.

The algorithm for detecting cellularity was again developed by Taylor (2008). The principle is based upon the premise that at the onset of cellularity, the flame undergoes a rapid segmentation process. An image containing a cellular flame will be expected to have a higher

number of edges within the frame. The MATLAB function *edge* is used, along with a suitable threshold level to enable the detection of edges. This is performed on each frame in the sequence and the number of edges detected is recorded. The sequence of number of edges is then smoothed with a moving average filter, allowing the result to be differentiated to obtain the rate of change of number of edges. Prolonged increases, reflected by large, wide peaks in this function are then flagged as cellularity events, which are sent to the *Burnvel* routine. Multiple cellularity events are representative of sequential 'bifurcation' of the cells on the surface of the flame.

An investigation into detection of cellularity from the pressure record during combustion has also been performed, with potential benefit to researchers using combustion vessels without optical access. Since this technique has not been used directly here, the results of this investigation are found in the Appendix, section A.2.

5.1.3 Burnvel

The *Burnvel* routine is once again a modified version of that used by Marshall (2010). Changes were made to the program to enable the inclusion of diluents. The aim of the routine is to calculate the burning velocity from the pressure record. The program takes each of the experiments in turn, reading the initial conditions from the experimental summary spreadsheet, and selecting the relevant experimental data files and BOMB program output files. This information is then passed to the *bvcalc* subroutine, which performs the calculations.

The pressure data file contains pressure data sampled at a rate of 10 kHz, for a pre-set number of samples, which if chosen correctly will continue past the peak pressure. Recorded pressure is relative to the initial pressure. Therefore, the first step of *bvcalc* is to restrict the data to that occurring before the pressure peak, and add the initial pressure to the datum pressure recorded. However, due to oscillation in the least significant bit recorded by the charge amplifier, and a 'dip' (attributed to HT noise from the spark) in the pressure, then the datum is taken to be the mean of the pressure measurements taken between 3 and 4 ms.

It is also necessary to filter the pressure trace with a low-pass filter to reduce noise which will be problematic during differentiation later in the routine. Filter parameters were kept the same as tested and used by Marshall (2010). For each data point in the filtered pressure trace, the mass fraction burned corresponding to the pressure is obtained by interpolation from the BOMB program output. Similarly, flame radius, temperature and ratio of specific heats of the unburned gas are obtained from interpolation. Burning velocity is then found from Equation (3.8). The value of initial radius r_i as given in Figure 3.1 is obtained from the interpolated value of mass fraction burned and Equation (3.9), and is also subsequently filtered to reduce noise when differentiated with respect to time.

As emphasised previously, it is important to exclude data that has been affected by cellularity. Similarly, the initial phase of combustion is subject to noise, and the small pressure rise leads to inaccurate determination of the burning velocity, and should be discarded. To enable the selection of the range of data to be included, the plot of burning velocity against pressure is displayed on the axis in the *BVICS* GUI, along with a line representing the point at which cellularity was detected by *BVImage* (section 5.1.2.2). The user can then select the valid range of data by clicking on the plot in the GUI axes. If cellularity is not detected in the image sequence, then the end of the range is identified as the point where burning velocity begins to fall as heat transfer to the vessel begins to take place at high pressures.

The selected data is then sent back to *Burnvel*, where the data is concatenated into a single large data matrix. The information contained in the matrix is the same as from the *BVImage* program.

5.1.4 Fitcorr

The aim of this routine is to obtain a burning velocity correlation (section 2.4) for the data set, as a function of temperature, pressure, equivalence ratio and diluent fraction. The *fitcorr* routine, developed by Marshall (2010), and based on the procedure of Clarke (1994), used the version of the correlation given in Equation (2.41). The routine has been modified in this work

to be able to fit to an adapted correlation, based upon the findings of Konnov *et al.* (2011) that the temperature exponent has a second order dependency upon equivalence ratio. The modified form of the correlation is therefore extended to 14 terms as follows:

$$S_{\mathrm{u}} = \left[S_{\mathrm{u},0} + S_{\mathrm{u},1}(\phi - 1) + S_{\mathrm{u},2}(\phi - 1)^2 + S_{\mathrm{u},3}(\phi - 1)^3 + S_{\mathrm{u},4}(\phi - 1)^4\right] \times T^{\alpha} \times P^{\beta} \times \left(1 - \mu_1 x_{\mathrm{r}}^{(\mu_2 + (\phi - 1)\mu_3)}\right) \quad \textbf{(5.8)}$$

where

$$\alpha = \alpha_0 + \alpha_1(\varphi - 1) + \alpha_2(\varphi - 1)^2 \quad \textbf{(5.9)}$$

$$\beta = \beta_0 + \beta_1(\varphi - 1) + \beta_2(\varphi - 1)^2 \quad \textbf{(5.10)}$$

$$T = \frac{T_{\mathrm{u}}}{298} \; ; \; P = \frac{P_{\mathrm{u}}}{1.0} \quad \textbf{(5.11)}$$

The *fitcorr* routine determines the correlation coefficients for a data set by taking the output matrix from *Burnvel* and using the method of least squares minimisation. The function to be minimised is the sum of the squares of the difference between the natural logarithm of the burning velocity calculated from experiment and that from the correlation at the same conditions, with the given coefficients:

$$\sum \left(\ln S_{\mathrm{u,corr}} - \ln S_{\mathrm{u,exp}}\right)^2 \quad \textbf{(5.12)}$$

The minimisation of the above function is performed using the MATLAB unconstrained minimisation routine *fminunc*. This requires a set of coefficients initially from which to start the minimisation process, so a set of coefficients from a previous run on a similar fuel is used. Most fuels will show similar behaviour, and so this will give a good approximate starting point. Since the number of free variables is high, and the data sets are large, the algorithm for minimisation is structured into 4 steps to reduce convergence time:

1. Fit stoichiometric data with no diluents. This reduces the 14 term correlation down to just 3 terms, enabling quick convergence.
2. Still for the case of no diluents, 1 in 10 data points from the rest of the data set (now including non-stoichiometric mixtures) are fitted, starting from the case of updated coefficients from the first step. Therefore, 11 coefficients are now involved.

3. Using the updated coefficients from step 2, the minimisation is performed again on the whole data set without diluents.
4. Finally, the remaining coefficients are found by performing the minimisation on the entire data set including those with diluents.

The gradient vector and Hessian matrix are determined for the function in given in Equation (5.12) to help speed up the convergence. Once the 14 correlation coefficients have been found, the correlation for the whole data set is compared graphically (plotted in the axes in the *BVICS* GUI) against each experiment in turn to allow the user to assess the quality of the correlation fit across the data set. Analysis of the quality of fit to the experimental data is given in section 6.2.2.9.

5.2 Engine burn rate analysis (CoBRA)

A software package developed in MATLAB by Ma (2006) called CoBRA (Combustion Burn Rate Analysis) is used for burn rate analysis from pressure measurements in the optical engine. The package is run from a parent program OEDA (Optical Engine Data Analysis), which allows batch running of the analysis software for multiple experimental sets. This takes the data from ETCS, HDAQ and LDAQ and passes the relevant data to the CoBRA routine.

The CoBRA package allows calculation of mass fraction burned (mfb), which can provide burn rates for comparison with the measured laminar burning velocities from the combustion bomb experiments. The technique used for calculating mfb is based on that of Rassweiler and Withrow (1938), reported in texts such as Stone (2012). In this approach, the pressure rise during a given crank angle interval ($\Delta\theta$) is considered to be the sum of that due to combustion (Δp_c) and that due to the change in volume of the cylinder (Δp_v):

$$\Delta p = \Delta p_c + \Delta p_v \qquad \textbf{(5.13)}$$

The pressure change due to change in volume is found by modelling polytropic process with an exponent k. Considering incrementing from i to i+1, then

$$p_{i+1} - p_i = \Delta p_c + p_i \left[\left(\frac{V_i}{V_{i+1}} \right)^k - 1 \right] \quad \textbf{(5.14)}$$

allowing Δp_c to be evaluated directly. However, this will not be directly proportional to the mfb, since combustion is not taking place at constant volume, and so needs to be normalised relative to an arbitrary volume; the clearance volume at top dead centre (TDC) is used for this:

$$\Delta {p_c}^* = \Delta p_c \frac{V_i}{V_c} \quad \textbf{(5.15)}$$

The mfb can then be estimated assuming proportionality to this pressure rise. If the end of combustion occurs after N increments, then:

$$\text{mfb} = \sum_0^i \Delta {p_c}^* \Big/ \sum_0^N \Delta {p_c}^* \quad \textbf{(5.16)}$$

Data acquisition is performed using two separate systems, low speed (LDAQ) and high speed (HDAQ). LDAQ allows slowly varying engine parameters to be monitored whilst HDAQ enables combustion analysis by providing high resolution, of the order of 1 degree crank angle (CA). For combustion analysis, multiple cycles can be logged to account for cycle by cycle variations, and values of the mean, standard deviation and coefficient of variation (CoV, ratio of standard deviation to the mean) can be calculated.

6 Validation of results

In this chapter, the reliability and accuracy of results obtained from the experimental procedures are examined. This is broadly sub-divided into validation of experimental procedures and validation of data processing and modelling procedures.

6.1 Experimental validation

To validate the values of burning velocities determined from experimental measurements, it is necessary to both validate the direct measurements made during the experimental procedure, and investigate the sensitivity of the determined result to these direct measurements.

6.1.1 Experimental measurement sensitivity

Burning velocities determined from the constant volume technique will be expected to be sensitive to varying degrees to measurement errors during both the mixture preparation process and the combustion event itself. Sensitivity analysis with regards to the combustion pressure, initial pressure and initial temperature were performed previously by Marshall (2010) but will be briefly summarised below. Accuracy of mixture preparation is discussed in section 6.1.2 for both gaseous and liquid fuels.

6.1.1.1 Combustion pressure measurement

During combustion only two measurements are made, namely vessel pressure and time. The high sample rate and timing accuracy of the DAQ mean that the biggest error in measurement will be in the pressure measurement. Sensitivity analysis of this pressure measurement showed that a zero error of 1% of the full span (0.2 bar) had no effect on subsequently determined burning velocity, and a span error of 1% resulted in error in burning velocity of less than 0.4%.

6.1.1.2 Initial temperature and pressure

Errors in initial temperature would cause incorrect calculation of burning velocities due to the fact that the calculation would be performed using results from the constant volume combustion model at a different temperature. A 1% error in initial temperature for a mixture at a nominal initial temperature of 380 K was shown to give a corresponding error in burning velocity of around 1%. When the same analysis is performed for pressure for a mixture with 2 bar initial pressure, the error introduced by the incorrect pressure measurement is again found to be less than 1%.

6.1.2 Equivalence ratio/Mixture preparation

To ensure accurate results, it is of high importance that the mixtures are being prepared to a sufficient degree of accuracy. Inaccurate equivalence ratios will have a twofold effect; measured flame speeds will be plotted against incorrect equivalence ratios, and the equivalence ratio input to the BOMB program will not correspond to the actual mixture, introducing a further error into the measured burning velocity.

6.1.2.1 Pressure measurement error

It would be expected that for the gaseous fuel mixture preparation using the method of partial pressures, that there will be some error on equivalence ratio introduced due to error in the pressure measurement. Using values of pressure measured during the preparation of methane-air mixtures at both 380 K and 450 K, and the transducer resolutions given in section 4.1.5.1, the error was found to be no worse than +0.004 and -0.002 on equivalence ratio, which is acceptable.

6.1.2.2 Leak rate

A key potential cause of inaccuracies in mixture preparation is the effect of leaks from the bomb and associated pipework. Leaks during mixture preparation will see gas leaking either into or out of the vessel, depending on the pressure in the vessel. For the gaseous fuel

preparation method, this will result in a loss of control over the equivalence ratio of the mixture given that the various components are being added at different pressures. It would be expected that a higher leak rate would result in a leaner mixture, since the fuel is added early on in the procedure, meaning that leakage will see fuel leak out over the course of the mixture preparation. Whilst preventing all leaks is not possible, minimising the leak rate as much as possible was a high priority. The leak rate was calculated by filling the bomb and pipework to around 4.5 barA, recording the pressure drop over a 5 minute period and applying equation (6.1), which applies for the isothermal case:

$$p\dot{v} = \dot{p}v \tag{6.1}$$

Initially, the leak rate at 4.5 barA was around 0.3ml/s. This corresponded to a drop in pressure of around 0.04 bar, which corresponded to 12-15 lsb recorded by the pressure transducer. Given the length of the mixture preparation process, this was deemed too high to tolerate. At elevated temperatures this rate was higher still, presumably due to differential rates of thermal expansion introducing larger leaks at joins in the pipework and fittings. The most significant leaks were found by filling the vessel with helium and tracing with a helium detector. These were addressed although notably, a leak around the spark plug fitting remained. Despite this, the leak rate was found to be reduced to around 0.045 ml/s, or 1-2 lsb on the transducer reading. This has therefore reduced the error down to the order of the measurement error, meaning that it should no longer be of concern as far as mixture preparation is concerned since it has been shown in section 6.1.2.1 that such error will have minimal impact upon the equivalence ratio of the mixture.

Tests conducted for nominally stoichiometric mixtures at ambient temperature at the two leak rates showed a difference of 11-14% in burning velocity between the two runs. The difference in initial temperature between the two runs would be expected to introduce a difference of less than 4% if the temperature correlation suggested by Andrews and Bradley (1972) in Equation (2.18) is used, suggesting that the effect of the higher leak rate was indeed

significant. It was therefore important that throughout a set of experiments the leak rate was checked and any increases in leak rate were suitably addressed. The 5 minute settling time during the mixture preparation procedure was used to monitor the leak rate.

For liquid fuel preparation procedure the leak rate for the system was found to be higher, however this was due to leaks around the air heater and so will not have an impact upon the equivalence ratio of the mixture, as this is upstream of the point of fuel injection and due to the fact that the fuel is injected into the air stream, this leak will consist only of small amounts of air.

6.1.2.3 Fuel mass measurement

For liquid fuel preparation as described in section 4.1.6.2, it is necessary to measure the mass of fuel injected into the bomb to be able to determine the equivalence ratio of the mixture. From this mass the partial pressure corresponding to the amount of fuel added is calculated from Equation (4.38), allowing the partial pressure of air to be deduced from the total pressure upon mixing. In section 4.1.6.2, it was explained that each measurement of mass was estimated to have an error of no more than 0.0005 g. Therefore, for a single injection event, which requires two measurements of mass to be made, the maximum possible error is 0.001 g. In the cases where the injection requires 2 separate injections, this maximum error will increase to 0.002 g. As an example, for the case of a stoichiometric hydrous ethanol blend consisting of 20% water by volume at an initial temperature of 380 K, this error in mass measurement will be less than 0.2%, corresponding to an overall error on equivalence ratio of 0.002.

6.1.2.4 Effect of injection pressure

It was found that under the old liquid fuel mixing system where the fuel was injected into a separate mixing loop that the pressure at which fuel was injected had an impact upon the mass of fuel injected, and subsequently the equivalence ratio. Whilst the equivalence ratio is determined from the mass of fuel injected and hence this effect will not influence the accuracy of the determined equivalence ratio, it may be considered to have the effect of lessening control

over the composition of the mixture. Therefore, tests were also performed to check the effect of varying the pressure at start of injection for the new mixture preparation system.

Iso-octane was chosen as the fuel to be tested, and the volume to be injected was chosen to create a stoichiometric mixture at a temperature of 380 K. Injections were performed at 0.2 barA, 0.5 barA and 1.0 barA. It was decided that higher injection pressures were unwise due to the fact that lower pressures ensured against vaporising fuel leaking back out past the needle septum. Due to the same final target pressure and temperature being used, the volume of fuel to be delivered by the actuator was set at a constant volume of 812 μL. The injection duration was also set to be a constant 5 minutes. Figure 6.1 shows the results of three tests performed at each injection pressure, with both the mass of fuel injected and the corresponding equivalence ratio presented. It can be seen that the largest scatter occurs at 0.2 bar, but by 0.5 bar the scatter had dropped to around 0.004 g in the mass of fuel added. This variation in mass of fuel introduces a scatter of 0.01 on the equivalence ratio. Whilst the equivalence ratio is not solely dependent upon the mass of fuel injected, since other factors such as the exact partial pressure of air added (and measurement errors introduced elsewhere) are significant, the equivalence ratio does follow the mass of fuel closely. Using the results of this test, it was decided to begin injection of fuel at around 0.5 bar in experiments using the new liquid fuel preparation procedure, since the

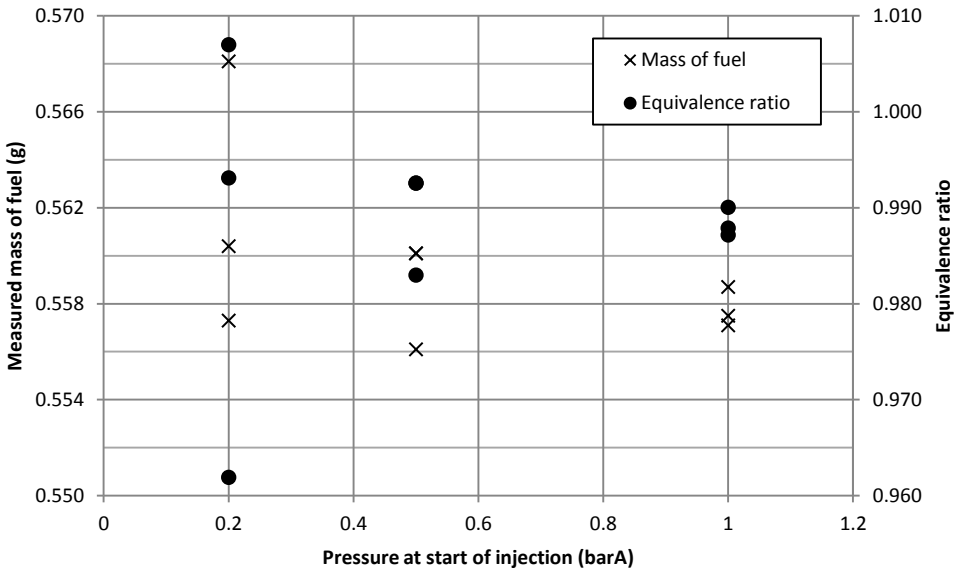

Figure 6.1 – Effect of pressure at start of injection upon mass of fuel delivered (crosses) and corresponding equivalence ratio (circles).

lower pressure is advantageous in ensuring vaporisation of less volatile fuels and reduces the risk of fuel leaks from the system.

6.1.3 Lambda sensor

The use of the lambda sensor as described in section 4.1.9 was investigated for consistency and reliability. Whilst in the previous work by Marshall (2010) good agreement was seen between the equivalence ratio determined by the lambda sensor and the expected equivalence ratio by either the partial pressure method in the case of gaseous fuels or the measured mass of fuel in the case of liquid fuels, a clear disparity was seen in the current work. For a selection of methane-air tests performed on mixtures in the equivalence ratio range 0.8 - 1.2 prepared using the partial pressure method, agreement was seen to be good for lean mixtures but a deviation was noted for stoichiometric and rich mixtures. This behaviour was found to be repeatable over a number of repeat tests and is apparent in Figure 6.2a. To determine whether this effect was specific to the ECM AFRecorder lambda sensor, a second lambda sensor manufactured by Innovate Motorsports was used for comparison. Aside from a small offset between the two sensors, the same behaviour was observed, as seen in Figure 6.2b.

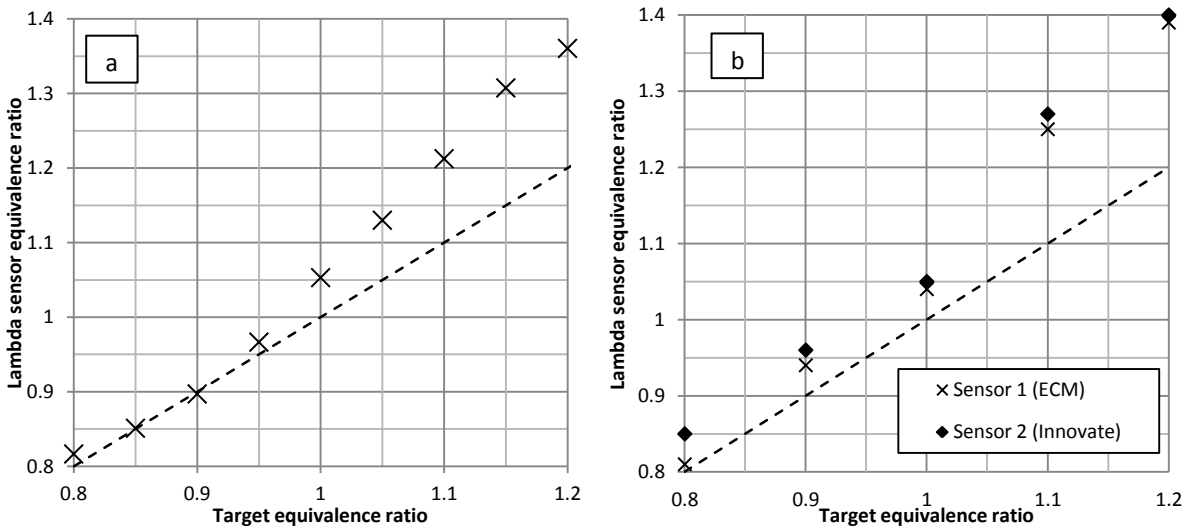

Figure 6.2 – Comparison between target equivalence ratio from the partial pressure method and equivalence ratio measured by lambda sensors for methane-air mixtures.

Due to the similarity in the behaviour of the two lambda sensors, it was determined that the fault was not specific to the ECM AFRecorder sensor. The possibility remained that the sensors

were reporting a correct result, and that the disparity occurred due to a procedural error in the mixture preparation procedure, resulting in richer mixtures being prepared than expected. Whilst this seemed unlikely due to the fact that precise measurements were made regarding the partial pressure of added gas (which were calculated to have negligible effect on the final equivalence ratio, section 6.1.2.1), and any effects of leaks (shown to be small in section 6.1.2.2) would be expected to cause the mixture to be leaner than expected due to the fact that gaseous fuel addition was performed at low pressures, the performance of the partial pressure mixture preparation system was compared against that of the MFC method. The results of both methods comparing the equivalence ratio measured by the sensor with the target equivalence ratio are presented in Figure 6.3. This clearly shows that the two methods are comparable, and that the deviation in the measured equivalence ratio from the target is not an effect of the mixture preparation procedure.

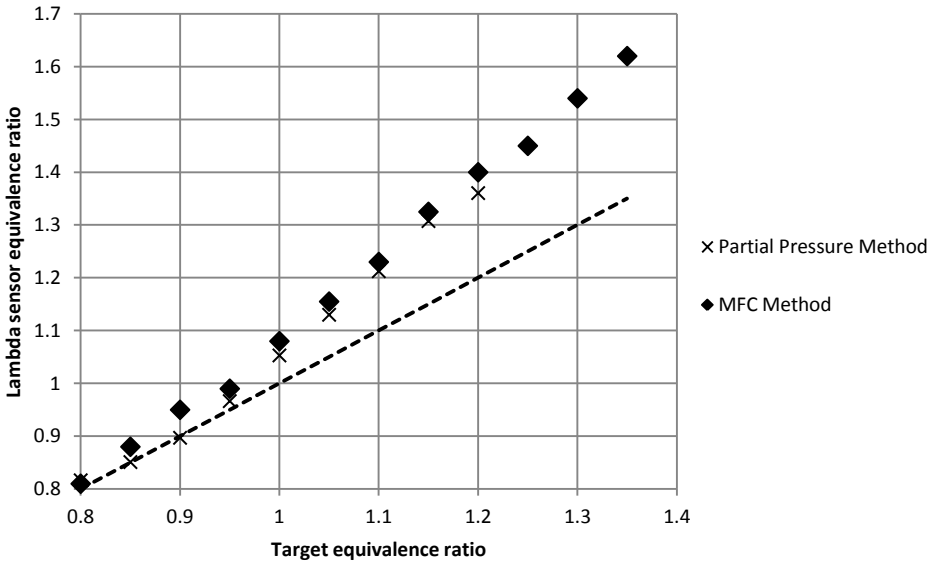

Figure 6.3 – Comparison between target equivalence ratio and equivalence ratio measured by ECM AFRecorder lambda sensor for methane-air mixtures by both partial pressure and MFC methods.

One explanation for the behaviour seen relates to the fact that the operation of the lambda sensor is different for the cases of lean and rich mixtures, as detailed in the Appendix, section A.1. In the case of exhaust gases from rich mixtures, the operation of the sensor requires oxidation of the partial products of combustion. These products will include CO and H_2 as well as unburned hydrocarbons. Oxidation of methane will be more difficult than for larger

hydrocarbons due to the high stability of the small molecule, meaning that the sensor reading is inaccurate for richer mixtures.

Further tests were performed using ethanol as the test fuel. Firstly, the equivalence ratios measured when using the two different liquid fuel delivery techniques were tested. For pure ethanol-air mixtures, no difference between the two methods was seen, validating the new mixture preparation layout. The new layout also allowed for the placement of the lambda sensor in different locations with respect to the bomb, to investigate the performance of the sensor in the different positions. Using the layout for liquid fuel delivery depicted in Figure 4.5 allows the movement of the vessel exhaust to the previous injection port in the mixing loop detailed in Figure 4.2, rather than in its original position on the manifold on the intake side. It was hypothesised that part of the issue is that the lambda sensor in the configuration for addition of gaseous fuel is located far from the bomb (see Figure 4.3), and whilst the sensor itself is heated, the gases reaching it will have cooled, affecting the result. Two positions for the sensor were trialled; one position approximately 2 m downstream from the bomb, connected by a length of nylon pipe, and a second where the sensor is located just outside the bomb chamber, with Swagelok connectors and the whole assembly insulated with Melafoam, to minimise heat losses from the gas. Figure 6.4 shows the results of tests performed for ethanol-air mixtures for a range of target equivalence ratios between 0.7 and 1.4. The equivalence ratio determined from the measured mass of fuel injected using the partial pressure from Equation (4.38), and that measured by the lambda sensor are plotted against the target equivalence ratio. Closed symbols represent tests performed with the sensor in the original position, and open symbols are tests with the sensor in the new position just outside of the bomb chamber. The equivalence ratio determined from the mass of fuel is seen to match closely to the target equivalence ratio, showing good control over fuel delivery, although inevitably there is more scatter than seen with gaseous fuels. Discrepancies will be due to small variations in either the amount of fuel or air added, but these will be logged during each experiment, and will only be expected to give

rise to a deviation in equivalence ratio of up to 0.01. As with the gaseous fuel preparation system, as the equivalence ratio is increased beyond stoichiometric, the difference between the theoretical equivalence ratio and that measured by the lambda sensor increases, with the sensor reporting a richer mixture than expected. This discrepancy also appeared larger when water was included in the fuel for testing of hydrous ethanol mixtures. For the experiments where the sensor was moved to the insulated position closer to the bomb, this discrepancy appears to be reduced, supporting the theory that the problem is the application of the sensor, which is designed to operate on hot exhaust gas flows at high flow rates. Since the volume of gas being tested is very low, flow rates past the sensor will be very low, and the gas temperature will be low compared with that experienced by a similar sensor in an engine exhaust, despite the sensor being heated.

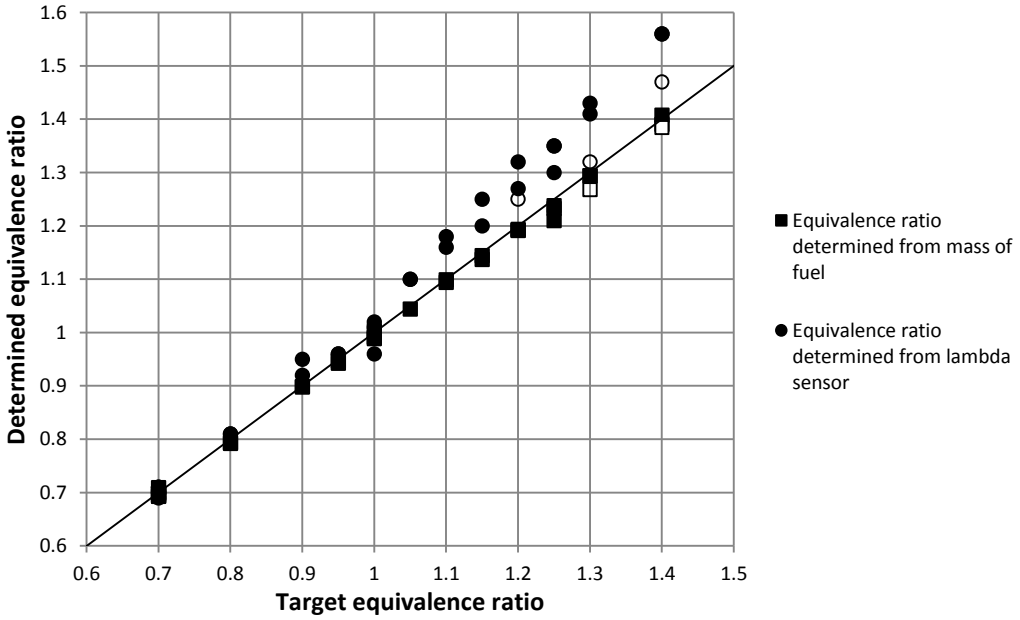

Figure 6.4 – Comparison of equivalence ratio determined from mass of fuel added and measured by lambda sensor against target equivalence ratio for ethanol-air mixtures. Solid symbols represent the original sensor position; open symbols represent the closer sensor position.

Considering these findings regarding the lambda sensor, it was decided to base the value of equivalence ratio on that based upon the partial pressure of fuel and air for gaseous fuels, and the measured mass of fuel for liquid fuels. The lambda sensor is used to check for larger than expected discrepancies, which would indicate a problem with the mixture preparation and a need to repeat the test.

6.1.4 Experimental consistency

Having investigated the sensitivity of the mixture preparation and combustion processes to various measurements, it is necessary to check for repeatability of results.

6.1.4.1 Repeat tests

Due to the time consuming nature of the mixture preparation procedure, and the large number of tests required per data set resulting from the need to test over a wide range of equivalence ratios at a number of different initial temperatures and pressures, full repeats of all experiments were not performed. To check for repeatability of results, repeat experiments were performed for stoichiometric biogas mixtures prepared by the partial pressure method. The biogas mixtures used were 80% CH_4 and 20% CO_2 at initial temperature and pressure of 380 K and 2 bar. This condition was chosen as it is representative of an experiment within the centre of the data range. Five repeats of the test at this condition were performed, and the pressure derived burning velocity for each experiment was calculated. The burning velocity against pressure curves for the five repeat tests are shown in Figure 6.5, and demonstrate very good repeatability. Similar tests were performed using the liquid fuel preparation procedure for mixtures of iso-octane and ethanol, with comparable results.

6.1.4.2 Mixing time

The mixture preparation procedure for gaseous fuels contained a 5 minute mixing time, during which the mixture was left to ensure homogeneity before being reduced down to the final pressure. The wait time of 5 minutes was chosen following tests by Marshall (2010) showing that this was sufficient. However, there were no details of whether a further time delay was introduced following the removal of mixture to obtain the desired P_0. Whilst the remaining mixture would be expected to remain homogeneous, it may no longer be stationary, which

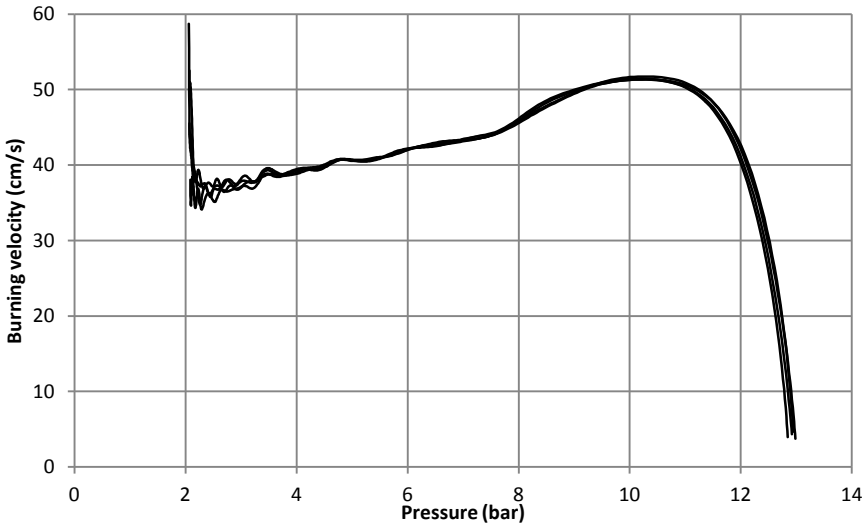

Figure 6.5 - Burning velocity against pressure for 5 tests of stoichiometric biogas-air mixtures (80% CH_4, 20% CO_2) with $T_0 = 380$ K, $P_0 = 2$ bar.

could have an effect on the flame propagation. A succession of tests was performed, with additional delay times of 1 - 10 minutes introduced. No noticeable change in burning velocity was seen as a result of introducing this time, since the mixture pressure was being reduced at a slow rate. Therefore a nominal 1 minute period was chosen for all tests.

6.2 Data analysis validation

With the accuracy of the direct measurements and the sensitivity of subsequently determined burning velocities to these measurements satisfied, it is next important to assess the accuracy and performance of the data analysis procedures. This includes the routines used by the *BVICS* package described in section 5.1 for determination of burning velocity by both the pressure record and flame front imaging methods. The performance of the correlation fitting routine is also assessed.

6.2.1 *BVICS* routines

6.2.1.1 BOMB program

The BOMB program is described in section 5.1.1, and is used in a format unchanged from its previous use by Marshall (2010), where performance of the program has been covered and so is simply summarised here.

The performance of the BOMB program was checked by comparing the output with that of the simpler linear model proposed by Lewis and von Elbe (1961). Whilst a difference in the mass fraction burned versus pressure curve was noticed, this is as reported elsewhere and is a result of the over-simplification of the linear method, and the otherwise close agreement demonstrates reliable performance of the BOMB program. The program was also shown to compare to simple equilibrium programs such as STANJAN and Gaseq. Whilst a discrepancy with the analytical method of Luijten and De Goey (2007) is seen, as explained previously in section 3.1.5.5 the assumption of constant specific heats, neglecting of the effects of dissociation, and the need to specify the theoretical end pressure account for this difference.

6.2.1.2 Burnvel

The *Burnvel* routine for calculating the burning velocity from the pressure trace using the analysis in section 3.1.4, was checked for accuracy by generating an artificial pressure trace to correspond to a constant burning velocity, which was then passed to the *Burnvel* program as if it were experimental data, Marshall (2010). The artificial pressure trace was based upon the linear mass fraction burned model, and so the *Burnvel* output differed slightly from the expected constant pressure. Even so, the error was generally less than $0.5\,\mathrm{cm\,s^{-1}}$ with the biggest difference occurring at lower pressures.

6.2.1.3 BVImage

The *BVImage* routine to determine flame speed and detect the onset of cellularity is based upon the ability to detect the position of the flame front using the algorithm described in section 5.1.2. As explained previously, the schlieren front will vary in thickness, requiring adjustment of the pin-hole depending on experimental conditions. Therefore it cannot be expected that the image brightness will remain constant across all experiments. In terms of detection of the flame front, the algorithm has an automatic threshold adjustment to respond to differing image brightness; however it remains important to ensure that the measured radius is consistent. To demonstrate this, experiments for methane-air flames were selected at a range of conditions to

overlay the radius determined from *BVImage* on the raw image files. Figure 6.6 shows two images from a stoichiometric methane-air mixture at 400 K and 1 bar, overlaid with the flame front position determined by *BVImage* (red), and the inner edge of the schlieren front (green). It can be seen that the algorithm consistently represents the outer edge of the schlieren front; this is also seen for image sequences with thicker schlieren fronts and with differing brightness levels. In this representative case, the green circle is a consistent number of pixels within the red. The centre of the schlieren front is hence found to be 0.6 mm within the outer edge detected by *BVImage*. Since this is an approximately constant value, the determined flame speed (represented by the rate of change of radius) is unaffected, although the corresponding stretch rate expressed by Equation (2.54) will have altered. Therefore the extrapolation will yield potentially different unstretched flame speeds and burned gas Markstein lengths. For the same example, the difference in unstretched flame speed is only 0.1cm s^{-1} (0.03%), and the change in unburned gas Markstein length is 0.0004 cm (approximately 8%, although for such values close to zero, percentage differences will be potentially misleading). This demonstrates that the potential error introduced by the flame front detection system is consistently of negligible magnitude. However, it is also important to consider the potential error introduced by the difference between the schlieren front and the flame front position defined by Bradley *et al.* (1996), described in section 2.2.3. This relates the cold front radius to the schlieren radius

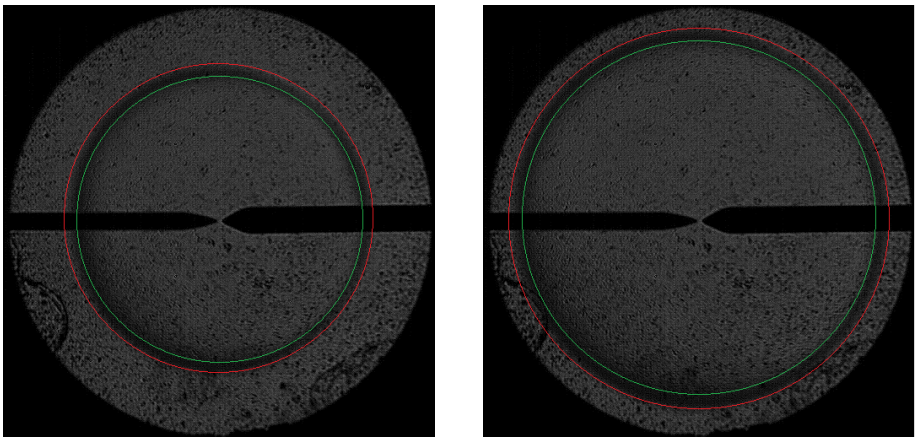

Figure 6.6 – Images from a stoichiometric methane-air mixture at 450 K and 1 bar. The red circle represents the radius as determined by *BVImage*; the green circle indicates the inner schlieren edge.

through the flame thickness. Figure 2.3, adapted from Andrews and Bradley (1972) shows the flame thickness of atmospheric methane-air flames for a range of equivalence ratios, with flame thicknesses between 1 and 2 mm. Note that whilst this demonstrates that flame thicknesses will only vary slightly for the equivalence ratios tested in this work (between 0.7 and 1.4), this does not directly correspond to the definition of flame thickness used in Equation (2.14), which uses a characteristic hydrodynamic length. In their assessment of the difference between cold front and schlieren front radii, Bradley *et al.* (1996) state that for their methane-air mixtures the difference is slightly less than 0.25 mm for stoichiometric mixtures and slightly more for rich and lean mixtures. Using values of density and kinematic viscosity from the Gaseq equilibrium solver, a similar value is easily demonstrated. Given that the distance between the detected radius and the centre of the schlieren edge was seen to be around 0.6 mm in the current investigation, then this difference can be assumed to add negligible error; the difference between the fronts is within the observed schlieren thickness, although the fact that the value of radius determined by *BVImage* relates to the outside of the schlieren edge will tend to reduce the error on flame speed and burned gas Markstein length compared to the values reported previously. Therefore it can be concluded that the detection of the flame front does not introduce significant error.

More difficult to quantify is the error introduced by the extrapolation procedure. Due to the limited optical access, in all cases a linear extrapolation of the flame speed to conditions of zero stretch is appropriate. Figure 6.7 shows some extrapolations for the case of ethanol-air mixtures at 2 bar and 380 K, which all demonstrate a linear trend. As seen in section 2.5.6, use of a linear extrapolation when non-linear behaviour is exhibited results in an over-prediction of the unstretched burning velocity. Therefore, for mixtures with a higher Markstein length, there will inevitably be some over-prediction of unstretched burning velocity, which cannot be quantified due to the inability to apply a non-linear fit to the available flame speed data. However, by ensuring that measurements made at small flame radii are excluded from the extrapolation as

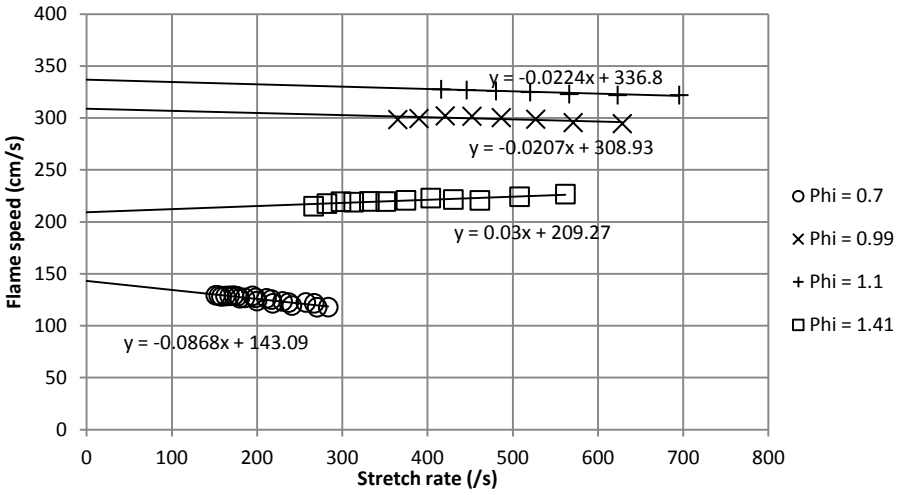

Figure 6.7 – Sample extrapolations for mixtures of W0 at $p_u = 2$ bar, $T_u = 380$ K.

suggested by Halter *et al.* (2010), the error introduced relative to the non-linear extrapolation can be reduced to around 10% for the worst affected mixtures.

Chen *et al.* (2009) developed the CCFS method (section 2.5.6) to account for compression effects in constant pressure combustion. For their example vessel with radius of 6 cm, they showed that the error is less than 5% for a flame radius of 40% of the vessel radius. In the current work, that would correspond to a radius of 3.2 cm, which is substantially greater than the radius of the windows, so compression effects can be ignored here.

6.2.2 Correlation fitting

Burning velocity data obtained using the pressure rise during constant volume combustion is fitted to a correlation due to the data from a single experiment corresponding to a wide range of pressures and temperatures. Data from all experiments within a set are fitted to a single correlation, meaning typically tens of thousands of data points are used in the fitting process. It is therefore important to assess the quality of the correlation fit to ensure that the determined coefficients are accurately fitting the data for all conditions of temperature, pressure and equivalence ratio.

6.2.2.1 Correlation form

The form of the correlation used as given in Equation 5.8, was chosen by combining the correlation developed by Marshall (2010) with the findings of Konnov *et al.* (2011) regarding

the temperature dependence of burning velocity with equivalence ratio. It is necessary to confirm that this form of the correlation is appropriate for describing the observed behaviour.

6.2.2.1.1 Equivalence ratio dependence

Marshall (2010) showed that the correlation with a 4th order dependence upon equivalence gave satisfactory fit to modelling data provided by Heghes (2006), when compared to 3rd or 5th order fits. This was checked in the current work by comparing the plotted correlations to individual data points, and again the 5th order correlation appeared to give little improvement in fit to the data, and so it was decided to continue to use the 4th order term.

6.2.2.1.2 Temperature and pressure dependence

Following the work of Konnov *et al.* (2011), the temperature dependence was modified so that the temperature exponent was a second order function of equivalence ratio rather than the linear dependence used previously. Figure 6.8 shows the temperature exponents obtained for the biogas correlation when the first and second order forms were used. The second order term seems consistent with the first order form used previously in the literature, showing that the use of this form does not produce unrealistic results. The same comparison is made for the pressure exponent and the results are given in Figure 6.9. It should be noted that the temperature and pressure exponents are each independent of both temperature and pressure.

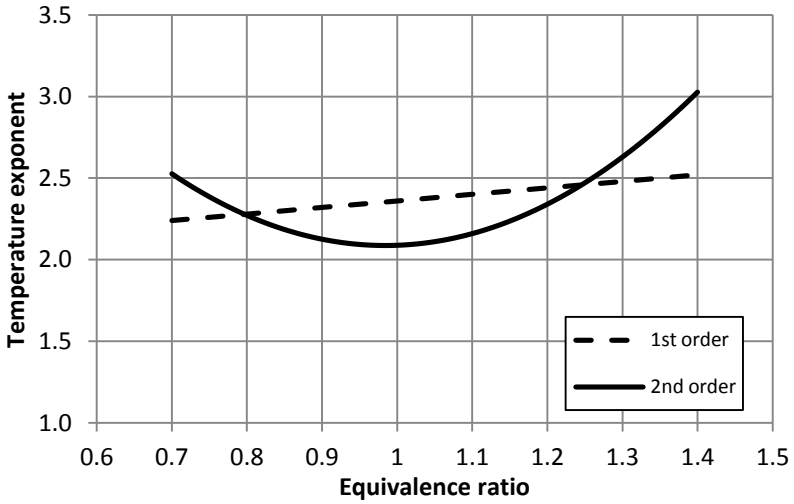

Figure 6.8 – 1st and 2nd order temperature exponents for the biogas correlation.

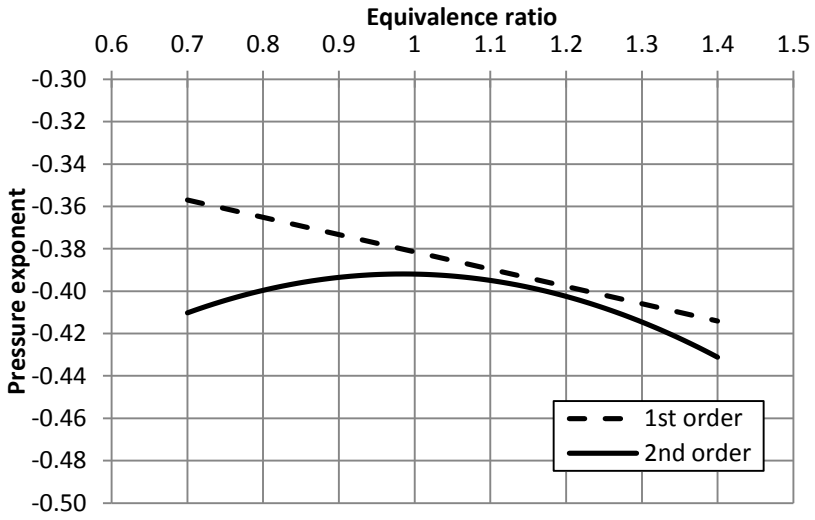

Figure 6.9– 1st and 2nd order pressure exponents for the biogas correlation.

Temperature exponents containing a temperature term and pressure exponents containing a pressure term, as shown in Equation (2.24) were trialled by Marshall (2010), though the inclusion of these dependencies made little difference to the obtained result.

The correlation developed by Vancoillie *et al.* (2012), Equation (2.46), to represent the results from a kinetic model by Li *et al.* (2007) uses a temperature exponent that is a function of equivalence ratio and pressure, including cross-terms resulting from what the authors noted to be a strong interaction between the variables. Figure 6.10 shows the temperature exponent described by Equation (2.47) using the correlation coefficients obtained by Vancoillie *et al.* (2012). This plot shows differing trends for lean and rich mixtures, with the temperature exponent increasing with pressure for lean mixtures, but decreasing with pressures for rich mixtures. This suggests that such complex fits for the temperature exponent are required to accurately represent the behaviour. However, given the range of pressures and equivalence ratios for which experimental data is collected, the effect of pressure on the temperature exponent would be expected to be small, and would not accurately be able to express the behaviour seen at higher pressures. This acts as sufficient justification for not including this cross-dependence in the correlation used in this study to express the temperature and pressure dependence of burning velocity.

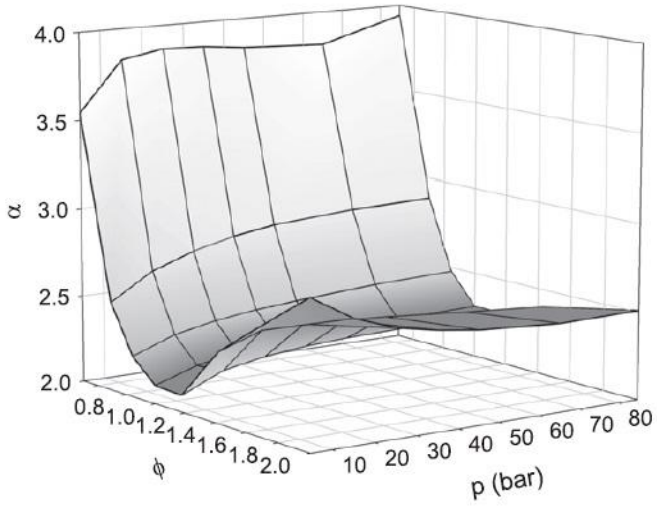

Figure 6.10 – Temperature exponent for ethanol-air mixtures for a range of pressures and equivalence ratios. Taken from Vancoillie *et al.* (2012).

6.2.2.2 Eliminating cellular data

As explained in section 2.6.4, the onset of cellularity results in an increase in the burning velocity as determined with the constant volume vessel technique, meaning that such data should not be included in the data set. The *BVImage* routine contains a cellularity detection algorithm described in section 5.1.1.2 to assist with data selection. Due to differences in darkness of edges in the schlieren images, resulting from slight differences in the schlieren system (as well as the variation in flame thickness and density gradients for cases where experiments were performed at different temperatures and pressures), the thresholding of the edge detection algorithm needed to be checked for each data set. The timing of onset of cellularity was checked against the image sequences to ensure it was behaving correctly. Apart from a few cases where the schlieren edges were faint, and in the case of very slow flames, the algorithm was found to be accurately representing the onset of cellularity, ensuring that no data from cellular flames was included within the data set.

In some cases the precise onset of cellularity can be hard to detect, for example when it occurs early in the flame propagation. Such flames appear cracked from the outset, before full cellularity occurs, meaning the precise point of onset is harder to determine. Marshall (2010) showed that greater selectivity made a difference to the burning velocity correlation compared to when only clear cellular data was excluded for the case of a n-butane data set. This

demonstrated the importance of strong selectivity when fitting data to the correlation, and so such an approach was used when cellularity occurred early in the flame propagation.

6.2.2.3 Eliminating buoyant data

Section 2.7 described how for slow flames, buoyancy effects causing flame distortion could result in inaccurate values of burning velocity being determined, dramatically reducing the range over which data can be obtained. From the schlieren images, the presence of buoyancy was clear to see in the slowest flames, such as in Figure 6.11 which shows a rising flame kernel in the case of a rich biogas (60% methane, 40% CO_2) flame at 4 bar initial pressure. Techniques for eliminating buoyancy, such as creating a microgravity environment with a drop tower were not available, and so the approach taken was simply to remove data affected by gravity. Ronney and Wachman (1985) found that for cases where the burning velocity was greater than 15 cm s^{-1} the effect of buoyancy was negligible. Therefore, data points corresponding to burning velocities slower than this were removed. This inevitably leads to less data for extremely rich or lean mixtures at lower temperatures, particularly when high levels of dilution are used.

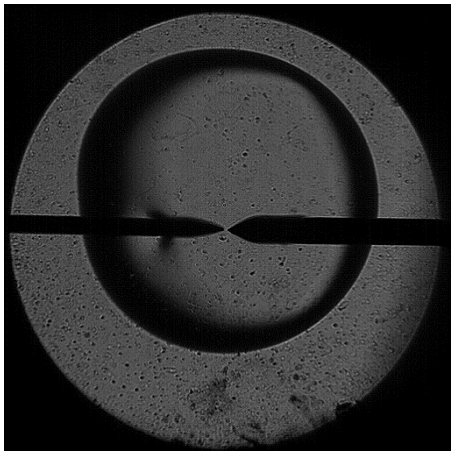

Figure 6.11 –Propagation of a biogas (60% CH_4, 40% CO_2) flame, T_0 = 380K, P_0 = 4 bar, ϕ = 1.4, showing the effects of buoyancy on flame front propagation.

6.2.2.4 Avoiding false minima

The *fitcorr* algorithm used to fit the data to the correlation determines the coefficients using an unconstrained least squares minimisation of the function given in Equation (5.12) which represents the difference between a data point and the correlation at the same conditions. It is

therefore important to ensure that the solution onto which the fitting process converges is in fact a correct minimum of the function, and not just a local minimum. This is tested by running the correlation fit from a number of different start points (sets of initial coefficients from which the minimisation begins and proceeds), to check for any significant discrepancies. Provided all runs of the fitting process tend towards the same solution, it can be assumed that the correct minimum has been found.

6.2.2.5 Effect of uneven data sets

As a result of discarding data affected by cellularity, and the differing burning velocities of mixtures with different compositions, certain regions of the data set will be under-represented. Since the correlation fitting algorithm seeks to minimise the sum of the square of the difference between the natural logarithms of the data and the correlation, then necessarily every point is 'weighted' evenly. This could lead the fitting procedure to bias towards fitting regions where many points exist, and sacrifice the quality of fit where the data is sparser, since this will lead to a smaller overall error. Typically this will manifest itself as a split in terms of equivalence ratio, as the onset of cellularity is strongly dependent upon the Lewis number of the mixture, with the majority of the data points existing for either lean or rich mixtures.

A number of techniques have been trialled by Marshall (2010) in an attempt to improve the performance of the fitting algorithm in light of this problem. These techniques were trialled on an iso-octane data set, which suffered from a significant lack of rich data due to cellularity. As a result, the correlation did not accurately reflect the behaviour of rich mixtures. Techniques trialled included: splitting data into rich and lean sets and fitting correlations to each separately; piece-wise regression, splitting the set into discrete steps in equivalence ratio to get a single correlation segment without equivalence ratio dependence, and treating these as points to which a quartic in equivalence ratio can be fitted; applying a Gaussian process to output predictions at specified points; and reducing the size of the data sets to even out the distribution of points, which had the effect of deleting a large number of points in the lean, low pressure region. None

of these techniques worked particularly successfully, and the best method found to improve the form of the correlation was based upon only using data that fitted the criterion $p_u \times \varphi^2 < k$, where k is a constant that is chosen for the fuel under investigation such that the data set is balanced.

6.2.2.6 Accounting for lack of data at ambient conditions

Whilst most data in the literature is presented at ambient conditions of temperature and pressure, this region is missing data for the correlations obtained using the pressure rise method. This is due to the fact that even if tests at ambient conditions are performed, the burning velocity cannot be deduced from the pressure record until there has been appreciable pressure rise, due to the levels of noise in the early burn phase. Additionally, for many fuels that are liquid at ambient conditions, it is not possible to accurately produce the desired mixture since condensation of the fuel will occur, preventing tests from being performed at ambient initial conditions. The result of this is that any correlation results presented at these conditions will be extrapolations beyond the range for which it has been fitted to data. However, it is desirable for correlations to extend to these conditions, both to enable direct comparison with existing values in the literature, and also to ensure correct capturing of the temperature and pressure dependence; this latter point is important since the $S_{u,0}$ term in the correlation represents the ambient stoichiometric burning velocity, and the effects of temperature and pressure are described with reference to these conditions. Extrapolating the correlation beyond the range for which data was included can result in incorrect values being obtained. This can be seen when the 14 term biogas correlation (section 7.2.2) is plotted for pure methane at conditions of 298 K and 1 bar. Figure 6.12 compares the correlation with a small selection of results for methane at atmospheric conditions found in the literature. Vagelopoulos and Egolfopoulos (1994) use a twin flame counterflow technique; Hassan *et al.* (1998), Gu *et al.* (2000), Rahim *et al.* (2002) and Chen *et al.* (2007) use a spherical expanding flame with flame front imaging to determine burning velocity. A significant amount of data exists in the literature for burning velocity of

methane at ambient conditions, although a large amount of scatter remains. It is clear that having not included any data at these conditions within the data set to which the correlation is fitted produces a correlation which, when extrapolated to these lower conditions of temperature and pressure, leads to a significantly lower result than would be expected at these conditions, despite the scatter in the published values.

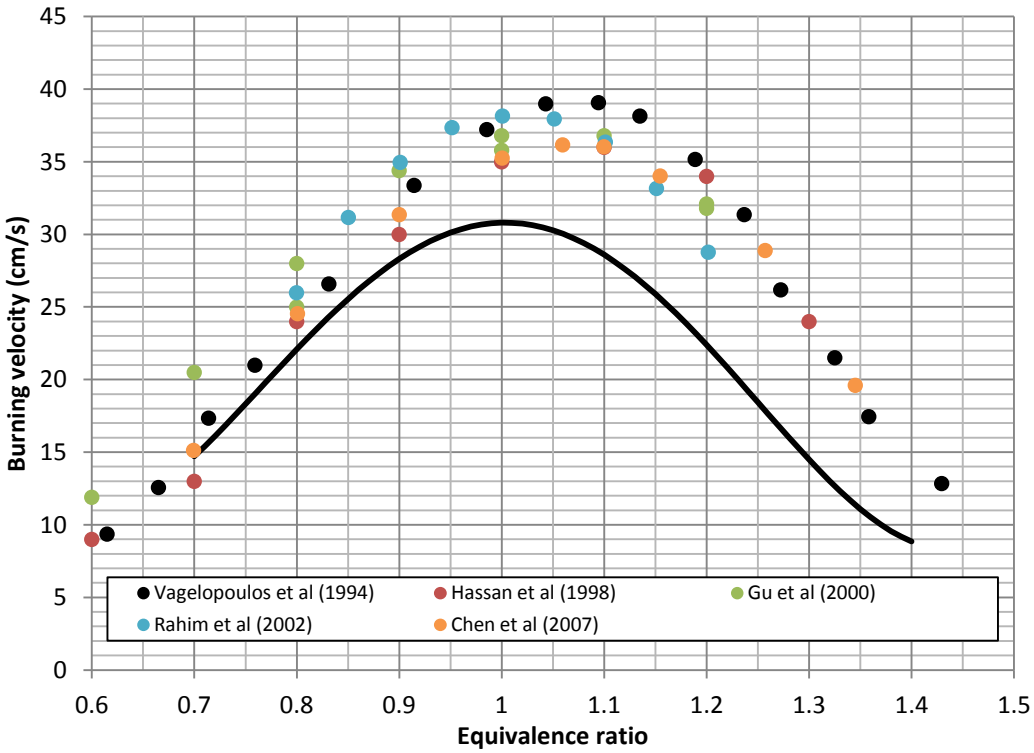

Figure 6.12 – 14 term biogas correlation (solid line) extrapolated for methane to 298 K and 1 bar, compared with existing results.

Since a significant amount of burning velocity data exists in the literature for methane at ambient conditions, it is possible to obtain data to include in the data set to assist with the correlation fitting at these conditions. For this to be successful, it is required that the correlation performance is improved at ambient conditions whilst for higher temperatures and pressures, the result should stay approximately the same. To provide the data at these conditions, the results of Gu *et al.* (2000) are added to the data set before fitting the correlation. This work was chosen as values were obtained with a careful correction for the effect of stretch, and rejection of values obtained during either the spark affected or cellular regimes. Data is presented at

ambient conditions, as well as elevated pressures of 5 bar and 10 bar, and temperatures of 360 K and 400 K.

In adding this data, a suitable weighting will need to be given to ensure an effect is seen. Each experiment performed in the work by Gu *et al.* (2000) gives a single data point, whereas each experiment using the pressure rise method results in many individual data points. For example, an experiment performed on a stoichiometric methane-air mixture at initial pressure of 1 bar and initial temperature 380 K will result in roughly 150 data points. For experiments with different flame speeds or onset of cellularity, this number will vary. In terms of the fitting algorithm, each point is weighted equally, so to appropriately weight the additional data the values are added multiple times. The effect of adding different numbers of points is demonstrated in Figure 6.13 and Figure 6.14, which show the correlation results for methane at 298 K and 500 K respectively, for a range of pressures. The solid lines represent the correlation without additional ambient data, whereas the dashed and dotted lines represent the addition of data from Gu *et al.* (2000) where 75 and 150 data points per experiment are used to ensure low pressure data in the set.

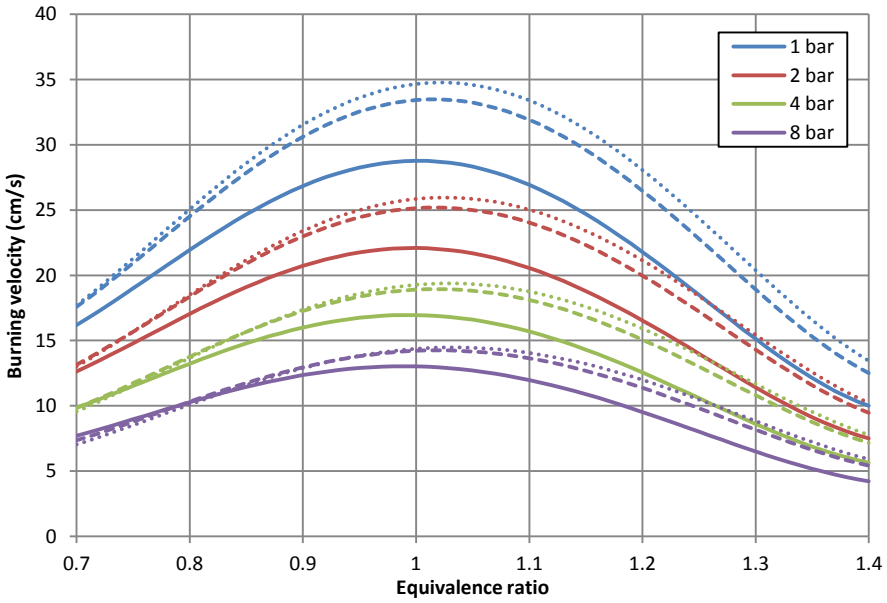

Figure 6.13 – Correlations for burning velocity of methane at 298 K at varying pressures. Solid lines represent the correlation without any additional data; dashed and dotted lines represent 75 and 150 points per experiment respectively added from the work of Gu *et al.* (2000).

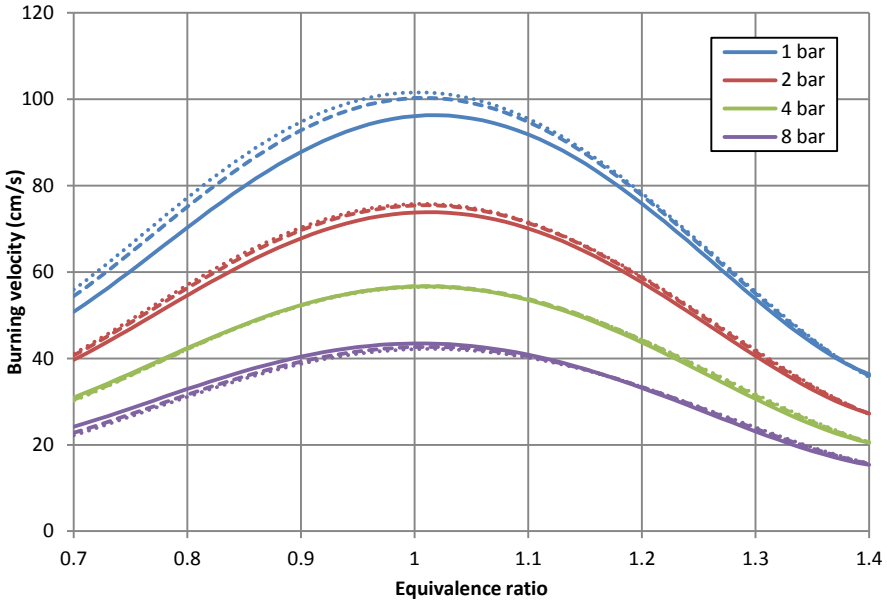

Figure 6.14 – Correlations for burning velocity of methane at 500 K at varying pressures. Solid lines represent the correlation without any additional data; dashed and dotted lines represent 75 and 150 points per experiment respectively added from the work of Gu *et al.* (2000).

From these plots, it can be seen that adding the low temperature and pressure data is to results in the correlation fit more closely to the expected values at these conditions when compared to Figure 6.12. For the 298 K case, it is clear that the additional data has the biggest effect on the correlation at lower pressures. This is to be expected since this is where the extrapolation in the correlation was greatest and so the fitting process is being improved most by the additional data. As the pressure increases, the effect diminishes, but is still noticeable since the correlation is still being extrapolated in terms of temperature. By contrast, in Figure 6.14 where the temperature is 500 K, extrapolation is only being performed in terms of pressure for the case where the correlation is being plotted at 1 bar. Hence for the other pressures, there is very little difference between the correlations for the two sets of data.

6.2.2.7 Correcting for stretch in pressure derived correlations

A potential problem with the correlation approach is that since the data used is from the pressure rise method, corrections will not have been made for stretch. The assumption of Andrews and Bradley (1972), which claims that for flames with radii greater than 50 mm the effect of stretch is negligible, suggests that this may not cause a significant problem, however

recent advances in the understanding of stretch and a need to quantify the effects of stretch more accurately calls for a check on this assumption.

Little data exists for values of unburned gas Markstein length L_u, since methods for measurement are not readily available; Markstein lengths obtained from the flame speed measurements using optical methods are referenced to the burned gas and so cannot be used to correct for stretch in burning velocity measurements made using the pressure rise method. The novel approach developed by Varea *et al.* (2012), outlined in section 2.5.6 provides a way of measuring this Markstein length, and presents limited data for methane, ethanol and iso-octane, using both linear and non-linear extrapolations. Varea *et al.* (2013) provides further data for unburned gas Markstein lengths for stoichiometric ethanol at varying pressures, shown in Figure 6.15. This data can be used to correct for stretch in the pressure derived burning velocity measurements of ethanol, and will serve as a way of assessing the impact of stretch on such measurements. From existing literature it is known that the Markstein length will vary greatly with equivalence ratio and pressure, with less dependence upon temperature (section 2.5.7).

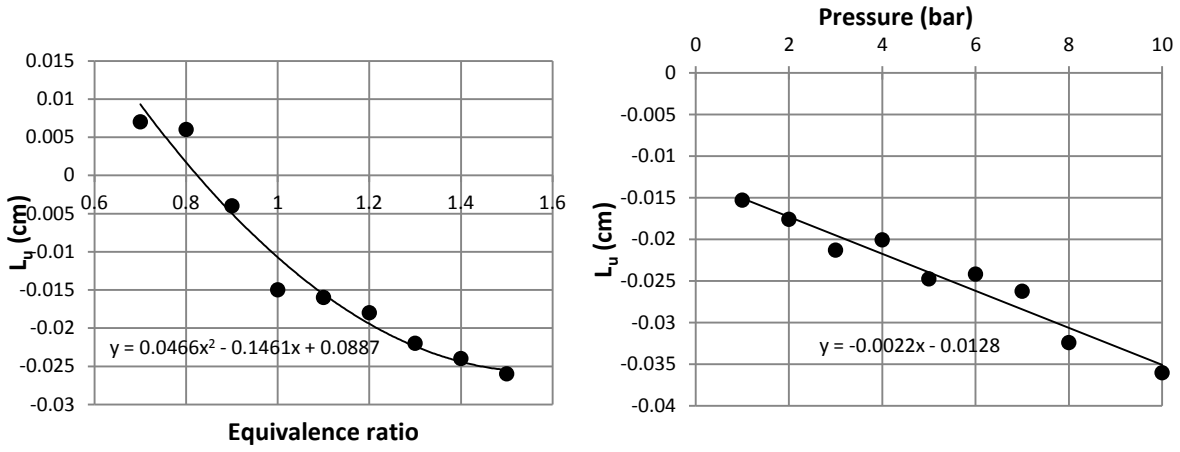

Figure 6.15 – Unburned gas Markstein lengths for ethanol from Varea *et al.* (2013). Left hand graph shows variation with equivalence ratio at 1 bar, 373 K; right hand graph shows variation with pressure for stoichiometric mixtures at 373 K.

By making the assumption that the Markstein length is completely unaffected by temperature, and that the effect of pressure is consistent across all equivalence ratios, an expression for unburned Markstein length with equivalence ratio and pressure can be obtained

by combining the fits to the experimental data presented in Figure 6.15 to form a single expression:

$$L_{\mathrm{u}} = 0.0466\varphi^2 - 0.1461\varphi + 0.0887 - 0.0022(P-1) \qquad \textbf{(6.2)}$$

The data matrix produced by the *Burnvel* routine contains information on the burning velocity, equivalence ratio, pressure and stretch rate for each data point. Therefore, using the linear relation between stretch rate and unburned gas Markstein length, it is possible to obtain a stretch-corrected burning velocity for each data point. In the case of the ethanol data set, the biggest difference in burning velocity seen when correcting for stretch was 3.3 cm s^{-1} on an unstretched burning velocity of 55.5 cm s^{-1}, which corresponded to an experiment where data with significant stretch rates were included, corresponding to a small flame radius, typically less than the 50 mm suggested by Andrews and Bradley (1972) as being sufficient to negate the effects of flame stretch. Only 1.9% of data points had a stretch correction of more than 2 cm s^{-1}, and only 15% greater than 1 cm s^{-1}. The effect of correcting for stretch on the correlation is checked by passing the corrected data to the *fitcorr* routine, and results are presented in section 7.3.2.

6.2.2.8 Quality of fit to raw data

The quality of the fit of the correlation to the raw data has been assessed by comparing the value of burning velocity at each point to the corresponding value from the correlation. In many cases, the calculated burning velocity from *Burnvel* contains some oscillations when plotted against pressure, so a polynomial is fitted to smooth out the fluctuations before assessing the error between the raw data and the correlation, as shown in Figure 6.16. This analysis will indicate regions of the data range where the correlation is not representing a close fit to the data. Figure 6.17 shows the percentage error resulting from fitting the hydrous ethanol correlation described in section 7.3.2, as defined by:

$$\text{Percentage error} = \frac{S_{\mathrm{u,corr}} - S_{\mathrm{u,exp}}}{S_{\mathrm{u,exp}}} \qquad \textbf{(6.3)}$$

where $S_{u,exp}$ is the value from the polynomial fitted to the determined burning velocity, and $S_{u,corr}$ is the value of the correlation at the same conditions.

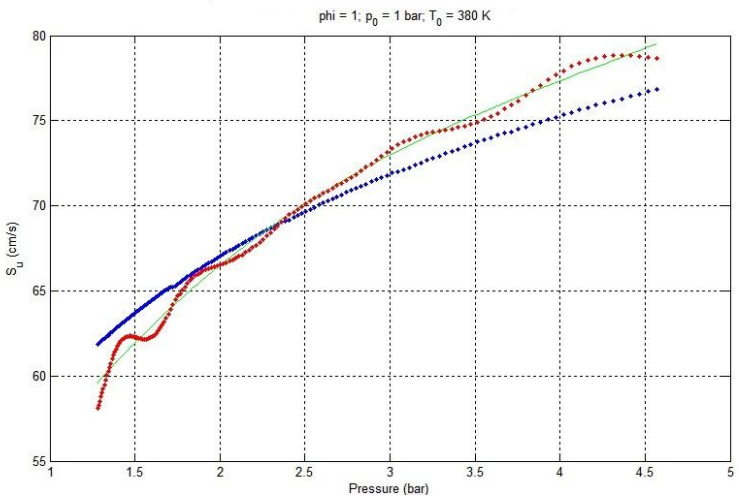

Figure 6.16 – Calculated burning velocity from a single stoichiometric ethanol-air experiment at 380 K and 1 bar (red points), polynomial fit to data (green line), and the correlations fitted to the whole data set (blue points) plotted at the same conditions of temperature and pressure.

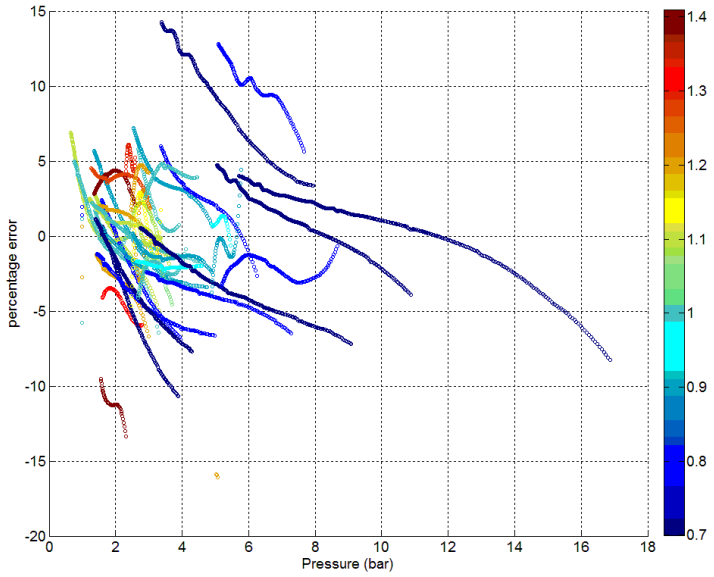

Figure 6.17 – Correlation error compared with experimental data for ethanol-air mixtures. Colour scale represents mixture equivalence ratio.

For most data points the error is seen to be within 5%, and appears to vary with pressure, with the correlation decreasing in value relative to the experimental data as pressure increases. The rate at which this effect occurs varies for each experiment, so it is not possible to use this to inform a general improvement to the correlation, but it can be shown that the deviation of the correlation from the experimental values is not limited to specific equivalence ratios or pressures.

7 Results

7.1 Overview

This chapter presents the experimental results; each fuel set is considered in turn, with an examination of the data set preceding the experimental results. For each fuel the burning velocity results from the image analysis and the correlations from the pressure rise method are presented and compared, with an evaluation of the performance of the correlations. Where possible, the results are compared with those available in the literature, and simulation results from the FlameMaster package. Markstein lengths and the onset of cellularity are also presented.

7.2 Biogas

Biogas (CH_4 and CO_2) mixtures have been tested for CO_2 fractions of 0%, 20% and 40% by mole, with the methane fraction described by the variable *X*. For example, pure methane is denoted as $X = 1.0$ and a biogas consisting of 60% methane and 40% CO_2 is denoted as $X = 0.6$. Note that this notation implies that the CO_2 is a diluent fraction within the fuel, and is not represented as a fraction of the overall fuel-air mixture, as is frequently seen elsewhere in the literature.

7.2.1 Data range

The biogas data set consists of a total of 32779 data points from 215 experiments, as shown in Table 7.1. Whilst a similar number of experiments were performed for each biogas composition, the number of data points and contributing experiments can be seen to decrease as the fraction of CO_2 in the biogas increases. This is due to the higher levels of dilution leading to slower burning flames, which become physically distorted due to the effects of buoyancy. As described in Section 6.2.2.3, data points corresponding to burning velocities of less than 15 cm s^{-1} were removed from the data set.

Table 7.1 – Number of experiments and data points included in biogas data set.

	Experiments	Data points
$X = 1.0$	79	14221
$X = 0.8$	54	11244
$X = 0.6$	31	7314

Tests were performed at initial temperatures of 298 K, 380 K and 450 K, initial pressures of 0.5 bar, 1 bar, 2 bar and 4 bar, and equivalence ratios between 0.7 and 1.4. The maximum and minimum values obtained are summarised in Table 7.2. Note that for the pure methane ($X = 1.0$) data, no ambient initial temperature data was collected. Also, whilst data was obtained for initial pressure of 0.5 bar, this was limited to a very small range of equivalence ratios, due to difficulties igniting rich and lean mixtures.

It is important to examine how the data is spread throughout the set, in terms of pressure, temperature and equivalence ratio, since these are the parameters to which the correlation is fitted and risks being skewed by particularly uneven distributions. Figure 7.1 shows the number of data points in each data set ($X = 1.0$, $X = 0.8$, $X = 0.6$ and the combined biogas data set), divided into brackets of equivalence ratio and pressure.

This shows that whilst there are variations in the number of points across the range of equivalence ratios tested, there is no particularly strong imbalance of data that would be expected to influence the correlation fitting. However, it can be seen that the pressure to which data extends is higher for rich mixtures than for lean mixtures. This is due to the onset of cellularity occurring earlier for lean and stoichiometric mixtures than for richer mixtures (see section 7.2.5), preventing data being obtained during the latter stages of combustion.

7.2.2 Burning velocity results

Results are obtained using both the flame front imaging and pressure rise methods though for much of the methane data set, experiments were run without schlieren photography, and only at 380 K and 450 K initial temperatures. A few repeat tests were made to obtain some limited

Table 7.2 - Minimum and maximum conditions in the biogas data sets.

		X = 1.0		X = 0.8		X = 0.6	
Property	Unit	Min	Max	Min	Max	Min	Max
T_0	K	380	450	298	450	298	450
P_0	barA	0.5	4.0	0.5	4.0	0.5	4.0
φ		0.70	1.40	0.70	1.30	0.70	1.20
P_u	barA	0.638	16.4	0.66	13.4	1.23	12.1
T_u	K	394	652	329	665	349	648
S_u	cm s^{-1}	15.6	106	15.4	92.1	15.6	68.3
S_f	cm s^{-1}	25.1	351	17.0	285	27.1	183
α	s^{-1}	7.13	148	5.91	147	7.05	77.8
r_b	mm	37.3	77.5	37.9	77.8	44.5	77.4
t	ms	16.1	159	16.1	155.4	25.4	123

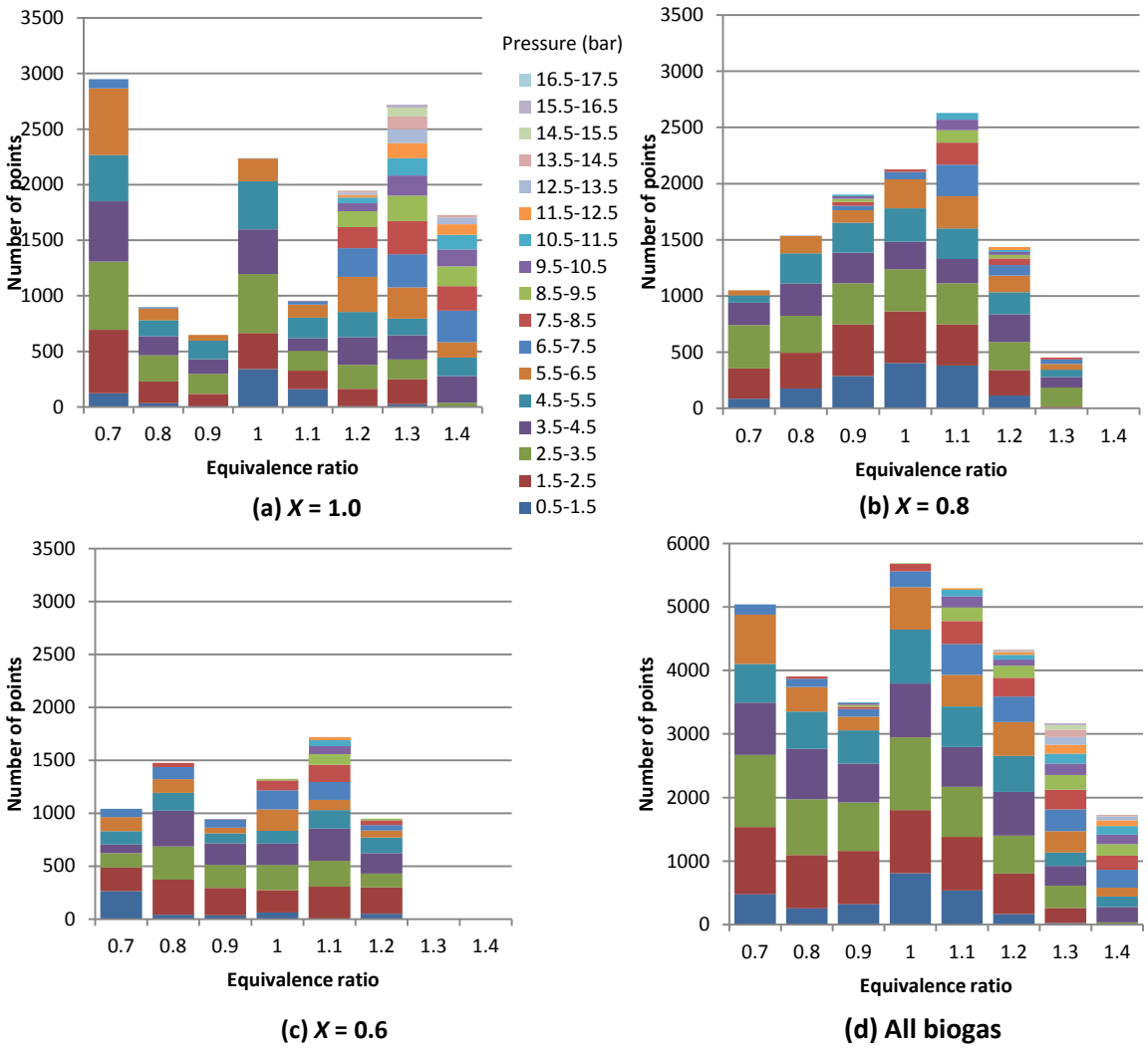

Figure 7.1 – Number of data points in each pressure and equivalence ratio bracket for a) X = 1.0, b) X =0.8, c) X = 0.6 and d) the entire biogas data set.

schlieren data. For the mixtures diluted with CO_2, tests were also performed at ambient conditions, although in many cases the low flame speeds resulted in heavily distorted flame fronts. Linear extrapolation of the stretched flame speed (where sphericity of the flame front is sufficiently undistorted by buoyancy) gives values of flame speed and Markstein length as described in section 5.1.2.1. Example flame speed extrapolations for methane-air mixtures at 4 bar and 450 K are presented in Figure 7.2. Unstretched burning velocities are calculated from the unstretched flame speeds by multiplying by the density ratio.

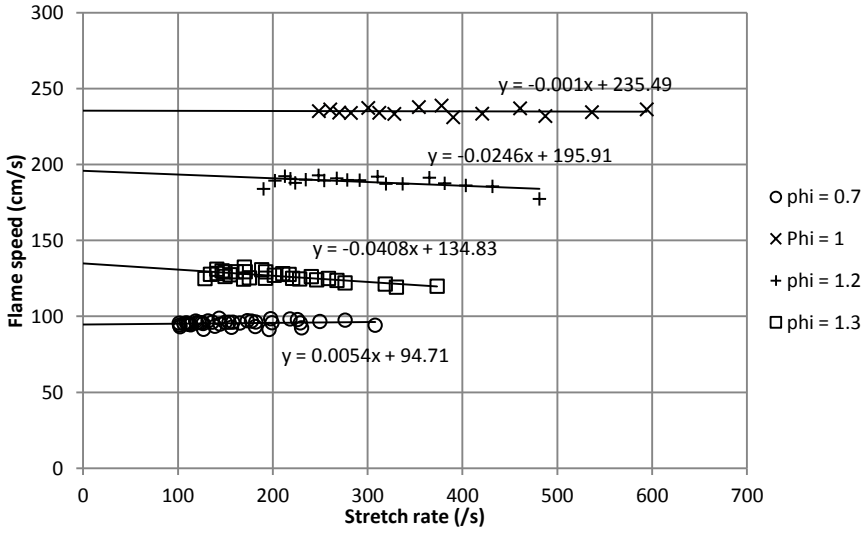

Figure 7.2 - sample extrapolations for methane-air mixtures at $p_u = 4$ bar, $T_u = 450$ K.

The biogas correlations use the 14 term form, with second order dependence on equivalence ratio for both the temperature and pressure exponents. The fraction of CO_2 in the biogas is represented by the x_r term in Equation (5.8). Correlation A corresponds to the correlation without additional ambient data from Gu *et al.* (2000), whereas Correlation B includes the ambient data as described in section 6.2.2.7. The correlation coefficients are given in Table 7.12 at the end of this chapter.

The results from both methods are shown for biogas mixtures in Figure 7.3 to Figure 7.5, along with the results of chemical kinetic modelling using the FlameMaster package. The GRI 3.0 mechanism has been used, which is a widely used mechanism for methane-air flames. In setting up the simulations, a 1D premixed flame solver is used, with the molar concentrations of the reacting species set to control the stoichiometry and mole fraction of CO_2. The

mechanism is optimised for methane-air flames, and so including additional CO_2 in the mixture allows assessment of the mechanism performance for higher CO_2 concentrations

Figure 7.3 shows the results for methane-air mixtures ($X = 1.0$), at 2 and 4 bar, and 380 K and 450 K. As expected, the two correlations show better agreement between each other at higher temperatures and pressures. In general, good agreement is seen between the schlieren and pressure derived results, although agreement is better with the correlation including ambient data. Considering the peak burning velocity, at 2 bar the correlation including ambient data agrees very closely with the modelling results, although the peak burning velocity occurs closer to stoichiometric; at 4 bar the correlation gives a slightly higher peak burning velocity than the modelling results, but agrees well with the image analysis results.

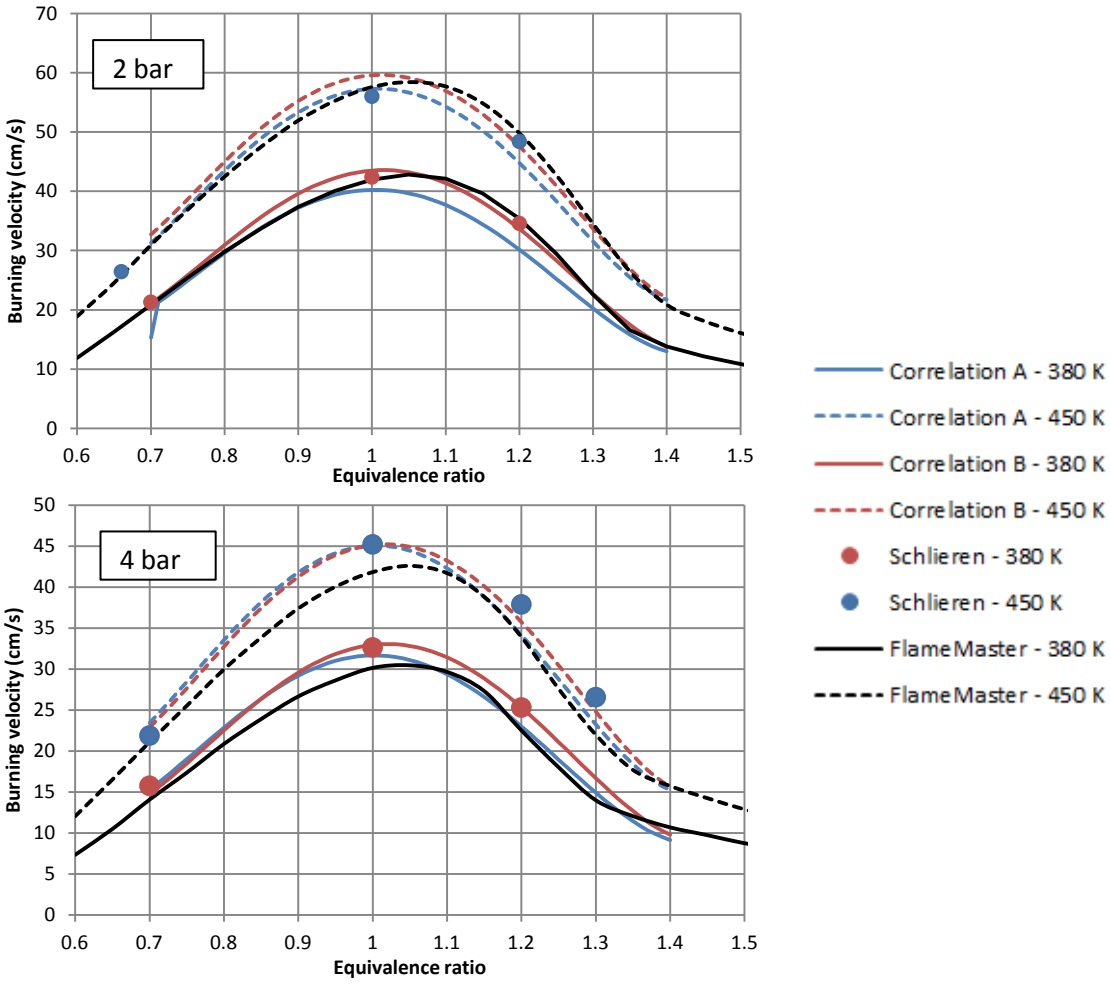

Figure 7.3 - Burning velocity of $X = 1.0$ at 2 bar and 4 bar. Lines represent the correlations and modelling results; points represent results from schlieren image analysis. Correlation A corresponds to the case where no additional data is included, correlation B includes ambient data from Gu *et al.* (2000).

Figure 7.4 shows the results for $X = 0.8$, for which experiments were performed at 298 K in addition to 380 K and 450 K. Again, agreement between the two correlations is better at elevated temperatures and pressures. Modelling results give the same peak burning velocity but again suggest that this occurs at a richer stoichiometry than the correlations. However, once again the trends shown by the schlieren data match those of the correlation more than the modelling results. Furthermore, whilst the differences are relatively small, the schlieren results are closer to the correlation that includes the ambient data when the correlations deviate.

Figure 7.5 shows the results for $X = 0.6$. Burning velocities are significantly slower here, which introduces larger errors into the measurements. Nevertheless, agreement between the schlieren and pressure measurements is still good. Peak burning velocities from the correlation appear to have shifted slightly lean of stoichiometric, and the modelling results also suggest a

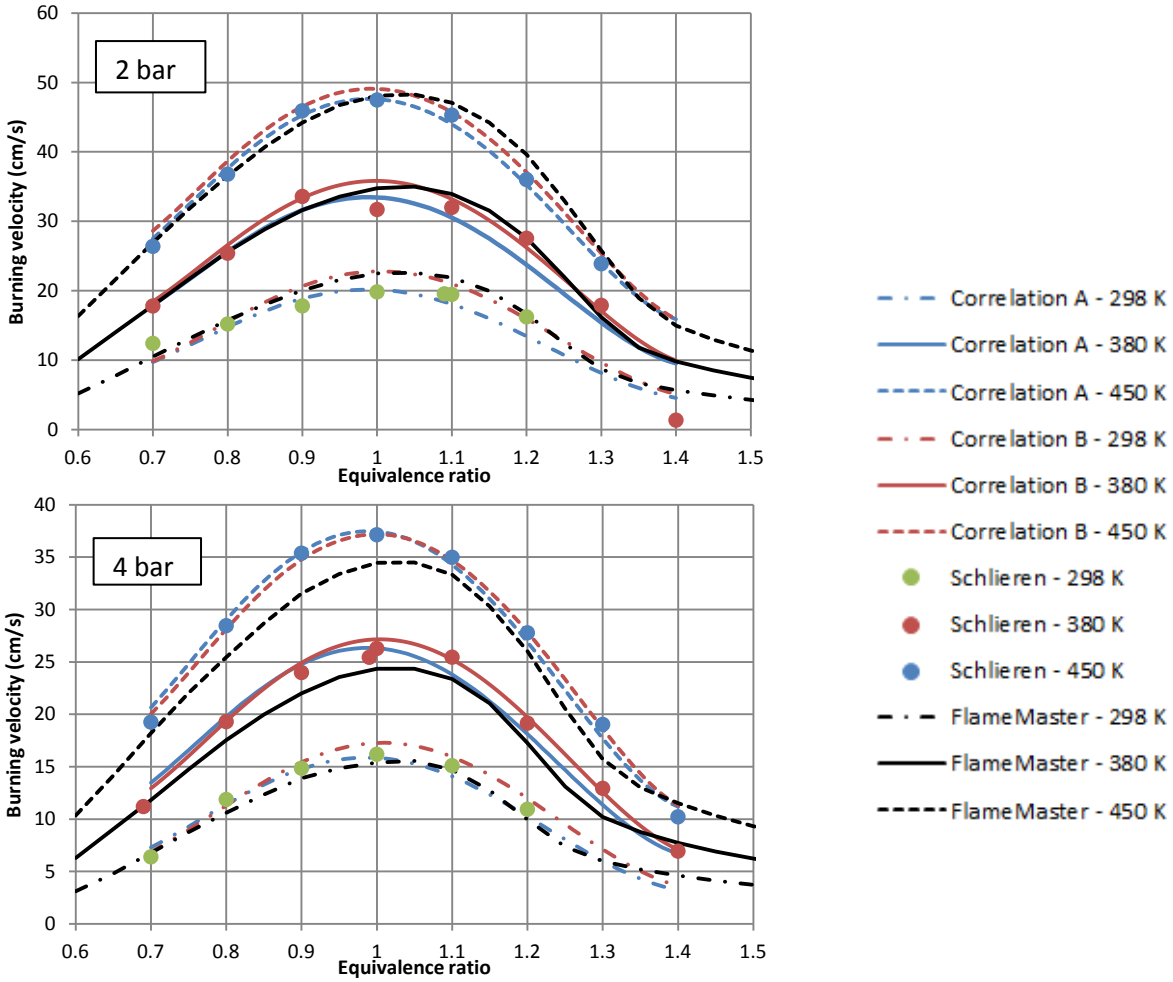

Figure 7.4 - Burning velocity of $X = 0.8$ at 2 bar and 4 bar. Lines represent the correlations and modelling results; points represent results from schlieren image analysis. Correlation A corresponds to the case where no additional data is included, correlation B includes ambient data from Gu *et al.* (2000).

shift of peak burning velocity towards lean mixtures. The schlieren results do not offer sufficient resolution to precisely locate the peak burning velocity, although it still appears to be very close to stoichiometric. Again, the modelling results suggest burning velocities of around 2 cm s^{-1} less than the experimental results at 4 bar, although this is equivalent to the error for pure methane-air mixtures, and so suggests that the GRI 3.0 mechanism continues to work well when the CO_2 content in the mixture is increased.

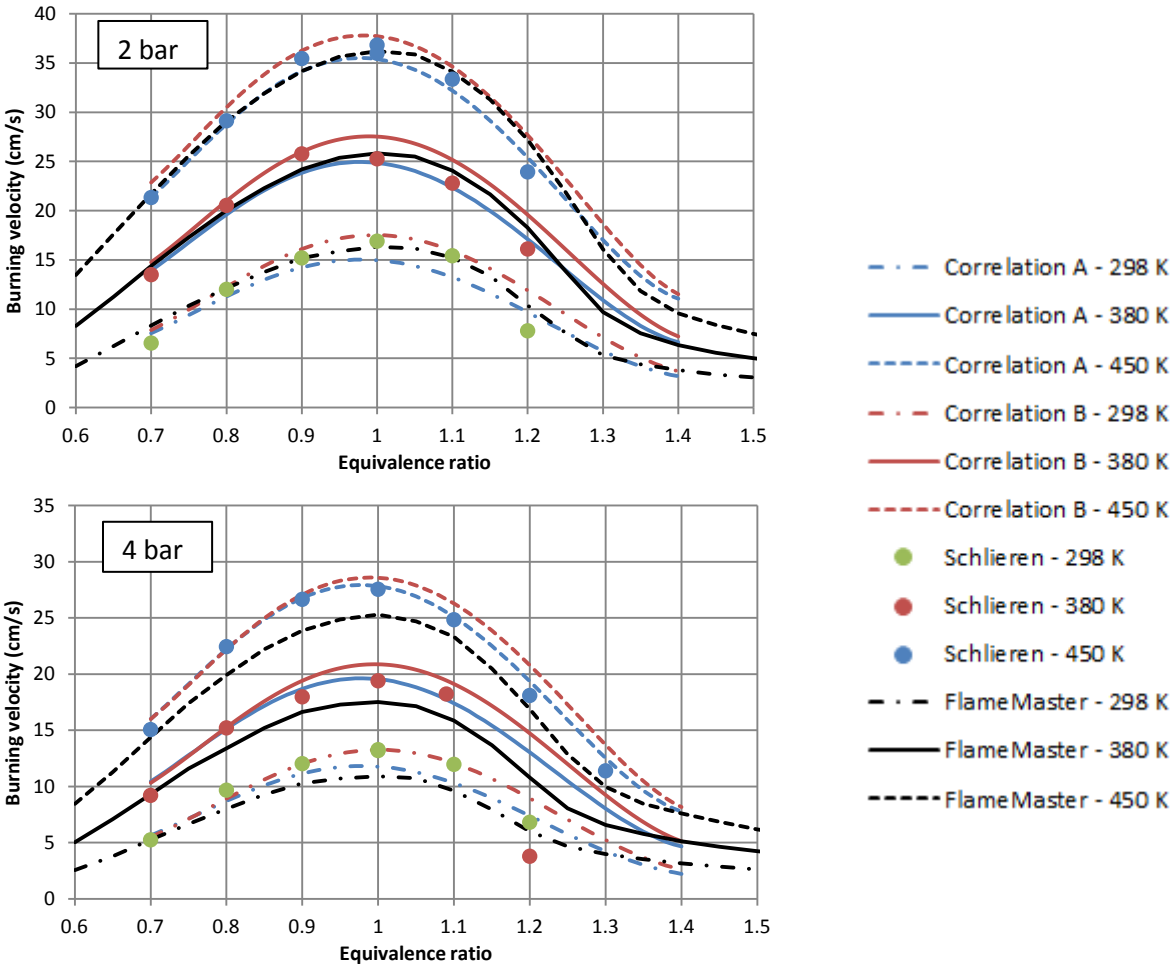

Figure 7.5 - Burning velocity of $X = 0.6$ at 2 bar and 4 bar. Lines represent the correlations and modelling results; points represent results from schlieren image analysis. Correlation A corresponds to the case where no additional data is included, correlation B includes ambient data from Gu *et al.* (2000).

Figure 7.6 directly compares mixtures containing varying CO_2 fractions at a fixed temperature and pressure of 450 K and 2 bar. Based on the correlation, for stoichiometric mixtures the $X = 0.8$ mixture has a burning velocity of 82% of that of pure methane-air and the $X = 0.6$ mixture 63% of that of pure methane-air. This shows that the reduction is roughly linear with mole fraction of methane. The results from FlameMaster agree well, with slightly more

variation based upon temperature and pressure, though at stoichiometric the X = 0.8 mixtures are consistently between 80% and 84% and $X = 0.6$ is 59% and 66% of pure methane-air mixtures. The increased variation is also partly due to the fact that the peak burning velocity appears to shift more in the modelling results than in the correlation. Nevertheless, it appears as though a linear dependence on mole fraction in the region of interest is still a good approximation.

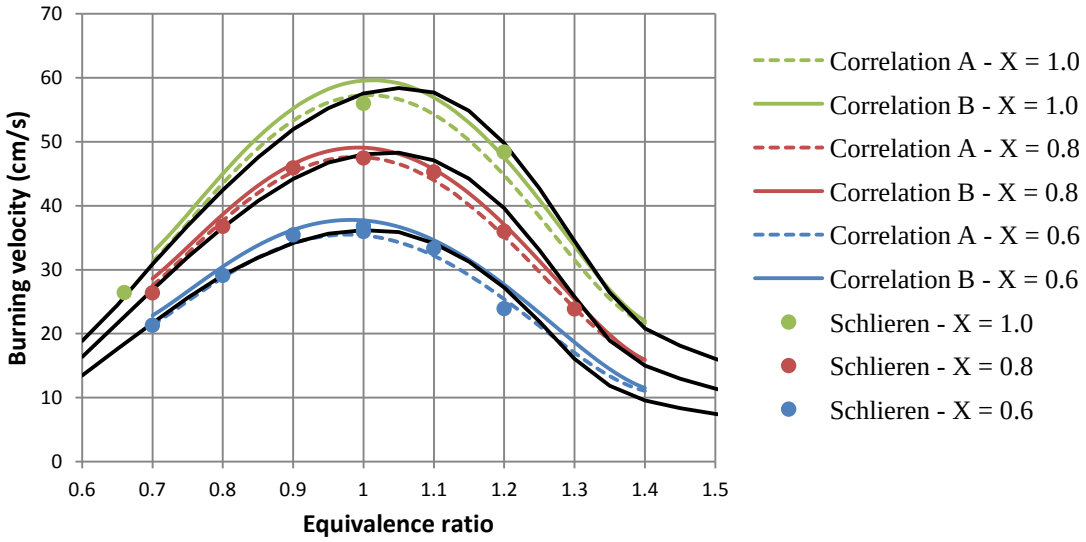

Figure 7.6 – Burning velocities of biogas-air mixtures with varying mole fraction of CO_2 at 450 K and 2 bar. Correlation A corresponds to the case where no additional data is included, correlation B includes ambient data from Gu *et al.* (2000).

Correlation A is plotted against equivalence ratio at elevated conditions of temperature and pressure; Figure 7.7 shows the 14 term biogas correlation plotted for pure methane-air mixtures ($X = 1.0$), at $T_u = 500$ K with varying pressure and $p_u = 5$ bar with varying temperature. Figure 7.8 and Figure 7.9 show the correlations for $X = 0.8$ and $X = 0.6$ respectively at the same conditions.

The trends in burning velocity with temperature and pressure shown by the correlation match those expected, with an increase with temperature and a decrease with pressure. The peak burning velocity occurs very slightly on the rich side of stoichiometric, with a small shift towards stoichiometric as the pressure increases. The shapes of the biogas curves closely follow those of the pure methane, and the trends with respect to pressure and temperature are similar since the exponents of temperature and pressure are not dependent upon the fraction of CO_2 in

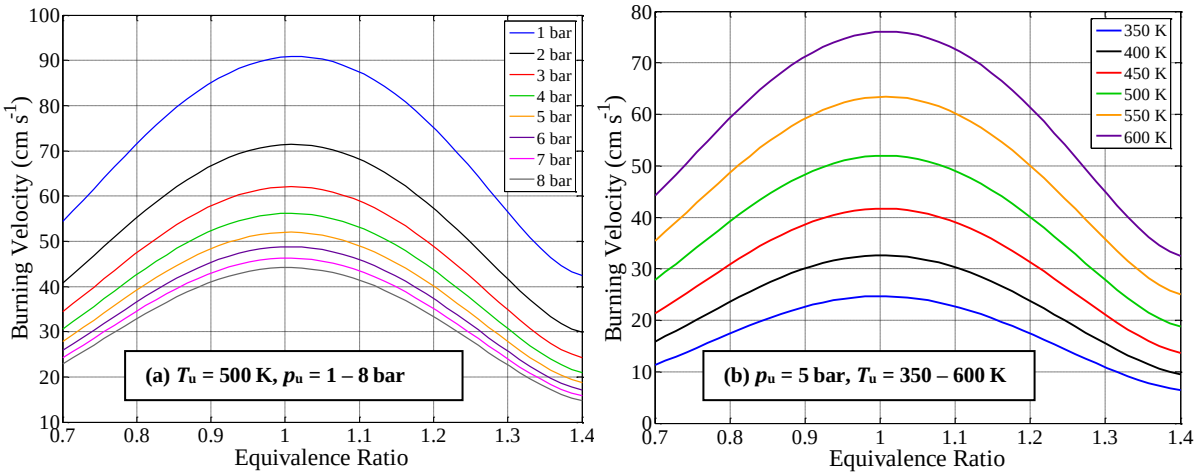

Figure 7.7 - Correlation for $X = 1.0$ at conditions of (a) $T_u = 500$ K and (b) $p_u = 5$ bar.

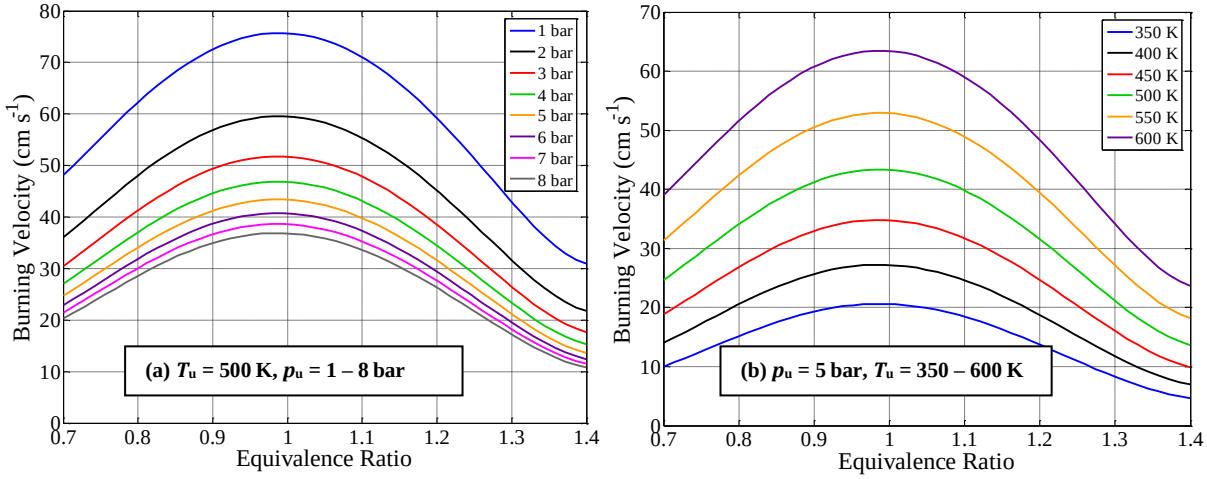

Figure 7.8 – Correlation for $X = 0.8$ at conditions of (a) $T_u = 500$ K and (b) $p_u = 5$ bar.

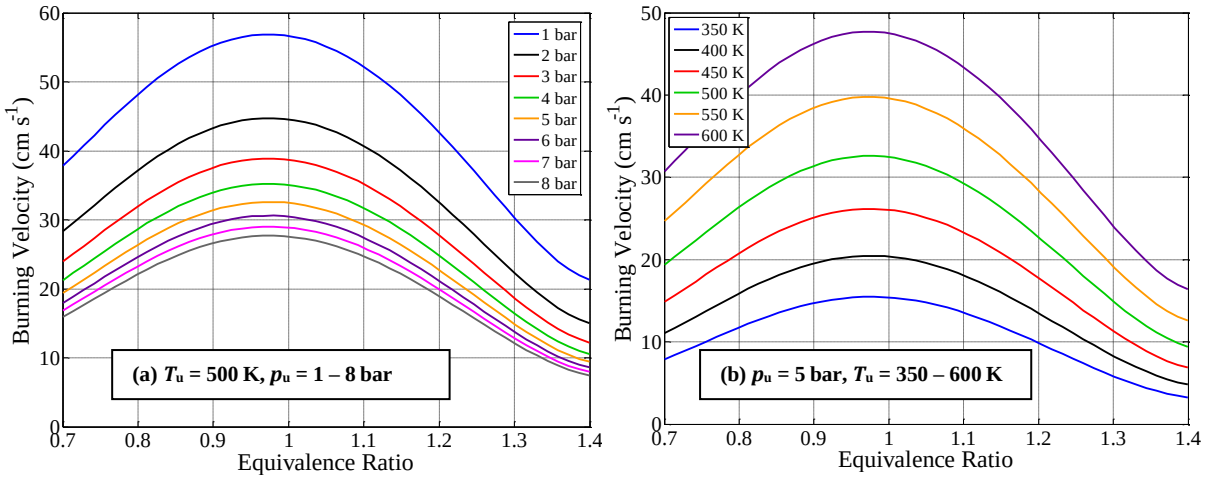

Figure 7.9 - Correlation for $X = 0.6$ at conditions of (a) $T_u = 500$ K and (b) $p_u = 5$ bar.

the fuel. However, we do see that the peak in burning velocity is shifted slightly towards the lean region as the fraction of CO_2 is increased. This is seen more clearly in Figure 7.10, which shows the effect of increasing the fraction of CO_2 in the biogas at conditions of $T_u = 500$ K and

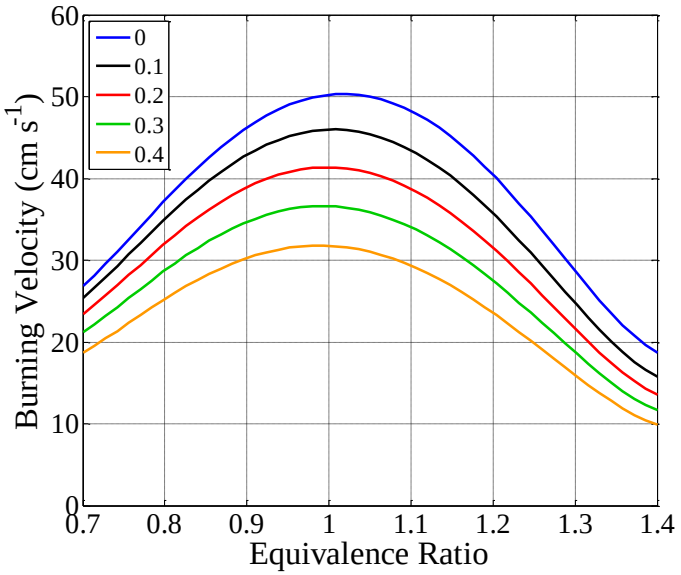

Figure 7.10 – Biogas correlation for varying CO_2 fraction at conditions of $T_u = 500$ K and $p_u = 5$ bar.

$p_u = 5$ bar. The peak in burning velocity is seen to shift towards the lean region as the fraction of CO_2 is increased.

7.2.2.1 Temperature and pressure exponents

As detailed in section 2.3.2, work by Konnov *et al.* (2011) showed that the temperature dependence of the burning velocity of ethanol-air flames is non-linear with equivalence ratio, prompting the use of a second order exponent in the correlation in Equation (5.8). The same form has also been used for the pressure exponent. It should be noted that the temperature and pressure exponents are each independent of both temperature and pressure.

The temperature exponent as determined by *fitcorr* is plotted in Figure 7.11, along with the results from previous work in the literature. The correlation form used is that obtained with the inclusion of the additional low temperature data from Gu *et al.* (2000), since this is expected to give the temperature exponent that fits the best across the full range of temperatures. Sharma *et al.* (1981) plotted values of burning velocity against temperature on a logarithmic scale for a variety of pressures, and took the average gradient to find the temperature exponent at each equivalence ratio, fitting the relationship in Equation (2.19). Iijima and Takeno (1986), Stone *et al.* (1998), Takizawa *et al.* (2005) and Marshall (2010) obtain a linear exponent of the form given in Equation (2.38). Only the work of Liao *et al.* (2004) uses a second order exponent; the

technique used only utilises the constant pressure stage of combustion in a constant volume spherical vessel, so this exponent is obtained by performing tests at various initial temperatures, fitting a power law curve to the data at each tested equivalence ratio, and fitting a second order dependence upon equivalence ratio to the determined power law coefficients. Note also that the tests of Liao *et al.* (2004) were performed using Chinese natural gas-air mixtures, which were claimed to be only 96.16% CH_4 by volume, with 2.54% CO_2, 1.096% C_2H_6, and the remainder composed of a combination of C_3H_8, C_4H_{10}, C_5H_{12}, H_2S and N_2. Figure 7.11 shows a slightly higher value of temperature exponent than seen elsewhere, but demonstrates the same trend with respect to equivalence ratio as demonstrated by Liao *et al.* (2004). The results of Stone *et al.* (1998) and Marshall (2010) show significantly different trends, showing how the second order term is needed to capture the temperature dependence.

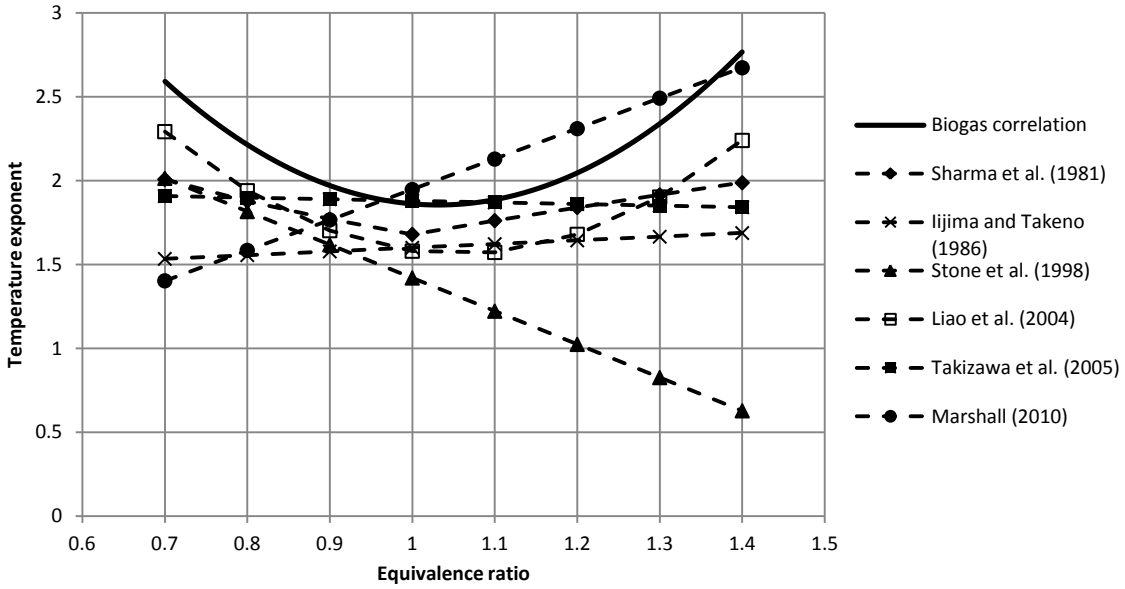

Figure 7.11 – Temperature exponent for biogas correlation compared with existing values from literature.

Figure 7.12 shows the pressure exponents obtained compared with those from elsewhere in the literature. Again, it can be seen that the shape closely reflects that of Liao *et al.* (2004), and along with the opposing trends of Stone *et al.* (1998) and Marshall (2010), it appears that a second order term for the pressure exponent is required to accurately describe the behaviour. The work of Goswami *et al.* (2013) investigates the effects of pressure on burning velocities of methane-air mixtures using the heat flux method. There is close agreement with the pressure

dependency determined by the biogas correlation, aside from the discontinuity in the rich region. This is also seen in the modelling results from the GRI 3.0 mechanism as presented by Goswami *et al.* (2013), and is attributed to competing reactions involving the CH_3 radical; in rich mixtures the relative reaction rates of the competing reactions are pressure dependent, and lead to the non-monotonic behaviour seen in the pressure exponent. Clearly this behaviour cannot be captured with a simple second order dependency in a correlation, although the close agreement elsewhere with the biogass correlation suggests that the more general behaviour is being represented well, and only modest adjustment is necessary.

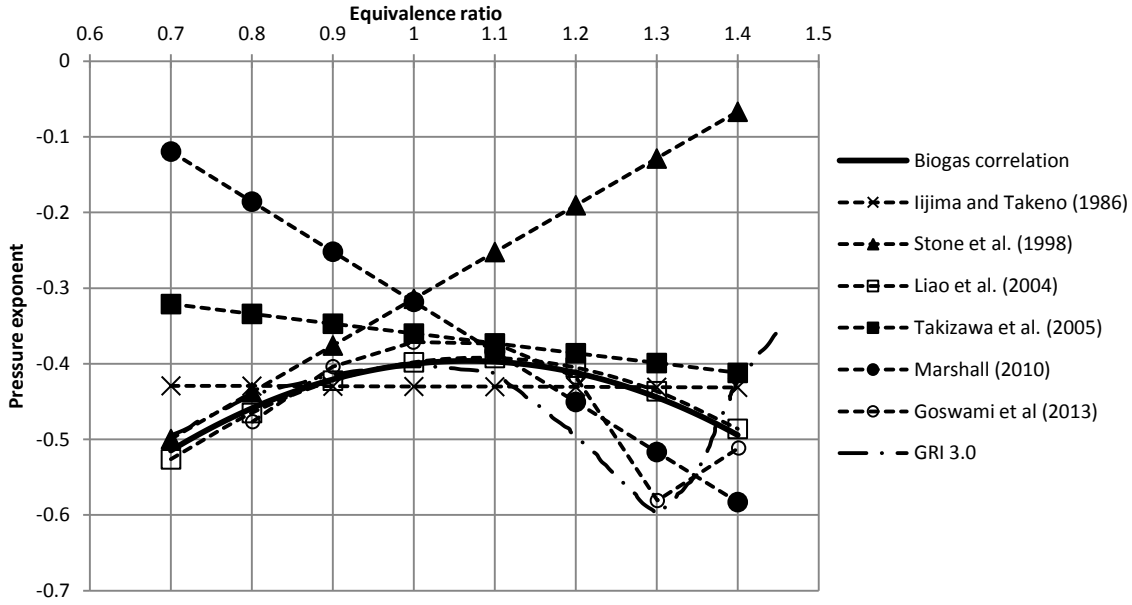

Figure 7.12 – Pressure exponent for biogas correlation compared with existing values from literature.

7.2.3 Comparison with existing data

Methane is one of the most extensively studied fuels in terms of burning velocity measurements, due to its wide range of applications as well as the fact that it has received the most attention in terms of chemical kinetic modelling thanks to the small size of the molecule. These measurements of burning velocity therefore span many years, and as shown in Figure 1.1, significant amount of scatter, showing convergence only recently. Much of this data exists at ambient conditions, so Figure 7.13 shows just a selection of the available results. This shows that the correlation fit is less good at these conditions of temperature and pressure. Comparing

correlations A and B, clearly the addition of ambient temperature data has improved the fit although there is still under predicting for rich mixtures. Regarding the peak burning velocity, the correlations predict a peak close to stoichiometric, whereas the majority of the literature results predict a peak at an equivalence ratio of around 1.05. However, this is not universal, for example the results of Rahim *et al.* (2002) match correlation B relatively closely.

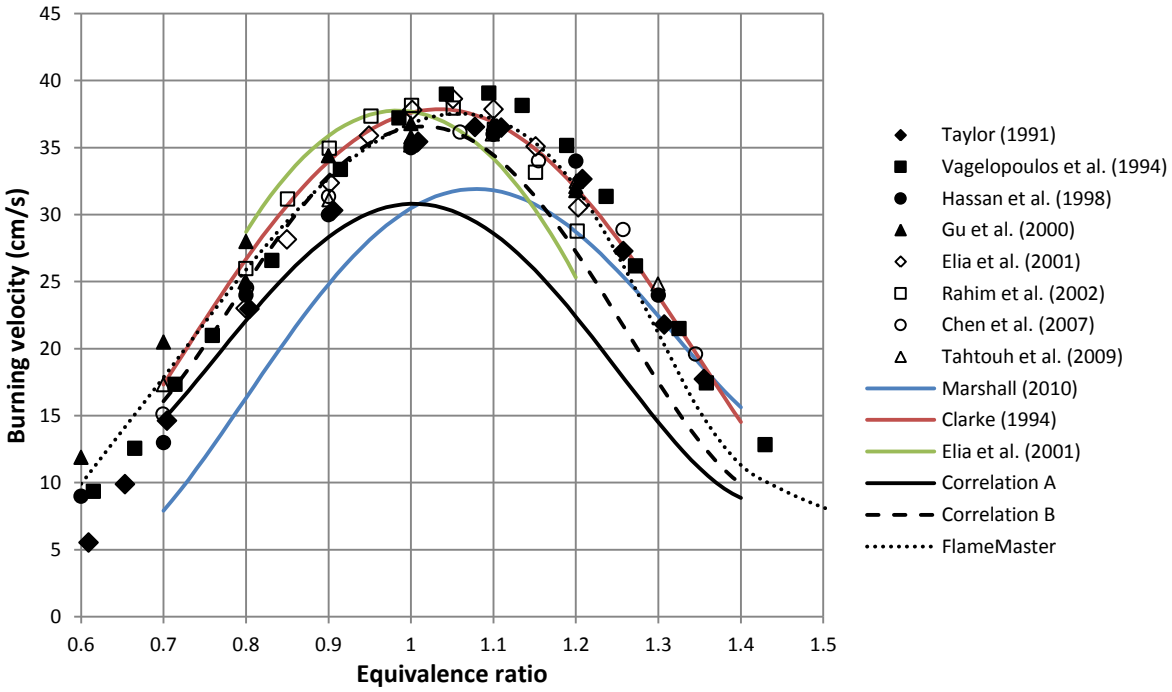

Figure 7.13 – Methane-air correlations at 298 K, 1 bar, compared with results from the literature and FlameMaster simulations.

Figure 7.14 compares the correlation for stoichiometric methane-air mixtures at 298 K with other available correlations and literature data for various pressures up to 20 bar. As expected, there is a large difference between correlations A and B at low pressures, but close agreement is seen at higher pressures. Correlation A is closely matched to that of Marshall (2010), though it is clear that neither correlation performs well at low pressures. At pressures up to about 4 bar, there is good agreement between the results from FlameMaster and correlation B, at which point the simulation begins to give lower values of burning velocity. Compared to the high pressure results of Gu *et al.* (2000) and Rozenchan *et al.* (2002), the results from the correlations are closer than those of the simulations. The correlation of Clarke (1994) reports significantly higher burning velocities at higher pressures but might have inadvertently included

data affected by cellularity. The results of Goswami *et al.* (2013), who obtained results from a range of equivalence ratios up to pressures of 5 bar using the heat flux burner method also found a shift in peak burning velocity towards stoichiometric as pressure increases, which agrees with the behaviour demonstrated by the current correlations, such as seen in Figure 7.7.

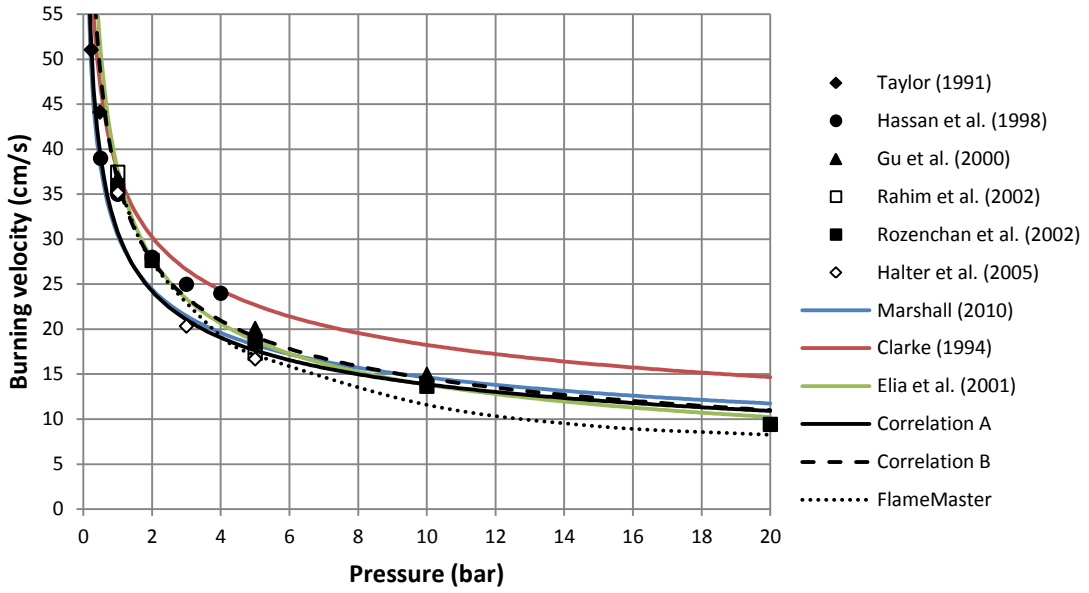

Figure 7.14 – Stoichiometric methane-air correlations at 298 K, varying pressure, compared with results from literature and FlameMaster simulations.

For mixtures of methane and CO_2, less data is available in the literature than for pure methane. Clarke (1994) presents results from a spherical vessel in microgravity in the form of a correlation, although the comparison in Figure 7.14 suggests that it fails to perform well at high pressures. Figure 7.15 compares correlation B with the correlation of Clarke (1994) at ambient conditions and at 5 bar, 500 K. Whilst agreement in terms of the magnitude of the peak burning velocity is good, the outcome of correlation B again appears to under-predict for rich mixtures and ambient conditions, although at elevated temperature and pressure the trends are much closer. Also, the correlation of Clarke appears to suggest an opposite trend in the position of the peak burning velocity when the fraction of CO_2 is increased, and this trend is opposite to that expected from considerations of dissociation.

Galmiche *et al.* (2011) and Halter *et al.* (2009) use flame front shadowgraphy of a spherical expanding flame along with a non-linear extrapolation to obtain burning velocities of

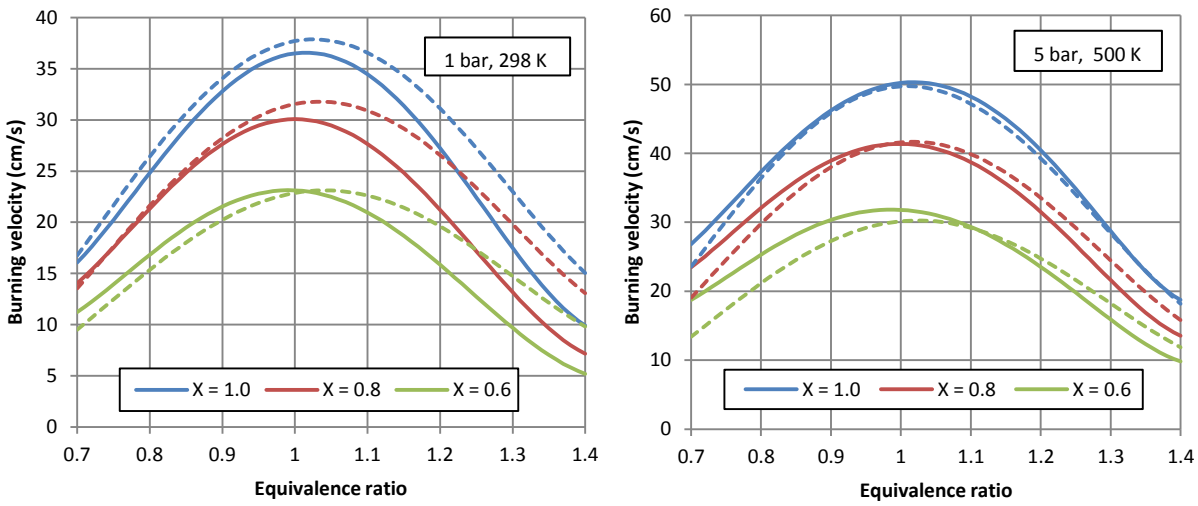

Figure 7.15 – Comparison of correlation B (solid lines) with Clarke (dashed lines) for X = 0.6.

methane-air flames diluted with CO_2. Qiao *et al.* (2008) and Cohé *et al.* (2009) tested lean mixtures using spherical flames in microgravity and a Bunsen burner respectively. Comparisons with this literature data are summarised in Table 7.3, along with the relative burning velocity compared with the pure methane-air mixtures. Note that in the case of Cohé *et al.* (2009), direct values were not given, and results are only presented as a fraction of the methane-air burning velocity. Agreement with Halter *et al.* (2009) at ambient conditions is extremely close, whereas the results of Qiao *et al.* (2008) suggest a slightly more rapid decrease in burning velocity with increasing CO_2 content, although the discrepancy is not large. At elevated temperatures, the comparison with Galmiche *et al.* (2011) is also very good, and the lean results of Cohé *et al.* (2009) agree well at both 1 and 2 bar.

7.2.4 Markstein lengths

Burned gas Markstein lengths are obtained from the gradient of the linear extrapolation of flame speed data. These are plotted in Figure 7.16 to Figure 7.18. Once again, due to the initial methane experiments being performed without schlieren photography, results for methane-air mixtures are limited. In addition, measured Markstein lengths typically demonstrate a significant degree of scatter. Nevertheless, there are some clearly visible trends. As expected, whilst there is noticeable scatter in the results it is clear that the variable with the biggest effect upon the burned gas Markstein length is the equivalence ratio. In all cases, the burned gas

Table 7.3 – Literature values for methane-CO_2-air mixtures compared with correlation results.

Reference	φ	P (bar)	T (K)	% CO_2	Data		Correlation B	
					S_u (cm/s)	Rel.	S_u (cm/s)	Rel.
Halter *et al.* (2009)	1.0	1	300	0	38	1.00	37.0	1.00
				20	31	0.82	30.4	0.82
				40	23	0.61	23.4	0.63
Qiao *et al.* (2008)	1.0	1.013	298	0	36	1.00	36.3	1.00
				20	28	0.78	29.9	0.82
				40	20	0.56	23.0	0.63
Galmiche *et al.* (2011)	1.0	1	393	0	56	1.00	61.3	1.00
				20	45	0.80	50.3	0.82
				40	37	0.66	38.7	0.63
Cohé *et al.* (2009)	0.88	1	300	0	-	1	31.9	1.00
				20	-	0.84	27.0	0.85
				40	-	0.67	21.1	0.66
	0.88	2	300	0	-	1	23.7	1.00
				20	-	0.83	20.1	0.85
				40	-	0.65	15.7	0.66

Markstein length is seen to increase with equivalence ratio. For some rich mixtures, very high values of L_b were obtained, but are missing from the charts to allow an appropriate scale for the rest of the data. These high values are obtained due to the use of a linear extrapolation, as explained by Figure 2.10. For lean mixtures, some negative values of Markstein length are found. With regards to the effect of temperature, comparing results at 380 K and 450 K shows no consistent trend within the range of scatter, although an increase in magnitude of the extreme equivalence ratios at lower temperatures is noticeable. Regarding the effect of pressure, it seems as though there is a slight trend of decreasing Markstein length as pressure increases in most cases. Again, the effect is small compared to the scatter of results, but does appear to be reasonably consistent. The effect of increasing the fraction of CO_2 in the mixture is best illustrated in Figure 7.19, which shows the burned gas Markstein lengths for all methane fractions at conditions of 4 bar and 450 K, since this is where the most complete set of data lies. It appears that the burned gas Markstein length increases with the fraction of CO_2 in the biogas.

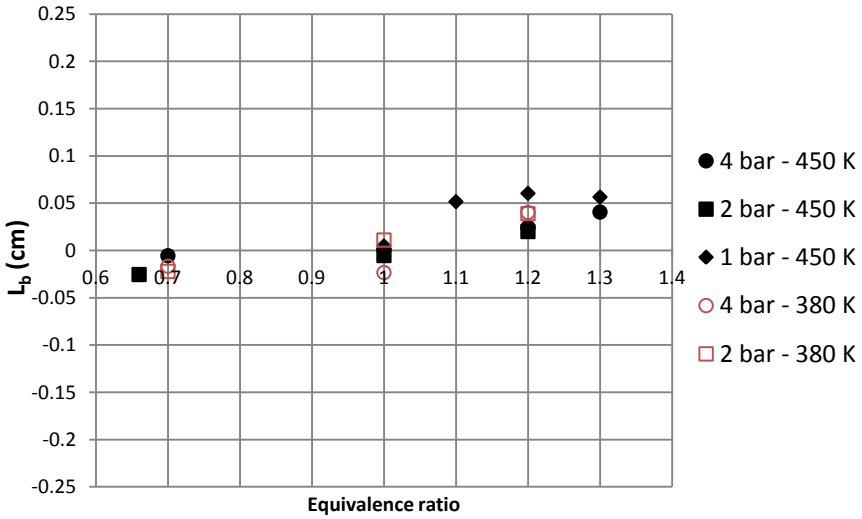

Figure 7.16 - Burned gas Markstein lengths for $X = 1.0$ at $T_u = 380$ K and $T_u = 450$ K.

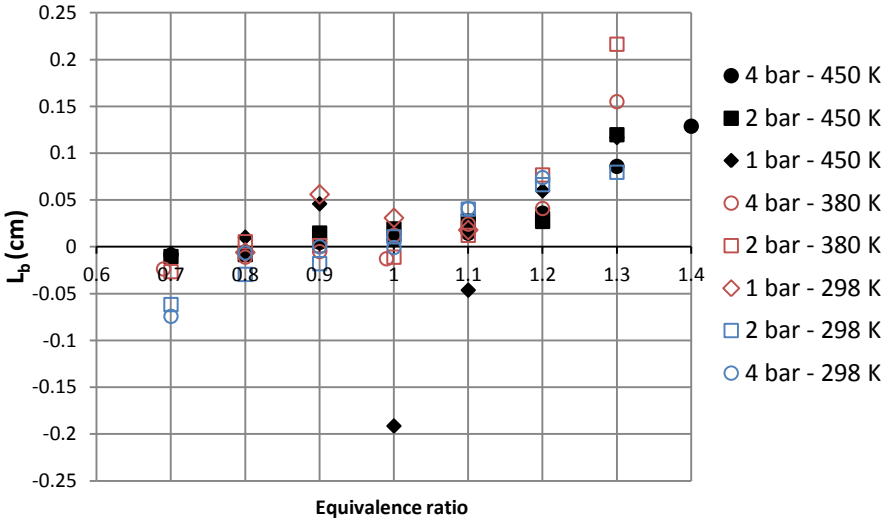

Figure 7.17 - Burned gas Markstein lengths for $X = 0.8$ at $T_u = 298$ K, $T_u = 380$ k and $T_u = 450$ K.

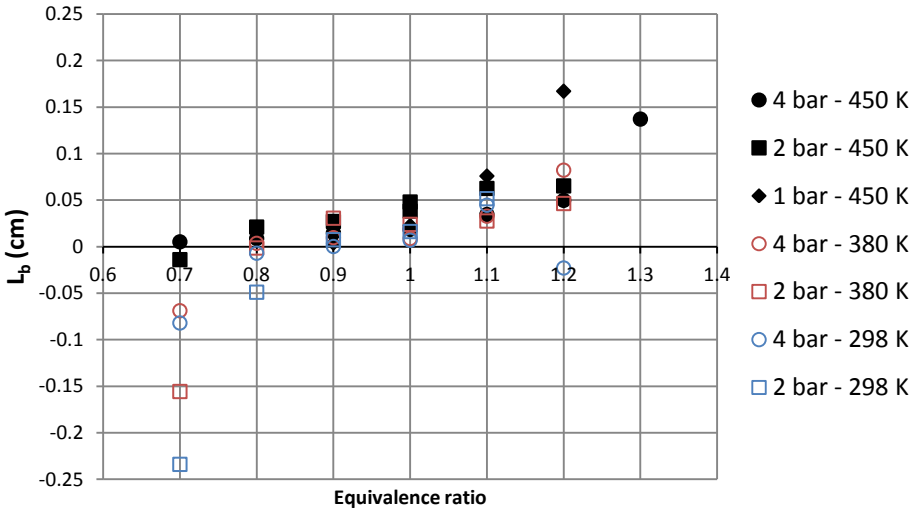

Figure 7.18 - Burned gas Markstein lengths for $X = 0.6$ at $T_u = 298$ K, $T_u = 380$ K and $T_u = 450$ K.

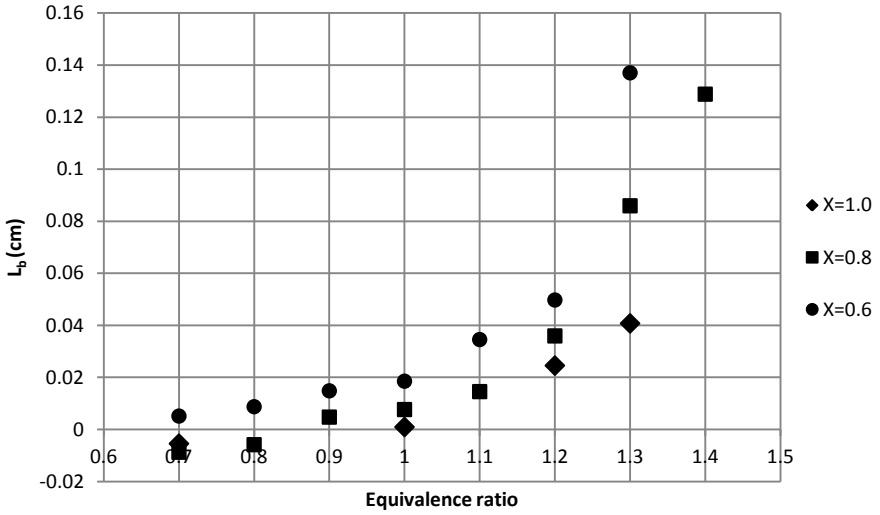

Figure 7.19 – Burned gas Markstein lengths for biogas with varying CO_2 fractions at T_u = 450 K, p_u = 4 bar.

Figure 7.20 compares the results for methane-air mixtures at 1 bar with a selection of existing values in the literature, representative of the range available. All results have been obtained using extrapolation of spherically expanding flames at atmospheric conditions. From the current work, 380 K data was used, but it has been shown that the effect of temperature is small. It can be seen that the burned gas Markstein lengths obtained in the current work are lower than those found elsewhere in the literature, though are fairly close to those reported by Hassan *et al.* (1998). A large discrepancy exists in the data, particularly for rich mixtures, and it is unclear as to why, though the measurement will be sensitive to the method of extraction of the value obtained in post-processing. For example, the work of Tahtouh *et al.* (2009) shows the difference resulting from different methodologies in determination of Markstein length (section 2.5.6). However, this does not explain the magnitude of the differences in results shown in Figure 7.20. Furthermore, a similar plot for Markstein lengths for ethanol in section 7.3.4 shows much closer agreement with the literature values.

Wang *et al.* (2010) present results for very lean methane-air mixtures in microgravity and find strongly negative Markstein lengths when approaching the lean flammability limit.

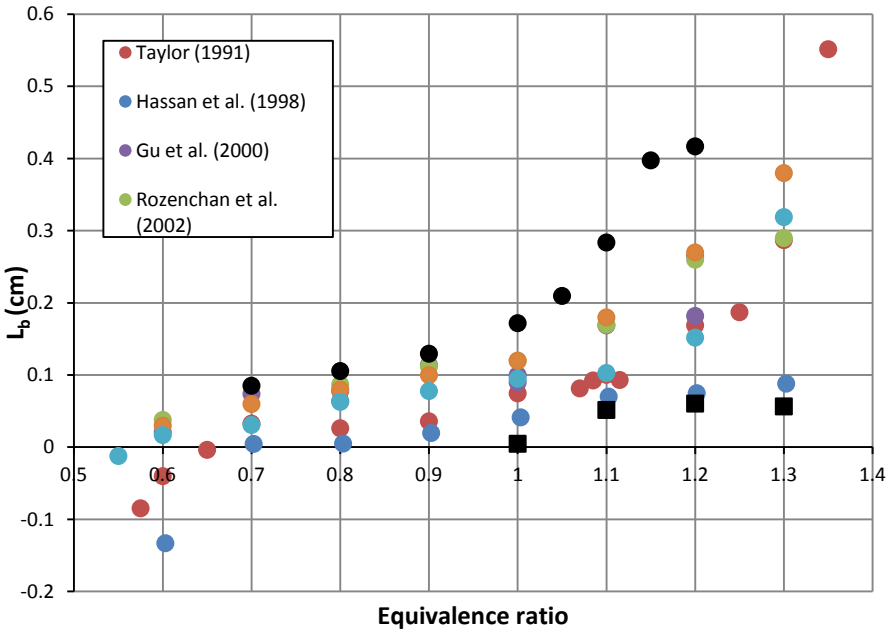

Figure 7.20 – Burned gas Markstein lengths for methane-air at 1 bar compared with literature values.

7.2.5 Onset of cellularity

Using the cellularity detection algorithm in the *BVImage* code, it is possible to identify the onset of cellularity for each mixture, and once *Burnvel* has subsequently been run, it is possible to find the pressure, temperature, burning velocity, flame radius and stretch rate corresponding to the onset of cellularity. Scatter in the results is expected, since the point of cellularity onset is somewhat dependent upon image thresholding (section 6.2.2.2), and at the point of cellularity it is likely that conditions of pressure and temperature will be rapidly changing, which will add inaccuracy to the determined value, but trends in the onset of cellularity should still be clear.

Considering the results for pure methane ($X = 1.0$), a trend in pressure at onset of cellularity can be seen in Figure 7.21. Each point on the plot represents a single experiment; in the left hand plot, both initial temperatures (380 K and 450 K) are shown at each initial pressure and in the right hand plot, both pressures (2 bar and 4 bar) are shown at each initial temperature.

Parabolas are fitted to the data sets simply to guide the eye, and are not intended to represent accurate fits. Whilst the number of data points for this data set are limited (due to much of the set being performed without schlieren photography), it seems that for lean and stoichiometric conditions, the data points collapse onto a single line. This suggests that the

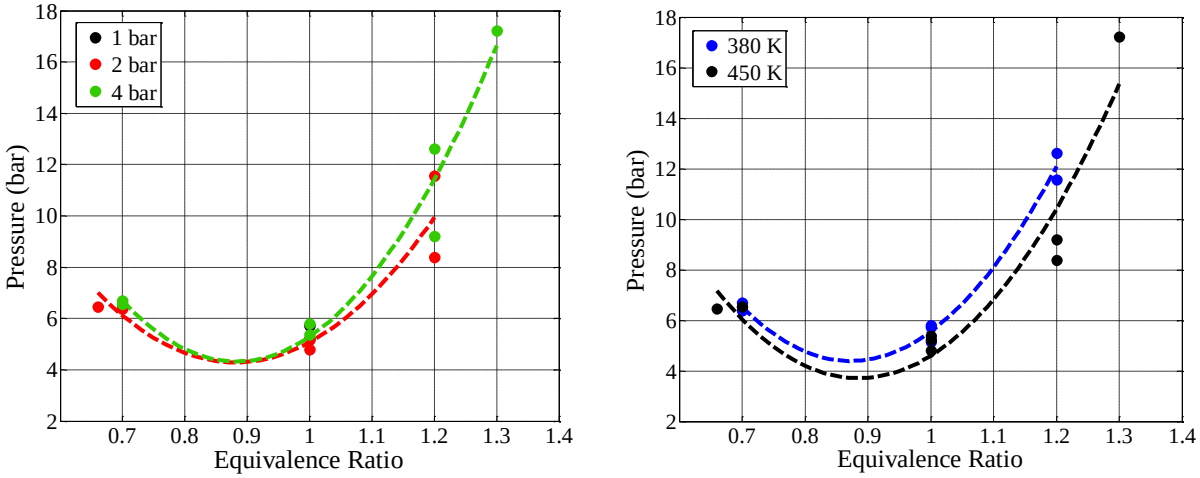

Figure 7.21 - Pressure at onset of cellularity for methane-air mixtures with varying initial pressure and temperature. Parabolas are fitted simply to guide the eye.

onset of cellularity is most strongly dependent upon the pressure, with the initial pressure and temperature being of less importance. The right hand figure suggests that the pressure at which the onset of cellularity occurs is partially dependent upon the initial temperature. For richer mixtures, whilst the mixtures at different initial pressures have closely matched pressures at the onset of cellularity, there appears to be a bigger discrepancy for mixtures with different initial temperatures. It is possible that this could be an effect of difficulty in determining the precise onset of cellularity at higher pressures since the conditions will be changing more rapidly during the later stages of combustion (and so the incremental change in pressure with each frame is larger), and for higher initial temperatures flame speeds, and therefore rate of change of temperature and pressure, will be correspondingly higher.

Plotting the temperature at onset of cellularity, for different initial pressures and temperatures suggests that this is not the governing factor in the onset of cellularity. Figure 7.22 shows the temperature at onset of cellularity for varying initial pressures, for initial temperature380 K in the left hand plot, and 450 K in the right hand plot. This clearly shows that the temperature at onset of cellularity is dependent upon the initial conditions, suggesting that it is not the critical factor.

Figure 7.23 shows the flame radius and stretch rate at the onset of cellularity, for mixtures with an initial temperature of 380 K. Clearly these are also not critical in defining the onset of

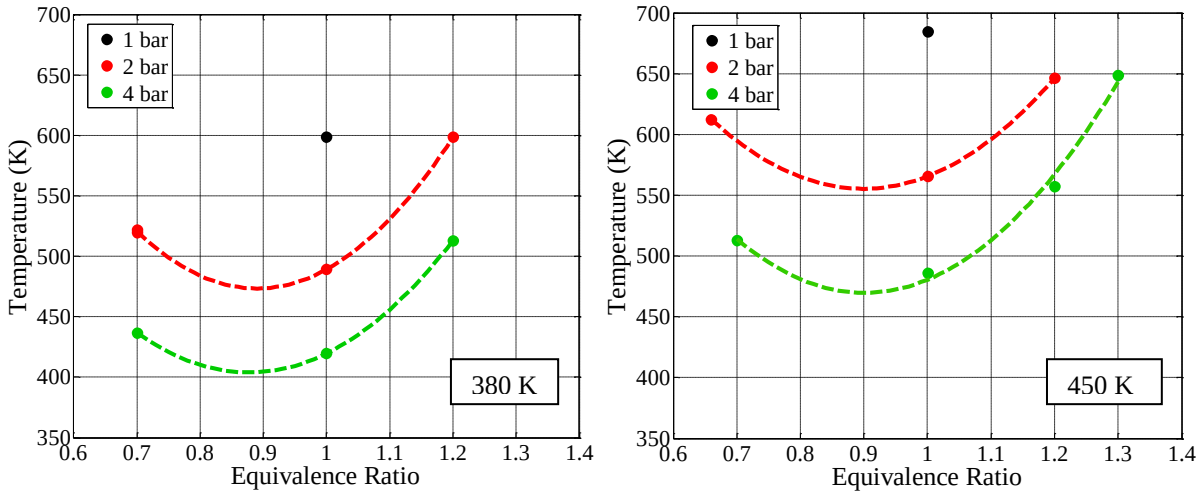

Figure 7.22 - Temperature at onset of cellularity for methane-air mixtures with varying initial pressure for initial temperatures 380 K and 450 K. Parabolas are fitted simply to guide the eye.

cellularity, but rather reflect the conditions at the point where the critical pressure is reached; hence the radius of the flame for higher initial pressures is lower, and the stretch rate is correspondingly higher. It would be expected that high stretch rates will inhibit the onset of cellularity (as discussed in section 2.6.1) however this is not clear from the plots since the effect of pressure dominates; the stretch rate at onset is higher for the mixtures ignited at higher initial pressure, since the critical pressure is reached earlier.

Therefore, it should be instructive to investigate the time at the onset of cellularity for the different mixtures, plotted in Figure 7.24. As with the pressure at the onset of cellularity, the results on the left hand plot (which represents both initial temperatures) are close to collapsing onto a single line, with the equivalence ratio having a more significant effect than initial pressure. The right hand plot shows the effect of initial temperature on the time taken for cellularity to occur. In all cases the cellularity occurs earlier for higher initial temperatures.

Both these findings imply that this is simply representing the time it takes to reach the critical pressure, which will be dependent upon the flame speed, hence faster for mixtures closer to stoichiometric and at a higher initial temperature. Conversely, higher initial pressures will lead to slower flame speeds. However as seen in Figure 7.23, the critical pressure is reached at much smaller radii, meaning that overall, cellularity occurs more quickly than for lower pressures. Additionally, faster flame speeds will lead to higher stretch rates, which will

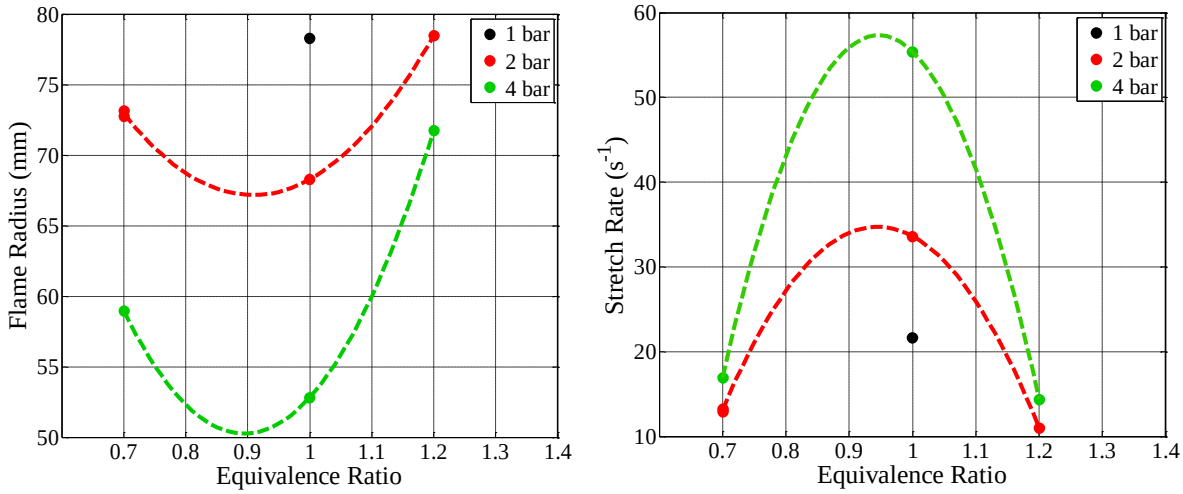

Figure 7.23 – Flame radius and stretch rate at onset of cellularity for methane-air mixtures with varying initial pressures with initial temperature 380 K. Parabolas are fitted simply to guide the eye.

be expected to delay the onset of cellularity. A similar trend is seen when CO_2 is added to the mixture. Figure 7.25 shows the pressure at onset of cellularity for mixtures where $X = 0.8$, with varying initial pressure in the left hand plot, and varying initial temperature with an initial pressure of 4 bar in the right hand plot. Note that two different initial temperatures (294 K and 303 K) represent ambient temperature. Whilst pressure still appears to be the dominant factor, a slightly larger scatter also implies that initial temperature has more of an effect than when no CO_2 was present in the mixture. Increasing the CO_2 fraction up to 40% results in an even bigger shift in this trend. Results are given in Figure 7.26, where the data no longer collapses close to a single line for mixtures of differing initial temperatures and pressures. Therefore, as the CO_2

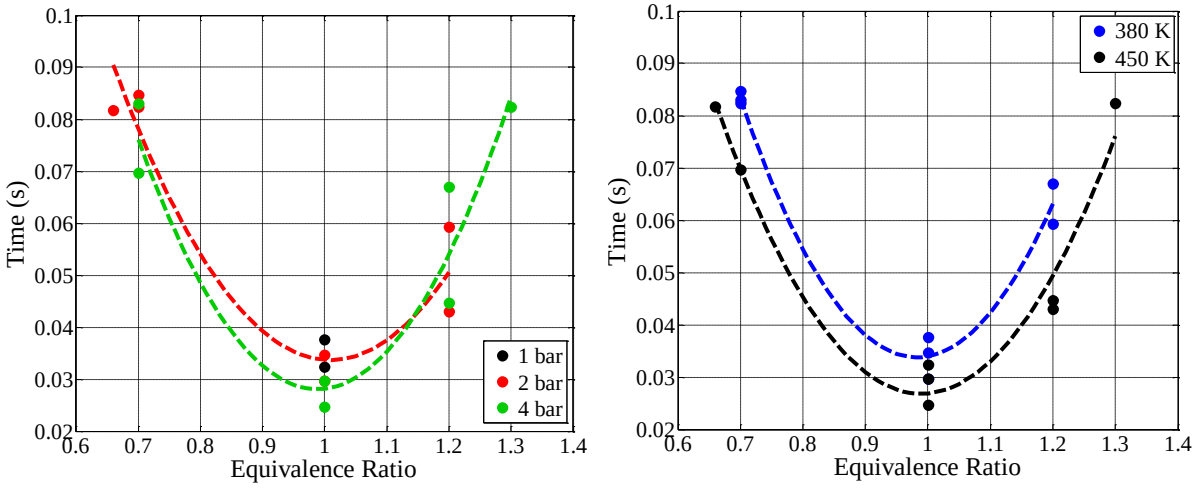

Figure 7.24- Time at onset of cellularity for biogas ($X = 1.0$) varying initial pressures and temperatures. Parabolas are fitted simply to guide the eye.

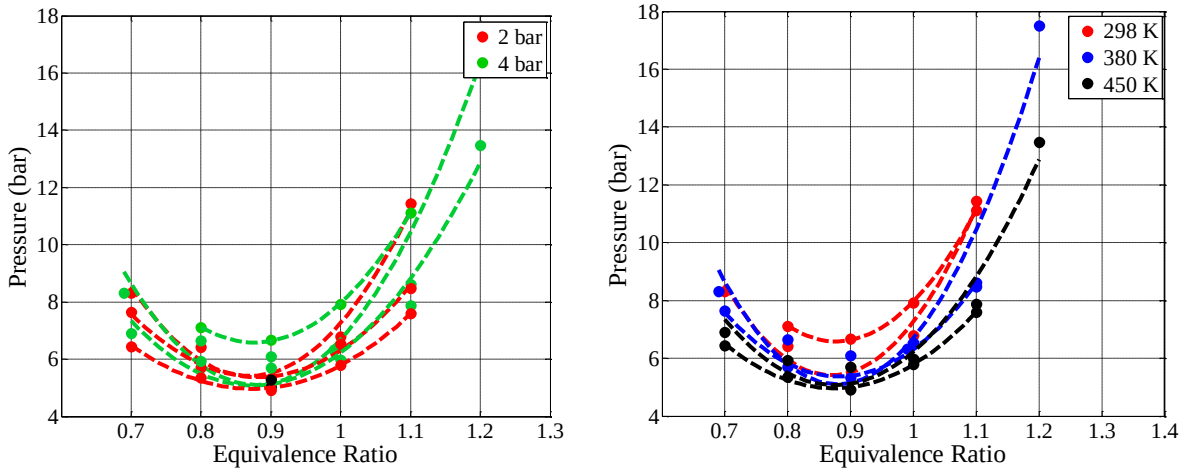

Figure 7.25 – Pressure at onset of cellularity for biogas ($X = 0.8$) with varying initial pressures and temperatures. Parabolas are fitted simply to guide the eye.

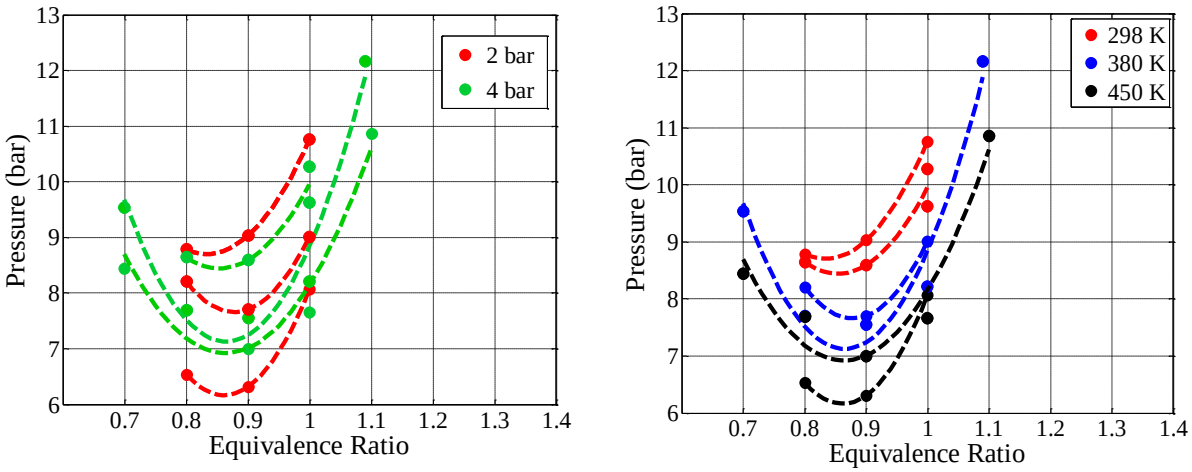

Figure 7.26 - Pressure at onset of cellularity for biogas ($X = 0.6$) with varying initial pressures and temperatures. Parabolas are fitted simply to guide the eye.

fraction has increased, so too has the dependence of critical pressure upon initial temperature and pressure. Furthermore, it can be seen that as the CO_2 fraction is increased, the critical pressure increases. Figure 7.27 shows the pressure at onset of cellularity for all tested methane fractions at an initial pressure of 4 bar and initial temperature of 380 K, showing that the effect of increasing CO_2 fraction is to inhibit the development of such instabilities.

Such results are of use in determining information regarding the inherent instabilities in flame propagation, but also could be used for assisting the detection of cellularity in vessels where optical access is not available. In this case, more studies are needed to determine the onset of cellularity in different sized bombs, as although the pressure appears to be the biggest

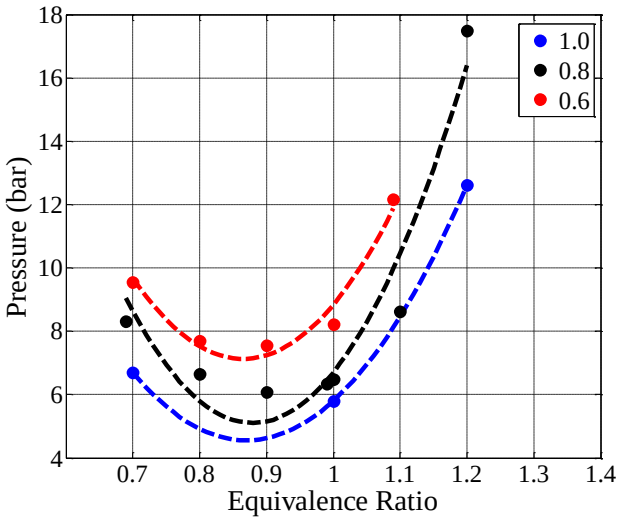

Figure 7.27 – Pressure at onset of cellularity for biogas experiments at initial pressure 4 bar and initial temperature 380 K, with varying methane fraction (*X*). Parabolas are fitted simply to guide the eye.

factor, stretch rates at a given pressure will be different in different vessels, which could have an impact upon the onset of cellularity.

7.3 Hydrous ethanol

Ethanol has been tested with a water content of up to 40% by volume. W0 refers to pure ethanol (commonly referred to as E100 in the context of blending ethanol with gasoline), W20 and W40 are ethanol-water blends containing 20% v/v and 40% v/v of water respectively.

7.3.1 Data range

The hydrous ethanol data set contains a total of 18689 data points from 162 experiments as detailed in Table 7.4. A slightly higher number of tests were performed for pure ethanol (W0) as a result of using smaller increments of equivalence ratio around the location of the peak burning velocity to enable more accurate determination of the point of peak burning velocity. However, it should be noted that the number of data points for W20 and W40 is greater than for

Table 7.4 – Number of experiments and data points included in hydrous ethanol data set.

	Experiments	Data points
W0	60	4840
W20	50	5492
W40	48	8357

W0, due to longer total burn durations and a later onset of cellularity (see section 7.3.5). Tests were performed at initial temperatures of 380 K and 450 K, initial pressures of 1, 2 and 4 bar, and equivalence ratios between 0.7 and 1.6. The maximum and minimum values obtained for each of the experimental parameters and measurements are summarised in Table 7.5. Note that a small number of tests at an initial pressure of 0.5 bar were carried out, though this number was limited due to difficulty igniting these low pressure mixtures. Regarding equivalence ratio, richer mixtures than intended were produced in some cases, particularly for mixtures containing a higher volume fraction of water due to difficulties in delivering the correct amount of fuel. Figure 7.28 shows the number of data points in each data set (W0, W20, W40 and the combined hydrous ethanol data set), divided into brackets of equivalence ratio and pressure.

Figure 7.28 shows that the data set is skewed towards lean mixtures, which is a result of the earlier onset of cellularity for rich mixtures, preventing selection of data beyond a limiting pressure. This effect is greatest for W0, where rich of stoichiometric there is no data obtained for pressures greater than 3.5 bar. For higher volume fractions of water, the range of pressure over which data points are included for rich mixtures is greater. This is a result of the later onset of cellularity as the water content is increased (see section 7.3.5), allowing data to be included for higher pressures. Whilst the range of pressures for rich mixtures is greater with increased water content, the increased number of data points is also largely due to the slower flame speed resulting in more data points being acquired over a given pressure range since the sample rate during combustion was the same for each experiment.

7.3.2 Burning velocity results

The results of the image analysis are presented alongside the results obtained from correlations derived from the pressure rise analysis. Schlieren image data has been analysed with linear extrapolation for initial pressures of 2 and 4 bar, and initial temperatures of 380 K and 450 K.

Table 7.5 – Minimum and maximum conditions in the hydrous ethanol data sets.

		W0		W20		W40	
Property	Unit	Min	Max	Min	Max	Min	Max
T_0	K	380	450	380	450	380	450
P_0	barA	0.5	4.0	1.0	4.0	1.0	4.0
Φ		0.70	1.41	0.62	1.39	0.70	1.59
P_u	barA	0.656	16.9	1.28	15.4	1.36	14.8
T_u	K	393	633	394	633	393	624
S_u	cm s^{-1}	21.9	106	19.9	92.1	12.3	68.3
S_f	cm s^{-1}	40.5	351	32.6	272	25.3	224
α	s^{-1}	10.8	146	8.81	105	7.20	78.8
r_b	mm	39.4	77.4	33.7	77.8	39.2	77.2
t	ms	14.5	92.3	19.0	130	25.4	159

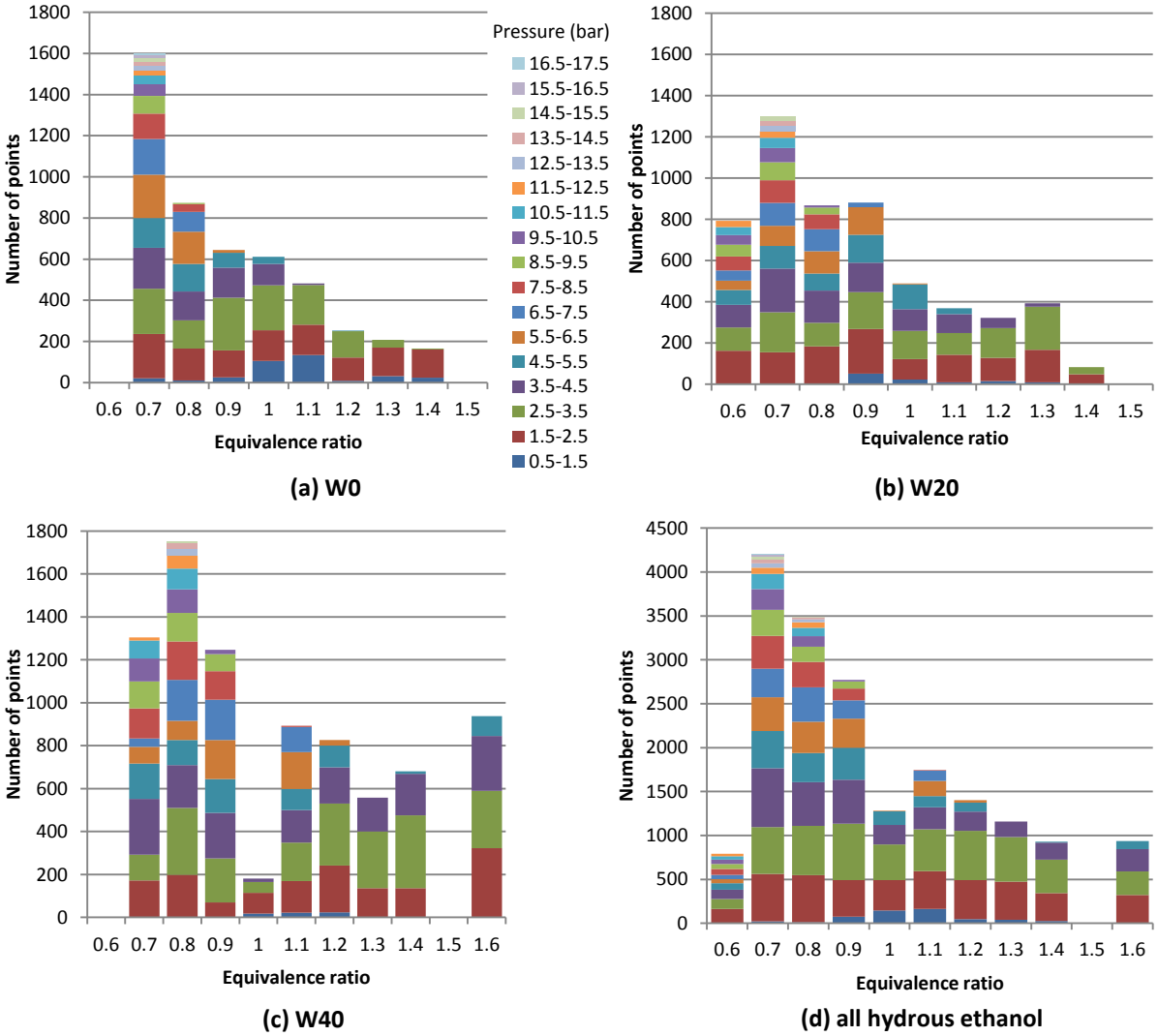

Figure 7.28 – Number of data points in each pressure and equivalence ratio bracket for a) W0, b) W20, c) W40 and d) the entire hydrous ethanol set.

The hydrous ethanol correlations use the 14 term form given by Equation (5.8), with second order dependence on equivalence ratio of both temperature and pressure exponent, and treatment of water volume fraction as a diluent. Several correlations are compared, based upon the evaluations in sections 6.2.2.6 and 6.2.2.7 to take into account the stretch correction and the addition of ambient data. In the case of ethanol, ambient temperature and pressure data from Konnov *et al.* (2011) is used, with 150 points per experiment at equivalence ratios 0.8, 1 and 1.2. The correlations are named A to D, and are summarised in Table 7.6. All coefficients are given in Table 7.21 at the end of this chapter.

Table 7.6 – Summary of hydrous ethanol correlations.

Correlation	Modification from base correlation
A	-
B	Ambient data (Konnov, 2011)
C	Stretch correction
D	Ambient data (Konnov, 2011) and stretch correction

Figure 7.29 to Figure 7.31 show the results of the image analysis for W0 to W40 at conditions tested, along with the various correlations plotted for the same conditions. Considering first the W0 results in Figure 7.29, there is good agreement between the results from the image analysis and the correlation. Comparing the correlations, for lean mixtures the results from all the correlations are consistent, with divergence occurring for rich mixtures. This divergence is almost 4 cm s^{-1} at its greatest point. In all cases, the correlation presented without modification for stretch or additional ambient data gives the lowest result. Including additional low pressure data and modifying for the effects of stretch increases the determined burning velocity at 2 bar, although the additional ambient data appears to make less of a difference at 4 bar, particularly at the higher temperature. This is consistent with the trend seen in section 6.2.2.6.

Since the differences between the correlations are relatively small, and some scatter in the schlieren results is evident, it is not clear which gives the best fit to the schlieren data, although it seems that the data falls into the lower end of the range specified by the correlations. Figure 7.30 shows the results for the W20 mixtures, and once again the correlations are very consistent

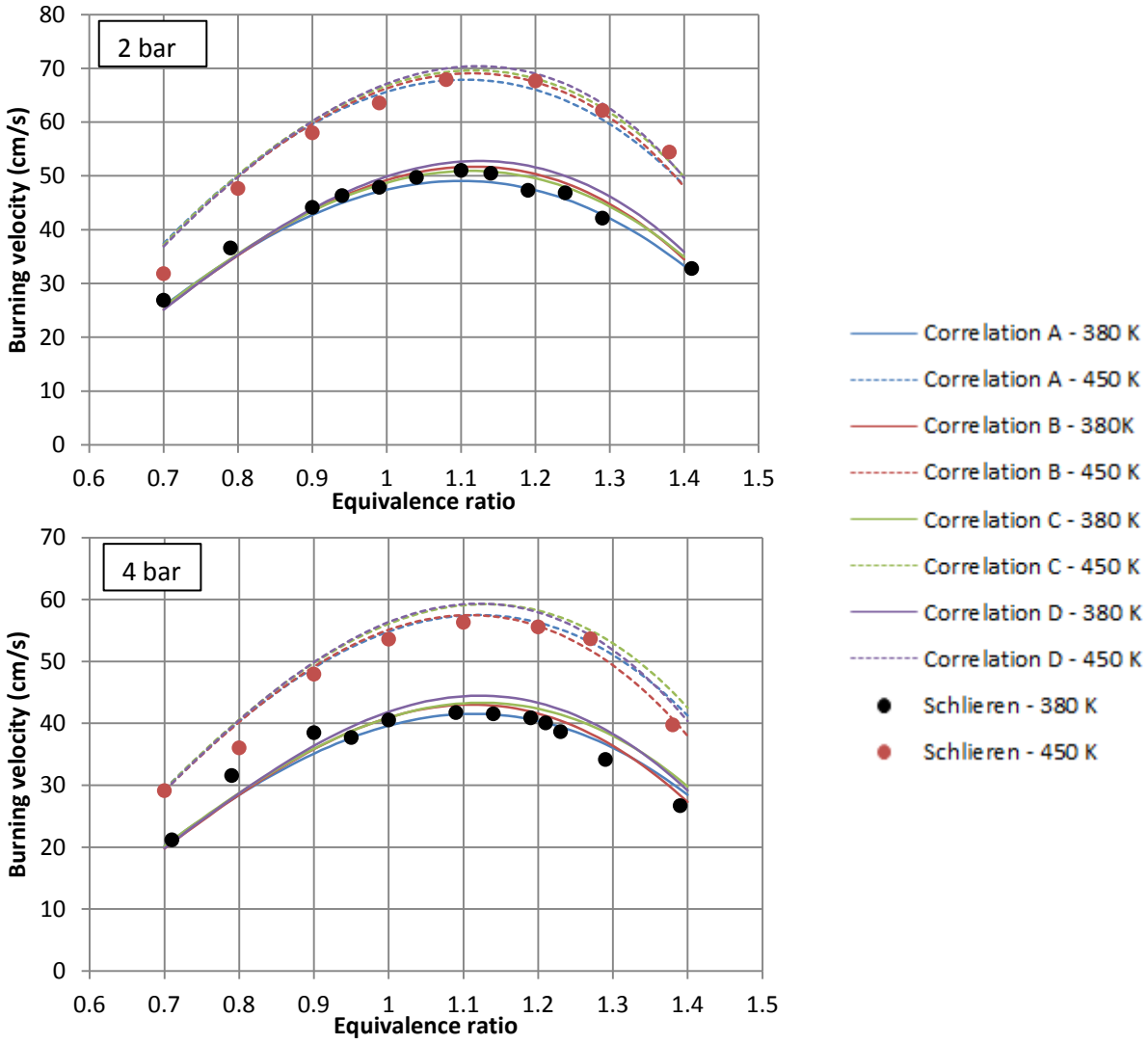

Figure 7.29 – Burning velocity of W0 at 2 bar and 4 bar. Lines represent the various correlations (defined in Table 7.6) at 380 K (solid) and 450 K (dashed); points represent results from schlieren image analysis.

up to around stoichiometric, at which point they diverge. At 2 bar the agreement between the schlieren results and the unmodified correlation is very good at both temperatures. At 4 bar however, the results from the image analysis are slightly lower than the correlation values, particularly at 450 K, for mixtures richer than stoichiometric. This trend is again seen for W40 mixtures, presented in Figure 7.31, with the correlation over-predicting for rich mixtures compared to the schlieren data. In all cases, the discrepancy is a maximum of 4 cm s^{-1} although for mixtures with a higher water content and hence lower burning velocity, this represents a larger percentage difference. This could be due either to reduced accuracy of the schlieren image analysis for the slower mixtures, or difficulty in fitting the correlation at elevated conditions when the water fraction is increased.

The correlation plotted in Figure 7.32 to Figure 7.34 corresponds to correlation D (which includes data from ambient conditions and corrections for stretch), plotted against equivalence ratio at elevated conditions of temperature and pressure, chosen to represent conditions within the range of validity of the correlation. Figure 7.32 illustrates the correlation for W0 at(a) T_u = 500 K with varying pressure and (b) p_u = 5 bar with varying temperature. These values of temperature and pressure have been chosen to represent roughly the middle of the data range, and are higher than the ambient conditions for which data in the literature is often presented. The correlation shows a trend of increasing burning velocity with temperature and decreasing burning velocity with pressure. In all cases, the peak burning velocity occurs rich of stoichiometric, shifting slightly further away from stoichiometric as temperature is increased,

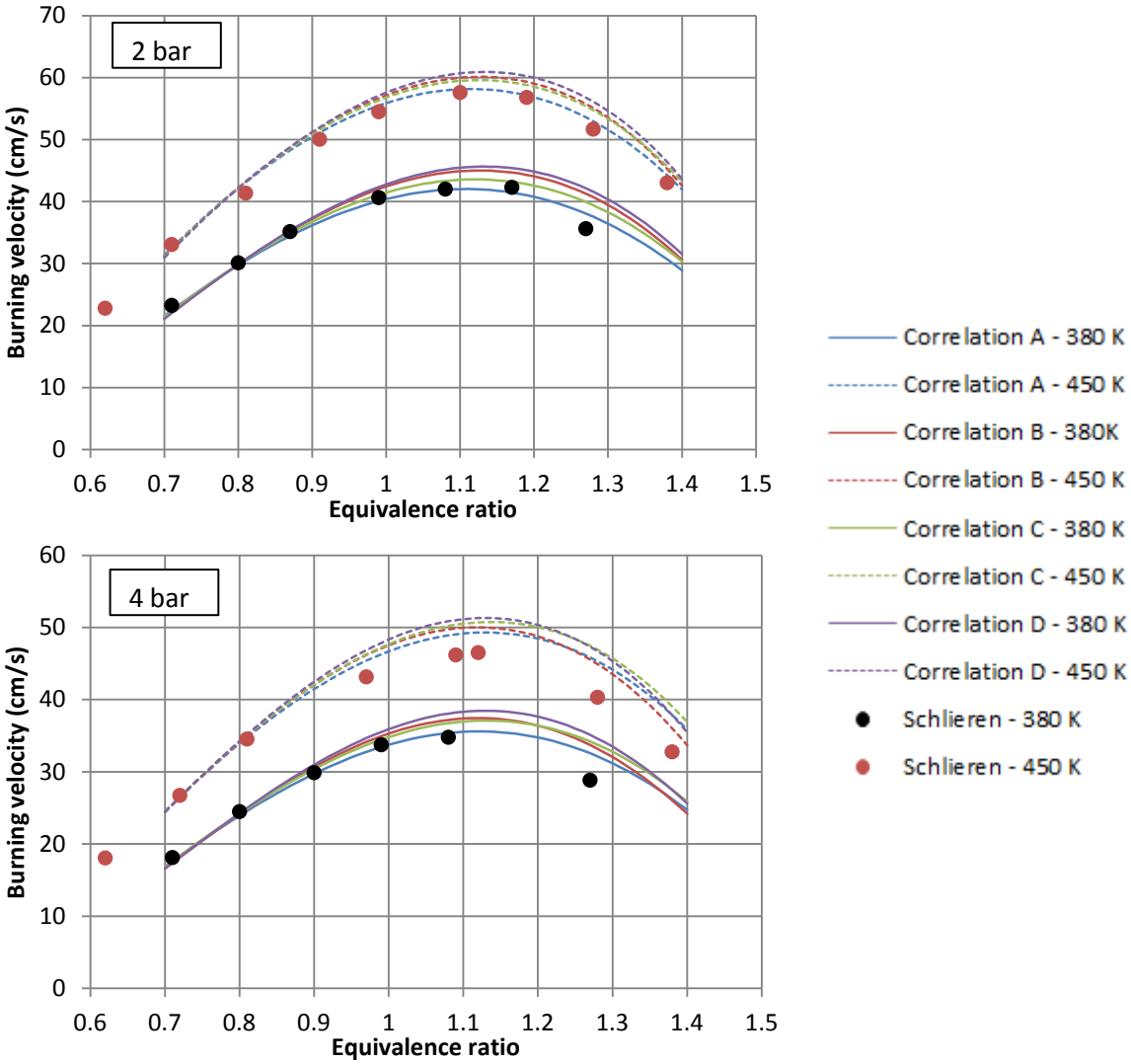

Figure 7.30 - Burning velocity of W20 at 2 bar and 4 bar. Lines represent the various correlations (defined in Table 7.6) at 380 K (solid) and 450 K (dashed); points represent results from schlieren image analysis.

and towards stoichiometric as pressure is increased. The shifts in peak burning velocity with increasing temperature can be explained as an effect of increased dissociation at higher temperatures, and is consistent with the trends seen from the image analysis. Likewise, the shift in peak with pressure would be expected, as increased pressure would lead to less dissociation. The schlieren data does not offer a more precise measurement of peak burning velocity due to the resolution in equivalence ratio. Figure 7.33 and Figure 7.34 show the correlations for W20 and W40 respectively at the same conditions of temperature and pressure. The same general trends regarding the effects of temperature and pressure are clear. It would be expected that the correlations for W20 and W40 show very similar trends in terms of effect of temperature and pressure due to the fact that the exponents of temperature and pressure are not dependent upon

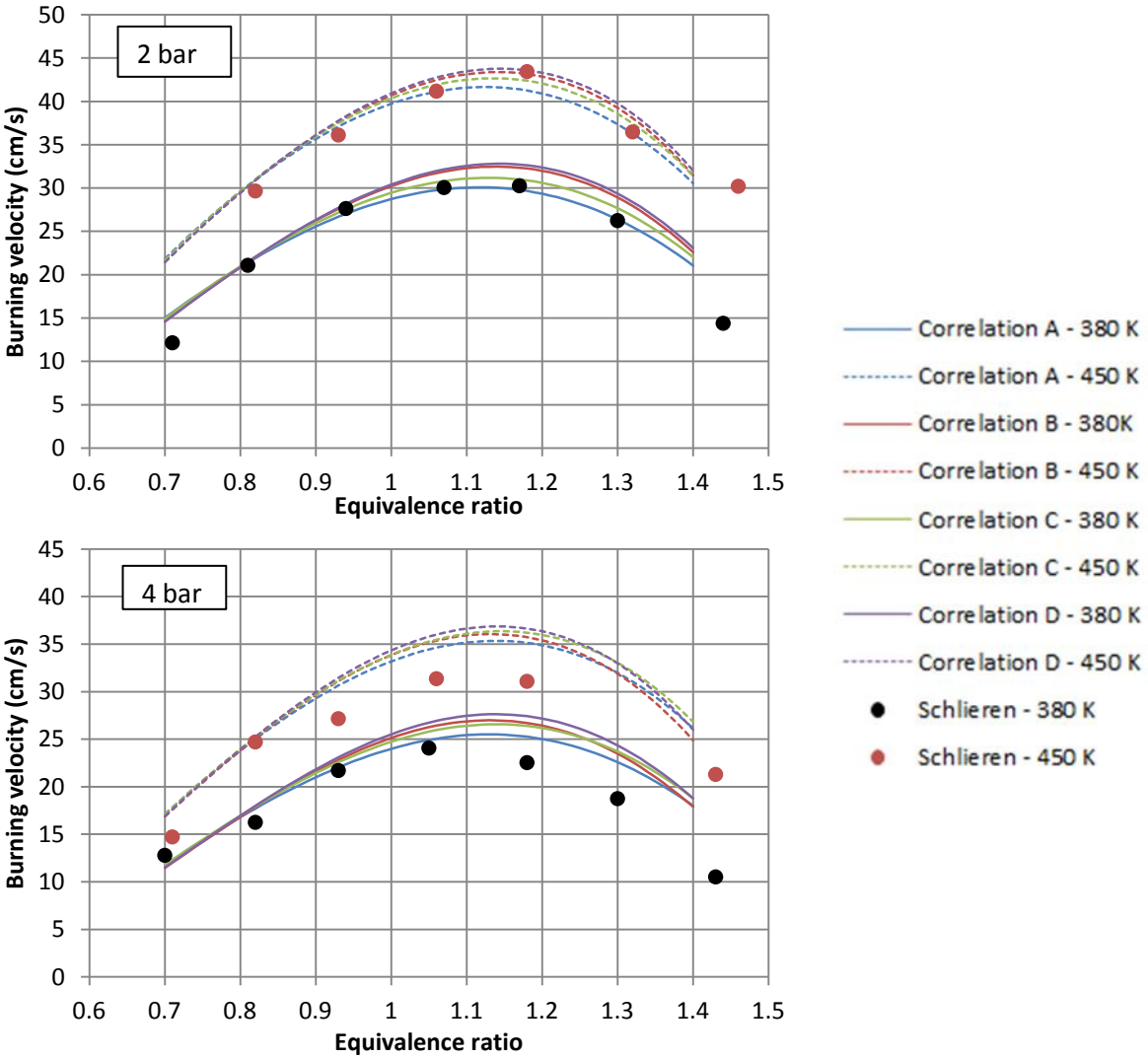

Figure 7.31 - Burning velocity of W40 at 2 bar and 4 bar. Lines represent the various correlations (defined in Table 7.6) at 380 K (solid) and 450 K (dashed); points represent results from schlieren image analysis.

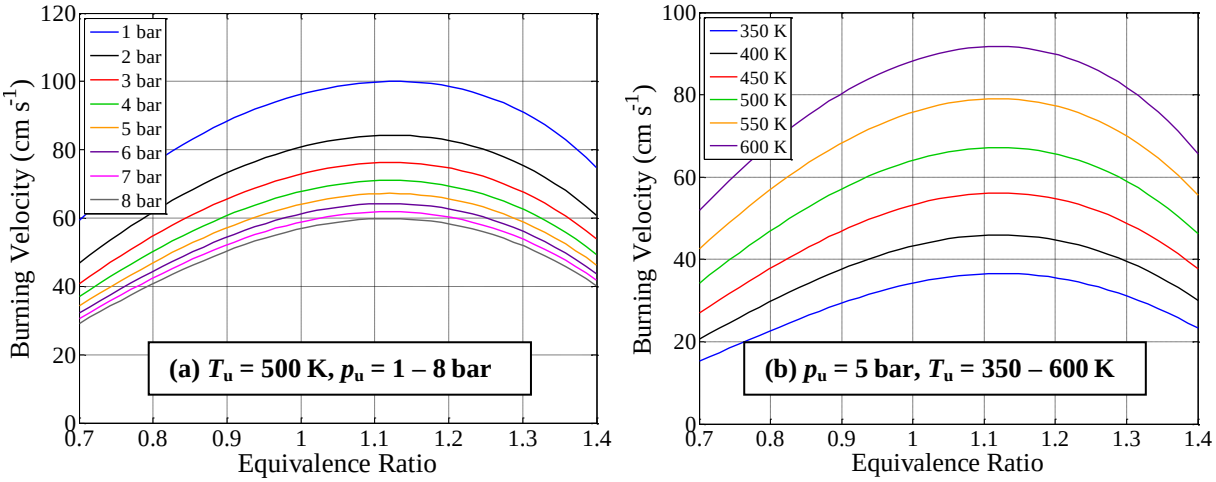

Figure 7.32– Correlation for W0 at conditions of (a) T_u = 500 K and (b) p_u = 5 bar.

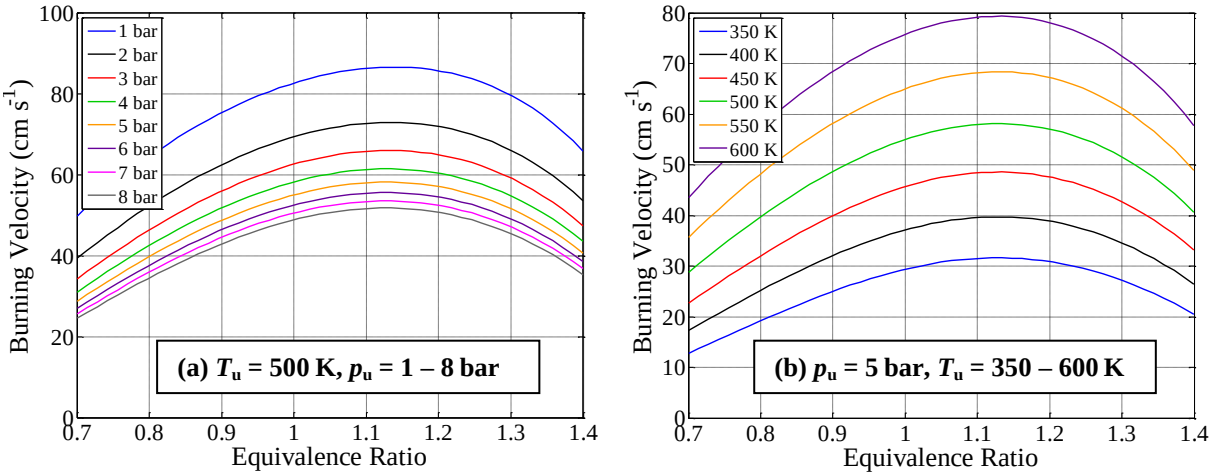

Figure 7.33 – Correlation for W20 at conditions of (a) T_u = 500 K and (b) p_u = 5 bar.

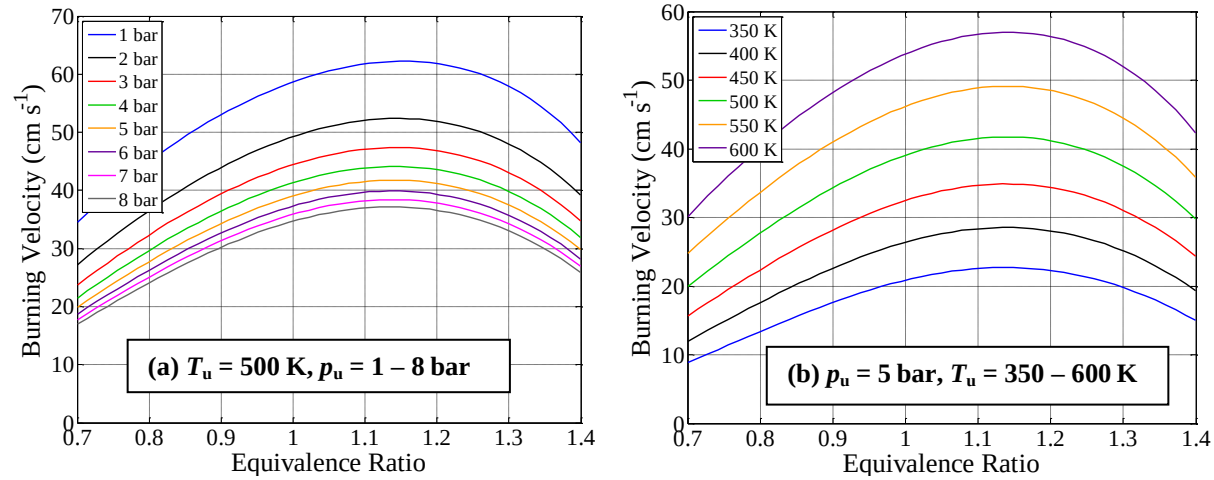

Figure 7.34 – Correlation for W40 at conditions of (a) T_u = 500 K and (b) p_u = 5 bar.

volume fraction of water. However, a first order dependence upon equivalence ratio is included to take account of the effect of increasing volume fraction of water, and so we may expect to see a change in the location of the peak burning velocity for example, as well as a change in the

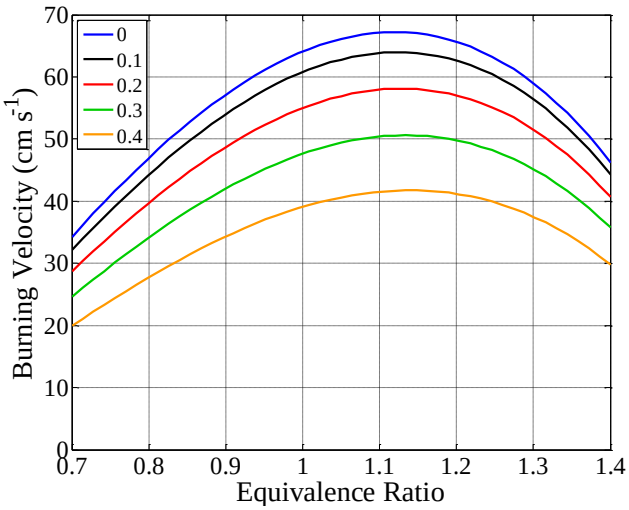

Figure 7.35 – Correlation for W0 – W40 at conditions of T_u = 500 K and p_u = 5 bar.

peak value itself. To allow a clearer comparison, Figure 7.35 shows the effect of increasing the volume fraction of water at the single condition of $T_u = 500$ K and $p_u = 5$ bar. This shows that the effect of increasing the volume fraction of water is to reduce the burning velocity in a non-linear fashion. Considering the stoichiometric case for the conditions of temperature and pressure given in Figure 7.35, the burning velocity of W20 is 85.2% of that of W0, whereas the W40 is just 60.5%. The position of peak burning velocity appears relatively unaffected by the increase in water fraction, although a very slight shift away from stoichiometric is perceptible. Compared with the schlieren results, the precise location of the peak burning velocity is difficult to determine, but seems to shift slightly towards stoichiometric as the water content is increased. This could be attributed to the cooling effect of the increased water content lowering the adiabatic flame temperature leading to less dissociation and hence, a peak burning velocity occurring closer to stoichiometric.

7.3.2.1 Temperature and pressure exponents

The temperature exponent as determined by *fitcorr* for the unmodified correlation (A) and the correlation modified for ambient conditions and stretch correction (D) is plotted in Figure 7.36 along with the results from some previous work in the literature. Gülder (1982) used the constant pressure period of combustion in a spherical constant volume bomb, and measured flame speeds with ionisation probes, applying a density ratio correction to determine burning

velocities. A mean power exponent was determined from the results. Liao *et al.* (2007) fitted a linear dependence upon equivalence ratio to their temperature exponent, using data from the constant pressure period of experiments performed in a cuboidal combustion vessel. Bradley *et al.* (2009) and Konnov *et al.* (2011) do not provide a temperature exponent based upon equivalence ratio, but instead present results determined from fitting an exponent at each tested equivalence ratio. Konnov (2009) also presented a temperature exponent based upon results from a chemical kinetic mechanism. It can be seen that the temperature exponents from the two correlations give similar but different results. This is expected, since inclusion of ambient data will be increasing the range of temperatures over which the data is fitted. The result from correlation D is close in trend to the results of Bradley *et al.* (2009) and Konnov *et al.* (2011).

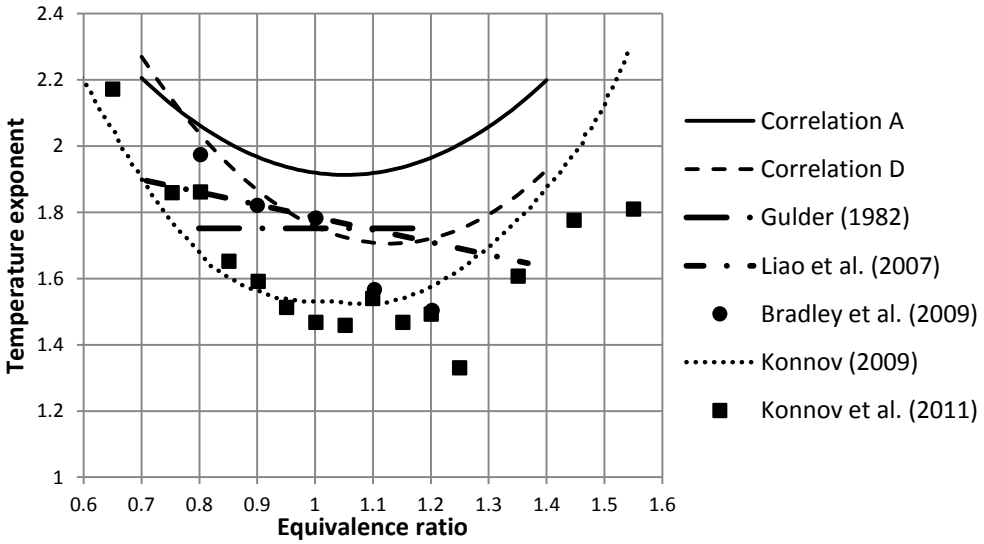

Figure 7.36 - Temperature exponent for ethanol correlations (defined in Table 7.6) compared with literature

The value of the temperature exponent obtained from schlieren images also demonstrated second order behaviour, although a large amount of scatter was seen as a result of fitting a power law fit to data at just two temperatures, greatly reducing the accuracy of the analysis. Nevertheless, this result shows that the fitting process is able to accurately represent the trends in temperature dependence.

Similarly, the pressure exponents obtained from *fitcorr* for correlations A and D are plotted in Figure 7.37 along with existing values from the literature. Once again, there is a deviation between the two correlations for rich mixtures. As shown in section 7.3.1, the lack of data at

rich conditions will be expected to influence the correlation fit, particularly with respect to pressure, due to the strong relationship between pressure and the onset of cellularity. There is clearly large scatter in the results presented in the literature, although the agreement with that of Bradley *et al.* (2009) is reasonably close.

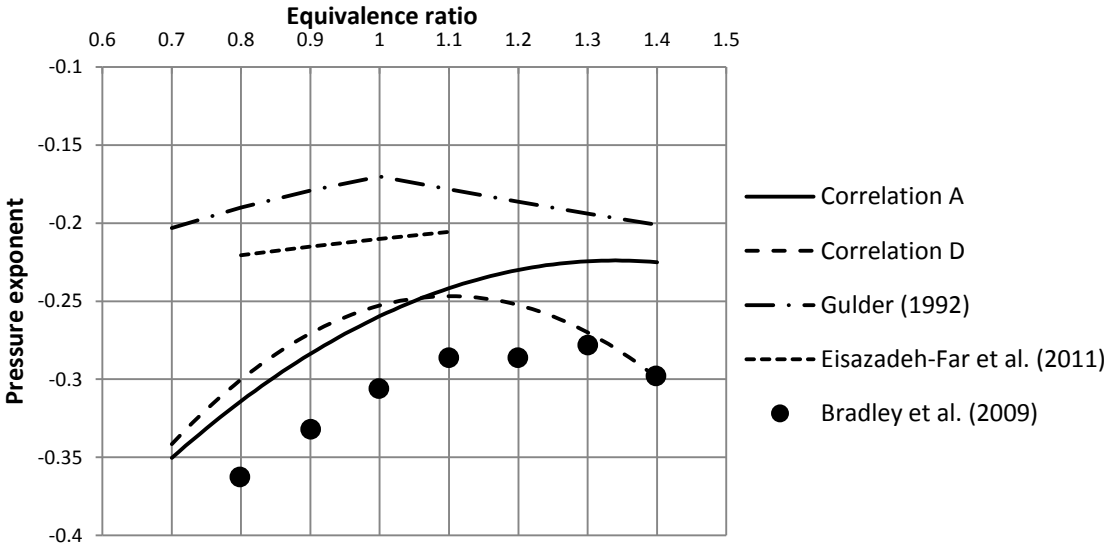

Figure 7.37 - Pressure exponent for ethanol correlations (defined in Table 7.6) compared with literature.

7.3.3 Comparison with existing data

Burning velocities of pure ethanol have been extensively reported in many studies found in the literature. Much of the data in the literature is at ambient conditions of temperature and pressure, which will fall outside the range of validity of the unmodified correlation, so comparisons with correlation D will be expected to provide the best fit. Figure 7.38 shows literature values for ethanol-air (W0) mixtures at 1 bar, 358 K, along with the various hydrous ethanol correlations. The results of Gülder (1982) are acknowledged to be slightly higher at the peak, and exhibit a steeper drop-off in the rich region. The results of Bradley *et al.* (2009) and Konnov *et al.* (2011) are in good agreement, whereas those of Liao *et al.* (2007) suggest lower burning velocities in the rich region. Comparing the correlations at these conditions, it appears that C and D provide the best agreement with the literature. This is as expected, since the other correlations would require significant extrapolation beyond the range to which data was fitted.

All correlations appear much more reliable than that of Marshall (2010), which may be due to erroneous readings from the lambda sensor described in section 6.1.3.

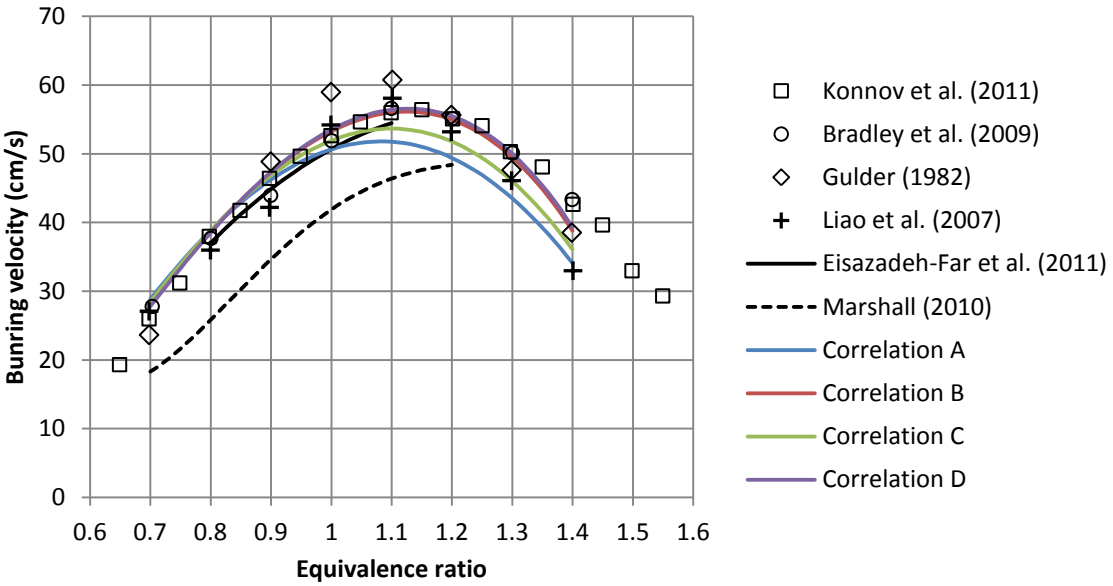

Figure 7.38 – Correlations (defined in Table 7.6) for W0 compared with literature values for 1 bar, 358 K.

Bradley *et al.* (2009) also present ethanol data at elevated pressures and the same temperature of 358 K, which is compared to correlation D in Figure 7.39. Whilst the agreement is good at lower pressures, at higher pressures the correlation gives higher results, except for rich mixtures. This is reflected in the fact that the pressure exponent determined empirically from the experimental data of Bradley *et al.* (2009) is of larger magnitude than that determined from *fitcorr*. The resolution of the data from Bradley *et al.* (2009) is not sufficient to determine small movements in the location of peak burning velocity. Figure 7.40 compares results at 1 bar with varying temperature. Agreement is good at 300 K and 358 K, but for 393 K the correlation gives higher burning velocities than the results of Bradley *et al.* (2009). Given the relative burning velocities at the three temperatures, it seems plausible that the 393 K results presented are unrealistically low, possibly due to some systematic error in the experiments at that temperature. Furthermore, using their empirically determined temperature exponent to represent even higher temperatures, agreement with correlation C and D is very good (Figure 7.41). Limited data exists for burning velocity blends of ethanol and water. Zhang *et al.* (2011) tested mixtures of hydrous ethanol (75% ethanol by volume) with hydrogen as part of a study into

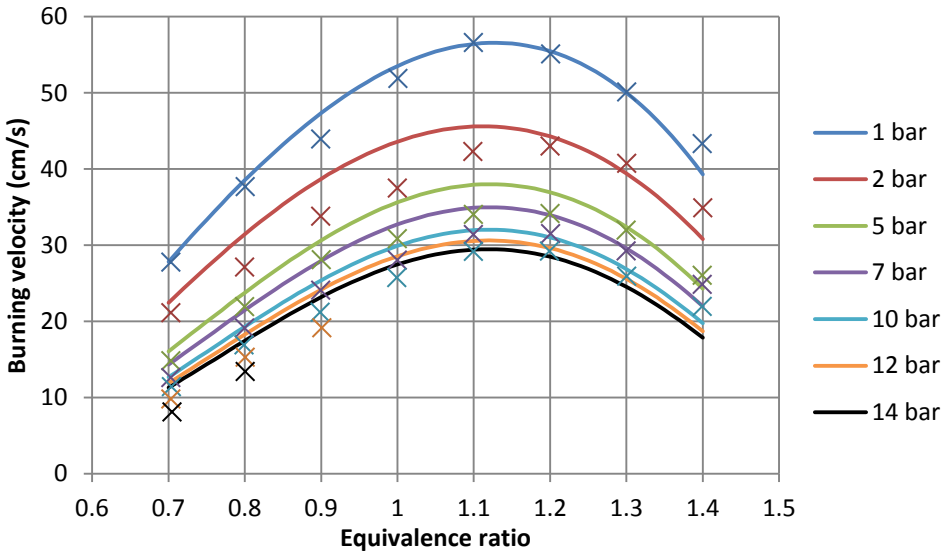

Figure 7.39 – Burning velocity of ethanol-air mixtures at 358 K and varying pressure. Crosses are results from Bradley *et al.* (2009); solid lines represent correlation D (defined in Table 7.6).

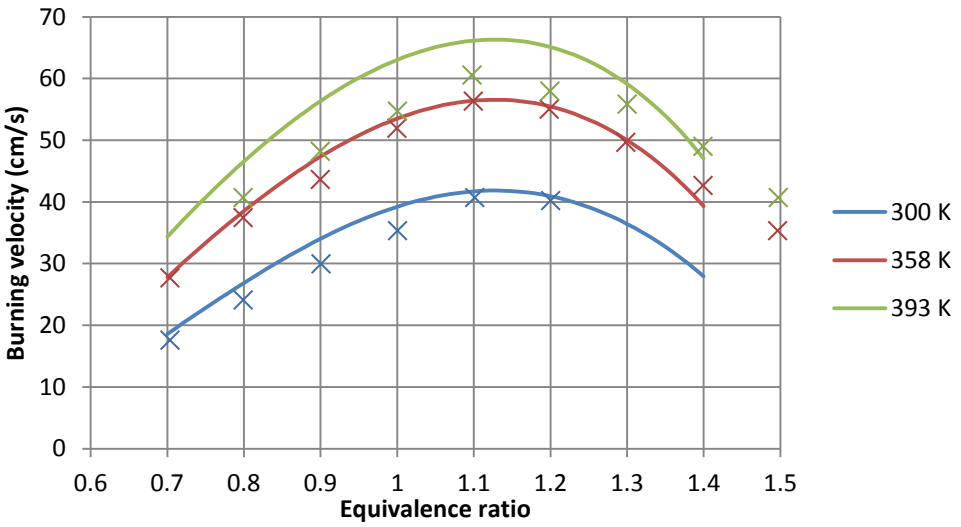

Figure 7.40 – Burning velocity of ethanol-air mixtures at 1 bar and varying temperature. Crosses are results from Bradley *et al.* (2009); solid lines represent correlation D (defined in Table 7.6).

reformer gas using flame front imaging in a cylindrical constant volume vessel. Their results include hydrous ethanol-air mixtures at 1 bar, 383 K, and are plotted in Figure 7.42. Compared with these results, the correlations appear to give lower values of burning velocity than the experimental values. Gülder (1984) also presents results for hydrous ethanol-air mixtures at1 bar and 400 K, although gives significantly higher burning velocities than obtained from the correlation, more than 10 cm s^{-1} at peak burning velocity. This is true for all water fractions, including W0, suggesting the data is erroneous, given that good agreement between the

correlation and other ethanol-air results has been seen at similar conditions elsewhere, e.g. Figure 7.40 and Figure 7.41.

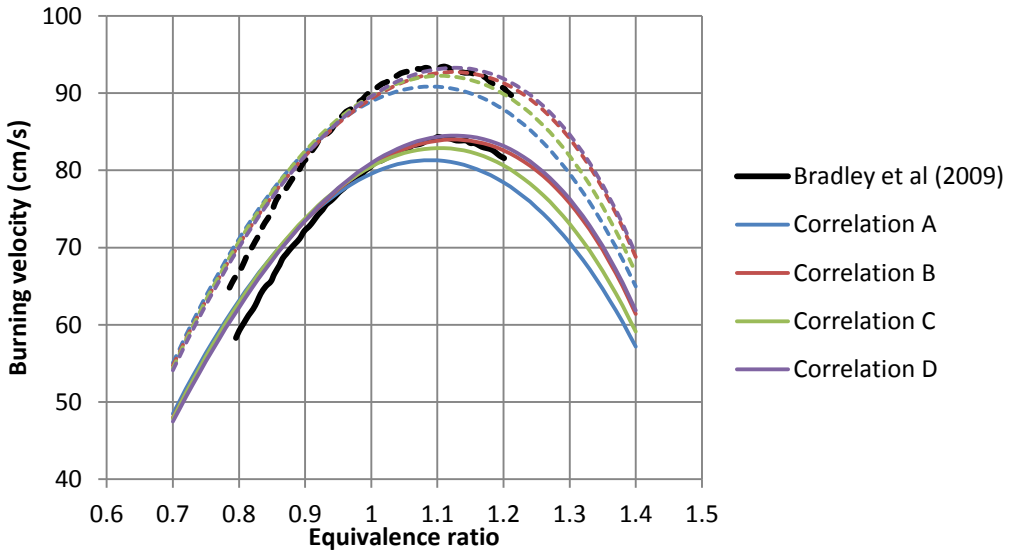

Figure 7.41 – Correlations for ethanol-air mixtures (defined in Table 7.6) at 1 bar, and the results from the computed temperature dependence of Bradley *et al.* (2009). Solid lines represent 453 K; dashed lines represent 480 K.

Comparisons with chemical kinetic simulations using the mechanisms of Saxena and Williams (2007) and Leplat *et al.* (2011) are shown in Figure 7.43. The simulations have been performed by Carsten Olm at Eötvös Loránd University, using the OpenSMOKE 1D premixed flame solver. Simulations were performed for all conditions tested, though only those at 2 bar, 450 K are plotted, since this is where the data is most complete. It is clear that the two mechanisms used give differing results, and that for the W0 and W20 mixtures, the measured burning velocities generally fit between the results from the two mechanisms, with the experimental results being higher on the rich side.

7.3.4 Markstein lengths

Results obtained for the burned gas Markstein lengths are presented for all hydrous ethanol mixtures in Figure 7.44 to Figure 7.46. As expected, there is some scatter in the measurements of Markstein length, but clear trends can be seen. At all conditions, there is a decrease in Markstein length as equivalence ratio is increased. The shape of this relationship also seems to

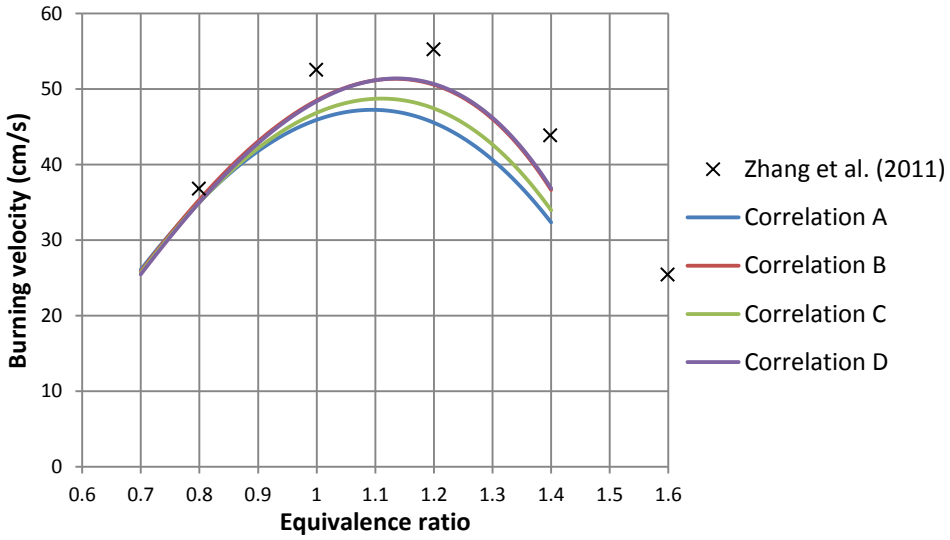

Figure 7.42 – Burning velocity for W25 mixtures at 1 bar, 383 K. Crosses represent results from Zhang *et al.* (2011); lines represent results of correlations (defined in Table 7.6).

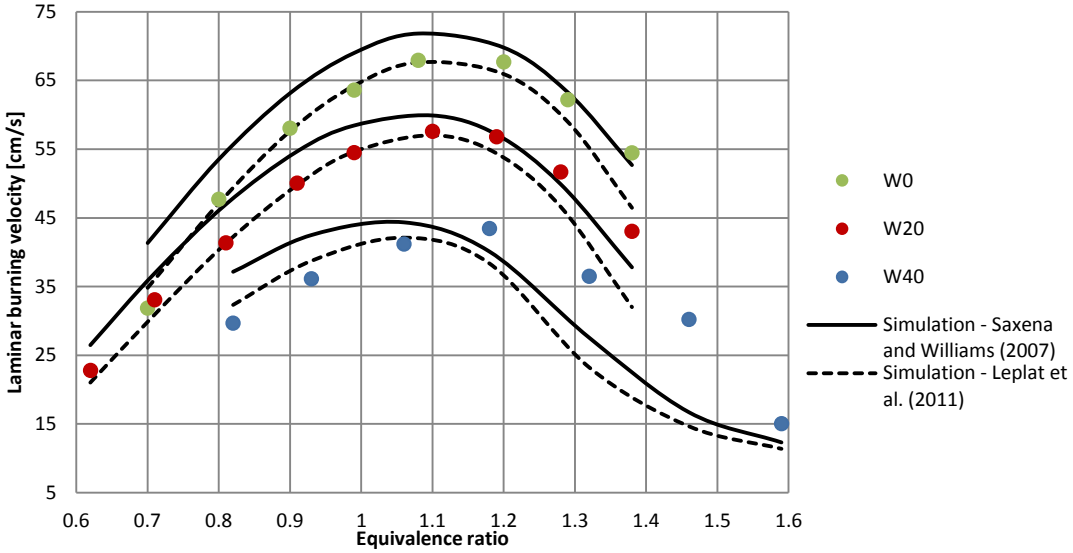

Figure 7.43 – Schlieren results for hydrous ethanol at 2 bar, 450 K compared with the mechanisms of Saxena and Williams (2007) and Leplat *et al.* (2011).

be fairly consistent, with the gradient around stoichiometric equivalence ratios appearing flatter than at equivalence ratios further from stoichiometric. It also appears that increasing the pressure has the effect of reducing the Markstein length, which is consistent with previous studies. The effect of temperature, which from studies of the literature would not be expected to show a clear trend, is not easily discernible. Equally, increasing water content does not appear to have a profound effect upon the measured values of Markstein length, apart from at the most lean and rich conditions tested. More tests would be required to confirm that this result is not a consequence of experimental scatter.

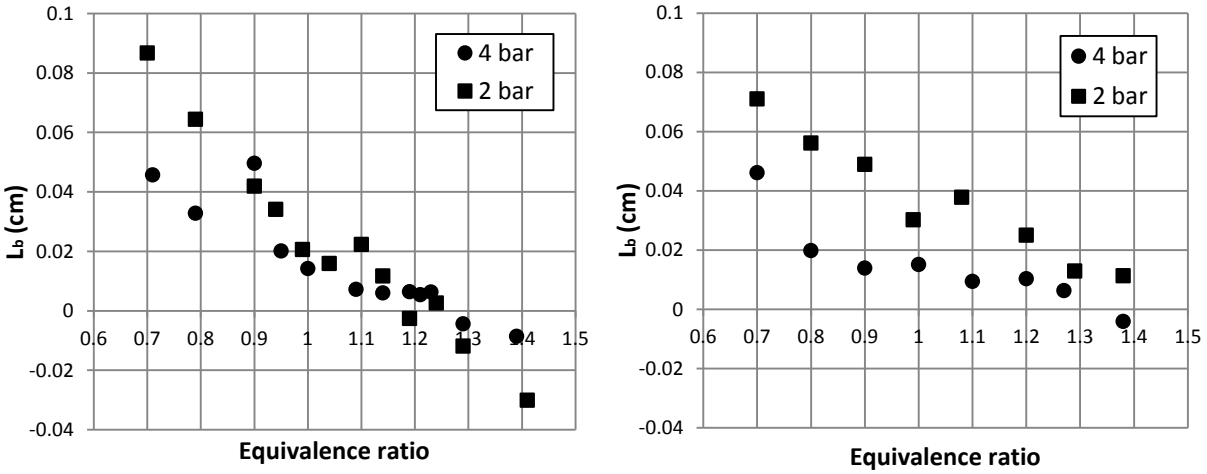

Figure 7.44 – Burned gas Markstein lengths for W0 at $T_u = 380$ K and $T_u = 450$ K.

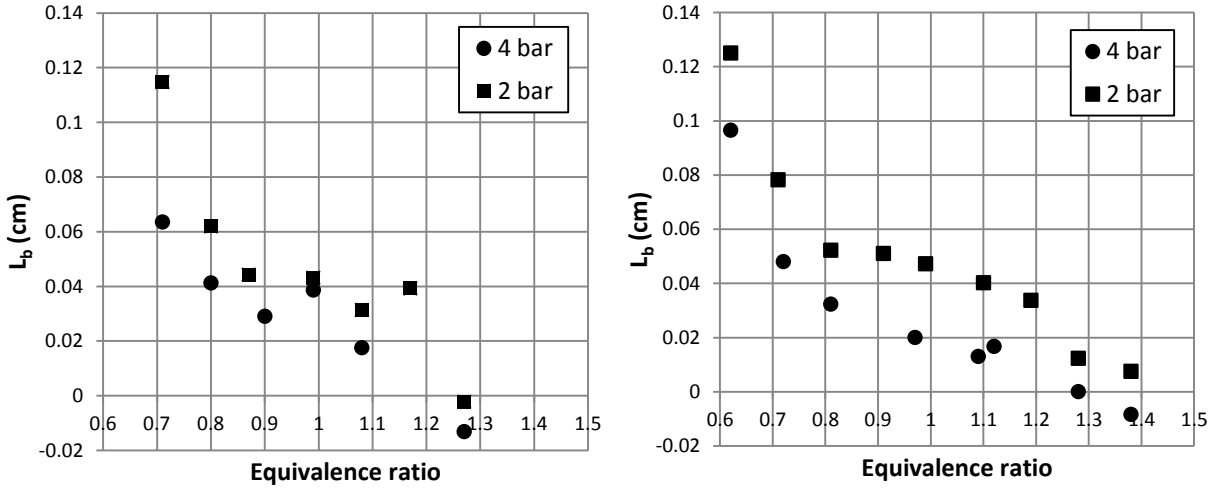

Figure 7.45 - Burned gas Markstein lengths for W20 at $T_u = 380$ K and $T_u = 450$ K.

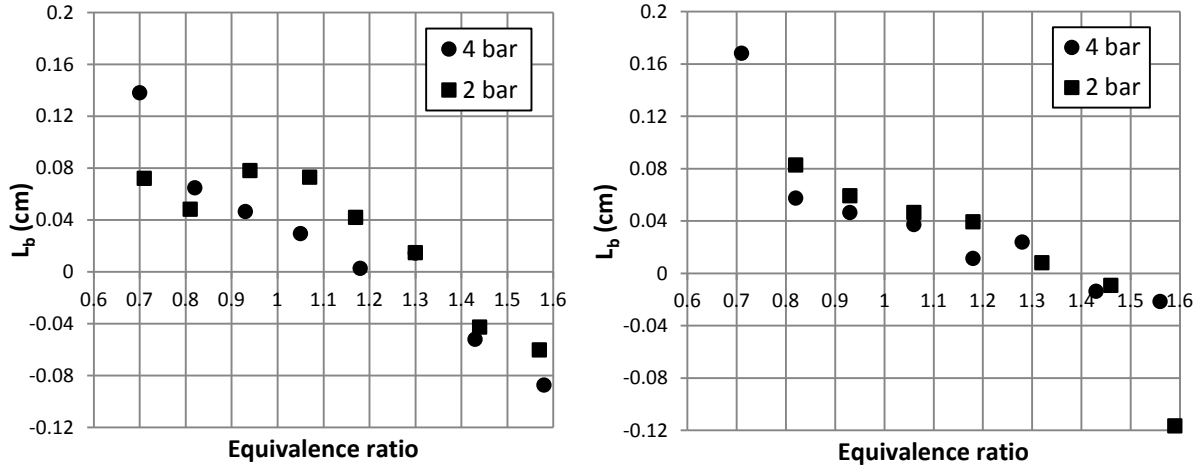

Figure 7.46 - Burned gas Markstein lengths for W40 at $T_u = 380$ K and $T_u = 450$ K.

Some data for burned gas Markstein lengths of ethanol (W0) is available in the literature. Bradley *et al.* (2009) presents results for ethanol-air mixtures obtained using a spherical vessel

with radius of 190 mm and windows with a radius of 75 mm, with images taken at a frame rate of 2000 fps, and a linear extrapolation of flame speed to zero stretch. Tests were performed up to 14 bar when the stability of the flame and maximum combustion pressure allowed, and appears to be the only data for Markstein lengths of ethanol at elevated pressures to date. Varea *et al.* (2012) used their novel PIV technique to determine L_b although only at the single condition of 1 bar and 373 K. A second study by the same authors, Varea *et al.* (2012), focuses on the effect of pressure on burning velocity and Markstein lengths of iso-octane-ethanol-air mixtures, including pure ethanol, although only unburned gas Markstein lengths, L_u, are reported, which cannot be determined with the current methodology. Broustail *et al.* (2011) also present values of L_b for ethanol from measurements made in a cylindrical vessel, again only at a single condition of 1 bar and 393 K, using a non-linear extrapolation to zero stretch.

A comparison of the current results at both 380 K and 450 K with those reported by the above workers is given in Figure 7.47. In general the values obtained here are lower than reported elsewhere. Noting that the results of Varea *et al.* (2012) and Broustail *et al.* (2011) are for conditions of 1 bar, we would expect that the higher pressure analysed here would result in a lower Markstein length. The results for 450 K are very close to those of Bradley *et al.* (2009) which are also for 2 bar. The difference between the results obtained at the two temperatures tested appears to be an anomaly, since the behaviour is not reflected in any of the other compositions, and existing investigations of Markstein lengths do not indicate any consistent trends for temperature dependence. As seen in section 2.5.7, measurements of Markstein length are subjected to considerable amounts of scatter. In this case it is possible that for some equivalence ratios this discrepancy is caused by having too few points for the extrapolation, a limitation resulting from the physical size of the windows.

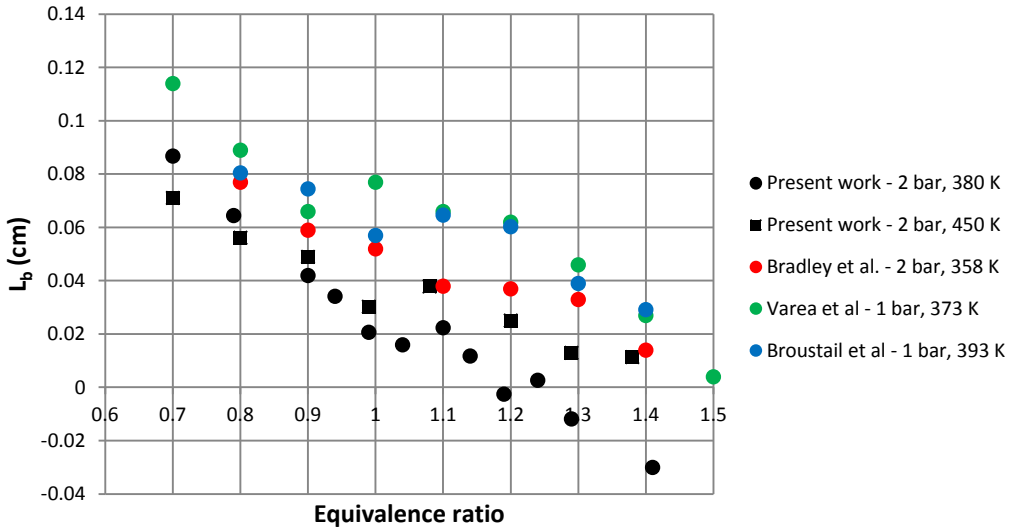

Figure 7.47 – Burned gas Markstein lengths for ethanol-air mixtures compared with literature values.

At higher pressures, Bradley *et al.* (2009) report Markstein lengths for 5 bar, which compare well to the results obtained for 4 bar, at both temperatures tested (Figure 7.48). From their range of results, and knowledge of the pressure dependence of Markstein lengths (e.g. Figure 2.15), we can expect that these two pressures would yield similar results.

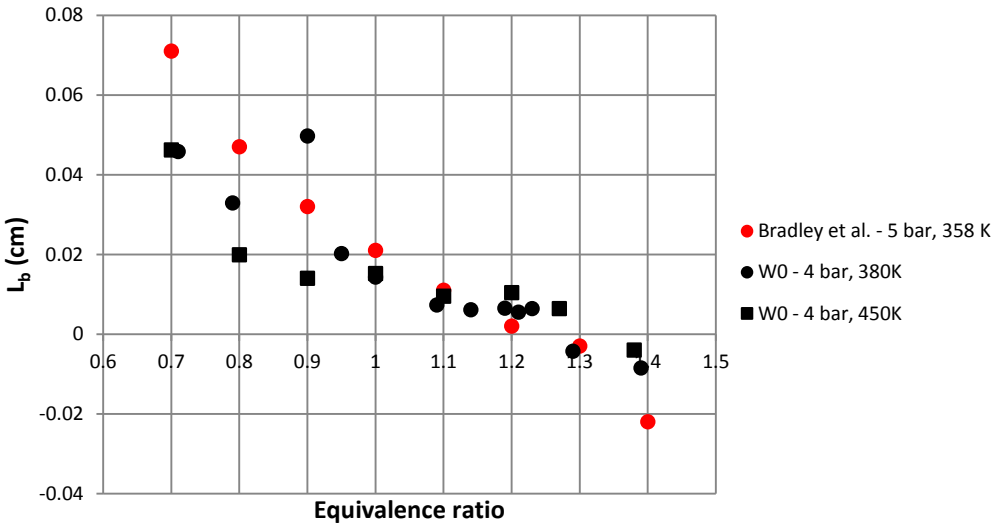

Figure 7.48 – Burned gas Markstein lengths for ethanol-air mixtures at elevated pressure compared with Bradley *et al.* (2009).

7.3.5 Onset of cellularity

As with the biogas data, the onset of cellularity is plotted for various conditions, using the results from the automatic cellularity detection algorithm in *BVImage*.

Considering first the W0 results, it can be seen from Figure 7.49 that there is a clear trend in the pressure at the onset of cellularity. The left hand plot shows all of the W0 experiments

where cellularity occurs for both initial temperatures, plotted for different initial pressures. Cellularity occurs at lower pressure as the equivalence ratio of the mixture increases, although this appears to be independent of initial pressure, as all the data points fall roughly on the same line. The exception to this is the 4 bar initial pressure results; however, this is clearly because the critical pressure is less than 4 bar (as seen in the experiments at lower initial pressures), and so cellularity occurs almost immediately. For cases where the onset of cellularity occurs slightly above 4 bar, the later onset relative to the experiments at lower initial pressures is likely to be as a result of inhibiting effect of the high stretch rate. The right hand plot shows the results for an initial pressure of 2 bar at the two different initial temperatures. Again, the results collapse onto a single line, showing that the pressure at onset of cellularity is independent of initial temperature.

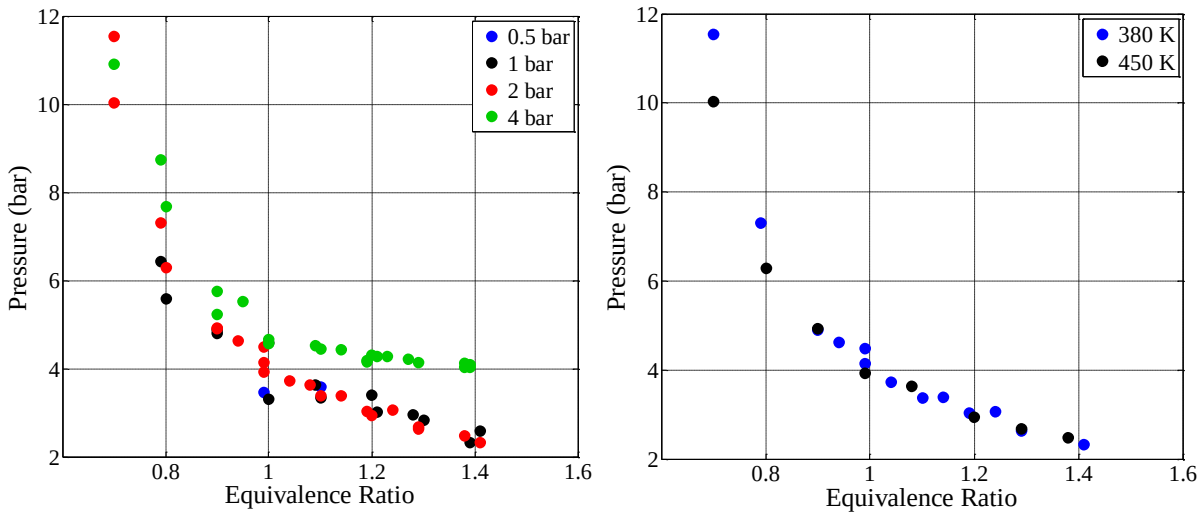

Figure 7.49 – Pressure at onset of cellularity for W0 with varying initial pressure and temperature. Left hand plot shows all experiments; right hand plot shows experiments at $P_0 = 2$ bar.

Since temperature and pressure are isentropically linked in the constant volume vessel, this dependence upon pressure again implies that the temperature at the onset of cellularity is insignificant. This is confirmed by Figure 7.50, which shows that the temperature at the onset of cellularity for experiments at 380 K in the left hand plot, and those at initial temperature of 450 K in the right hand plot. This shows that the temperature at the onset of cellularity increases as pressure reduces or as initial temperature increases, implying that the temperature is not the

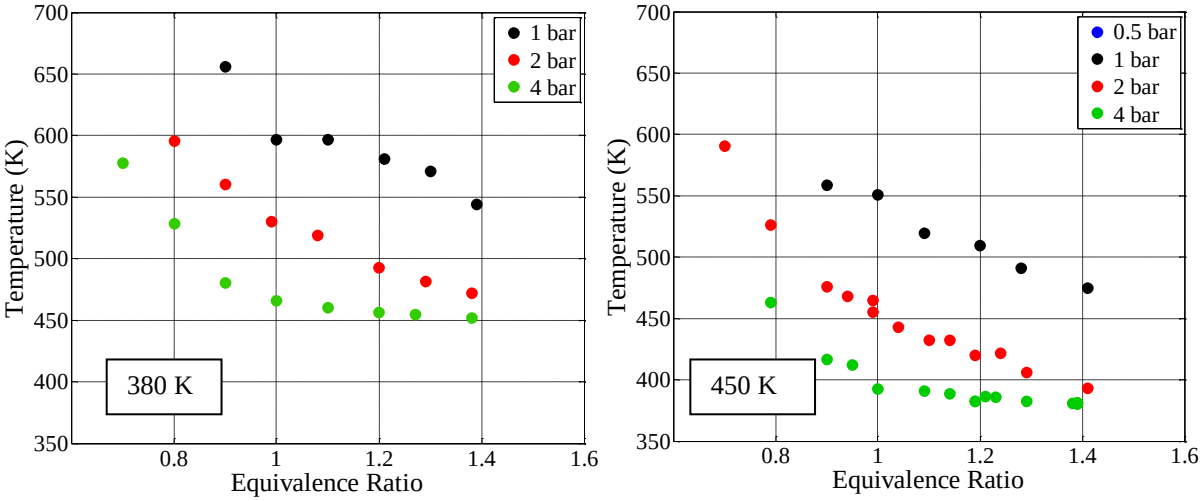

Figure 7.50 – Temperature at onset of cellularity for W0 with varying initial temperature and pressure.

critical factor. Rather, it is indicative of the length of time taken to reach the critical pressure at the onset of cellularity. The effect of increased water content upon the pressure at onset of cellularity is shown in Figure 7.51 for experiments with $T_0 = 450\,\text{K}$ and $P_0 = 2\,\text{bar}$, where it is seen that the increase in water content in the hydrous ethanol leads to a more delayed onset of cellularity.

7.3.6 Engine test results

Tests were performed on hydrous ethanol mixtures using the single cylinder optical engine as described in section 4.2, to provide an opportunity to compare the fundamental burning velocity obtained from the combustion bomb with burn rate in the context of an internal combustion

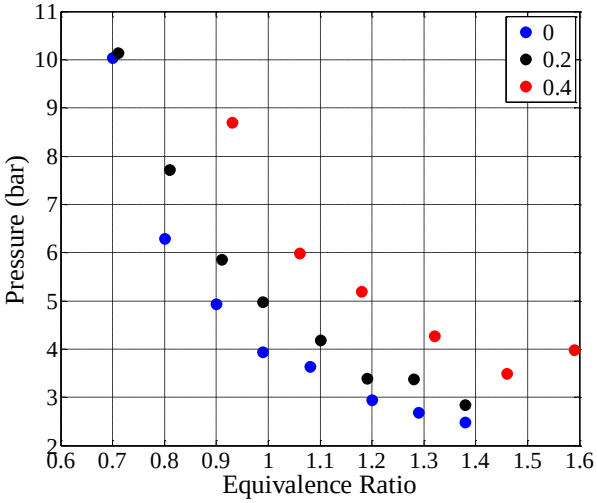

Figure 7.51 – Onset of cellularity for hydrous ethanol with varying water fraction for experiments with $T_0 = 450$ K and $P_0 = 2$ bar.

engine. It would be expected that a faster burn rate will be seen for cases where the laminar burning velocity is higher, due to the direct effect of laminar burning velocity upon the initial stages of flame growth, as well as its impact upon the subsequent turbulent burning velocity, see section 2.9. Whilst strongly influenced, initial flame speed will not be equal to the laminar flame speed as there will need to be time for the flame to stabilise after ignition, Kalghatgi (1985).

Hydrous ethanol blends of water volume fractions up to 40% were tested in both Gasoline Direct Injection (GDI) mode and Port Fuel Injection (PFI) mode, for both stoichiometric ($\lambda \approx 1.01$) and rich ($\lambda \approx 0.9$) conditions. Note that the stoichiometric condition was kept just slightly lean of stoichiometric, since the tests were also used for particulate measurements for another project, and so it was important that at no point a rich mixture was produced. All tests were performed at an engine speed of 1500 rpm, an air flow rate of 2 l/s and injection at 280 crank angle degrees before top dead centre (°ca bTDC). Data was logged at high speed (1°ca resolution) for approximately 70 cycles at each condition, allowing mean, standard deviation and coefficient of variance (COV) values to be obtained. Initial tests were performed on each blend and equivalence ratio by sweeping the ignition timing to determine the minimum ignition advance for best torque (MBT). MBT was estimated by using the spark timing corresponding to highest indicated mean effective pressure (IMEP), and the need for 10% mfb to occur at top dead centre (TDC) and 50% to occur at around 10°ca aTDC. Mass fraction burned is determined using the analysis detailed in section 5.2. For GDI mode, the curves of IMEP against spark timing (shown for W0 in Figure 7.52) appeared relatively flat, yet were able to imply a suitable value of MBT at 25°ca bTDC. Figure 7.53 shows the angle after ignition at which various values of mass fraction burned occur, for varying spark timing. Again, 25°ca bTDC sees the 10% mfb occur at TDC and 50% mfb at around 10°ca aTDC.

Similar analysis was performed for the lean condition and the various hydrous ethanol blends to determine the value of MBT. These are given in Table 7.7 for all the mixtures tested

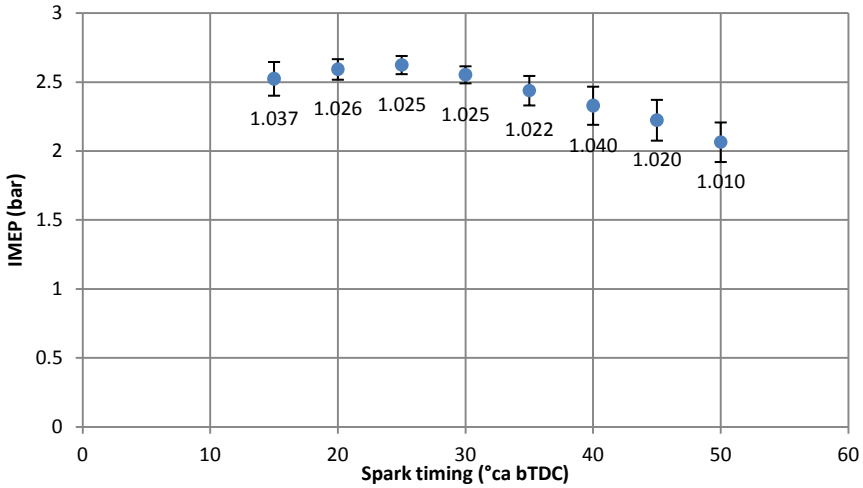

Figure 7.52 – IMEP against spark timing for nominally stoichiometric W0 mixtures in GDI mode. Spot values show the measured value of lambda for each experiment; error bars show the standard deviation.

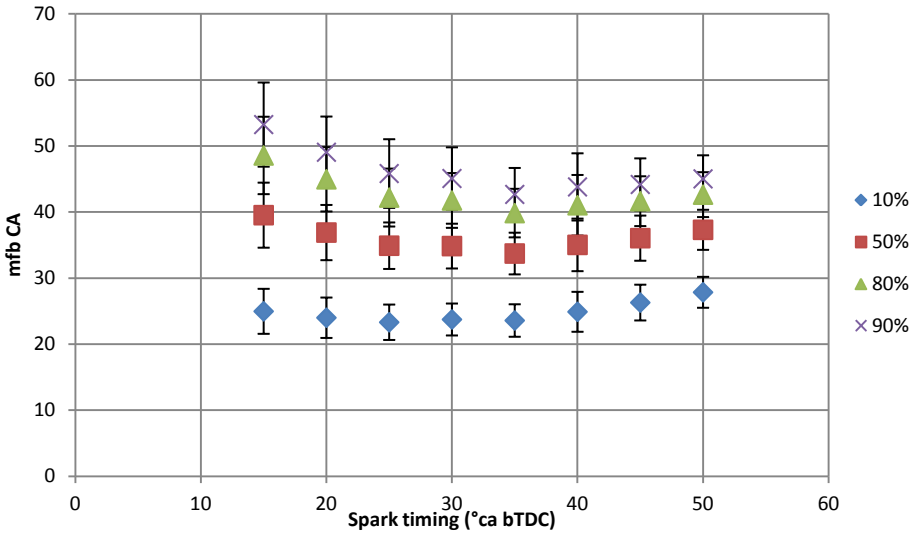

Figure 7.53 – °ca after ignition for various mfb against spark timing for W0 mixtures in GDI mode. Error bars represent the standard deviation at each condition.

in GDI operation mode. Note that the results of PFI mode have not been presented, due to unclear trends being seen. It appears that this was caused by difficulty in ensuring complete vaporisation of the fuel in PFI mode; as the water content is increased, preferential evaporation occurs with significant amounts of water remaining in the intake plenum, meaning that the concentration of water in the mixture entering the combustion chamber is no longer equivalent to that intended, invalidating the results. This could be solved by heating the intake plenum and intake air temperature to encourage vaporisation, but this was not pursued since good results were obtained with GDI operation. It is clear that for rich mixtures, MBT occurs closer to TDC than for the stoichiometric mixtures.

Table 7.7 – MBT for hydrous ethanol mixtures in GDI mode.

	λ = 1.01	**λ = 0.90**
W0	25 CA	20 CA
W20	30 CA	25 CA
W40	40 CA	35 CA

The values for 10, 50, 80 and 90% mfb are plotted for the hydrous ethanol blends for $\lambda = 1.01$ and $\lambda = 0.9$ in Figure 7.54 and Figure 7.55 respectively. Comparing the two figures, it appears that slightly faster burn rates are experienced at $\lambda = 0.9$ than at $\lambda = 1.01$. This is as expected, since for the hydrous ethanol mixtures, determined burning velocities are clearly higher for richer mixtures than for stoichiometric or lean mixtures, with the peak occurring at an equivalence ratio of around 1.1 ($\lambda \approx 0.9$).

The clearest trend here is that the increase in water content results in a longer burn duration for all mfb. The trend here appears to be non-linear by volume, with a bigger increase in burn durations from W20 to W40 than from W0 to W20. The 90% mfb results seem to show a more linear development and a much larger standard deviation in results; in the case of the optical engine, the 90% mfb value is unreliable due to the large crevice volumes compared with a thermodynamic engine, where the 90% mfb point is a more reliable indicator of combustion performance. If this is ignored, the consistency of results is very good. A non-linear trend by volume does not necessarily imply a non-linear trend by mole. Figure 4.7 shows the relationship between ethanol volume fraction and mole fraction when mixed at a constant temperature of 25°C. Using this relationship, it is determined that W20 and W40 blends correspond to 44.8% and 68.4% water by mole respectively. Figure 7.54 and Figure 7.55 can be re-plotted in terms of mole fraction. Figure 7.56 shows the burn durations plotted against water molar fraction for the stoichiometric mixtures. This clearly shows exaggerated non-linear behaviour as W20 and W40 are much closer together in terms of water content when a molar basis is used rather than volumetric basis. A non-linear relationship is reasonable, given the exponential dependence of the rate of reaction upon temperature.

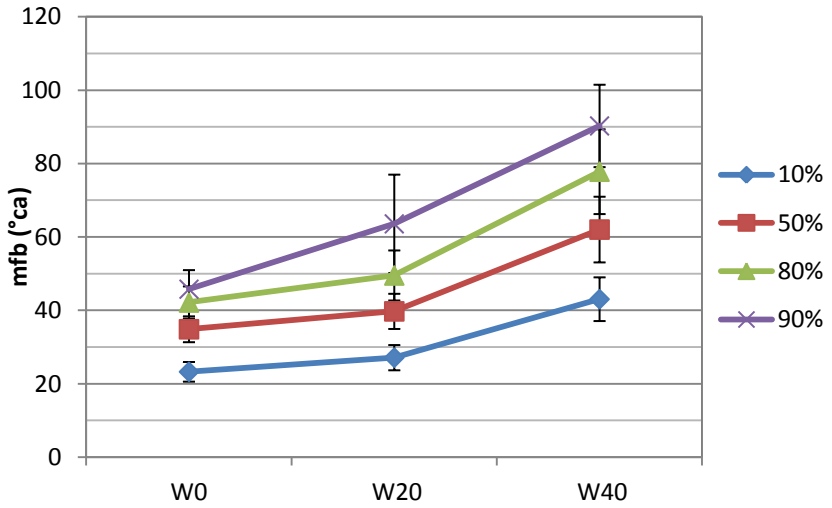

Figure 7.54 – 10, 50, 80 and 90% mfb for hydrous ethanol blends with λ = 1.01.

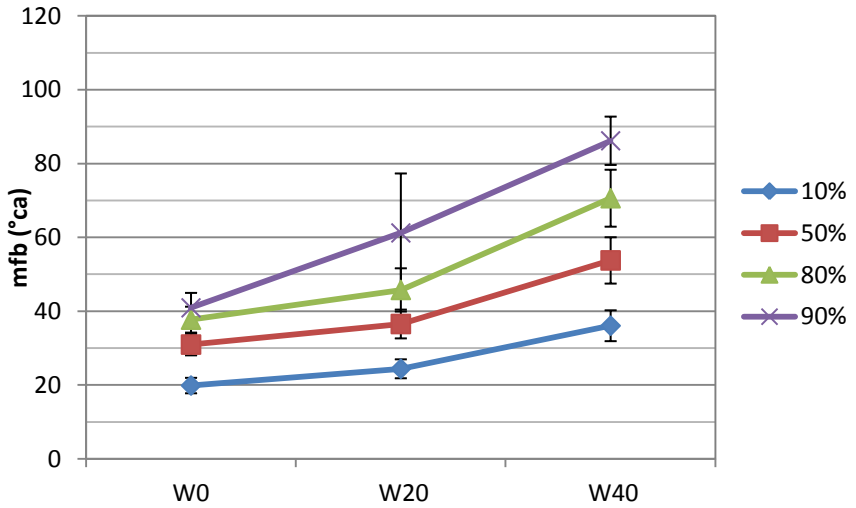

Figure 7.55 – 10, 50, 80 and 90% mfb for hydrous ethanol blends with λ = 0.9.

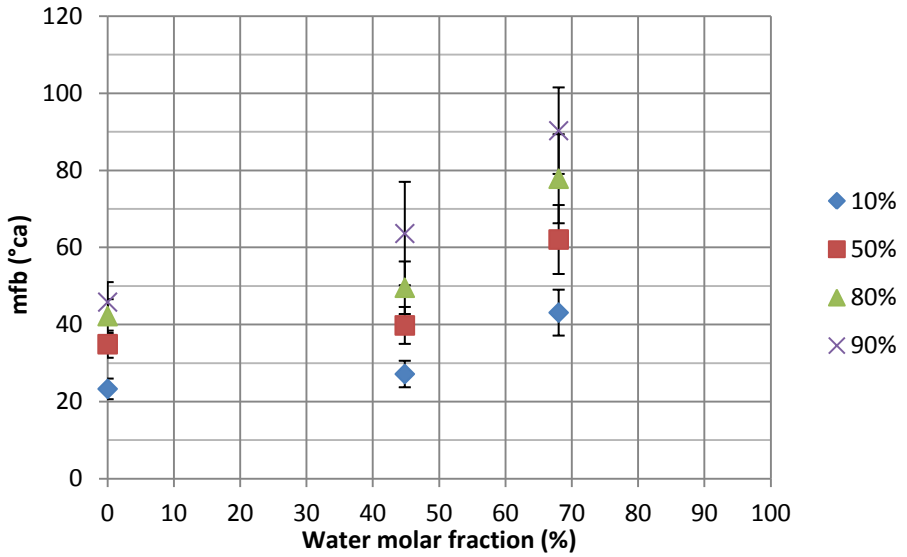

Figure 7.56 - 10, 50, 80 and 90% mfb for hydrous ethanol blends with λ = 1.01.

Drawing a comparison between this result and that seen in the burning velocity correlation plotted in Figure 7.35, the non-linear trend is apparent in both, showing a clear link between the burning velocity obtained from fundamental tests and the effect transferred to engine combustion. The conditions at which the correlation was evaluated in Figure 7.35 were $T_u = 500$ K and $p_u = 5$ bar, which is clearly a single condition which will not directly represent in-cylinder conditions, but it does allow a comparison to be made between the fuels tested. In-cylinder temperature measurements by Williams *et al*. (2014) and the measurements of in-cylinder pressure made during testing suggest that this is roughly representative of the conditions at ignition.

Table 7.8 compares values from the correlation at this condition for each blend, and represents the reduction in burning velocity as the water content is increased, compared with the burning velocity for W0. Also presented are the mfb durations for each fuel, again with the difference relative to W0 represented as a percentage. Whilst the comparison of burning velocities and burn rates begins to demonstrate how our fundamental measurements and engine measurements complement each other, there are other factors to be considered related to the engine performance of these hydrous ethanol blends. In particular, the effect of cycle-by-cycle variations (or cyclic dispersion) is an important consideration. The CoV of IMEP is considered a good indicator, since this is most closely linked to the engine output. For good driveability the

Table 7.8 – Burning velocities from the correlation at T_u = 500 K and p_u = 5 bar, and burn rates from the engine tests. Percentage difference in burning velocity and burn rates are given relative to W0.

		Correlation		10% mfb		50% mfb		80% mfb		90% mfb	
		(cm/s)	% diff	CA	% diff.	CA	% diff.	CA	% diff.	CA	% diff.
λ = 1.0	W0	63.3	-	23.30	-	34.89	-	42.18	-	45.81	-
	W20	53.9	14.8	27.15	16.5	39.76	14.0	49.54	17.4	63.61	38.9
	W40	38.3	39.5	43.08	84.9	62.05	77.8	77.83	84.5	90.29	97.1
λ = 0.9	W0	66.7	-	19.83	-	30.94	-	37.69	-	40.90	-
	W20	57.1	14.3	24.38	22.9	36.52	18.0	45.75	21.4	61.19	49.6
	W40	40.9	38.7	36.04	81.7	53.74	73.7	70.60	87.3	86.15	110.6

CoV of IMEP should be no greater than 5 - 10 %. The CoV of IMEP for the blends tested is shown in Figure 7.57, and shows a surprisingly good level of consistency with regards to cycle-by-cycle variations, even when the water content is high.

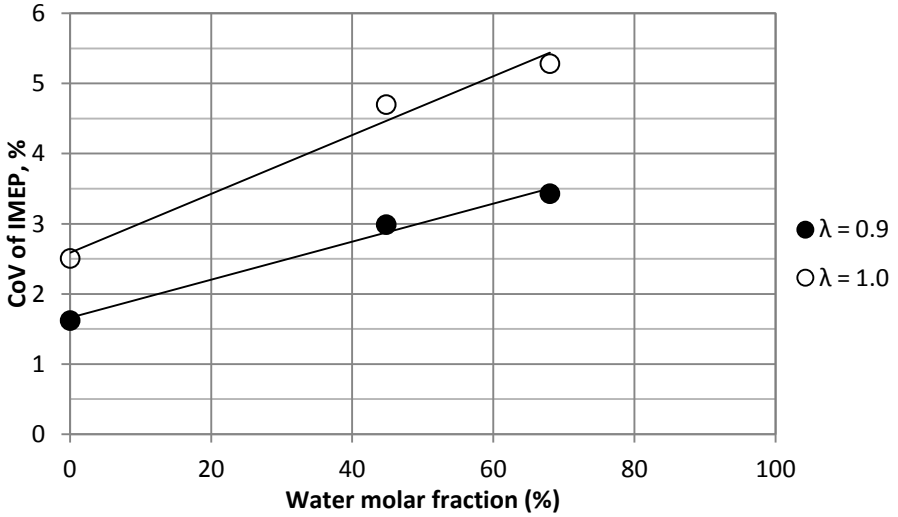

Figure 7.57 – CoV of IMEP for hydrous ethanol mixtures tested at MBT.

7.4 THEO fuels

As described in section 2.8.3, the term THEO fuels is used to describe blends of toluene, n-heptane, ethanol and iso-octane. These blends are of interest, as blends of iso-octane and n-heptane (known as primary reference fuels or PRFs), and blends of iso-octane, n-heptane and toluene (known as toluene reference fuels or TRFs), are widely used as gasoline surrogates. The inclusion of ethanol will represent the blending of such a gasoline surrogate with ethanol. It is hypothesised that such blends may show non-linear behaviour in terms of burning velocity, since studies of the auto-ignition properties of the TRFs showed unexpected behaviour. Therefore, studies of these blends are of interest to observe the effect of blending on the burning velocities of the blends.

7.4.1 Blends tested

It was decided to test all combinations of the four pure components. Since this would result in 11 blends (6 binary, 4 ternary and 1 quaternary), as well as 4 pure components, mixtures tested were limited to those blended equally by volume. More information regarding the composition

of blends is given in section 4.1.7.2. This approach would still be expected to allow the performance of mixing rules to be tested. In addition, due to the time consuming nature of the experimental process, testing was limited to stoichiometric mixtures at this stage. Therefore, correlation results are limited to stoichiometric mixtures, which reduces the number of coefficients down to three, with just the $S_{u,0}$, α_0 and β_0 terms being determined.

7.4.2 Pure component results

Here the results for the pure components are presented. The three term correlation coefficients are presented in Table 7.12, and plotted with the results from the image analysis in Figure 7.58. Due to the small number of experiments performed, the correlation does not have a large number of points to fit. Similarly, each data point from image analysis corresponds to a single experiment rather than an average of a number of experiments. This is a limitation of choosing to test a large number of blends. Nonetheless, there is again reasonable agreement between the correlation values and the values determined from image analysis.

The order of burning velocities of the components follows the trends seen in the existing literature. Iso-octane has the slowest burning velocity, followed by toluene, n-heptane and ethanol. However, the determined burning velocities of ethanol and n-heptane are very close. Few other studies have compared the relative burning velocities directly; from a single study, Farrell *et al.* (2004) presents results from all four components and compares the peak burning velocities, finding the same order as shown here. All results from Farrell *et al.* (2004) are at 450 K and 3 atm, but are acknowledged to be significantly higher than comparable data elsewhere. Nevertheless, the results do allow for comparison of relative burning velocities. Marshall (2010) determined an order based upon the correlations produced for each component, at the same conditions and at an equivalence ratio of 1.1, as a representation of peak burning velocity. From these correlations, it was found that n-heptane had a faster burning velocity than ethanol. However, as has been seen previously, these correlations have not always agreed well with the literature.

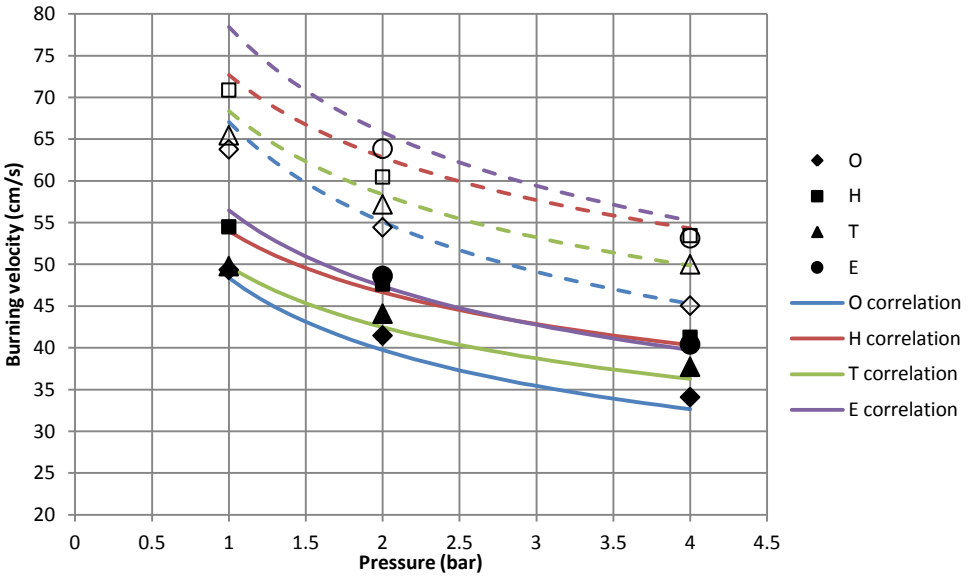

Figure 7.58 – Results from image analysis (points) and correlation (lines) for pure THEO components. Solid lines and symbols represent 380 K, open symbols and dashed lines represent 450 K.

Figure 7.59 shows the correlations derived for stoichiometric mixtures of each of the THEO components at 1 bar and 298 K respectively, along with the corresponding correlations from Marshall (2010). Note that in each case, extrapolation in terms of either temperature or pressure is required. It is clear that for all fuels the correlation results are higher than those of Marshall. For ethanol and n-heptane, the higher temperature exponent of Marshall is evident, although except for n-heptane, the current correlation continues to give higher burning velocities at all temperatures. The current correlations suggest that ethanol is more strongly affected by increases in temperature and pressure than n-heptane.

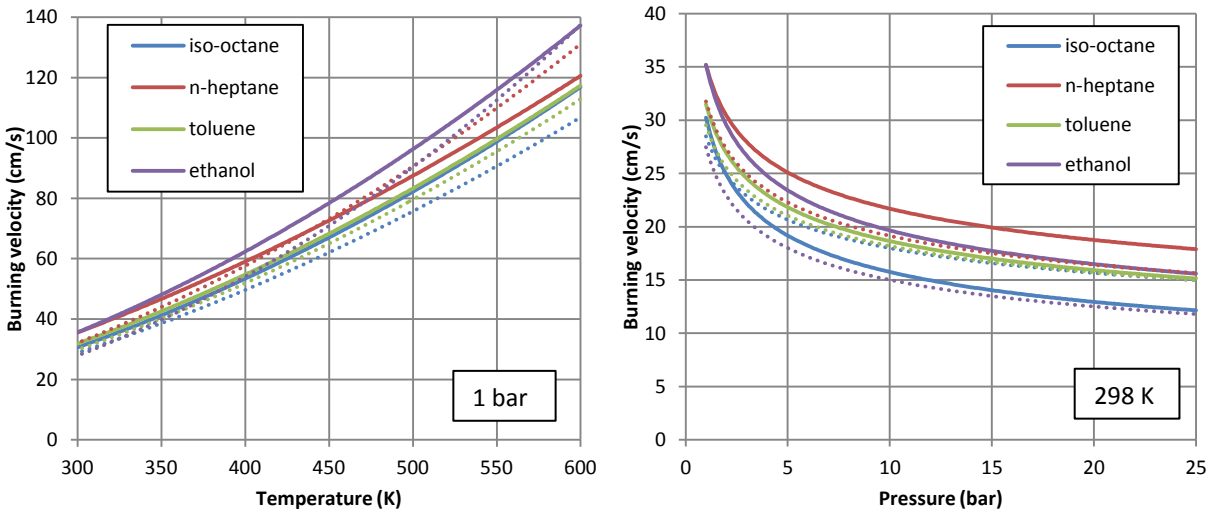

Figure 7.59 – Comparison of correlation results (solid lines) with the correlation of Marshall (dotted lines) for stoichiometric THEO components at 1 bar and 298 K respectively.

Heat flux burner experiments reported in van Lipzig *et al.* (2011) compare n-heptane, iso-octane and ethanol, as well as their binary and tertiary mixtures. Tests were performed at 298 K and 338 K, at atmospheric pressure. It is clear from their results that ethanol gives a faster burning velocity than n-heptane, at both temperatures. Sileghem *et al.* (2014) also use the heat flux burner to investigate primary reference fuels (blends of iso-octane and n-heptane) and simple alcohols, and includes the pure components, also at 338 K. The results also show that ethanol has a faster burning velocity than n-heptane. Dirrenberger *et al.* (2014) present results from heat flux burner measurements for all four THEO components and also find the same order in terms of relative burning velocity.

Burning velocity results of the pure components found in the literature, as well as the results from image analysis are presented in Table 7.9, along with the corresponding results from the 3 term correlations given in Table 7.12. Direct comparison of schlieren results with most of the data in the literature is not possible due to the fact that tests were only performed at 380 K and 450 K whereas much of the literature data is for ambient conditions. Also note that in many cases, correlation values will be an extrapolation beyond the range of fitted data.

Study of Table 7.9 shows that for all the THEO components, the correlations give lower burning velocities than most of the literature data, especially extrapolations to ambient conditions. For toluene, the results of Hirasawa *et al.* (2002) and Kumar and Sung (2010), which use PIV of a counterflow flame, are close to the correlation, whereas other ambient data is somewhat higher. At elevated temperature, discrepancy between the correlation and results of Sileghem *et al.* (2013) and Dirrenberger *et al.* (2014) from heat flux burner measurements is much reduced. For n-heptane, the correlation gives results that are consistently about 2 cm s^{-1} lower than the heat flux burner measurements (the results of van Lipzig *et al.* (2011) are acknowledged to be too high). Jerzembeck *et al.* (2009) present high pressure results at 373 K from spherically expanding flames, with flame speeds extrapolated linearly back to zero stretch. The results for their study give much lower burning velocities at elevated pressures, indicating

Table 7.9 – Burning velocities of stoichiometric pure THEO components from the literature compared with results from the 3 term correlations (values in brackets represent extrapolated conditions).

Fuel	Temperature (K)	Pressure (bar)	Reference	Burning velocity (cm s^{-1})	
				Data	Correlation
Toluene	298	1.0	Dirrenberger *et al.* (2014)	35.8	(31.5)
			Davis and Law (1998)	35.2	
			Hirasawa *et al.* (2002)	31.9	
			Kumar and Sung (2010)	32.1	
			Sileghem *et al.* (2013)	34.1	
	353	1.0	Ji *et al.* (2012)	44.4	(43.3)
	358	1.0	Sileghem *et al.* (2013)	45.8	(44.5)
			Dirrenberger *et al.* (2014)	45.7	
	380	1.0	Current work (from image processing)	49.8	49.7
		2.0		44.1	42.5
		4.0		37.8	36.3
	398	1.0	Dirrenberger *et al.* (2014)	55.2	54.2
	400	1.0	Kumar and Sung (2010)	56.7	54.8
	450	1.0	Current work (from image processing)	65.5	68.3
		2.0		57.2	58.4
		4.0		50.0	49.9
		3.0	Johnston and Farrell (2005)	49.5	53.1
	470	1.0	Kumar and Sung (2010)	76.2	74.2
n-heptane	298	1.0	van Lipzig *et al.* (2011)	39.6	(35.2)
			Sileghem *et al.* (2013)	37.3	
			Davis and Law (1998)	36.8	
			Huang *et al.* (2004)	38.2	
			Kumar and Sung (2010)	41.8	
			Dirrenberger *et al.* (2014)	37.3	
	338	1.0	van Lipzig *et al.* (2011)	48.0	(43.9)
			Sileghem *et al.* (2014)	45.5	
	358	1.0	Dirrenberger *et al.* (2014)	52.0	(48.6)
	373	10.0	Jerzembeck *et al.* (2009)	33.3	(32.2)
		15.0		28.1	(29.6)
		20.0		26.0	(27.8)
		25.0		19.4	(26.6)
	380	1.0	Current work (from image processing)	54.5	54.0
		2.0		47.7	46.7
		4.0		41.3	40.3
	393	1.0	Dirrenberger *et al.* (2014)	59.4	57.3
	400	1.0	Kumar and Sung (2010)	64.4	59.1
	450	1.0	Current work (from image processing)	70.9	72.7
		2.0		60.5	62.8
		4.0		53.5	54.3
	470	1.0	Kumar and Sung (2010)	88.0	78.4

Ethanol	298	1.0	van Lipzig *et al.* (2011)	42.1	(35.2)
			Sileghem *et al.* (2014)	39.5	
			Dirrenberger *et al.* (2014)	41.2	
			Konnov *et al.* (2011)	40.1	
	300	1.0	Bradley *et al.* (2009)	35.3	(35.6)
	338	1.0	van Lipzig *et al.* (2011)	51.1	(44.9)
			Konnov *et al.* (2011)	48.9	
			Sileghem *et al.* (2014)	48.1	
	358	1.0	Konnov *et al.* (2011)	52.5	(50.3)
			Sileghem *et al.* (2014)	53.5	
			Dirrenberger *et al.* (2014)	55.4	
		1.0	Bradley *et al.* (2009)	51.9	(50.3)
		2.0		37.5	(42.2)
		5.0		30.9	(33.5)
		7.0		28.1	(30.7)
		10.0		25.8	(28.1)
	373	10.0	Beeckmann *et al.* (2009)	27.0	(30.4)
	380	2.0	Current work (from image processing)	48.6	47.4
		4.0		40.4	39.8
	393	1.0	Dirrenberger *et al.* (2014)	64.5	60.3
			Bradley *et al.* (2009)	54.7	
	398	1.0	Broustail *et al.* (2011)	63.6	61.8
	450	2.0	Current work (from image processing)	63.9	65.8
		4.0		53.2	55.2
Iso-octane	298	1.0	van Lipzig *et al.* (2011)	34.8	(30.3)
			Sileghem *et al.* (2013)	32.8	
			Dirrenberger *et al.* (2014)	33.3	
			Kelley *et al.* (2011)	35.6	
			Kumar and Sung (2010)	33.0	
	338	1.0	van Lipzig *et al.* (2011)	42.6	(38.6)
			Sileghem *et al.* (2014)	40.1	
	358	1.0	Bradley *et al.* (1998)	46.5	(43.1)
			Dirrenberger *et al.* (2014)	44.3	
			Sileghem *et al.* (2013)	44.3	
	373	1.0	Varea *et al.* (2013)	50.1	(46.7)
		10.0	Beeckmann *et al.* (2009)	25.3	(24.3)
		10.0	Jerzembeck *et al.* (2009)	27.8	(24.3)
		15.0		25.2	(21.7)
		20.0		22.6	(20.0)
		25.0		20.9	(18.7)
	380	1.0	Current work (from image processing)	49.4	48.4
		2.0		41.5	39.7
		4.0		34.1	32.7
	398	1.0	Broustail *et al.* (2011)	50.9	52.9
			Dirrenberger *et al.* (2014)	53.6	
	400	1.0	Kumar and Sung (2010)	56.7	53.4
	450	1.0	Current work (from image processing)	63.8	67.0
		2.0		54.5	55.1
		4.0		45.1	45.3
	470	1.0	Kumar and Sung (2010)	77.0	72.9

much stronger pressure dependence. For the ethanol results, the results of the simple 3 term stoichiometric correlation can be compared with the complete 14 term correlations derived in section 7.3.2 with the 3 term correlation around $3.5\,cm\,s^{-1}$ lower. The heat flux burner measurements are higher still, whereas the results from the spherical flame experiments of Bradley *et al.* (2009) are close to that of the 3 term correlation. A difference of 3-4 $cm\,s^{-1}$ remains at elevated temperatures, showing comparable temperature dependence. The high pressure results of Bradley *et al.* (2009) suggest a stronger pressure dependence (as also seen in Figure 7.39). For iso-octane, once again the correlation gives lower values at ambient conditions, with the disrepancy decreasing as the temperature or pressure is increased, although th results of Kumar and Sung (2010) seem particularly high.

7.4.3 Binary mixture results

Binary mixtures of the THEO components have been tested at the same conditions of temperature and pressure as the individual components. Each binary blend is mixed to be 50% by volume of each component. Further compositions were not tested due to the number of tests that would be required. Binary blends are denoted by the initials of the components, e.g. OH is a binary blend of iso-octane and n-heptane. The six binary blends tested are OH, OT, OE, EH, ET and HT, and the results from the image analysis and correlation are presented in Figure 7.60 at both 380 K and 450 K. Based upon the image analysis results, the variation in burning velocities of the binary fuels is greatest at 450 K. The fastest blend is EH and the slowest is OT, which would perhaps be the expected behaviour based upon the burning velocities of the individual components and a simple mixing rule. However, the order of fuels at 4 bar differs from that at 1 bar, with OE and ET dropping down the order as pressure increases.

In order to determine the effect on burning velocity of blending in binary mixtures, the results for each blend are compared with those of the corresponding pure components in Figure 7.61. In the majority of cases, the burning velocity of the blend remains bounded by that of the pure components, advocating the use of a simple mixing rule. The exception appears to be the

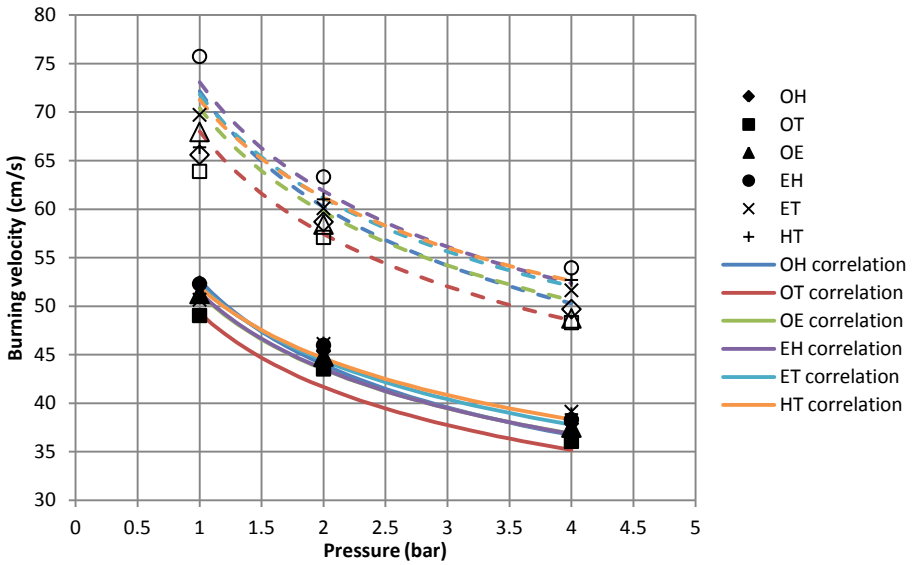

Figure 7.60 – Burning velocities from image analysis of stoichiometric binary blends at 380 K (solid symbols) and 450 K (open symbols).

EH blend at 380 K, with a burning velocity based on the image analysis of 1-2 cm s^{-1} less than the pure components, which have very similar values. The results from the correlations also show the same trend. At elevated temperatures, the EH results begin to match those of the pure ethanol, which are slightly higher than those of n-heptane.

Binary blends of THEO components have not been widely tested in the literature, although the work of van Lipzig *et al.* (2011) does present results for blends of 50% by volume as tested here. The results of van Lipzig *et al.* (2011), given in Table 7.10, are consistently 2-3 cm s^{-1} higher than elsewhere in the literature. However, for the EH results, there is a large discrepancy which is likely to be due to the high value of temperature exponent when extrapolating to low temperatures. Iso-octane and ethanol blends have received wider attention. Broustail *et al.* (2011) perform tests on iso-octane-ethanol blends in increments of 25% by volume at 393 K, using a non-linear extrapolation of spherically propagating flames at 1 bar. Sileghem *et al.* (2014) tested similar blends but at 338 K using the heat flux burner method.

Marshall (2010) presents correlations for stoichiometric iso-octane, ethanol, and a 50/50 mix by volume. These results are compared to the O, E and OE correlations in Figure 7.62. The results of Marshall are lower than the current results, although similar trends in terms of temperature and pressure are seen.

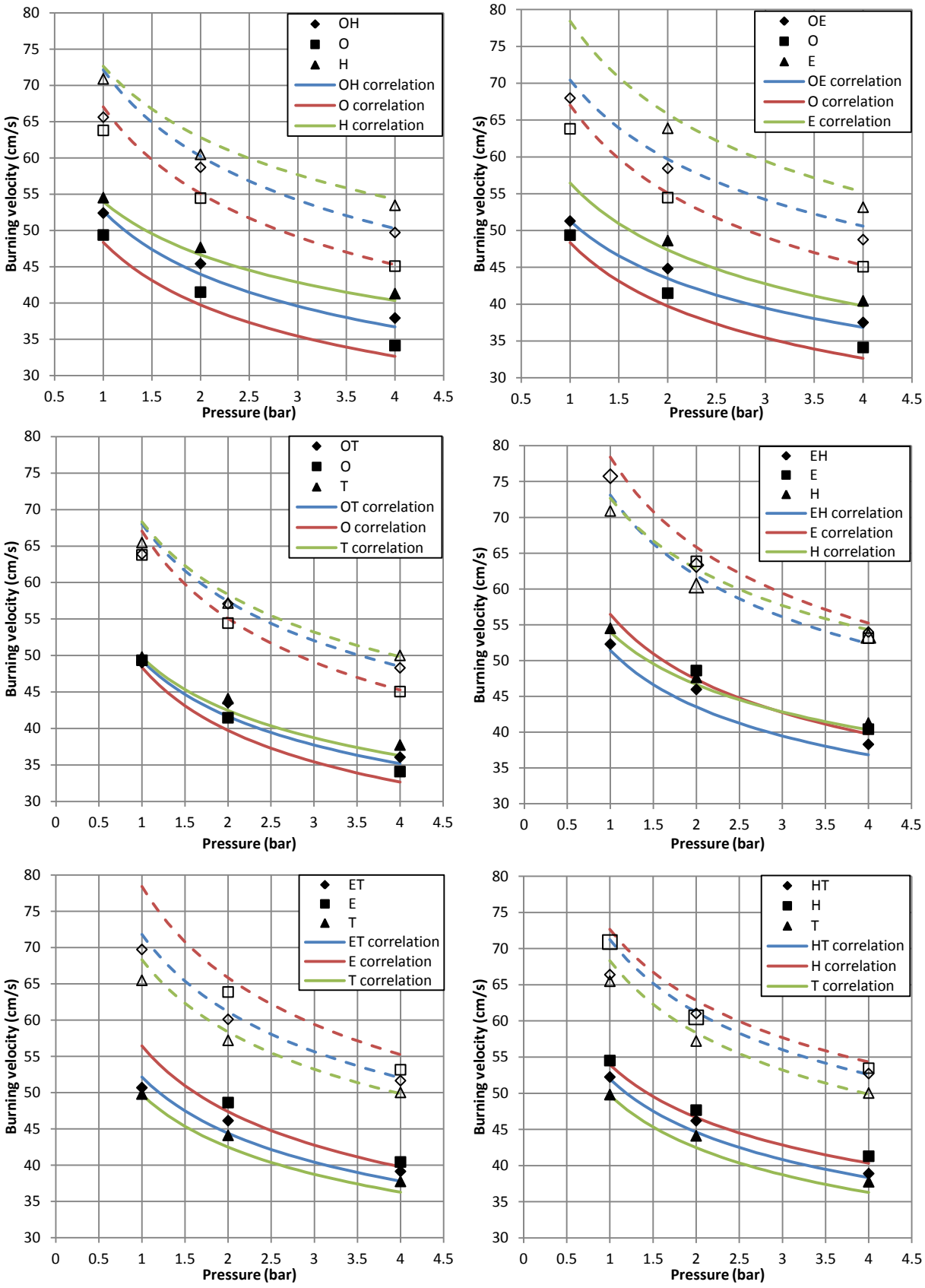

Figure 7.61 – Burning velocity results from image analysis (points) and correlation (lines) for stoichiometric binary blends and their pure components. Solid symbols and lines represent 380 K, open symbols and dashed lines represent 450 K.

Table 7.10 - Burning velocities of stoichiometric binary blends of THEO components from the literature compared with results from the 3 term correlations (values in brackets represent extrapolated conditions).

Fuel	Temperature (K)	Pressure (bar)	Reference	Burning velocity (cm s^{-1})	
				Data	Correlation
OH	298	1.0	van Lipzig *et al.* (2011)	37.4	(33.5)
	338	1.0	van Lipzig *et al.* (2011)	45.2	(42.4)
EH	298	1.0	van Lipzig *et al.* (2011)	40.6	(31.0)
	338	1.0	van Lipzig *et al.* (2011)	49.3	(40.3)
OE	298	1.0	van Lipzig *et al.* (2011)	37.6	(32.5)
	338	1.0	van Lipzig *et al.* (2011)	45.6	(41.2)
	338	1.0	Sileghem *et al.* (2014)	42.8	(41.2)
	393	1.0	Broustail *et al.* (2011)	56.4	54.6

A number of other studies have investigated blends of iso-octane and ethanol, though in ratios other than equal by volume. Gülder (1984) investigated blends up to 20% ethanol, whilst Beeckmann *et al.* (2009) investigated just 10% ethanol. This study showed the interesting result that for lean mixtures, the blend resulted in higher burning velocities than either pure component, although only stoichiometric blends were tested here and such behaviour is not apparent at the conditions tested. Varea *et al.* (2013) tested blends in increments of ethanol by mole rather than by volume, none of which can allow a direct comparison. Huang *et al.* (2004) test PRFs with octane numbers between 85 and 100 to span the range of commercial gasolines, and in general finds that the burning velocity deviates only slightly from that of iso-octane, particularly around stoichiometric. Jerzembeck *et al.* (2009) only investigate a single PRF with 87% iso-octane.

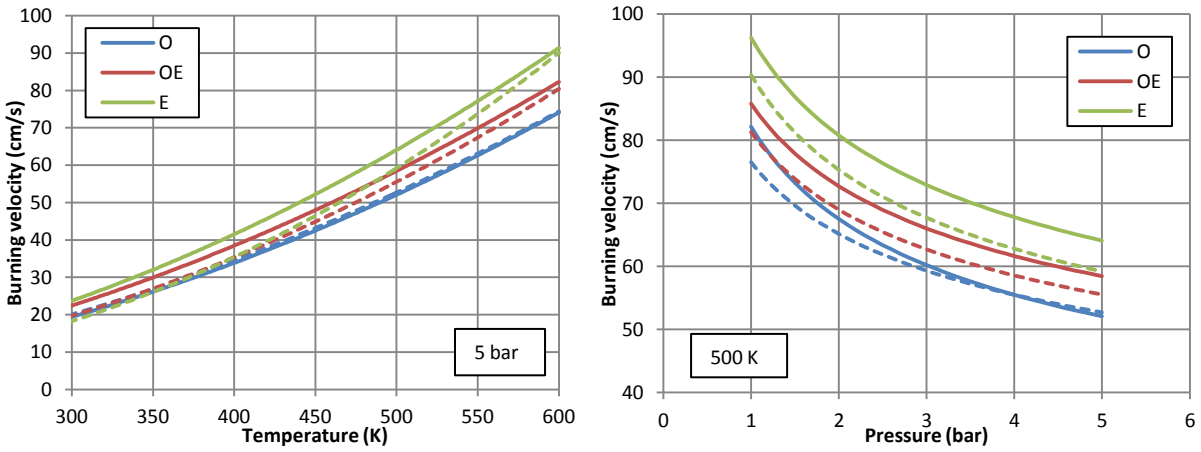

Figure 7.62 – Correlation for O, E and OE (solid lines) compared with that of Marshall (dashed lines) at 5 bar, varying temperature and 500 K varying pressure respectively.

Recent studies have begun to introduce mixing rules to describe the burning velocity of blends, which are summarised in section 2.3.5. These rules are applied to the binary blends and compared with experimental results from the image analysis in Figure 7.63. In the case of OH, OT and HT, it is clear that there is not much difference between the mixing rules for blends of equal volume, making it impossible to determine which gives the best fit to the experimental data. In the case of OT and in particular OE, the different mixing rules give more substantial differences, with the direct molar fraction and the molar fraction based upon Le Chatelier's principle (Equations (2.32) and (2.34) respectively) giving the higher burning velocities, and those based upon energy fraction, Equation (2.33), giving the lowest. For the OE blend, the mixing rule based upon energy fraction seems to be the best fit to the experimental data, and the same could be argued for ET, although the spread of results is much smaller. It is clear that the unexpected behaviour of EH described earlier is not reflected by simple mixing rules. However, Sileghem (2012) shows more consistent agreement with the mixing rules, suggesting that this is likely to be due to the fact that the measurements for E and H are so close, that the measurements made here are not precise enough to capture the behaviour.

7.4.4 Ternary blends

Ternary blends were mixed on the basis of equal volume and tested at the same conditions of temperature and pressure as the pure components and binary blends. Relative burning velocities of the ternary blends are shown in Figure 7.64. Again, the difference in burning velocities is greatest at higher temperatures. The blends including both iso-octane and toluene have the lowest burning velocities, whereas those with both n-heptane and ethanol are fastest, as would be expected from the component burning velocities. At both temperatures, the HET blend is significantly faster at 1 bar, yet drops rapidly to match that of OET as the pressure increases.

The burning velocities from both the image analysis and from the correlation are compared along with the relevant pure components in Figure 7.65. As with the binary blends, the correlation values are slightly below those of the image analysis. The results of the image

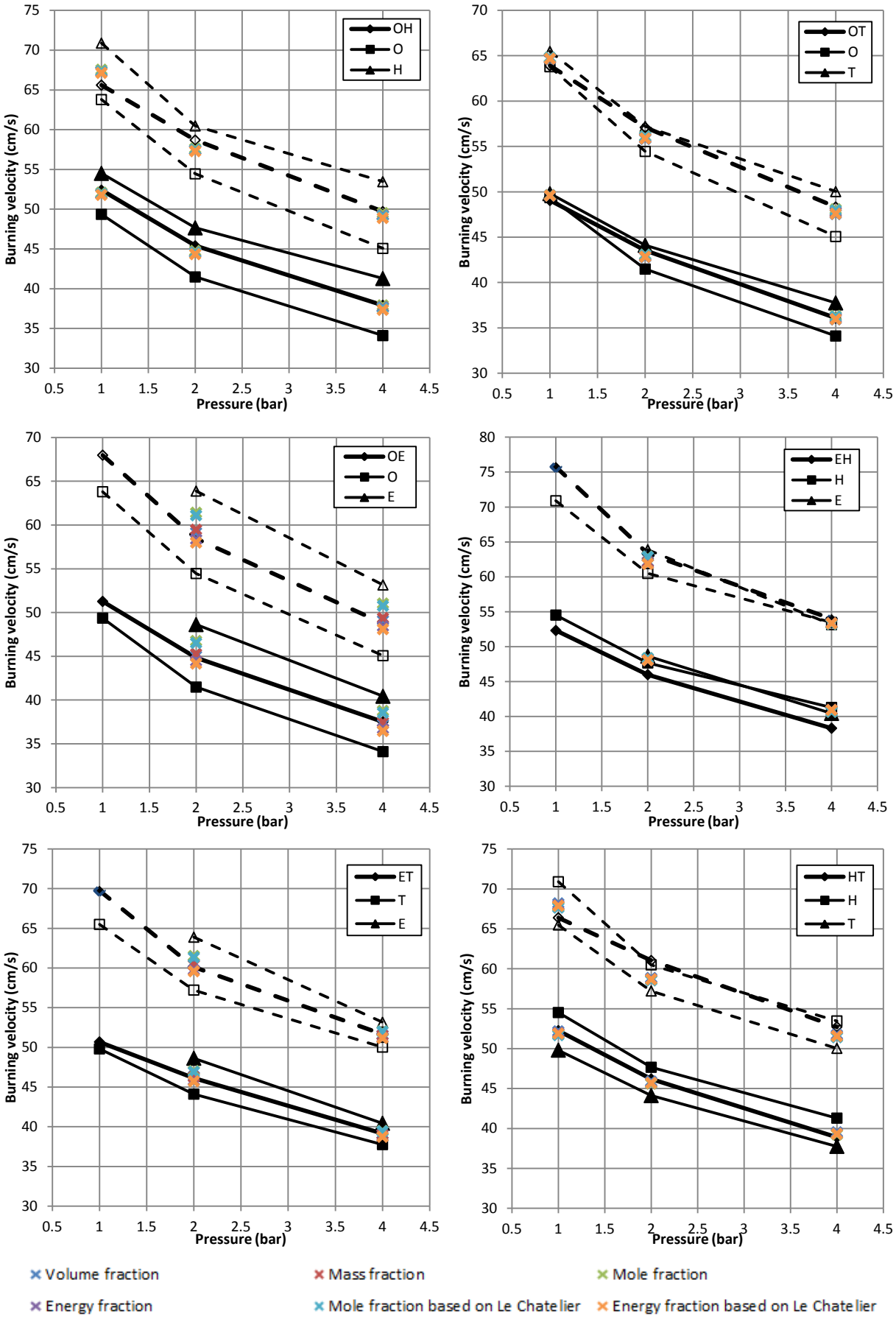

Figure 7.63 – Mixing rules for binary blends compared with results from image analysis at 380 K (solid symbols) and 450 K (open symbols).

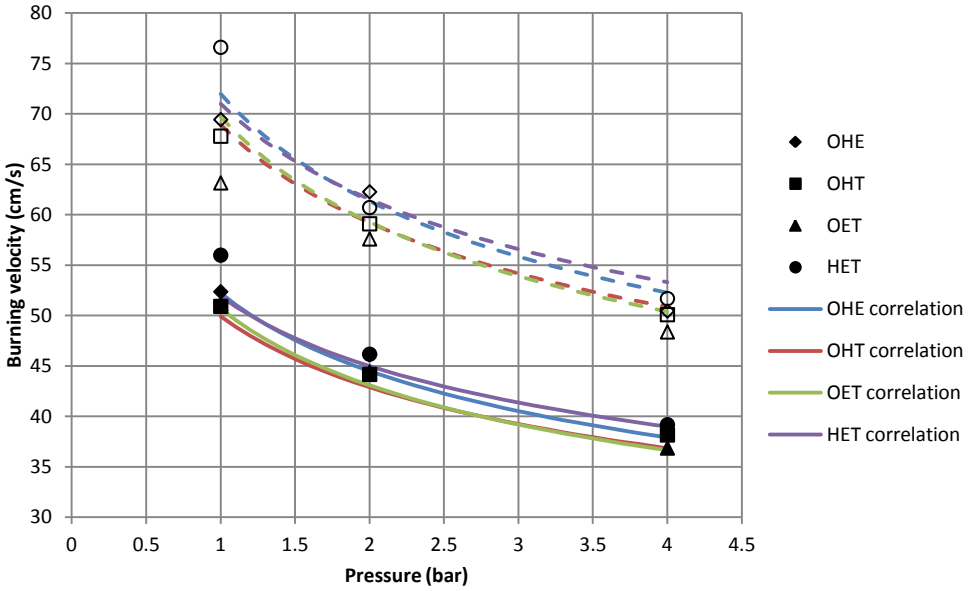

Figure 7.64 - Burning velocities from image analysis of stoichiometric ternary blends at 380 K (solid symbols) and 450 K (open symbols).

analysis are compared with the mixing rules in Figure 7.66. For the OHT blend, the mixing rules display little variation and all fit the experimental data well, particularly at 380 K. The introduction of ethanol to the blends results in bigger differences, although the range is still relatively small, particularly for HET. For the OET blend, the mixing rules based upon energy fraction appear to give the best match to the experimental data.

Fewer studies of ternary blends exist than of binary blends. van Lipzig *et al.* (2011) present results for an OHE mix and whilst their results are shown to be generally high, the discrepancy is larger for the ternary than binary blends as shown by comparison of Table 7.11. Elsewhere, ternary blends have been tested, although at different compositions to those tested here. Dirrenberger *et al.* (2014) proposed a surrogate gasoline in the form of a TRF blended in order to match the properties of the commercial gasoline TAE7000. Their surrogate blend contained 13.7% n-heptane, 42.9% iso-octane and 43.4% toluene by volume and matched the burning velocities of the TAE7000 reasonably well at 1 bar, 358 K. TAE7000 itself is shown to be close to toluene, though with a slightly higher burning velocity between equivalence ratios of 0.9 and 1.2. Whilst the composition of the surrogate differs from the OHT blend, in both cases there is close agreement between the burning velocity of the blend and that of toluene, particularly at 380 K. At 450 K, the OHT blend image results are above that of toluene, which could be due to

the increased fraction of n-heptane elevating the result; however, the correlations in Figure 7.65 and mixing rules shown in Figure 7.66 suggest a much closer fit to toluene than the experimental result. Sileghem *et al.* (2012) compared the mixing rules to simulations of a TRF (69% iso-octane, 14% n-heptane and 17% toluene) using the chemical kinetic mechanism of Andrae *et al.* (2008). Again, whilst different in composition, agreement with the OHT blend can be seen; at conditions of 1 bar, 600 K, the mechanism of Andrae *et al.* (2008) gives a burning velocity of 117 cm s^{-1}, whereas the OHT correlation gives 119 cm s^{-1}; at 40 bar, the burning velocities are 47.4 cm s^{-1} and 53.1 cm s^{-1} respectively.

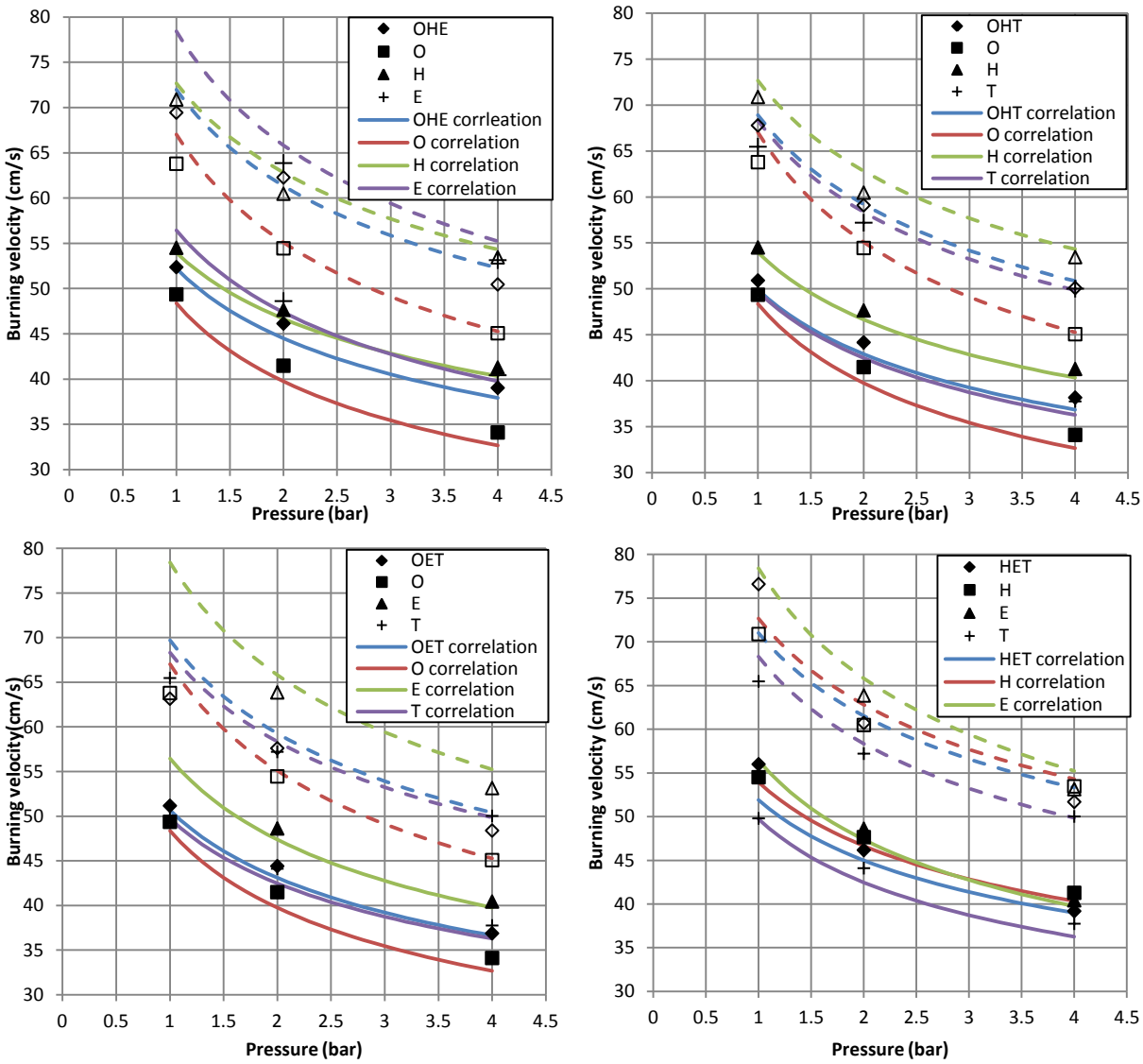

Figure 7.65 - Burning velocity results from image analysis (points) and correlation (lines) for stoichiometric ternary blends and their pure components. Solid symbols and lines represent 380 K, open symbols and dashed lines represent 450 K.

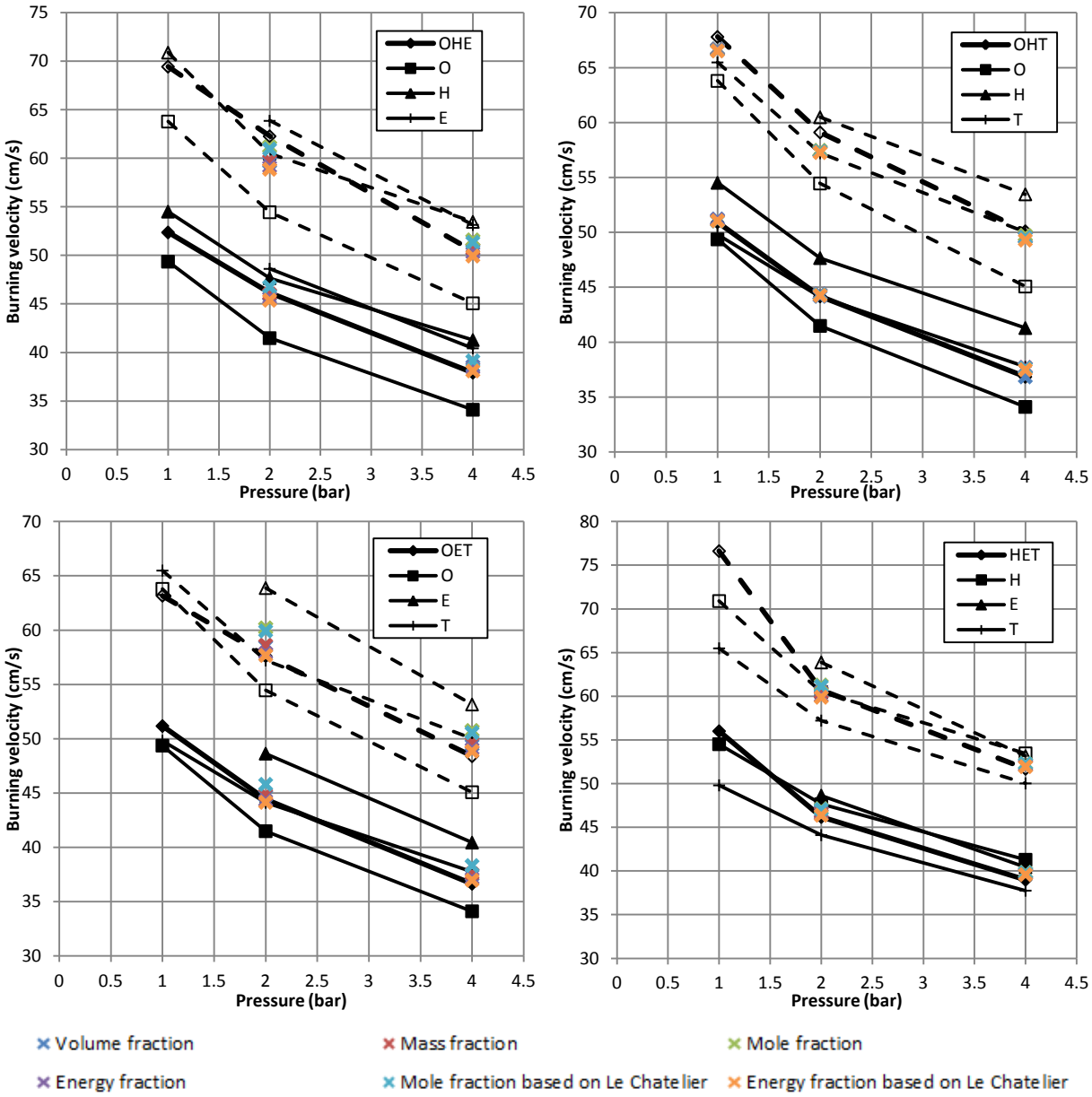

Figure 7.66 – Mixing rules for ternary blends compared with results from image analysis at 380 K (solid symbols) and 450 K (open symbols).

Table 7.11 - Burning velocities of stoichiometric ternary blends of THEO components from the literature, compared with results from the 3 term correlations (values in brackets represent extrapolated conditions).

Fuel	Temperature (K)	Pressure (bar)	Reference	Burning velocity (cm s^{-1})	
				Data	Correlation
OHE	298	1.0	van Lipzig *et al.* (2011)	38.0	(32.9)
	338	1.0	van Lipzig *et al.* (2011)	46.1	(41.8)

Röhl and Peters (2009) performed numerical simulations of a PRF87 mixed with 10% ethanol, giving a composition of 78.3% iso-octane, 11.7% n-heptane and 10% ethanol by volume, quite substantially different to the OHE blend. At 1 bar, 373 K the burning velocity of the blend is 28.9 cm s^{-1} according to the mechanism and 29.6 cm s^{-1} from the OHE correlation; at 20 bar these values reduce to 22.9 and 25.2 cm s^{-1} respectively.

7.4.5 THEO blend

The THEO blend is an equal by volume mixture of the four components. The results of the image analysis and correlations are plotted in Figure 7.67. At 380 K the correlation appears to give lower values than the image analysis results but at 450 K the agreement is closer. The burning velocity of the THEO blend most closely resembles that of toluene.

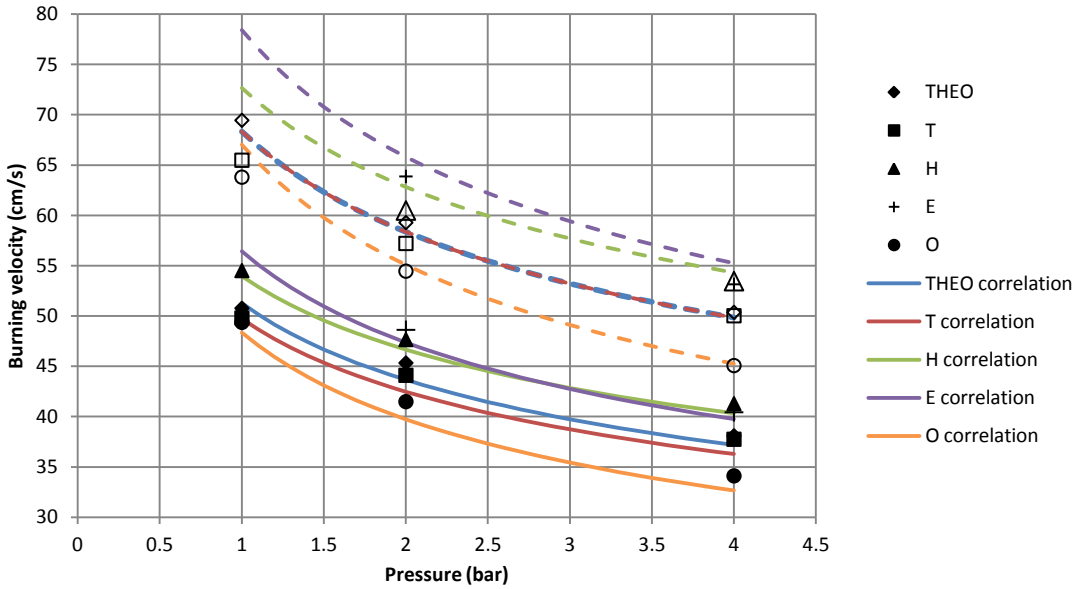

Figure 7.67 - Results from image analysis (points) and correlation (lines) for the HET blend. Solid lines and symbols represent 380 K, open symbols and dashed lines represent 450 K.

The image analysis results are compared to the mixing rules in Figure 7.68. The spread of mixing rules is much reduced for the quaternary blend, making a conclusion on the best fit difficult. In the case of 380 K, the rules based upon energy fraction could once again be considered to give the best fit.

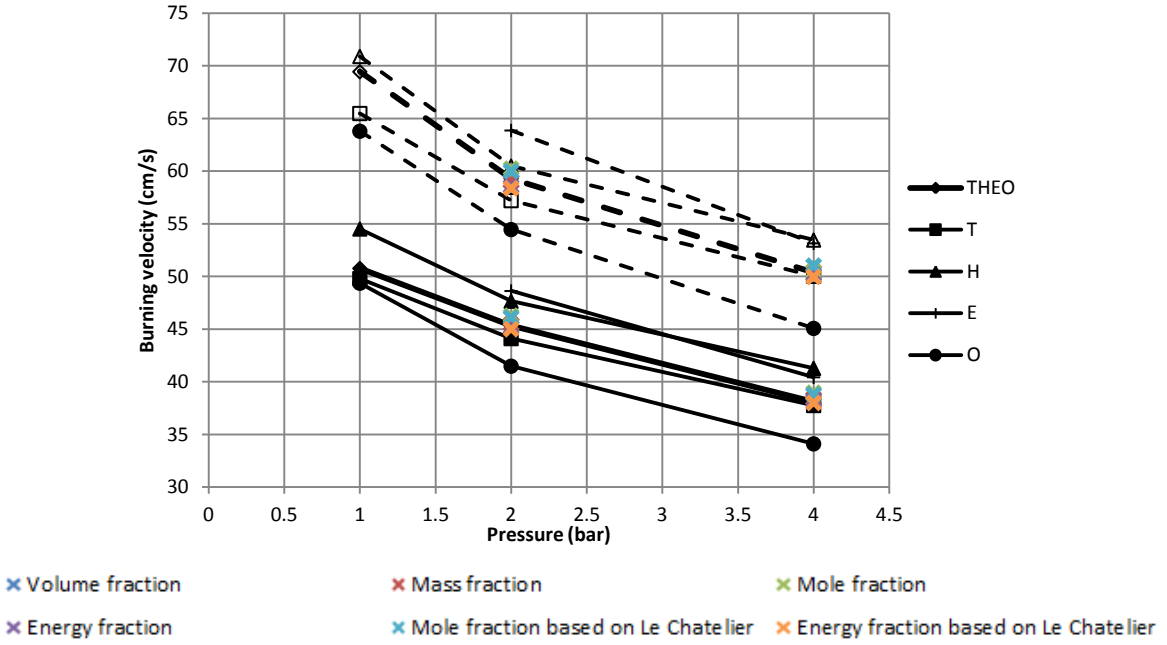

Figure 7.68 - Mixing rules for the THEO blend compared with results from image analysis at 380 K (solid symbols) and 450 K (open symbols).

No studies of quaternary blends blended on an equal volume basis have been found in the literature, although other blends have been studied. Dirrenberger *et al.* (2014) add 15% ethanol by volume to TAE7000 and their TRF described in section 7.4.4 making the blend 11.6% n-heptane, 36.5% iso-octane, 36.9% toluene and 15% ethanol. However, the addition of ethanol was found to have negligible effect upon the burning velocities of both the surrogate and the TAE7000 fuel. This is loosely reflected in the current results where the THEO blend is found to have only a slightly higher burning velocity than the OHT blend.

Sileghem *et al.* (2012) extended the simulation of a TRF to include ethanol in two blends, E20 and E75. The E20 is the closest representation to the current THEO blend, with a composition of 55.2% iso-octane, 11.2% n-heptane, 13.6% toluene and 20% ethanol. At 40 bar 600 K, this E20 blend has a burning velocity of 48.9 cm s^{-1} using the chemical kinetic mechanism of Andrae *et al.* (2008) at the same conditions, the experimental THEO correlation gives a burning velocity of 51.6 cm s^{-1}.

7.4.6 Further properties

For the other fuels investigated, trends in Markstein lengths and onset of cellularity were investigated, although for the various blends of THEO components, the fact that only stoichiometric mixtures were tested limits the usefulness of this analysis. Burned gas Markstein lengths for the pure components and various blends at 380 K are shown in Figure 7.69. Firstly, it can be seen that the burned gas Markstein lengths are positive for all stoichiometric mixtures. Whilst the same general trends with pressure are seen for all the fuel components and blends, there is no consistent trend with regards to the relative Markstein lengths of the blends. Indeed, it does not appear that the Markstein lengths of blends can be represented by mixing rules in the same way as burning velocities have been. Much of this may be due to the difficulties in determining Markstein lengths experimentally with the current experimental apparatus.

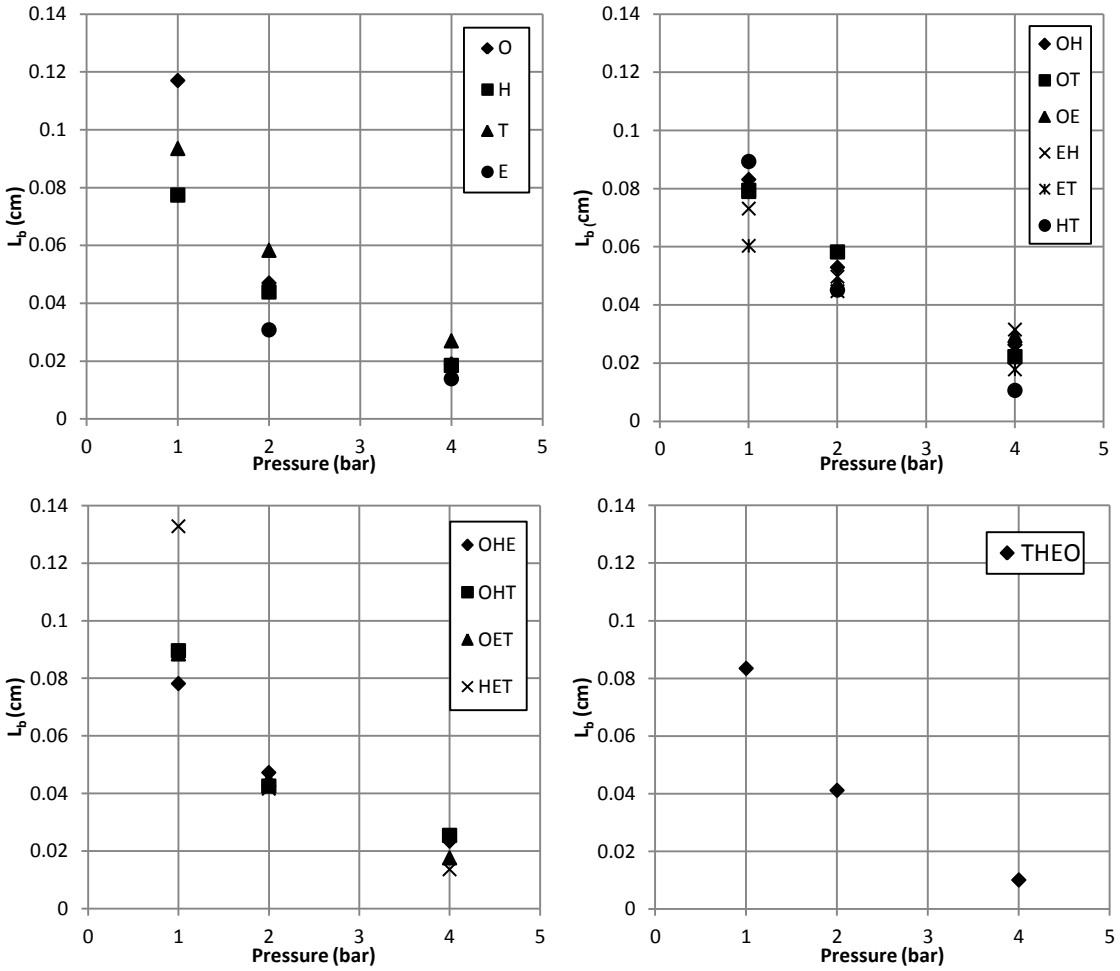

Figure 7.69 - Burned gas Markstein lengths for THEO components and blends at T_u = 380 K.

Broustail *et al.* (2011) present burned gas Markstein lengths for their blends of iso-octane and ethanol, and generally found that the value for the blend would be bounded by the pure components, although their results show similar inconsistencies as seen in the present work.

In the work of Beeckmann *et al.* (2009), it was reported that the addition of 10% ethanol to iso-octane resulted in a later onset of cellularity for rich mixtures. Since only stoichiometric mixtures were tested it is not possible to draw direct comparisons, but in the case of stoichiometric mixtures, a similar effect was not seen. In fact, it is not possible to determine any consistent trends in the onset of cellularity between the blends, although in the case of the binary blends, the pressure at onset of cellularity is bounded by those of the pure components, the exception being that of EH, which did show a later onset of cellularity than either pure ethanol or n-heptane.

7.4.7 Conclusions

In summary, it has been shown that behaviour of stoichiometric THEO blends can be well approximated by mixing rules presented in the literature. In most cases, since the measured burning velocities of the individual components are close in value, the burning velocities of blends predicted by the mixing rules are also close in value, and all show good agreement with experimental results. Where the difference between individual components is larger, resulting in greater differences in the burning velocities, the mixing rules based upon energy fraction of the mixture appear to give the best fit to the experimental data. Burned gas Markstein lengths are presented, and show consistent behaviour with pressure. Blends also showed similar behaviour with respect to onset of cellularity.

Table 7.12 – Correlation coefficients for all correlations developed in the current work

	$S_{u,0}$	$S_{u,1}$	$S_{u,2}$	$S_{u,3}$	$S_{u,4}$	α_0	α_1	α_2	β_0	β_1	β_2	μ_0	μ_1	μ_2
Biogas A	30.799	1.6141	-241.19	-22.214	680.84	2.0879	0.17135	5.4338	-0.34631	-0.04190	-0.90674	1.1050	1.1779	-0.76207
Biogas B	36.505	8.9356	-296.05	-72.852	854.10	1.8613	-0.42076	6.7162	-0.40025	0.11708	-0.88005	0.96849	1.0575	-0.69112
Ethanol A	35.616	21.159	-130.38	-38.952	79.839	1.9195	-0.24630	2.3624	-0.25960	0.21003	-0.30893	1.4380	1.4111	0.20056
Ethanol B	38.563	37.923	-134.70	-104.97	64.071	1.7610	-0.79184	3.1811	-0.26597	0.08143	-0.65099	1.5080	1.4875	0.20056
Ethanol C	36.891	27.326	-132.93	-60.926	73.593	1.8628	-0.40651	2.4956	-0.25193	0.19953	-0.34566	1.4364	1.4069	0.20056
Ethanol D	38.770	39.242	-134.84	-108.96	65.828	1.7574	-0.79509	3.0486	-0.25280	0.11923	-0.58752	1.4843	1.4573	0.20056
O	30.241					1.9315			-0.28327					
H	35.179					1.7601			-0.20999					
T	31.486					1.8799			-0.22747					
E	35.176					1.9455			-0.25282					
OH	33.505					1.8612			-0.26054					
OT	31.077					1.9000			-0.24356					
OE	32.520					1.8746			-0.23838					
EH	31.021					2.0797			-0.24068					
ET	32.931					1.8920			-0.23235					
HT	32.982					1.8694			-0.21921					
OHE	32.924					1.8975			-0.23078					
OHT	31.411					1.9064			-0.21911					
OET	32.039					1.8860			-0.23384					
HET	33.110					1.8512			-0.20664					
THEO	32.407					1.8882			-0.23211					

8 Conclusions and future work

8.1 Conclusions

This work presents laminar burning velocity results for a variety of different fuels, using constant volume combustion vessel techniques. Burning velocity data is required for understanding of combustion, use in engine simulations, and for validation of chemical kinetic mechanisms. Laminar burning velocity has been shown to be a fundamental property of a fuel-air mixture, which is dependent upon the mixture composition, conditions of temperature and pressure, and the presence of any diluent components. Much of the existing laminar burning velocity data is presented at low temperatures and pressures, and there is a need for data at elevated conditions relevant to combustion in engines.

Two techniques have been used to determine burning velocities: flame front imaging at conditions of constant pressure and analysis of the pressure rise during constant volume combustion. Reconciliation of these two methods has been demonstrated for the first time, providing a strong cross validation of the two methods. The first method requires extrapolation of flame speed data to provide an unstretched burning velocity at a single condition of temperature and pressure, as well as a Markstein length to represent the effect of stretch upon the flame. The second method requires a combustion model, and provides results at elevated pressures and temperatures, which are fitted to a general correlation. The experimental results presented in chapter 7 have shown that agreement can be seen between the burning velocity results determined from both constant pressure flame front image analysis and those from a pressure history derived burning velocity correlation.

The correlation has been developed to include pressure and temperature exponents with a second order dependence upon equivalence ratio. The second order dependence seen in the fits is in agreement with the most recent investigations, demonstrating the improvement in

understanding in this area. This inclusion of the second order dependence has allowed a more reliable representation of the temperature dependence of the burning velocity within derived correlations, which is of great importance in engine modelling where knowledge of behaviour at elevated conditions of temperature and pressure is vital.

It has been shown that by comparing correlations from different data sets that the spread of data included within the set to which the correlation is fitted has an effect upon the quality of the correlation; when extrapolating back beyond the range of temperatures and pressures to which data has been fitted, the correlation can no longer be expected to produce reliable results. Including additional data for ambient conditions has been shown to improve the performance of the correlation when extrapolated, without adversely affecting the results at elevated conditions. This addresses one of the enduring problems of the technique of fitting correlations to pressure derived measurements of burning velocity.

The problem of stretch in correlations obtained from pressure derived burning velocity measurements has been addressed by correcting for stretch in the data and has been demonstrated using values of unburned gas Markstein lengths obtained by Varea *et al.* (2013) measured directly using novel imaging and post-processing techniques. The difference is shown to be relatively modest as a result of the decreasing stretch rates once the flame radius increases. However, use of the technique has allowed a more accurate correlation to be derived.

The effects of stretch on flames at conditions of constant pressure have been investigated by determining Markstein lengths and their dependence upon mixture composition and conditions of temperature and pressure. The analysis used is limited to linear extrapolation, due to the limitations imposed by available window diameter. However, where existing data is available, results determined here are in good agreement, despite the large scatter apparent in the published results. To address this variation in reported vessels, collaboration will be needed between research groups with different sized vessels and analysis routines.

Conditions at the onset of cellularity have been identified and compared for different mixtures at differing initial pressures. In all cases, pressure appears to be the most important factor in the onset of cellularity, and this is a key finding that could enable burning velocity measurements obtained using pressure rise data from constant volume vessels without optical access to be used without including data compromised by such instabilities.

Tests have been performed on biogas (mixtures of CH_4 and CO_2), for fractions of CO_2 up to 40% by mole. Increasing the CO_2 fraction results in decreased burning velocities, and a shift in the peak burning velocity towards stoichiometric mixtures, trends which are also seen in chemical kinetic modelling and elsewhere in the literature. Markstein lengths were shown to increase and the onset of cellularity is delayed as CO_2 content increased. The correlation developed (including additional low temperature data) showed good agreement in terms of the temperature and pressure exponents with those found elsewhere in the literature. Chemical kinetic modelling has been performed using the GRI 3.0 mechanism and the FlameMaster package to simulate 1D premixed combustion. Results were obtained for a range of equivalence ratios, temperatures, pressures and CO_2 fractions, and good agreement was seen. As the CO_2 content is increased, there is noticeably less good agreement with the mechanisms at elevated conditions, which implies the possibility of the temperature and pressure dependence terms being themselves dependent upon the diluent fraction.

Hydrous ethanol showed stable combustion up to 40% water content by volume, with a non-linear decrease in burning velocity with increasing water content. The effect of water on the stoichiometry of the peak burning is small in the experimental results, although the simulation results suggest that there should be a shift towards stoichiometric. Markstein lengths appear relatively unaffected by the addition of water, although the onset of cellularity is delayed. Once again, the correlation gives a good agreement with existing data when additional data are included, and demonstrates that the temperature and pressure dependence is well captured. Chemical kinetic modelling has been performed by Carsten Olm at Eötvös Loránd

University, using the OpenSMOKE 1D premixed flame solver at the same conditions as the experimental data, and shows good agreement. Once again, agreement becomes less good at higher volume fractions of water, suggesting that the temperature and pressure dependence terms are again dependent upon diluent fraction. Tests have been performed with hydrous ethanol in a single cylinder engine, and results suggest a good correlation between the measured laminar burning velocities and early burn rates in the engine, which show a similarly non-linear behaviour. Combustion stability remained good for all water fractions up to 40%, although there are of course practical implications of such high water content in the case of real engines and fuelling systems.

Binary, ternary and quaternary blends of THEO components have been tested on an equal-by-volume basis. Such blends are roughly representative of PRFs, TRFs and blends of such reference fuels with ethanol. Blends tested generally showed good agreement with the various mixing rules, particularly those based upon energy fraction. Only the blend of ethanol and n-heptane showed any real deviation from this trend, having a lower burning velocity than the two components at 380 K, yet higher burning velocity at 450 K, although this is in contrast to a previous study of blends of ethanol and n-heptane. Further tests would be required to investigate this further, such as testing of the blends over a range of equivalence ratios.

8.2 Future work

A number of potential studies arise from the conclusions of this work. The most obvious extensions of the work will be to perform further tests using the same techniques but for a range of different fuels, to increase the available data for fuels of interest at conditions of elevated temperature and pressure. Of interest will be extending the THEO data set. This would require testing of all blends at equivalence ratios lean and rich of stoichiometric to determine more precisely the effect of equivalence ratio, and perhaps more importantly the accurate temperature and pressure dependence as equivalence ratio is varied. In this work binary, ternary and quaternary blends have been mixed on an equal-by-volume basis for the purpose of identifying

any unexpected trends and for assessment of the performance of mixing rules, but to determine the performance of these mixing rules more fully, blends of different compositions will need to be tested. Testing 4-component blends across a full range of compositions and equivalence ratios is a potentially huge project (hence limiting to stoichiometric mixtures and equal-by-volume blends in this study), so a few select test conditions should be considered to assess whether mixing rules are sufficiently accurate to determine intermediate values. Since the burning velocities are relatively close in value, it will be necessary to make repeat measurements to ensure consistency. Concentrating instead on just the components of a TRF (iso-octane, n-heptane and toluene) would allow a ternary diagram to be plotted for burning velocities, which can be compared against kinetic models for TRFs.

Testing of fuels other than hydrocarbons and oxygenates presents interesting opportunities. For example, ammonia has potential as a store of hydrogen which with some enrichment can be burned in combustion engines. Some work on determining laminar burning velocities has been done, e.g. Lee *et al.* (2010); however, further investigations for engine relevant conditions would be beneficial to research.

With advances in chemical kinetic modelling, it is increasingly important that studies of burning velocity are carried out in conjunction with kineticists, to obtain a more complete picture of laminar combustion. This would also ensure that the appropriate data for mechanism validation is being obtained. Of particular interest is the disagreement between the mechanisms and the experimental correlations at elevated conditions when the fraction of diluent was increased in both the biogas and hydrous ethanol mixtures.

With the current experimental apparatus, it is clear that some limitations have been reached. With regards to flame speed measurements, and investigations of the effects of stretch, useful data extraction is limited by the physical size of the windows. This limit on the range of data that can be extracted has implications on the accuracy of extrapolated values of flame speed and Markstein length. To improve the range of flame radii that can be observed, a larger

vessel would need to be commissioned, since an increase in window radius would also require a larger vessel radius to maintain conditions of constant pressure when imaging the flame front and avoid the need for the kind of correction detailed in section 2.5.6. A larger vessel will also allow direct comparison of results from different sized vessels, which offers the potential to investigate the effects of stretch more thoroughly.

A further limitation of the current apparatus is the maximum temperature and pressure that can be tested. Initial pressures are limited by the expected peak pressures during combustion, which must remain below the rated pressure of 34 bar for the vessel. Increasing the rated pressure of the vessel will allow higher initial pressures to be tested, although for many fuels the useful pressure range is limited by the onset of cellularity.

An important direction for the combustion community as a whole is to improve burning velocity measurements at elevated temperature and pressure. For this reason, more collaboration is needed between workers using the constant volume combustion vessel method to determine the cause of discrepancies in measurements of burning velocity and Markstein lengths, and to understand better the effect of vessel size and analysis procedures upon the determined results.

Bibliography

Agnew, J. T. and L. B. Graiff (1961). "The pressure dependence of laminar burning velocity by the spherical bomb method." Combustion and Flame **5**: 209-219.

Al-Baghdadi, M. A. R. S. (2008). "Measurement and prediction study of the effect of ethanol blending on the performance and pollutants emission of a four-stroke spark ignition engine." Proceedings of the Institution of Mechanical Engineers, Part D: Journal of Automobile Engineering **222**(5): 859-873.

Andrae, J. C. G., T. Brinck and G. T. Kalghatgi (2008). "HCCI experiments with toluene reference fuels modeled by a semidetailed chemical kinetic model." Combustion and Flame **155**(4): 696-712.

Andrews, G. E. and D. Bradley (1972). "The Burning Velocity of Methane-Air Mixtures." Combustion and Flame **19**: 275-288.

Andrews, G. E. and D. Bradley (1972). "Determination of burning velocities A critical review." Combustion and Flame **19**: 275-288.

Andrews, G. E. and D. Bradley (1973). "Limits of flammability and natural convection for methane-air mixtures". 14th Symposium (International) on Combustion. 1119-1128

Atkins, P. W. (1994). "Physical Chemistry". Oxford University Press.

Aucejo, A., M. C. Burguet, R. Muñoz and J. L. Marques (1995). "Densities, viscosities, and refractive indices of some n-alkane binary liquid systems at 298.15K." Journal of Chemical and Engineering Data **40**: 141-147.

Bedoya, I. D., A. A. Arrieta and F. J. Cadavid (2009). "Effects of mixing system and pilot fuel quality on diesel-biogas dual fuel engine performance." Bioresource technology **100**(24): 6624-6629.

Beeckmann, J., O. Röhl and N. Peters (2009). "Experimental and Numerical Investigation of Iso-Octane, Methanol and Ethanol Laminar Burning Velocity at Elevated Pressure and Temperature." SAE paper 2009-01-1774

Bosschaart, K. J. and L. P. H. de Goey (2003). "Detailed analysis of the heat flux method for measuring burning velocities." Combustion and Flame **132**: 170-180.

Bradley, D., P. H. Gaskell and X. J. Gu (1996). "Burning Velocities, Markstein Lengths and Flame Quenching for Spherical Methane-Air Flames A Computational Study." Combustion and Flame **104**: 176-198.

Bradley, D., S. E.-D. Habik and S. A. El-Sherif (1991). "A generalization of laminar burning velocities and volumetric heat release rates." Combustion and Flame **87**: 336-346.

Bradley, D. and C. M. Harper (1994). "The development of instabilities in laminar explosion flames." Combustion and Flame **99**: 562-572.

Bradley, D., R. A. Hicks, M. Lawes, C. G. W. Sheppard and R. Woolley (1998). "The measurement of laminar burning velocities and Markstein numbers for iso-octane and iso-octane-air mixtures at elevated temperatures and pressures in an explosion bomb." Combustion and Flame **115**: 126-144.

Bradley, D., M. Lawes and M. S. Mansour (2009). "Explosion bomb measurements of ethanol–air laminar gaseous flame characteristics at pressures up to 1.4MPa." Combustion and Flame **156**(7): 1462-1470.

Bradley, D., C. G. W. Sheppard, I. M. Suardjaja and R. Woolley (2004). "Fundamentals of high-energy spark ignition with lasers." Combustion and Flame **138**(1-2): 55-77.

Brewster, S. (2007). "Initial Development of a Turbo-charged Direct Injection E100 Combustion System". 14th Asia Pacific Automotive Engineering Conference. Hollywood, California, USA. SAE.

Brewster, S., D. Railton, M. Maisey and R. Frew (2007). The Effect of E100 Water Content on High Load Performance of a Spray Guide Direct Injection Boosted Engine. Congresso SAE Brasil. Sao Paulo. **2007-01-2648**.

Broustail, G., P. Seers, F. Halter, G. Moréac and C. Mounaim-Rousselle (2011). "Experimental determination of laminar burning velocity for butanol and ethanol iso-octane blends." Fuel **90**(1): 1-6.

Burluka, A., M. Fairweather, M. Ormsby, C. Sheppard and R. Woolley (2007). "The laminar burning properties of premixed methane-hydrogen flames determined using a novel analysis method". Third European Combustion Meeting.

Candel, S. and T. Poinsot (1990). "Flame Stretch and the Balance Equation for the Flame Area." Combustion Science and Technology **70**(1): 1-15.

Chen, Z. (2011). "On the extraction of laminar flame speed and Markstein length from outwardly propagating spherical flames." Combustion and Flame **158**(2): 291-300.

Chen, Z., M. Burke and Y. Ju (2009). "Effects of Lewis number and ignition energy on the determination of laminar flame speed using propagating spherical flames." Proceedings of the Combustion Institute **32**(1): 1253-1260.

Chen, Z., M. P. Burke and Y. Ju (2009). "Effects of compression and stretch on the determination of laminar flame speeds using propagating spherical flames." Combustion Theory and Modelling **13**(2): 343-364.

Chen, Z. and Y. Ju (2007). "The stretch effect on the accurate determination of laminar flame speed using expanding flames in a spherical bomb." 2007 Fall Technical Meeting Eastern States Section of the Combustion Institute

Chen, Z., X. Qin, Y. Ju, Z. Zhao, M. Chaos and F. L. Dryer (2007). "High temperature ignition and combustion enhancement by dimethyl ether addition to methane–air mixtures." Proceedings of the Combustion Institute **31**(1): 1215-1222.

Clarke, A. (1994). Measurement of laminar burning velocity of air/fuel/diluent mixtures in zero gravity. DPhil thesis, Department of Engineering Science, University of Oxford.

Cohé, C., C. Chauveau, I. Gökalp and D. F. Kurtuluş (2009). "CO2 addition and pressure effects on laminar and turbulent lean premixed CH4 air flames." Proceedings of the Combustion Institute **32**(2): 1803-1810.

Costa, R. C. and J. R. Sodré (2010). "Hydrous ethanol vs. gasoline-ethanol blend: Engine performance and emissions." Fuel **89**(2): 287-293.

Crookes, R. J. (2006). "Comparative bio-fuel performance in internal combustion engines." Biomass and Bioenergy **30**(5): 461-468.

Curran, H. J., P. Gaffuri, W. J. Pitz and C. K. Westbrook (1998). "A comprehensive modeling study of n-heptane oxidation." Combustion and Flame **114**: 149-177.

Daubert, T. E. and R. P. Danner (1997). "Physical and thermodynamic properties of pure chemicals", Taylor and Francis.

Davis, S. G. and C. K. Law (1998). "Determination of and Fuel Structure Effects on Laminar Flame Speeds of C1 to C8 Hydrocarbons." Combustion Science and Technology **140**(1): 427-449.

Davy, M. H. and R. Kowsari (2010). "Effect of ethanol content and fuel temperature on the macroscopic spray characteristics of a multi-hole DISI fuel injector." Fuel (In print).

"Directive 2009/28/EC of the European Parliament and of the Council of 23 April 2009 on the promotion of the use of energy from renewable sources and amending and subsequently repealing Directives 2001/77/EC and 2003/30/EC". Official Journal of the European Union. 2009/28/EC: 16-62.

Dirrenberger, P., P. A. Glaude, R. Bounaceur, H. Le Gall, A. P. da Cruz, A. A. Konnov and F. Battin-Leclerc (2014). "Laminar burning velocity of gasolines with addition of ethanol." Fuel **115**: 162-169.

Disarli, V. and A. Benedetto (2007). "Laminar burning velocity of hydrogen–methane/air premixed flames." International Journal of Hydrogen Energy **32**(5): 637-646.

Edmondson, H. and M. P. Heap (1969). "The burning velocity of methane-air flames inhibited by methyl bromide." Combustion and Flame **13**(5): 472-478.

Egolfopoulos, F. N., P. Cho and C. K. Law (1989). "Laminar Flame Speeds of Methane-Air Mixtures Under Reduced and Elevated Pressures." Combustion and Flame **76**: 375-391.

Egolfopoulos, F. N., N. Hansen, Y. Ju, K. Kohse-Höinghaus, C. K. Law and F. Qi (2014). "Advances and challenges in laminar flame experiments and implications for combustion chemistry." Progress in Energy and Combustion Science **43**: 36-67.

Eisazadeh-Far, K., A. Moghaddas, F. Rahim and H. Metghalchi (2010). "Burning Speed and Entropy Production Calculation of a Transient Expanding Spherical Laminar Flame Using a Thermodynamic Model." Entropy **12**(12): 2485-2496.

Elia, M., M. Ulinski and M. Metghalchi (2001). "Laminar Burning Velocity of Methane–Air–Diluent Mixtures." Journal of Engineering for Gas Turbines and Power **123**(1): 190.

Farrell, J. T., R. J. Johnston and I. P. Androulakis (2004). "Molecular Structure Effects On Laminar Burning Velocities At Elevated Temperature And Pressure." SAE paper 2004-01-2936

Ferguson, C. R. (1985). "International combustion engines; Applied thermosciences", Wiley.

Filho, O. V. (2008) Gasoline C made with Hydrous Ethanol.

Fiock, E. F., C. F. Marvin, F. R. Caldwell and C. H. Roeder (1940). "Flame speeds and energy considerations for explosions in a spherical bomb", National Advisory Comittee on Aeronautics, Report 682.

Galmiche, B., F. Halter, F. Foucher and P. Dagaut (2011). "Effects of Dilution on Laminar Burning Velocity of Premixed Methane/Air Flames." Energy & Fuels **25**(3): 948-954.

Garforth, A. M. and C. J. Rallis (1978). "Laminar burning velocity of stoichiometric methane-air pressure and temperature dependence." Combustion and Flame **31**: 53-68.

Goswami, M., S. C. R. Derks, K. Coumans, W. J. Slikker, M. H. de Andrade Oliveira, R. J. M. Bastiaans, C. C. M. Luijten, L. P. H. de Goey and A. A. Konnov (2013). "The effect of elevated pressures on the laminar burning velocity of methane+air mixtures." Combustion and Flame **160**(9): 1627-1635.

Gu, X. J., M. Z. Haq, M. Lawes and R. Woolley (2000). "Laminar Burning Velocity and Markstein Lengths of Methane-Air Mixtures." Combustion and Flame **121**: 41-58.

Gülder, O. L. (1982). "Laminar burning velocities of methanol, ethanol and isooctane-air mixtures." Proceedings of the Combustion Institute **19**: 275-281.

Gülder, O. L. (1984). "Burning velocities of ethanol-isooctane blends." Combustion and Flame **56**(3): 261-268.

Gülder, O. L. (1984). "Correlations of Laminar Combustion Data for Alternative SI Engine Fuels." SAE

Halter, F., F. Foucher, L. Landry and C. Mounaïm-Rousselle (2009). "Effect of Dilution by Nitrogen and/or Carbon Dioxide on Methane and Iso-Octane Air Flames." Combustion Science and Technology **181**(6): 813-827.

Halter, F., T. Tahtouh and C. Mounaïm-Rousselle (2010). "Nonlinear effects of stretch on the flame front propagation." Combustion and Flame **157**(10): 1825-1832.

Harris, M. E., J. Grumer, G. von Elbe and B. Lewis (1949). "Burning velocities, quenching, and stability data on nonturbulent flames of methane and propane with oxygen and nitrogen." Proceedings of the Combustion Institute **3**: 80-89.

Hassan, M. I., K. T. Aung and G. M. Faeth (1998). "Measured and Predicted Properties of Laminar Premixed Meathane-Air Flames at Various Pressures." Combustion and Flame **115**: 539-550.

Heghes, C. I. (2006). "C1-C4 Hydrocarbon Oxidation Mechanism", University of Heidelberg.

Heywood, J. B. (1988). Internal Combustion Engines Fundamentals, McGraw-Hill.

Hirasawa, T., C. J. Sung, A. Joshi, Z. Yang, H. Wang and C. K. Law (2002). "Determination of laminar flame speeds using digital particle image velocimetry - Binary Fuel blends of ethylene, n-Butane, and toluene." Proceedings of the Combustion Institute **29**(1427-1434).

Hu, E., Z. Huang, J. He, C. Jin and J. Zheng (2009). "Experimental and numerical study on laminar burning characteristics of premixed methane–hydrogen–air flames." International Journal of Hydrogen Energy **34**(11): 4876-4888.

Hu, M. (2013). "Measurements of OH* and CH* in a combustion volume combustion bomb", DPhil thesis, Department of Engineering Science, University of Oxford.

Huang, J. and R. J. Crookes (1998). "Assessment of simulated biogas as a fuel for the spark ignition engine." Fuel **77**(15): 1793-1801.

Huang, Y., C. Sung and J. Eng (2004). "Laminar flame speeds of primary reference fuels and reformer gas mixtures." Combustion and Flame **139**(3): 239-251.

Iijima, T. and T. Takeno (1986). "Effects of temperature and pressure on burning velocity." Combustion and Flame **65**(1): 35-43.

Jerzembeck, S., C. Glawe, J. Keppner and N. Peters (2008). "Laminar burning velocities from Schlieren- and pressure history measurements". 5th WSEAS International Conference on Fluid Mechanics, Acapaluco, Mexico.

Jerzembeck, S., N. Peters, P. Pepiotdesjardins and H. Pitsch (2009). "Laminar burning velocities at high pressure for primary reference fuels and gasoline: Experimental and numerical investigation." Combustion and Flame **156**(2): 292-301.

Ji, C., E. Dames, H. Wang and F. N. Egolfopoulos (2012). "Propagation and extinction of benzene and alkylated benzene flames." Combustion and Flame **159**(3): 1070-1081.

Johansen, T. and J. Schramm (2009). "Low-Temperature Miscibility of Ethanol-Gasoline-Water Blends in Flex Fuel Applications." Energy Sources, Part A: Recovery, Utilization, and Environmental Effects **31**(18): 1634-1645.

Johnston, R. J. and J. T. Farrell (2005). "Laminar burning velocities and Markstein lengths of aromatics at elevated temperature and pressure." Proceedings of the Combustion Institute **30**(1): 217-224.

Kalghatgi, G. (2014). "Fuel/Engine Interactions", SAE International.

Kalghatgi, G. T. (1985). "Early flame development in a spark-ignition engine." Combustion and Flame **60**: 299-308.

Karlovitz, B., J. Denniston, D. W., D. H. Knapschaefer and F. E. Wells (1953). "Studies on Turbulent Flames." Proceedings of the Combustion Institute **4**: 613-620.

Kelley, A. P. and C. K. Law (2007). Nonlinear Effects in the Experimental Determination of Laminar Flame Properties from Stretched Flames. Eastern State Fall Technical Meeting - Physical and Chemical Processes in Combustion. University of Virginia.

Kelley, A. P., W. Liu, Y. X. Xin, A. J. Smallbone and C. K. Law (2011). "Laminar flame speeds, non-premixed stagnation ignition, and reduced mechanisms in the oxidation of iso-octane." Proceedings of the Combustion Institute **33**(1): 501-508.

Konnov, A. A. (2009). "Implementation of the NCN pathway of prompt-NO formation in the detailed reaction mechanism." Combustion and Flame **156**(11): 2093-2105.

Konnov, A. A., R. J. Meuwissen and L. P. H. de Goey (2011). "The temperature dependence of the laminar burning velocity of ethanol flames." Proceedings of the Combustion Institute **33**(1): 1011-1019.

Ku, H.-C. and C.-H. Tu (2005). "Densities and Viscosities of Binary and Ternary Mixtures of Ethanol, 2-Butanone and 2,2,4-Trimethylpentane at T=(298.15,308.15 and 318.15) K." Journal of Chemical and Engineering Data **50**(2): 608-615.

Kumar, K. and C.-J. Sung (2010). "Flame Propagation and Extinction Characteristics of Neat Surrogate Fuel Components." Energy & Fuels **24**(7): 3840-3849.

Kuo, K. (1986). “Principles of Combustion”, Wiley.

Law, C. (2006). “Combustion Physics”, Cambridge University Press.

Lee, J. H., J. H. Kim, J. H. Park and O. C. Kwon (2010). "Studies on properties of laminar premixed hydrogen-added ammonia/air flames for hydrogen production." International Journal of Hydrogen Energy **35**(3): 1054-1064.

Leplat, N., P. Dagaut, C. Togbé and J. Vandooren (2011). "Numerical and experimental study of ethanol combustion and oxidation in laminar premixed flames and in jet-stirred reactor." Combustion and Flame **158**(4): 705-725.

Lewis, B. and G. von Elbe (1934). "Determination of the Speed of Flames and the Temperature Distribution in a Spherical Bomb from Time-Pressure Explosion Records." Journal of Chemical Physics **2**: 283-290.

Lewis, B. and G. von Elbe (1961). “Combustion, Flames and Explosions of Gases”. Academic Press Inc, London, UK.

Li, J., A. Kazakov, M. Chaos and F. Dryer (2007). “Chemical kinetics of ethanol oxidation”. 5th US Combustion Meeting, San Diego.

Liao, S., D. Jiang, Z. Huang, K. Zeng and Q. Cheng (2007). "Determination of the laminar burning velocities for mixtures of ethanol and air at elevated temperatures." Applied Thermal Engineering **27**(2-3): 374-380.

Liao, S. Y., J. Gao and Z. H. Huang (2005). "Measurements of Markstein Numbers and Laminar Burning Velocities for Natural Gas-Air Mixtures.2004,18, 316−326." Energy & Fuels **19**(1): 328-328.

Liao, S. Y., D. M. Jiang, J. Gao and Z. H. Huang (2004). "Measurements of Markstein Numbers and Laminar Burning Velocities for Natural Gas−Air Mixtures." Energy & Fuels **18**(2): 316-326.

Lindström, F., H.-E. Ångström, G. Kalghatgi and C. E. Möller (2005). "An Empirical Si Combustion Model Using Laminar Burning Velocity Correlations." SAE paper 2005-01-2106

Linnet, J. W. (1953). "Methods of measuring burning velocities." Proceedings of the Combustion Institute **4**: 20-35.

Liu, S., J. C. Hewson, J. H. Chen and H. Pitsch (2004). "Effects of strain rate on high-pressure nonpremixed n-heptane autoignition in counterflow." Combustion and Flame **137**(3): 320-339.

Luijten, C. C. M. and L. P. H. De Goey (2007). "New, Accurate, Analytical Relations for Fractional Pressure Rise, Laminar Burning Velocity, and the Cubic Root Law in Constant Volume Combustion". European Combustion Meeting.

Luijten, C. C. M., E. Doosje and L. P. H. de Goey (2009). "Accurate analytical models for fractional pressure rise in constant volume combustion." International Journal of Thermal Sciences **48**(6): 1213-1222.

Ma, H. (2006). "Optical Diagnostics and Combustion Analysis in a Gasoline Direct Injection Engine". DPhil thesis, Department of Engineering Science, University of Oxford.

Mack, J. H., S. M. Aceves and R. W. Dibble (2009). "Demonstrating direct use of wet ethanol in a homogeneous charge compression ignition (HCCI) engine." Energy **34**(6): 782-787.

Marinov, M. N. (1999). "A detailed chemical kinetic model for high temperature ethanol oxidation." International Journal of Chemical Kinetics **31**: 183-220.

Marshall, S. (2010). "Measuring Laminar Burning Velocities". DPhil thesis, Department of Engineering Science, University of Oxford.

Marshall, S., R. Stone, C. Heghes, T. Davies and R. Cracknell (2010). "High pressure laminar burning velocity measurements and modelling of methane and n-butane." Combustion Theory and Modelling **14**(4): 519-540.

Marshall, S. P., S. Taylor, C. R. Stone, T. J. Davies and R. F. Cracknell (2011). "Laminar Burning Velocity Measurements of Liquid Fuels at Elevated Pressures and Temperatures with Combustion Residuals." Combustion and Flame **158**: 1920-1932

Martinez-Frias, J., S. M. Aceves and D. L. Flowers (2007). "Improving Ethanol Life Cycle Energy Efficiency by Direct Utilization of Wet Ethanol in HCCI Engines." Journal of Energy Resources Technology **129**(4): 332.

Melo, T. C. C. d., G. B. Machado, C. R. P. Belchior, M. J. Colaço, J. E. M. Barros, E. J. de Oliveira and D. G. de Oliveira (2012). "Hydrous ethanol–gasoline blends – Combustion and emission investigations on a Flex-Fuel engine." Fuel **97**: 796-804.

Metghalchi, M. and J. C. Keck (1980). "Laminar Burning Velocity of Propane-Air Mixtures and High Temperature and Pressure." Combustion and Flame **38**: 143-145.

Metghalchi, M. and J. C. Keck (1982). "Burning Velocities of Mixtures of Air with Methanol, Isooctane and Indolene at High Pressures and Temperatures." Combustion and Flame **48**: 191-210.

Morgan, N., A. Smallbone, A. Bhave, M. Kraft, R. Cracknell and G. Kalghatgi (2010). "Mapping surrogate gasoline compositions into RON/MON space." Combustion and Flame **157**(6): 1122-1131.

Morley, C. (2005). "Gaseq: a chemical equilibrium program for Windows." http:// www.gaseq.co.uk.

Pepiot-Desjardins, P. and H. Pitsch (2008). "An efficient error-propagation-based reduction method for large chemical kinetic mechanisms." Combustion and Flame **154**(1-2): 67-81.

Pitsch, H. (1993). "FlameMaster: A C++ computer program for 0D combustion and 1D laminar flame calculations", Stanford University.

Plombin, C. (2003). “Biogas as Vehicle Fuel - A European Overview”. Trendsetter Report No 2003:3 Stockholm.

Poling, B., J. Prausnitz and J. O’Connell (2001). "The properties of liquids and gases." McGraw-Hill, New York.

Porpatham, E., A. Ramesh and B. Nagalingam (2008). "Investigation on the effect of concentration of methane in biogas when used as a fuel for a spark ignition engine." Fuel **87**(8-9): 1651-1659.

Powling, J. (1949). "A new burner method for the determination of low burning velocities and limits of inflammability." Fuel **28**(2): 25-29.

Qiao, L., W. J. A. Dahm, G. M. Faeth and E. S. Oran (2008). "Burning Velocities and Flammability Limits of Premixed Methane/Air/Diluent Flames in Microgravity." 46th AIAA Aerospace Sciences Meeting

Rahim, F., M. Ulinski and M. Metghalchi (2002). "Burning velocity measurements of methane-oxygen-argon mixtures and an application to extend methane-air burning velocity measurements." International Journal of Engine Research **3**(2): 81-92.

Raine, R. R., C. R. Stone and J. Gould (1995). "Modelling of Nitric Oxide Formation in Spark Ignition Engines with a Multi-zone Burned Gas." Combustion and Flame **102**: 241-255.

Rallis, C. J. and A. M. Garforth (1980). "The Determination of Laminar Burning Velocity." Progress in Energy and Combustion Science **6**: 303-329.

Rassweiler, G. M. and L. Withrow (1938). “Motion pictures of engine flames correlated with pressure cards”, SAE Technical Paper.

Reid, R. C., J. M. Prausnitz and B. C. Poling (1987). “The Properties of Gases and Liquids”, Mc-Graw Hill Book Company.

Reynolds, W. (1986). "The element potential method for chemical equilibrium analysis: Implementation in the interactive program STANJAN, version 3." Technical Report.

Rhodes, D. B. and J. C. Keck (1985). “Laminar burning speed measurements of indolene-air-diluent mixtures at high pressures and temperatures”, SAE Technical Paper.

Röhl, O. J., Beeckmann, J. and N. Peters (2009). “Numerical investigation of laminar burning velocities of high octane fuel blends containing ethanol”. SAE paper 2009-01-0935.

Rohl, O. P., Norbert (2009). “A reduced mechanism for ethanol oxidation”. European Combustion Meeting, Vienna.

Ronney, P. D. and H. Y. Wachman (1985). "Effect of Gravity on Laminar Premixed Gas Combustion I - Flammability Limits and Burning Velocities." Combustion and Flame **62**: 107-119.

Rozenchan, G., D. L. Zhu, C. K. Law and S. D. Tse (2002). "Outward Propagation, Burning Velocities, and Chemical Effects of Methane Flames up to 60 atm." Proceedings of the Combustion Institute **29**: 1461-1469.

Saeed, K. and C. R. Stone (2004). "The modelling of premixed laminar combustion in a closed vessel." Combustion Theory and Modelling **8**(4): 721-743.

Saxena, P. and F. A. Williams (2007). "Numerical and experimental studies of ethanol flames." Proceedings of the Combustion Institute **31**(1): 1149-1156.

Sharma, S. P., D. D. Agrawal and C. P. Gupta (1981). "The pressure and temperature dependence of burning velocity in a spherical combustion bomb." Proceedings of the Combustion Institute **18**: 493-501.

Shimada, A. and T. Ishikawa (2013). "Improved thermal efficiency using hydrous ethanol reforming in SI engines." SAE paper 2013-24-0118

Sileghem, L., V. A. Alekseev, J. Vancoillie, E. J. K. Nilsson, S. Verhelst and A. A. Konnov (2014). "Laminar burning velocities of primary reference fuels and simple alcohols." Fuel **115**: 32-40.

Sileghem, L., V. A. Alekseev, J. Vancoillie, K. M. Van Geem, E. J. K. Nilsson, S. Verhelst and A. A. Konnov (2013). "Laminar burning velocity of gasoline and the gasoline surrogate components iso-octane, n-heptane and toluene." Fuel **112**: 355-365.

Sileghem, L., J. Vancoillie, J. Demuynck, J. Galle and S. Verhelst (2012). "Alternative Fuels for Spark-Ignition Engines: Mixing Rules for the Laminar Burning Velocity of Gasoline–Alcohol Blends." Energy & Fuels **26**(8): 4721-4727.

Singer, J. M. (1953). "Burning-velocity measurements on slot burners; comparison with cylindrical burner determinations." Proceedings of the Combustion Institute **4**: 352-358.

Stone, R. (2012). "Introduction to Internal Combustion Engines", Palgrave Macmillan.

Stone, R., A. Clarke and P. Beckwith (1998). "Correlations for the Laminar-Burning Velocity of Methane-Diluent-Air Mixtures Obtained in Free-Fall Experiments." Combustion and Flame **114**: 546-555.

Strahle, W. C. (1993). "An Introduction to Combustion", Gordon and Breach Science Publishers.

Swami Nathan, S., J. M. Mallikarjuna and A. Ramesh (2010). "An experimental study of the biogas–diesel HCCI mode of engine operation." Energy Conversion and Management **51**(7): 1347-1353.

Tabaczynski, R. J., F. H. Trinker and B. A. S. Shannon (1980). "Further refinement and validation of a turbulent flame propagation model for spark-ignition engines." Combustion and Flame **39**: 111-121.

Tahtouh, T., F. Halter and C. Mounaïm-Rousselle (2009). "Measurement of laminar burning speeds and Markstein lengths using a novel methodology." Combustion and Flame **156**(9): 1735-1743.

Takizawa, K., A. Takahashi, K. Tokuhashi, S. Kondo and A. Sekiya (2005). "Burning velocity measurement of fluorinated compounds by the spherical-vessel method." Combustion and Flame **141**(3): 298-307.

Taylor, S. (2008). "Radius detection of a spherical flame observed with schlieren photography", Internal Report, University of Oxford.

Taylor, S. C. (1991). "Burning velocity and the influence of flame stretch", PhD thesis, University of Leeds.

Tse, S. D., D. L. Zhu and C. K. Law (2000). "Morphology and Burning Rates of Expanding Spherical Flames in H2-O2-Inert Mixtures Up To 60 Atmospheres." Proceedings of the Combustion Institute **28**: 1793-1800.

Tse, S. D., D. L. Zhu and C. K. Law (2004). "Optically accessible high-pressure combustion apparatus." Review of Scientific Instruments **75**(1): 233.

Turns, S. R. (1996). "An Introduction to Combustion: Concepts and Applications", McGraw-Hill.

Twiney, B. W. (2010)." Investigation of combustion robustness in catalyst heating operation on a spray guided DISI engine", DPhil thesis, Department of Engineering Science, Oxford University.

Vagelopoulos, C. M. and F. N. Egolfopoulos (1994). "Further considerations on the determination of laminar flame speeds with the counterflow twin-flame technique". Twenty-fifth Symposium (International) on Combustion, The Combustion Institute 1341-1347

van Lipzig, J. (2010). "Flame speed investigation of ethanol, n-heptane and iso-octane using the heat flux method." Masters Thesis, Division of Combustion Physics, Lund Institute of Technology, Lund, Sweden.

van Lipzig, J. P. J., E. J. K. Nilsson, L. P. H. de Goey and A. A. Konnov (2011). "Laminar burning velocities of n-heptane, iso-octane, ethanol and their binary and tertiary mixtures." Fuel **90**(8): 2773-2781.

Vancoillie, J., J. Demuynck, J. Galle, S. Verhelst and J. A. van Oijen (2012). "A laminar burning velocity and flame thickness correlation for ethanol–air mixtures valid at spark-ignition engine conditions." Fuel.

Varea, E., V. Modica, B. Renou and A. M. Boukhalfa (2013). "Pressure effects on laminar burning velocities and Markstein lengths for Isooctane–Ethanol–Air mixtures." Proceedings of the Combustion Institute **34**(1): 735-744.

Varea, E., V. Modica, A. Vandel and B. Renou (2012). "Measurement of laminar burning velocity and Markstein length relative to fresh gases using a new postprocessing procedure: Application to laminar spherical flames for methane, ethanol and isooctane/air mixtures." Combustion and Flame **159**(2): 577-590.

Verhelst, S., C. T'Joen, J. Vancoillie and J. Demuynck (2011). "A correlation for the laminar burning velocity for use in hydrogen spark ignition engine simulation." International Journal of Hydrogen Energy **36**(1): 957-974.

Verhelst, S., R. Woolley, M. Lawes and R. Sierens (2005). "Laminar and unstable burning velocities and Markstein lengths of hydrogen–air mixtures at engine-like conditions." Proceedings of the Combustion Institute **30**(1): 209-216.

Wang, S.-F., H. Zhang, J. Jarosinski, A. Gorczakowski and J. Podfilipski (2010). "Laminar burning velocities and Markstein lengths of premixed methane/air flames near the lean flammability limit in microgravity." Combustion and Flame **157**(4): 667-675.

Warnatz, J., U. Maas and R. W. Dibble (2006). "Combustion: Physical and Chemical Fundamentals, Modeling and Simulation, Experiments, Pollutant Formation", Springer.

West, C. and C. Hull (1933). "International critical tables." IIIMcGraw-Hill, New York: 370.

Williams, B., M. Edwards, R. Stone, J. Williams and P. Ewart (2014). "High precision in-cylinder gas thermometry using Laser Induced Gratings: Quantitative measurement of evaporative cooling with gasoline/alcohol blends in a GDI optical engine." Combustion and Flame **161**(1): 270-279.

Wu, C. K. and C. K. Law (1984). "On the determination of laminar flame speeds from stretched flames." Proceedings of the Combustion Institute **20**: 1941-1949.

Wyman, C. and N. Hinman (1990). "Ethanol: Fundamentals of production from renewable feedstocks and use as a transportation fuel." Applied Biochemistry and Biotechnology **24-25**(1): 735-753.

Zhang, Z., G. Li, L. Ouyang, Z. Pan, F. You and X. Gao (2011). "Experimental determination of laminar burning velocities and Markstein lengths for 75% hydrous-ethanol, hydrogen and air gaseous mixtures." International Journal of Hydrogen Energy **36**(20): 13194-13206.

Zhao, H. and N. Ladommatos (2001). "Engine combustion instrumentation and diagnostics." SAE, 842.

A. Appendix

A.1 Lambda sensor operation

Lambda sensors are required in automotive applications as part of the feedback control of the equivalence ratio, allowing the ratio and fuel and air to be adjusted depending upon the requirements of the engine. Lambda refers to the symbol commonly used to express the ratio of the actual air-fuel ratio (AFR) to the stoichiometric AFR; it is the inverse of the equivalence ratio used more widely in this work.

The lambda sensor, described in various works such as Stone (2012) and also commonly referred to as an oxygen sensor, is designed to output a voltage based upon the partial pressure of oxygen in the exhaust gas; in a weak mixture, there will be excess oxygen whereas in the rich case, there will be high levels of the partial products of combustion (CO, H_2 and hydrocarbons). A simple exhaust oxygen sensor element will contain two platinum electrodes separated by a layer of zirconia (ZrO_2) stabilised with yttrium oxide, which acts as a solid electrolyte for oxygen ions (O^{2-}) at high temperatures so that a voltage difference is established between the two electrodes. One electrode is exposed to air and the other to the exhaust gas, and the difference in partial pressures of oxygen will lead to a flow of electrons related to this difference in partial pressures. Since the platinum electrode also acts as a catalyst for the exhaust gases, the output from the lambda sensor for rich or stoichiometric air/fuel ratios will be high (just below 1 V), since the partial pressure of the oxygen will be many orders of magnitude lower than for air.

To allow accurate measurement of lean mixtures (important for lean burn engine control), the Universal Exhaust Gas Oxygen (UEGO) sensor was developed, as represented schematically in Figure A.1. This is essentially two lambda sensors back to back, with three zirconia layers, with platinum electrodes on the top two. The UEGO sensor aims to maintain a constant partial pressure of oxygen in the cavity between the pumping cell and sensing cell. The

sensing cell measures the oxygen partial pressure, and the current imposed on the pumping cell seeks to maintain a constant oxygen partial pressure in the measurement cavity between the sensing cell and the pumping cell. This effectively leads to two ‘modes’ of operation of the sensor, represented schematically in Figure A.1, one for lean mixtures and one for rich mixtures, which is hypothesised to be the cause of the difficulties encountered and described in section 6.1.3.

For weak mixtures, there will be excess oxygen in the exhaust gas, meaning a concentration gradient and hence oxygen diffusion across the porous gas intake to the measurement cavity. To maintain the low oxygen concentration in the measurement cavity, the pumping cell will be removing oxygen, and the current in that cell will be proportional to the exhaust gas oxygen concentration. For rich mixtures, there will be diffusion of the partial products of combustion into the measurement cavity, which will be oxidised, causing more products to diffuse in. The richer the mixture, the more products diffusing in, hence the greater the current in the pumping cell which is adding oxygen to maintain the oxygen concentration in the measurement cavity.

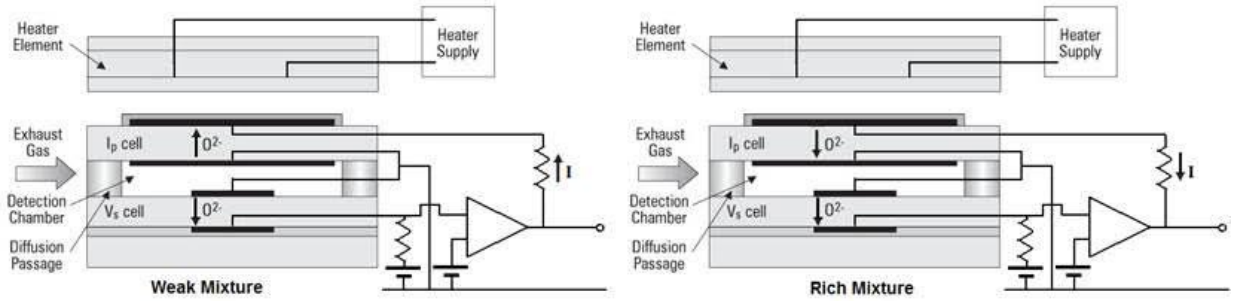

Figure A.1– The Universal Exhaust Gas Oxygen (UEGO) sensor structure and operation. Adapted from Zhao and Ladommatos (2001).

A.2 Detection of cellularity from the pressure record

To make use of the pressure record during constant volume combustion, it is important to be able to detect the onset of cellularity. This is relatively straightforward in vessels with optical access, though this is not always available. Detection of cellularity from the pressure record alone could potentially increase the ability of the research community to determine burning velocities using this technique.

Three terms involving pressure in Equation (3.21) were investigated for a single iso-octane-air experiment with an equivalence ratio of 1.22, at 2 bar and 380 K, as an example showing clear cellularity, and it was determined that the first derivative of pressure with respect to time had the largest influence upon the determined burning velocity. As the onset of cellularity is accompanied by a steep rise in the burning velocity, it would also be expected that the rate of increase of the derivative of pressure should increase also. The second derivative of pressure is therefore chosen as a potential representative. Figure A.2 shows the second derivative of pressure against time, along with the number of edges detected by *refreshbg*. Lines on the plot correspond to the schlieren images in Figure A.3.

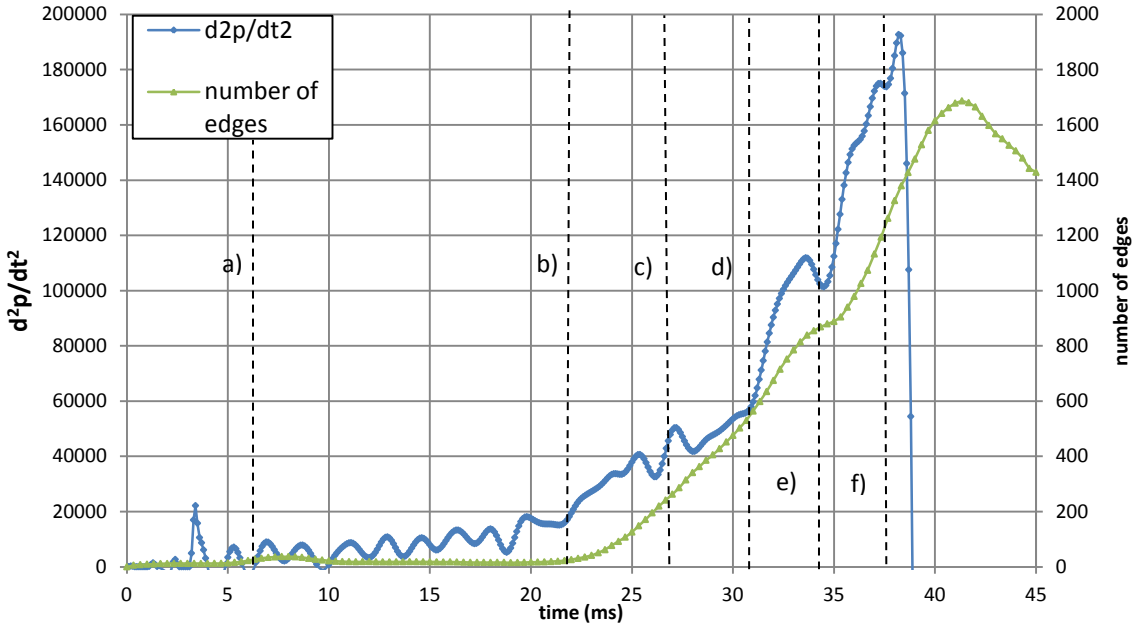

Figure A.2 –Second derivative of pressure and number of detected edges against time for a single rich iso-octane experiment at 2 bar, 380 K. Letters represent the equivalent point in combustion illustrated by the images in Figure A.3.

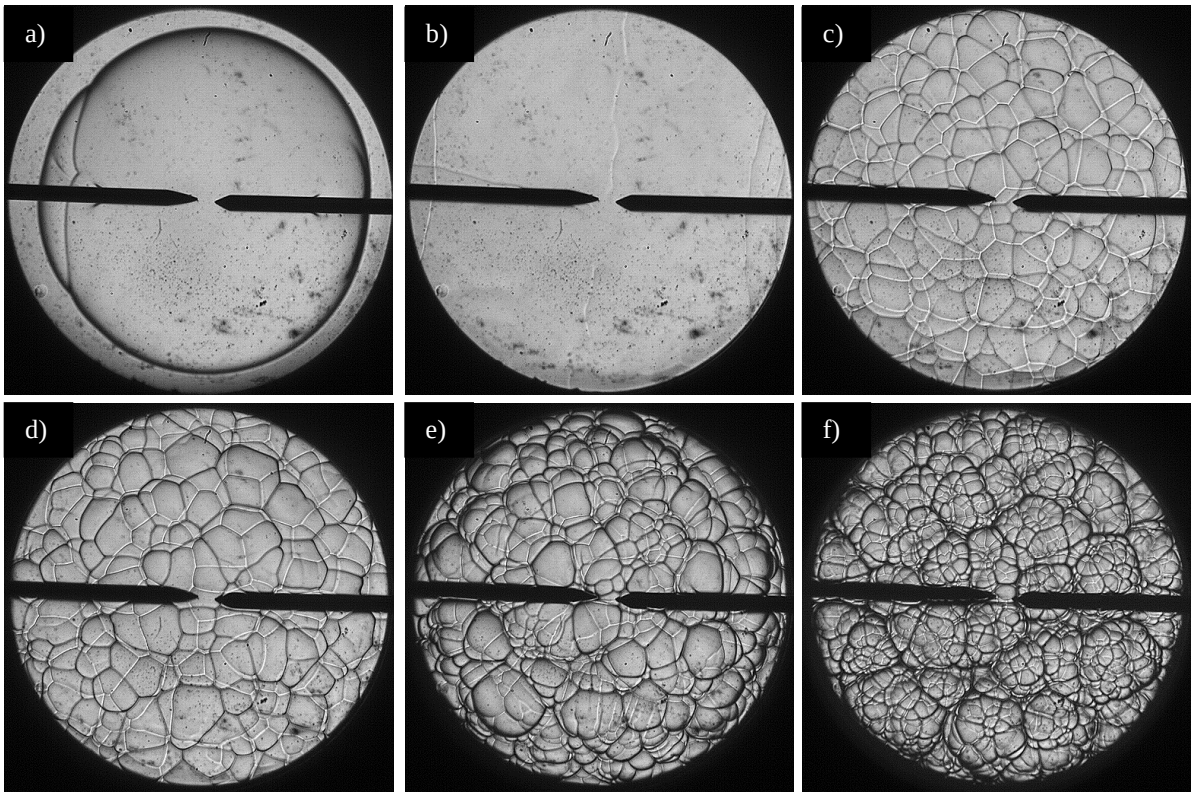

Figure A.3 – Schlieren images corresponding to points (a) to (f) on the plot in Figure A.2.

It can be seen that there appears to be a link between the successive stages of development of cellularity and step changes in the second derivative of pressure. However, for accurate detection, it would be vital that an event was picked up between points b) and c). Given the noise associated with the pressure measurement, and amplification of this upon differentiating, a consistent criteria will be hard to define with respect to pressure, compared to the edge detection algorithm, which offers a much clearer detection. In addition, the rate of change of pressure, and subsequent derivatives is likely to depend upon the exact mixture and conditions, as well as vessel size. Development of a robust detection process has not been pursued further, although this preliminary study does demonstrate a reasonable basis for such a technique, which can be developed further in future work.